
Nume Prenume: **Adrian Augustin POP**

Gradul didactic: Asistent Dr.Ing

Instituția unde este titular: Universitatea
Tehnică din Cluj-Napoca

Facultatea: Inginerie Electrica

Departamentul: Masini si Actionari Electrice

LISTA LUCRĂRILOR ȘTIINȚIFICE

A – Teza de doctorat

*Contributions to the study of small electronically-commutated axial-flux permanent-magnet machines.
Contributions à l'étude des petites machines électriques à aimants permanents, à flux axial et à auto-commutation électronique*

conducător științific: Prof.Dr.Ing Frédéric Gillon

École Centrale de Lille- Département d' Electrotechnique, Electronique, Automatique

conducător științific: Prof.Dr.Ing Mircea M.Radulescu

Universitatea Tehnică din Cluj-Napoca

Susținere publică: 15 Decembrie 2012.

B – Cărți și capitole în cărți publicate în ultimii 10 ani

CĂRȚI

1. Adrian Augustin Pop, Frederic Gillon, Mircea M. Radulescu - Small Electronically-Commutated Axial-Flux Permanent-Magnet Machines. LAMBERT Academic Publishing. Copyright 2013 AV Akademikerverlag GmbH &Co, Saarbrucken. ISBN 978-3-659-42624-7
2. Radu A. Munteanu, Adrian Augustin Pop, Horia Bălan -Tehnica măsurării marimilor electrice în sisteme de protecție a energiei electrice. Lucrări de laborator. Mediamira-2014. ISBN 978-973-713-316-8

C – Lucrări indexate

1. A. A. Pop, F. Jurca, C. Oprea, M. Chirca, S. Breban and M. M. Radulescu, "Axial-flux vs. radial-flux permanent-magnet synchronous generators for micro-wind turbine application," *2013 15th European Conference on Power Electronics and Applications (EPE)*, Lille, 2013, pp. 1-10.
doi: 10.1109/EPE.2013.6634639.
SCOPUS: ISBN: 978-147990116-6
<http://ieeexplore.ieee.org/document/6634639/>
2. A. A. Pop, F. Gillon and M. M. Radulescu, "Modeling and permanent-magnet shape optimization of an axial-flux machine," *2012 XXth International Conference on Electrical Machines*, Marseille, 2012, pp. 357-363.
doi: 10.1109/ICEIMach.2012.6349891
WOS:000333806700054
<http://ieeexplore.ieee.org/abstract/document/6349891/>

3. M. V. Zaharia, A. A. Laczko, A. A. Pop, M. M. Radulescu and F. Gillon, "Optimal commutation angles of a switched reluctance motor/generator," *2015 Tenth International Conference on Ecological Vehicles and Renewable Energies (EVER)*, Monte Carlo, 2015, pp. 1-8.
doi: 10.1109/EVER.2015.7113015
WOS:000380443100101
<http://ieeexplore.ieee.org/document/7113015/>
4. A.A. Pop, M. M. Radulescu, H. Balan, M. Chirca and V. Zaharia, "Electromagnetic design and finite-element analysis of an axial-flux permanent-magnet machine," *2014 International Conference on Applied and Theoretical Electricity (ICATE)*, Craiova, 2014, pp. 1-4.
doi: 10.1109/ICATE.2014.6972638
WOS:000352737400050
<http://ieeexplore.ieee.org/document/6972638/>
5. I. Lar, M. M. Radulescu, E. Ritchie and A. A. Pop, "Current control methods for grid-side three-phase PWM voltage-source inverter in distributed generation systems," *2012 13th International Conference on Optimization of Electrical and Electronic Equipment (OPTIM)*, Brasov, 2012, pp. 859-867.
doi: 10.1109/OPTIM.2012.6231945
WOS:000398866700129
<http://ieeexplore.ieee.org/document/6231945/>
6. A.A. Pop, M. Radulescu, H. Balan and H. Kanchev, "Electromagnetic torque capabilities of axial-flux and radial-flux permanent-magnet machines," *2013 4th International Symposium on Electrical and Electronics Engineering (ISEEE)*, Galati, 2013, pp. 1-4.
doi: 10.1109/ISEEE.2013.6674365
WOS:000335153400059
<http://ieeexplore.ieee.org/document/6674365/>
7. T. Varodi, H. Balan, A. A. Pop and M. Buzdugan, "Diagnosis of short circuit and the earthing of a transformer station," *2014 International Conference on Applied and Theoretical Electricity (ICATE)*, Craiova, 2014, pp. 1-6.
doi: 10.1109/ICATE.2014.6972613
WOS:000352737400025
<http://ieeexplore.ieee.org/abstract/document/6972613/>
8. A.A. Pop, M. Radulescu and H. Balan, "Flux-density space-harmonics minimization for an axial-flux permanent-magnet machine," *2013 4th International Symposium on Electrical and Electronics Engineering (ISEEE)*, Galati, 2013, pp. 1-5.
doi: 10.1109/ISEEE.2013.6674327
WOS:000335153400021
<http://ieeexplore.ieee.org/document/6674327/>
9. R. A. Munteanu, H. Balan, A. A. Pop and M. Buzdugan, "Wavelet analysis in monitoring and diagnosis of power circuit breakers," *2014 International Conference on Applied and Theoretical Electricity (ICATE)*, Craiova, 2014, pp. 1-6.
doi: 10.1109/ICATE.2014.6972669
WOS:000352737400080
<http://ieeexplore.ieee.org/document/6972669/>
10. H. Balan, M. Buzdugan, A. A. Pop and R. A. Munteanu, "Performances optimization and characteristics of the voltage generated by multilevel inverters," *2014 International Conference on Applied and Theoretical Electricity (ICATE)*, Craiova, 2014, pp. 1-6.
doi: 10.1109/ICATE.2014.6972647
WOS:000352737400059
<http://ieeexplore.ieee.org/document/6972647/>

11. D. L. Irimie, M. M. Radulescu, A. A. Pop and A. Laczko, "Loss analysis of small three-phase cage-induction motors under sinusoidal and PWM voltage supply," *2014 International Conference on Applied and Theoretical Electricity (ICATE)*, Craiova, 2014, pp. 1-5.
doi: 10.1109/ICATE.2014.6972642
WOS:000352737400054
<http://ieeexplore.ieee.org/document/6972642/>
12. Horia, P. A. Augustin, B. Mircea and B. Ioan, "Analysis of multilevel converters operation through programmable source emulators," *2014 49th International Universities Power Engineering Conference (UPEC)*, Cluj-Napoca, 2014, pp. 1-6.
doi: 10.1109/UPEC.2014.6934804
WOS:000364087800193
<http://ieeexplore.ieee.org/document/6934804/>
13. Horia, B. Mircea, P. A. Augustin and B. Ioan, "Modeling and simulation of current digital relays," *2014 49th International Universities Power Engineering Conference (UPEC)*, Cluj-Napoca, 2014, pp. 1-6.
doi: 10.1109/UPEC.2014.6934805
WOS:000364087800194
<http://ieeexplore.ieee.org/document/6934805/>
14. P. D. Teodosescu, M. Bojan, A. A. Pop and R. Marschalko, "Buck-boost corrector implementing for compact fluorescent lamp applications," *2012 13th International Conference on Optimization of Electrical and Electronic Equipment (OPTIM)*, Brasov, 2012, pp. 833-838.
doi: 10.1109/OPTIM.2012.6231878
WOS:000398866700125
<http://ieeexplore.ieee.org/document/6231878/>
15. Balan, H., Buzdugan, M., & Pop, A. A. (2014). Series Resonance Technique for Short-circuit Current Limiting Devices in DC Grids. In *Materials Science Forum* (Vol. 792, pp. 293-298). Trans Tech Publications.
ISSN: 1662-9752, vol 792, pp 293-298
<https://doi.org/10.4028/www.scientific.net/MSF.792.293>
16. Turcu Antoniu, Balan Horia, Pop Adrian Augustin, Sefanescu Silviu
"Insulation Resistance Testing Procedures",
Acta Electrotehnica, ISSN: 1841-3323, Vol. 54, No. 5, Special Issue: Proceedings of the 5th International Conference on Modern Power Systems (MPS), pp. 502-508, Cluj-Napoca, Romania, May 28-31, 2013.
https://ie.utcluj.ro/files/acta/2013/Number5/e-journalsummary_MPS2013.pdf
17. Varodi Traian, Balan Horia, Pop Adrian Augustin
"Monitoring 110/10kV Power Stations. A Case Study."
Acta Electrotehnica, ISSN: 1841-3323, Vol. 54, No. 5, Special Issue: Proceedings of the 5th International Conference on Modern Power Systems (MPS), pp. 522-526, Cluj-Napoca, Romania, May 28-31, 2013.
https://ie.utcluj.ro/files/acta/2013/Number5/e-journalsummary_MPS2013.pdf
18. Horia Balan, Mircea Buzdugan, Adrian Augustin Pop, Cristina Chiorean
"Reducing short circuit current in continuous voltage networks through hybrid commutation",
Acta Electrotehnica, ISSN: 1841-3323, Vol. 54, No. 5, Special Issue: Proceedings of the 5th International Conference on Modern Power Systems (MPS), pp. 45-51, Cluj-Napoca, Romania, May 28-31, 2013.
https://ie.utcluj.ro/files/acta/2013/Number5/e-journalsummary_MPS2013.pdf

D. Membru în proiecte câștigate prin competiții naționale

1. **Sisteme hibride de conversie a energiei regenerabile de mica putere integrate într-o micro retea** -MICROREN- denumirea programului din PN II: parteneriate in domenii prioritare, Cod proiect: PN-II-PT-PCCA-2011-3.2-1519 Autoritate contractanta (Sursa de finantare): U.E.F.I.S.C.D.I. Prof.dr.ing. Octavian PROȘTEAN – director de proiect, Universitatea din Timisoara

Data: Decembrie 2020

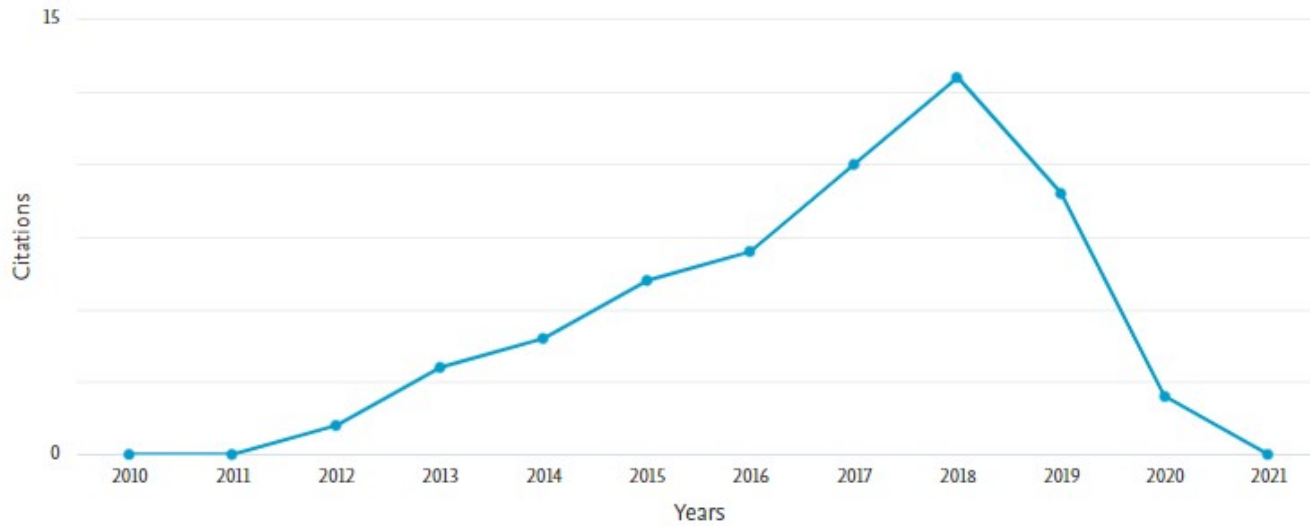
Semnătura



13 Cited Documents from "Pop, Adrian Augustin" [+ Save to list](#)

Author ID:10739106300

Date range: 2010 to 2021 Exclude self citations of selected author Exclude self citations of all authors Exclude citations from books [Update](#)



Sort on: Citation count (descending)

Page Remove

Documents	Citations	<2010	2010	2011	2012	2013	2014	2015	2016	2017	2018	2019	2020	2021	Subtotal	>2021	Total
	Total	0	0	0	1	3	4	6	7	10	13	9	2	0	55	0	55
<input type="checkbox"/> 1 Axial-flux vs. radial-flux permanent-magnet synchronous gene...	2013						2	1	5	5	6	2			21		21
<input type="checkbox"/> 2 Electromagnetic torque capabilities of axial-flux and radial...	2013							1	1			4			6		6
<input type="checkbox"/> 3 Optimal commutation angles of a switched reluctance motor/ge...	2015								1	2	1	1			5		5
<input type="checkbox"/> 4 Electromagnetic design and finite-element analysis of an axl...	2014										3	2			5		5
<input type="checkbox"/> 5 Modelling and permanent-magnet shape optimization of an axial...	2012					3	1	1							5		5
<input type="checkbox"/> 6 Wavelet analysis in monitoring and diagnosis of power circul...	2014										2		2		4		4
<input type="checkbox"/> 7 Flux-density space-harmonics minimization for an axial-flux ...	2013							3		1					4		4
<input type="checkbox"/> 8 Current control methods for grid-side three-phase PWM voltag...	2012						1			1					2		2
<input type="checkbox"/> 9 Diagnosis of short circuit and the earthing of a transformer...	2014										1				1		1
<input type="checkbox"/> 10 Series resonance technique for short-circuit current limitin...	2014									1					1		1
<input type="checkbox"/> 11 Buck-boost corrector implementing for compact fluorescent la...	2012				1										1		1
<input type="checkbox"/> 12 Performances optimization and characteristics of the voltage...	2014														0		0
<input type="checkbox"/> 13 Loss analysis of small three-phase cage-induction motors und...	2014														0		0

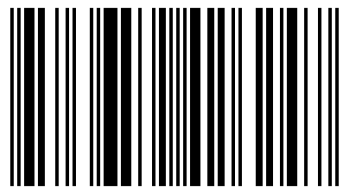
The research work presented is about small electronically-commutated axial-flux permanent-magnet (AFPM) machines having the double-sided topology of an inner rotor with surface-mounted Nd-Fe-B magnets, sandwiched between two outer slotted stators with distributed three-phase windings. After reviewing the small double-sided AFPM machine candidate topologies for low-speed direct-drive applications, the book hinges on the size equations and the analytical electromagnetic design of the inner-rotor AFPM (AFIPM) machine topology under study. Original methods of modelling and design optimization of a small prototype AFIPM machine are then proposed with the view to reducing the airgap flux density space-harmonics and the torque ripple by rotor-PM shape modification. Extensive experimental tests are carried out on the small three-phase AFIPM machine prototype in order to validate its proper design and to check its electronic commutation and basic control technique.

Axial flux permanent magnet machines



Adrian Augustin Pop

Phd. Eng. Adrian POP is an Assistant Professor at Technical University of Cluj Napoca, Faculty of Electrical Engineering where he serves as researcher in Electrical Machines domain. He is a member of Electrical Engineering and Power Electronics Research Laboratory (L2EP), Ecole Centrale de Lille, France.



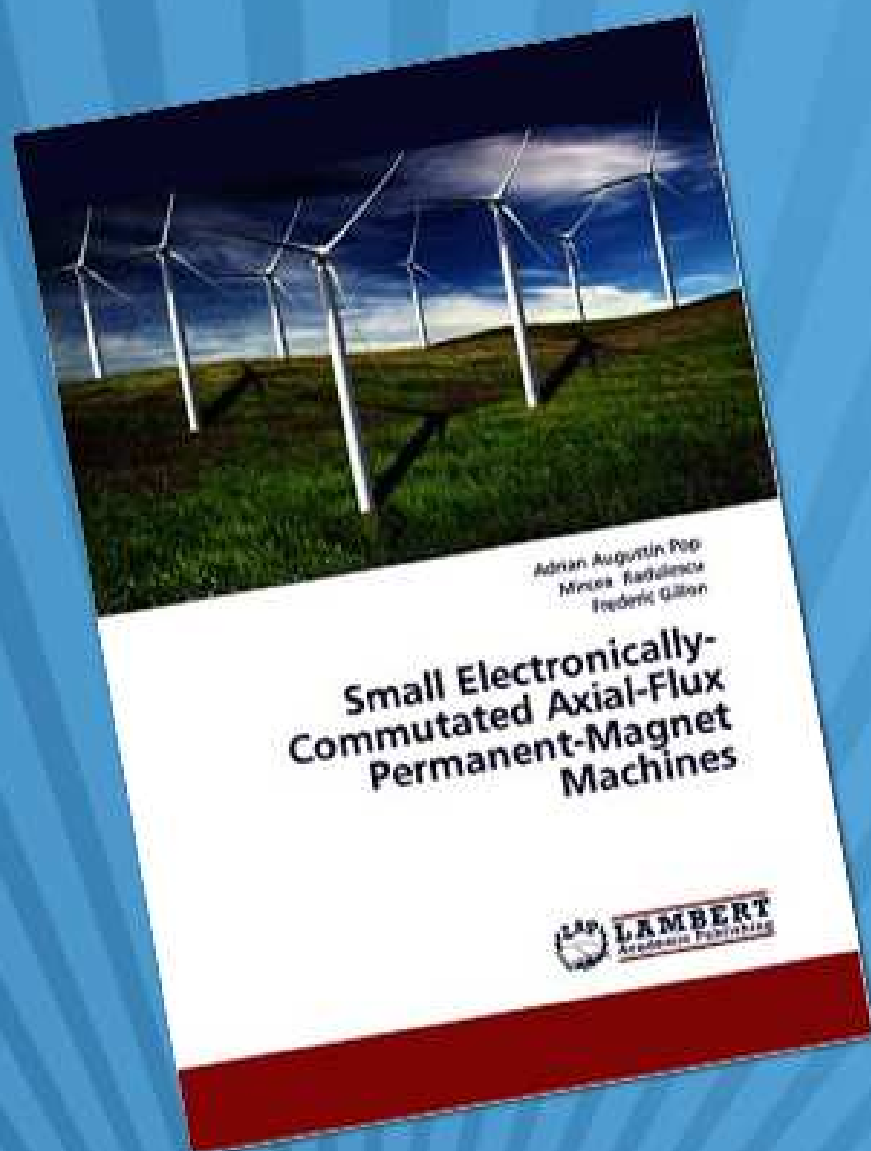
978-3-659-42624-7

Pop, Radulescu, Gillon

Adrian Augustin Pop
Mircea Radulescu
Frederic Gillon

Small Electronically-Commutated Axial-Flux Permanent-Magnet Machines





Small Electronically-Commutated Axial-Flux Permanent-Magnet Machines

Adrian Augustin Pop, Mircea Radulescu, Frederic Gillon

 1 days 1 h 42 min left

Default retail price ~~Price 55.90 €~~

Reduced retail price when buying

-  3 copies => Retail Price 44.90 €
-  5 copies => Retail Price 36.90 €
-  20 copies => Retail Price 33.90 €
-  50 copies => Retail Price 30.90 €
-  200 copies => Retail Price 24.90 €

ISBN-13: 978-3-659-42624-7

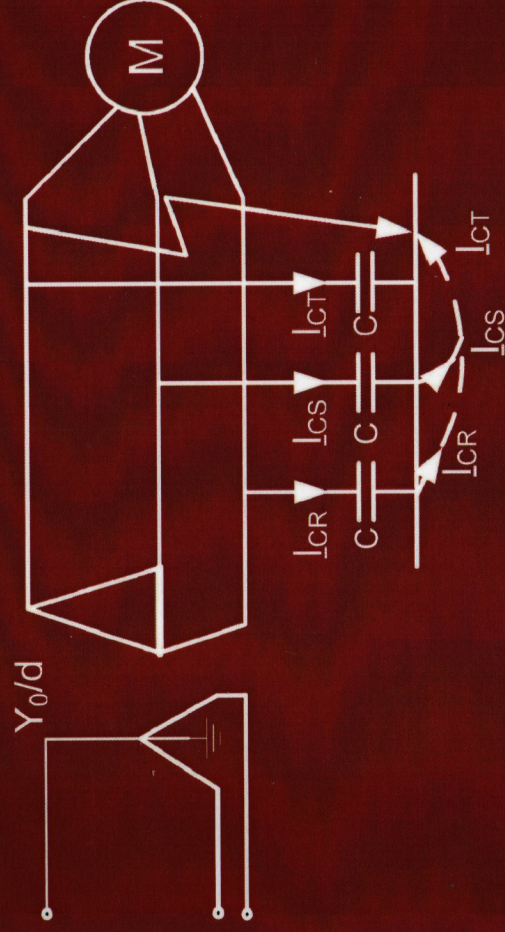
ISBN-10: 3659426245

EAN: 9783659426247

RADU A. MUNTEANU
ADRIAN AUGUSTIN POP
HORIA BĂLAN

TEHNICA MĂSURĂRII MĂRIMILOR ELECTRICE ÎN SISTEME DE PROTECȚIE A ENERGIEI ELECTRICE

Lucrări de laborator



MEDIAMIRA
2014



EDITURA MEDIAMIRA
C.P. 117, O.P. I, CLUJ
Str. Horea nr. 47-49 / I
400275 Cluj-Napoca

COLECȚIA INGINERULUI

Radu A. Munteanu, Adrian Augustin Pop, Horia Bălan

Tehnica măsurării mărimilor electrice

în sisteme de protecție a energiei electrice

- lucrări de laborator -



ISBN: 978-973-713-316-8

Radu A. Munteanu, Adrian Augustin Pop, Horia Bălan -Tehnica măsurării marimilor electrice în sisteme de protecție a energiei electrice. Lucrări de laborator. Mediamira. **ISBN 978-973-713-316-8**

Modeling and permanent-magnet shape optimization of an axial-flux machine

A.A. Pop, F. Gillon, M. M. Radulescu

Abstract – This paper proposes a modeling method for axial-flux permanent-magnet machine (AFPMM) based on a finite elements analysis, and achieves a shape optimization of AFPMM poles. To solve the questions regarding the modeling of AFPMM with surface-mounted PMs, an axial 3-D to radial 2-D finite-element transformation is proposed. A special analytical method for back-emf computation is also provided. The results related to 2-D finite-element analysis are presented and compared with the experimental ones, validating the proposed approach.

The amount of space-harmonic content in AFPMM is a primary concern to the machine designer due to its impact on the AFPMM performances. These harmonics are directly related to the flux-density and mmf distributions in the airgap, which are mainly determined by the PM excitation. Therefore, the slotless machine is analyzed. The influence of design parameters on the total harmonic distortion (THD) and the methodology to reduce space harmonics by selecting the appropriate PM shape and size are also addressed in this paper. The space-harmonic analysis is carried out according to the variety of design parameters of the finite element models.

Index Terms-- axial-flux permanent-magnet machine, finite-element modeling and analysis, total harmonic distortion, design optimization

I. INTRODUCTION

Axial-flux permanent magnet machines (AFPMMs) have higher torque, better power density and lower noise as compared to traditional radial-flux permanent magnet machines, and thus have gained popularity in recent years [1,2].

AFPMMs consist of a rotor-disc carrying magnets that produce the axial flux [3], and a stator-disc containing the phase windings. There are possible many variations in this basic design [4], including single-sided [5], double-sided [6], toroidal [7], and multi-disc designs [8].

The AFPMM considered in this paper is a two-stators, and one-rotor topology. The rotor is sandwiched between the two stators. The studied prototype machine is a three-phase AFPMM with one-rotor-two-stators topology and 4 pole-pairs. The rated power is 0.3 kW and the rated rotational speed is 1500 rpm. The magnets are of high-energy NdFeB-type, and are glued on the solid-iron disc-rotor. The material of the stator core is a fully-processed electrical steel sheet M600-50A. The stator has a particular construction because it is formed by 25 slots.

The torque developed by AFPMM is often affected by harmonics of various origins, such as

- space harmonics of the MMF, which are due to the non-sinusoidal distribution of the armature phase windings;
- space harmonics caused by the presence of stator slots;

- time harmonics related to the power electronic supply, and affecting the stator-armature current.

Space harmonics in AFPMMs are the main concern of the present paper. Starting from a simplified model but enough accurate and fast, the authors present a technique allowing to modify automatically the space harmonics. Finally, the shape optimization technique, as a way to solve this problem, is described and applied on the AFPMM.

II. MODELING OF AFPMMs

In modeling of AFPMMs, the fastness and accuracy of the computations are very important aspects. Using finite-element (FE) field analysis, we can take into account the 3-D structure of the machine, but performing the computations is often too hard and time-consuming. In order to evaluate quickly the performance of the AFPMM, the 2-D FE analysis, which is performed on the average radius of the machine, is a time-saving option, especially if the model will be further optimized. The main idea of the design method is to subdivide the AFPMM into independent computation planes, and to use the average radius of the machine as a design plane. This approach is sufficiently accurate to predict the motor performance, and for validation the finite element results will be compared with the experimental ones.

The airgap flux density is an important design parameter, having notable effect on the machine performances. Therefore, in order to optimize the machine, the airgap flux density must be determined correctly [9].

The airgap flux-density modeling method is based on Fourier-series development. This technique enables to identify the cross-coupling between different spatial and temporal field components, and thus provides a very useful insight into the relationship between different design variables and machine performances. For the first analysis, the effect of stator slots on the magnetic field is taking into account.

A. Axial 3-D to radial 2-D finite element transformation

From the modeling point of view, an axial flux machine has a 3D geometry but using the 2-D FEA, which is performed on the average radius of the machine, is a time saving solution and it is also providing sufficiently accurate computation results.

The method of transforming the 3-D geometry of an AFPMM into the corresponding 2-D model is illustrated in Fig.1.

The 3D rotational movement of the machine (θ_{3D}) Fig. 1. (a) is transformed into 2D linear motion (L_{2D}), Fig. 1. (c). The 3D to 2D conversion formula is:

$$L_{2D} = \theta_{3D} R_{average} \quad (1)$$

The transformation presented in (1) is performed as follows (Fig.1.): we take a straight parallel cut to the axis of the AFPMM by an average radius; because of machine symmetry only half of model needs to be analyzed (the symmetry is fixed by a straight cut along the rotor). The extracted pole with the average computation radius ($R_{average}$) can be visualized in Fig. 1. (b).

The 2-D representative design plane is set on the average radius of the AFPMM [10]. The 3D extracted pole is then transformed into 2D linear pole (c). The discoid shape is built with a constant magnet width / pole-pitch ratio for all diameters of the machine, and thus the angular width for the magnets remain constant. The width of the slots is constant throughout the radial length of the machine, but for different diameters the angular widths of slots and teeth are variable.

The structure from Fig. 1 (c) can be analyzed with a 2D model, easier to use and much faster in computation time.

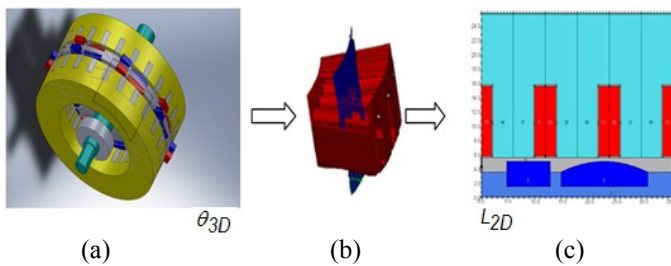


Fig. 1. (a) Design of the AFPMM under study; (b) 3-D FE-model for one magnetic pole; (c) 3-D model reduced to 2-D representative plane.

2D-model simulations can be performed in static but taking into consideration the rotation, the currents time variation and the coupling with external circuits, another transformation can be applied to create a rotating movement.

In order to use the finite-element rotation module, the model needs to be analyzed in such a way that the linear machine obtained in Fig. 2 needs to be placed at a large curvature radius from the origin. The curvature radius is chosen in such way that the rotating structure will be almost equivalent to the linear model and the rotor will be able to move without interacting with the stator.

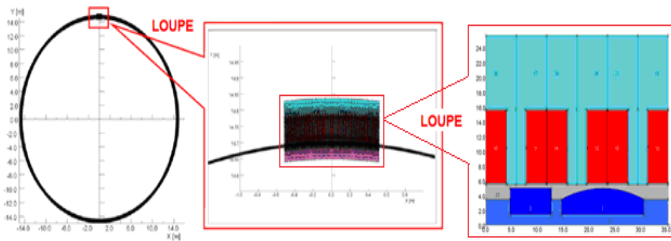


Fig. 2. Linear 2-D motion to rotating 2-D motion transformation.

The aim of this section is to obtain a 2D model which will be utilized to generate correctly, rapidly and efficiently the flux density and electromotive force waveforms of the AFPMM. Then in order to modify the space harmonics the shape of permanent magnet will be furthermore optimize.

III. MODELING RESULTS

A. Effect of nonsymmetrical pole

The effect of stator slotting on the no-load magnetic flux distribution is now investigated. The airgap flux density always drops at stator slot openings, and this effect has a significant influence on the values of the flux and back-emf. For this reason, it is important to accurately analyze the airgap flux density. The rotor-PM arrangement is shown in Fig.3. It can be seen that there are 16 magnets glued on the rotor body. There are two separated PMs for each pole. Due to this PM arrangement, the flux density distribution has an unusual waveform. The first PM has a rectangular geometry and the second PM has an arch form. The PMs of one pole are shown in Fig.4. This rotor-PM arrangement needs a special approach in order to analyze correctly the AFPMM airgap flux density.



Fig.3 (a) The rotor with permanent magnets (b) One of the two stators and the rotor with its PM arrangement.

The 2-D representation of one pole of the AFPMM, and the no-load magnetic flux distribution in the airgap are shown in Fig.4. A and A' represent the winding of the phase A , and B denotes the PM-created flux density in the airgap. The superposition of the flux density with the AFPMM geometry allows pointing out the effect of the slots on the flux-density waveform.

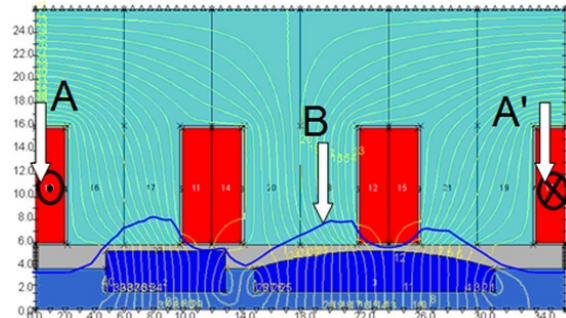


Fig. 4. No-load magnetic flux distribution for one PM-rotor pole.

The angular variation of the airgap flux density due to the rectangular and arch-shaped rotor-PMs for one pole is shown in Fig.5. The first curve of the flux density in the airgap is due to the shape of rectangular magnet and the second curvature is due to the arc shape magnet. The stator slotting effect has a large impact on the flux density shape. We can see a flux density decreasing in the areas where the flux density crosses the slots. There the flux density amplitude is oscillating due to the slotting effect. In the FE model the flux captured by the coils of one phase is computed with the subtraction between the vector potential in the slot with the go conductor (A) and the return conductor (A') multiplied by the length. The captured magnetic flux is presented in Fig. 6.

Using Faraday's law, emf is the time derivative of flux presented in Fig. 7. These computations allow us to see the interconnection between the airgap magnetic flux-density (Fig. 5), flux distribution (Fig. 6) and electromotive force (Fig. 7).

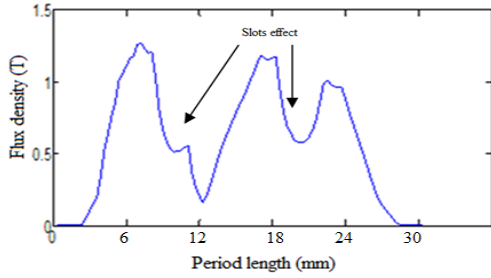


Fig. 5. Airgap magnetic flux-density due to rotor-PMs.

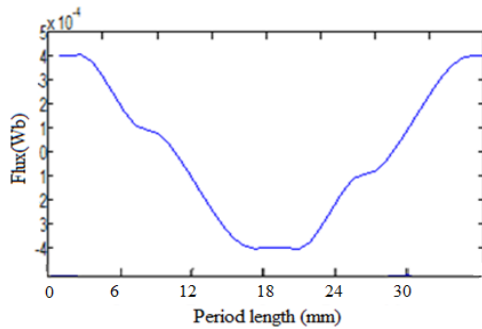


Fig. 6. Flux distribution in the stator core.

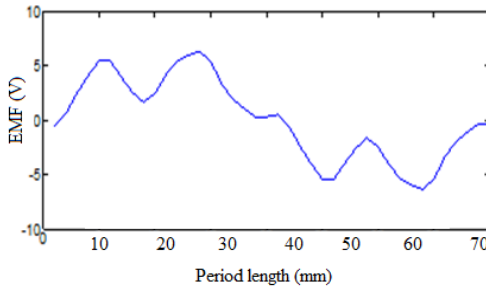


Fig. 7. FE-computed back-emf waveform.

B. Back-emf computation

In order to minimize de cogging torque the AFPMM is composed of 25 teeth. The 2D finite element simulation has been performed for 3 teeth/pole.

An important simulation result is related to the back-emf waveform (Fig.7). It is to be pointed out that the pole-pitch is $\frac{2 \cdot \pi}{8}$, whereas the coil pitch is $\frac{2 \cdot \pi}{25} \cdot 3$. The phase shift between these two angles defines the phase shift that's need to be add between each electromotive forces Fig. 8. The phase difference between the coil pitch and magnetic pole is 1.8 degrees. The signal obtained is shifted by 1.8 degrees for all 8 poles of the machine. The coils with a phase shift of 1.8 degree are allowing making an estimation of the phase back-emf (Fig. 9). Finally, composed signals are collected and divided by the number of coils. The obtained back-emf signal is presented in Fig. 10.

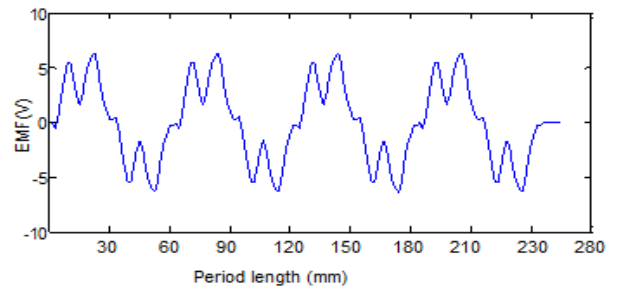


Fig. 8. Analytically-obtained back-emf waveform.

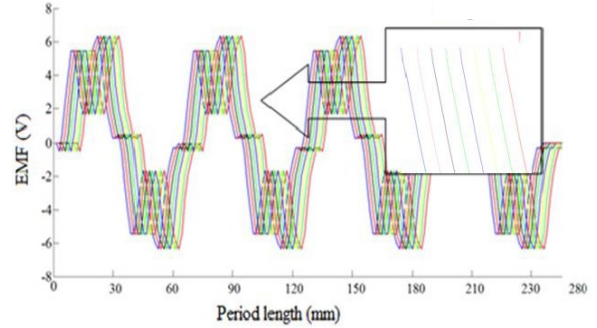


Fig. 9. Analytically-obtained open-circuit (no-load) back-emf.

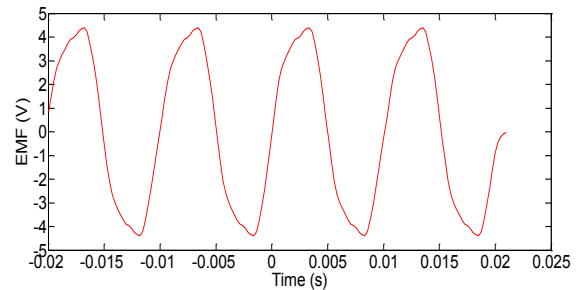


Fig. 10. Analytically-computed open-circuit (no-load) back-emf signal.

If we take a closer look at the Fig. 9 and Fig. 10 we can see that the flux oscillations disappear, and the new signal obtained is close to an ideal sinusoidal waveform.

In this section, a special analytical method for back-emf computation was provided. In order to validate the results obtained by 2-D finite element analysis, the computations will be compared with experimental tests.

C. Testing the prototype

A comparison between FE-computed flux-related values and the experimental ones is provided. Hence, no-load tests were performed under open-circuit (generator-mode) conditions using the DC machine drive as a prime mover. The no-load test was done to evaluate the back-emf values.

The back-emf measurements were carried out for a nominal speed of 1500 rpm. The voltage measurements are made with the high-precision voltage oscilloscope probe. The test results captured on the oscilloscope are presented in Fig.11. The colored signals represent the induced voltage for the three stator phases. The open-circuit back-emfs for forward and reverse rotation are presented in Fig.12 and Fig.13, respectively. It can be observed that the back-emf waveforms have the amplitude equal to 4.4 V. Depending on the rotation

sense the shape of those waveforms have different shapes; this is attributable to the rotor-PM arrangement.

In order to compare the computed and experimental results, the corresponding back-emf waveforms are superposed in Fig.14, which shows a good agreement.

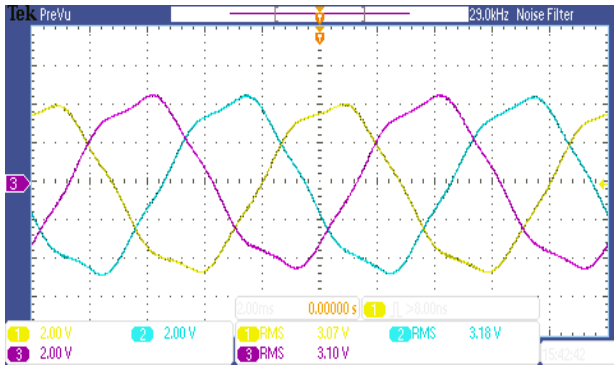


Fig. 11. Experimental open-circuit (no-load) back-emf waveform

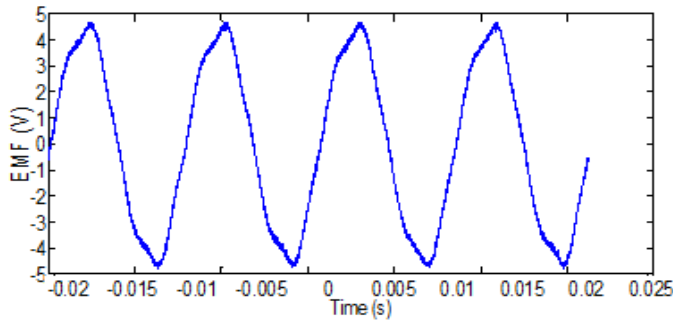


Fig. 12. Experimental open-circuit (no-load) back-emf for clockwise rotation.

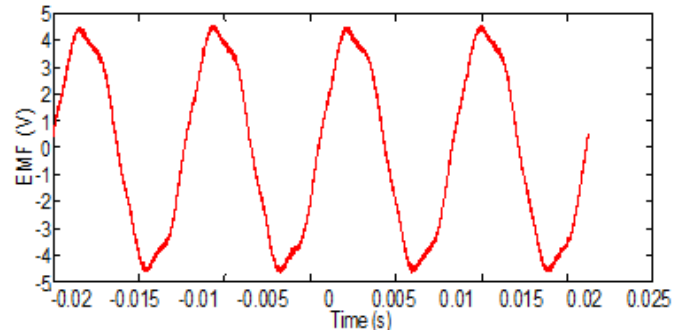


Fig. 13. Experimental open-circuit (no-load) back-emf for counter-clockwise rotation.

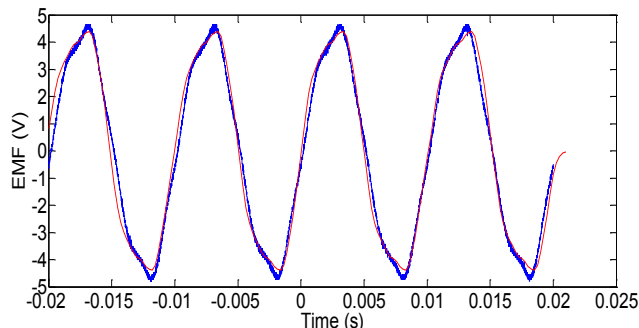


Fig. 14. Comparative experimental and FE-computed back-emfs under open-circuit (no-load) condition.

IV. SPACE HARMONICS IMPROVEMENT BY DESIGN OPTIMIZATION

The harmonics of electromotive force are due to the windings and the shape of the permanent magnets. In order to have a lower distribution of space harmonics in flux density the shape of permanent magnet needs to be optimized. To analyze the flux density harmonics the effect of stator slots is not taken into account. Finding the exponential harmonics in the flux density waveform, it will be possible to decrease them by optimizing the rotor-PM shape. Optimizing the PM size allow us to obtain a flux-density waveform with reduced space harmonics distribution.

A. Slotless AFPMM analysis

The pulsations of torque in permanent magnet machines are the result of the interaction of electromotive force harmonics and current harmonics [11]:

$$C_{elmg} = \frac{3E_1 \cdot I}{2 \cdot \Omega} + \frac{3 \cdot I}{2 \cdot \Omega} \cdot \sum_{i=1}^3 [(E_{6k-1} + E_{6k+1}) \cos(6k\theta)] \quad (2)$$

E represents the electromotive force and I the phase current.

In the first instance of our work we will take into account the two important torque components like flux density and electromotive force. Our study will focused on analysis of those two components in order to modify the space harmonics distribution. Modifying the space harmonics distribution of flux density and EMF will have an important impact in improving the electromagnetic torque as it's possible to see in (2).

Supposing an ideal stator-winding, the back-emf results as

$$e = n \frac{\partial \phi}{\partial t} = n \frac{\partial \int B dS}{\partial t} = n \frac{\partial \int BLR d\theta}{\partial t} \quad (3)$$

ϕ is the flux density in the airgap, L and R are, respectively, the length of the machine and the radius of the rotor.

So, one may write:

$$e = n \frac{\partial \int BLR d\theta}{\partial t} \frac{dt}{d\theta} \Omega = nB(\theta)LR\Omega \quad (4)$$

Neglecting the effect of the winding, the harmonics of the EMF are those of the flux density $nLR\Omega$, reducing these harmonics will permit to reduce the harmonics of the EMF. The objective will be to find a proper way to optimize the flux density harmonics.

The influence of rotor magnets design parameters on the magnetic flux distribution and its total harmonic distortion (THD) in surface-type AFPMM is very important to our work.

The flux density distribution in the AFPMM under study is presented in Fig. 15. The AFPMM was simulated under no-load condition to monitor the airgap flux pattern. This signal is the subject of Fast Fourier Transformation. This technique considers the time-space distribution of electromagnetic variables so that it enables to identify the cross-coupling between different spatial and temporal field components. Therefore, it provides a very interesting insight into the correlation between different design variables and machine performances. The shape of the spatial waveform is defined

by solving in polar coordinates the magnetic potential equations in the air-gap.

The airgap flux density can be expressed in Fourier series as:

$$B(\theta) = \sum_{n=1}^{\infty} (a_n \cos(n\theta) + b_n \sin(n\theta)) = \sqrt{a_n^2 + b_n^2} \cdot e^{j\varphi} \quad (5)$$

where $n=1$ corresponds to the fundamental component. The objective is to reduce the airgap flux-density harmonics and thus the back-emf harmonics.

The frequency spectrum of flux density is displayed in Fig.16. The axial component of the no-load airgap flux density due to rotor-PMs in the middle of the airgap plane is emphasized. It shows that the main harmonic in the flux-density spectrum is the first-order harmonic and then the third harmonic. Fifth- and seventh-order airgap flux-density harmonics are also significant. The study only considers the harmonic orders less than 50, whilst only the orders less than 15 are presented in figure.

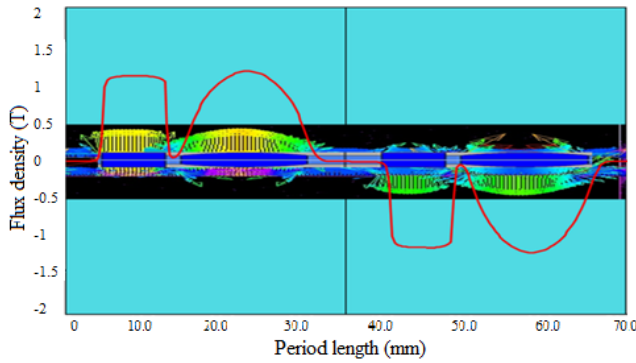


Fig. 15. Flux-density distribution in the airgap of the AFPMM under study.

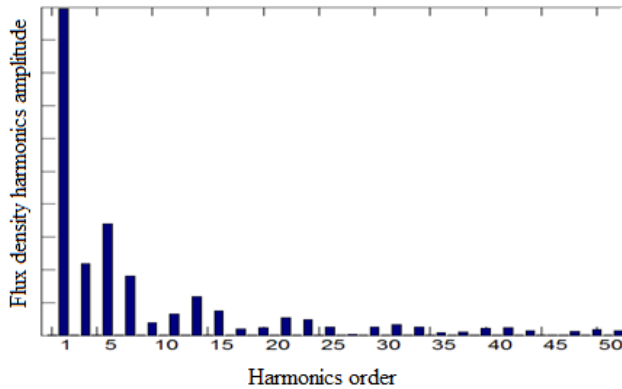


Fig. 16. Frequency spectrum of the flux-density harmonics of the AFPMM under study.

The airgap flux density distribution produced by rectangular and sinusoidal magnets in a surface-mounted AFPM machine (neglecting the slot effect) is a square and sinusoidal waveform consisting of all odd harmonics.

The amount of distortion in the AFPMM back-emf, quantified by the total harmonic distortion (THD), is defined by

$$THD = \frac{\sqrt{\sum_{h=3,5,7,\dots,13}^{\infty} B_h^2}}{\sqrt{B_1^2}} \quad (6)$$

From (5) and (6), we know that the harmonic component of B_h is inversely proportional to the harmonic order h , so the distortion is mainly determined by the low harmonics. Knowing the distribution of representative harmonics in the flux density, the shape of permanent magnets will be furthermore optimized in order to modify those harmonics.

B. Rotor-PM shape optimization

As with conventional synchronous machines, and for a variety of reasons, sinusoidal flux density waveforms are also desirable for many permanent magnet machine applications. Because of the low magnet permeability, which is comparable to that of air, the shape of the airgap flux density depends not only on the airgap length, but also on the shape and dimensions of the magnet itself.

The purpose of this section is to achieve a design optimization with two objectives as:

- First, optimization objective is to minimize the total harmonic distortion (THD) of the airgap flux density.
- The second objective is to find alternative magnet design that would minimize the amplitude of odd harmonics and maximize the fundamental.

Accordingly, an optimization method is introduced that allows improving the rotor-PM shape and dimensions in order to minimize key harmonic components that exist in the given design. The analysis aimed at the rotor structure, especially at rotor-PM shape is presented in Fig. 17.

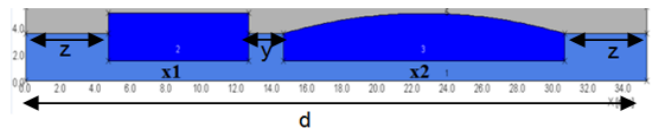


Fig. 17. Initial rotor structure of the AFPM.

The optimization is performed using GA (genetic algorithm) method to explore global space solutions.

In searching for PM dimensions alternatives both magnet length x_1 and x_2 are varied in the limits of Table I, subject to the geometrical constraint given by Eq. (7). The shape and height of the rectangular and arc-shaped PM remain constant. The objective function is described by Eq. (7).

TABLE I
OPTIMIZATION VARIABLES

Variables	Rated values	Variation interval	Units	Name
x_1	8	$2.99 < x_1 < 16$	mm	First Magnet length
x_2	16	$2 < x_2 < 16$	mm	Second Magnet length
y	1.95	1.95	mm	Space between the magnets
z	-	-	mm	The left and right extremities of the rotor pole
d	33.34	33.34	mm	Length of one rotor pole

The optimization problem is formulated as:

$$\begin{cases} \min THD(x_1, x_2) \\ x_{1\min} \leq x_1 \leq x_{1\max} \\ x_{2\min} \leq x_2 \leq x_{2\max} \end{cases} \quad (7)$$

Global space solution is explored using GA method. Optimal result is given after 3000 iterations, as provided by Table II.

TABLE II
GA OPTIMIZATION RESULT

Population size	Number of generation	X1	X2	F
30	100	15.995	4.769	0.39

The THD obtained from the original AFPMM model, with the given geometrical PM shapes, was 0.47. It can be notice an improvement of THD to 0.39.

The optimized PM-rotor geometry is presented in Fig.18. It can be seen that the PM dimensions have been successfully changed in order to minimize the flux-density THD. The GA convergence is shown in Fig.19.

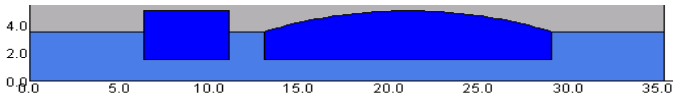


Fig. 18. Optimized rotor structure of AFPMM.

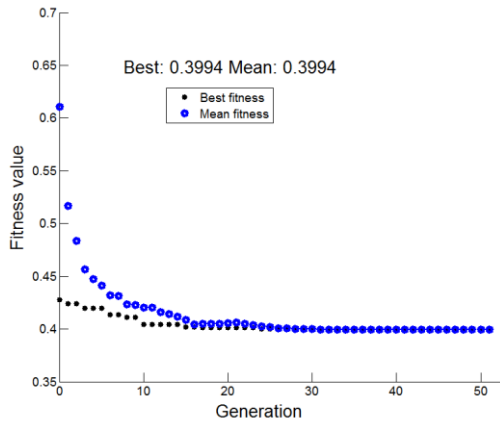


Fig. 19. Fitness generation.

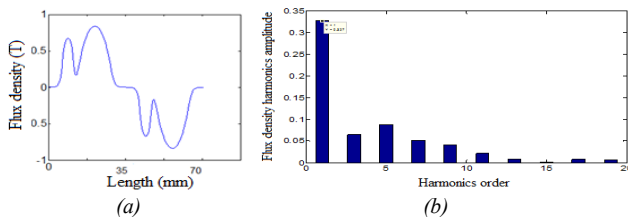


Fig. 20. (a) Optimized flux density waveform; (b) Flux-density harmonics order.

Numerical optimization method has been applied to identify optimal permanent magnets design in order to reduce the total harmonic distortion. The optimize flux density waveform and the fast Fourier transformation of the signal is presented in Fig. 20. Furthermore, optimal permanent magnet design in order to minimize the odd harmonics components and maximize the fundamental harmonic amplitude will be further investigated using multi-objective methods.

C. Multi-objective optimization

Taking into account the geometrical constraints given by (5) the objective function is defined by

$$F_{obj} = \left[\begin{array}{l} \sqrt{\sum_{h=3,5,7,\dots,13}^{\infty} B_h^2} = \text{Numerator} \\ \left(\sqrt{B_1^2} \right) = \text{Denominator} \end{array} \right] \quad (8)$$

The objective is to minimize the amplitude of odd harmonics and to maximize the fundamental.

The 3-D representation of *Numerator* as a function of PM length is presented in Fig. 21.

The optimal results are displayed in Fig.21. Here the 3D Pareto front, for the optimization problem (two objectives) is pointed out. The dots marked with (blue) circles are Pareto solutions, while the (red) stars are the tested points. It can be seen that the extreme Pareto front intersection gives a relative solution for the two search objectives. Thus, the *Numerator* (representing the odd harmonics) is 0.12, while the *Denominator* is increased to 1.32.

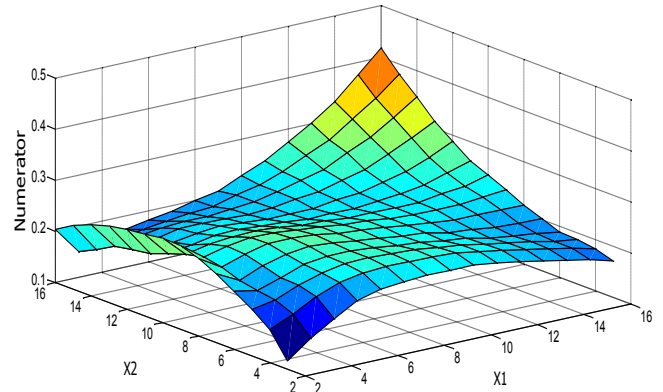


Fig. 21. The odd harmonics in function of x1 and x2.

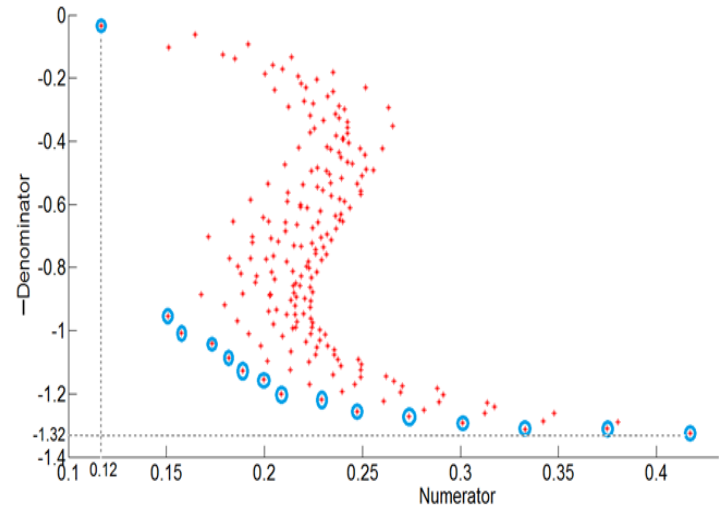


Fig. 22. Pareto front.

V. CONCLUSIONS

A small double-sided AFPMM has been presented in this paper.

To solve the questions regarding the modeling of axial-flux surface-mounted PM machines, an axial 3-D to radial 2-D finite-element transformation has been proposed. A special analytical method for back-emf computation was provided. An important aspect of this computation is regarding the flux density to back-emf waveform transformation. From an oscillating flux-density waveform a close to ideal sinusoidal back-emf waveform was obtained. The FE field analysis models have been developed in order to predict the AFPMM flux density distribution. FE-computed and measured results, for the open-circuit (no-load) back-emf have been compared, showing good agreement. The no-load tests were performed under open-circuit (generator-mode) conditions.

The possibility of reducing the harmonic content of the airgap flux density waveforms in surface-mounted PM machines has been presented. This approach was primarily formulated from the mathematical point of view and then formulated into a minimization problem. Computerized minimization optimization techniques were applied to systematically modify a composite function of odd harmonics contents while simultaneously maximizing the fundamental component.

REFERENCES

- [1] J.F. Gieras, R. Wang, and M.J. Kamper, "Axial-flux permanent-magnet brushless machines", Springer, The Netherlands, 2nd edition, 2008.
- [2] Patterson, D.J.; Colton, J.L.; Mularcik, B.; Kennedy, B.J.; Camilleri, S.; Rohoza, R.; "A comparison of radial and axial flux structures in electrical machines," *Electric Machines and Drives Conference, 2009. IEMDC '09. IEEE International*, pp.1029-1035, 3-6 May 2009
- [3] S. Tounsi, F. Gillon, S. Brisset, P. Brochet, R. Neji, "Design of an axial flux brushless DC motor for electric vehicle", *Proceedings of International Conference on Electrical Machines – ICEM, 2002*, CD-ROM.
- [4] A. Parviainen, "Design of axial-flux permanent magnet low-speed machines and performance comparison between radial-flux and axial-flux machines", Ph.D. Thesis, Lappeenranta University of Technology, Finland, 2005.
- [5] S.M. Mirimani, A. Vahedi, F. Marignetti, "Effect of inclined static eccentricity fault in single stator-single rotor axial flux permanent magnet machines", *IEEE Transactions on Magnetics*, vol.48, no.1, pp.143-149, 2012.
- [6] T.-F. Chan, W. Wang, L.-L. Lai, "Analysis of an axial-flux permanent-magnet synchronous generator with a double-sided rotor," *Electromagnetic Field Computation (CEFC), 2010 14th Biennial IEEE Conference on*, 9-12 May 2010
- [7] A. Mahmoudi, H.W. Ping, N.A. Rahim, "A comparison between the TORUS and AFIR axial-flux permanent-magnet machine using finite element analysis," *Electric Machines & Drives Conference (IEMDC), 2011 IEEE International*, pp.242-247, 15-18 May 2011
- [9] A. Egea, G. Almandoz, J. Poza, A. Gonzalez, "Analytic model of axial flux permanent magnet machines considering spatial harmonics", *Proc. International Symposium on Power Electronics, Electrical Drives, Automation and Motion – SPEEDAM*, 2010.
- [11] D. Vizireanu, S. Brisset, P. Brochet, Y. Milet, D. Laloy, "Study of Current and Electromotive Force Waveforms in Order to Improve the Performance of Large PM Synchronous Wind Generator", in *Recent Developments of Electrical Devices*, Springer, The Netherlands, 2006, pp. 397-413

BIOGRAPHIES

Adrian A. POP was born in Romania in 1984. He received the Dipl. Ing. degree from Faculty of Electrical Engineering, Technical University of Cluj-Napoca, Cluj-Napoca, Romania, in 2009. Since October 2009, he pursues a three-year full-time Ph.D. study program at the Technical University of Cluj-Napoca under international co-supervision of Ecole Centrale de Lille, France. He is a member of the Special Electric Machines and Light Electric Traction (SEMLET) Research Laboratory, Technical University of Cluj-Napoca, Romania and of the Laboratory of Electrical Engineering and Power Electronics Research Laboratory (L2EP), Ecole Centrale de Lille, France. His research interests are in special electric machines for automotive applications and railway propulsion systems.

Frédéric GILLON was born in France in 1967. He obtained an Engineer Diploma in 1992 and a Ph.D. in 1997 at Université des Sciences et Technologies de Lille. He is Associated Professor at Ecole Centrale de Lille, since 1999. His research area is optimal design of electric motor drive systems. The applications are linear motors, axial- and radial-flux synchronous motors, and railway propulsion systems.

Mircea M. RADULESCU (IEEE Senior Member 99) received the Dipl. Ing. degree in electrical engineering (with honors) from the Technical University of Cluj-Napoca, Cluj-Napoca, Romania, in 1978, and the Ph.D. degree in electrical engineering from the Polytechnic University of Timisoara, Timisoara, Romania, in 1993. Since 1983, he has been with the Faculty of Electrical Engineering, Technical University of Cluj-Napoca, where he is currently Full Professor in the Department of Electric Machines and Head of the Special Electric Machines and Light Electric Traction (SEMLET) Research Laboratory. He is the author or coauthor of more than 120 published scientific papers in refereed technical journals and international conference and symposium proceedings. He is an Associate Editor of the international scientific quarterly *Electromotion*. His biography is listed in several editions of *Who's Who in the World* and *Who's Who in Science and Engineering*. His teaching and research activities include computer-aided design of electro-mechanical devices, field analysis of electro-magnetic structures, the design and control of small electric motors, actuators and mechatronic drives, and light electric traction systems. Prof. Radulescu is a member of the International Steering Committees of several conferences and symposia in the field of electric motor drives and electric traction.

Optimal commutation angles of a switched reluctance motor/generator

M.V. Zaharia^{1,2}, Andreea Adriana Laczko (Zaharia)^{1,2}
A.A. Pop¹, M.M. Radulescu¹

¹Technical University of Cluj-Napoca
Cluj-Napoca, Romania
(Valentin.Zaharia@mae.utcluj.ro)

F. Gillon²

²L2EP, Ecole Centrale de Lille
Villeneuve d'Ascq, France
(frederic.gillon@ec-lille.fr)

Abstract — For switched reluctance machines, a major problem is the torque ripple, which causes increased and undesirable acoustic noise and possible irregular speed. This paper aims at determining optimal turn-on and turn-off angles for torque ripple reduction of a three-phase 6/8 switched reluctance motor/generator. A commutation-angle optimization technique is therefore implemented for both motoring and generating operation modes over an extended speed range.

Keywords — switched reluctance motor/generator, torque ripple, turn-on and turn-off angles, optimization

I. INTRODUCTION

Switched reluctance machine is capable of operating as motor and also as generator (SRM/G) by adjusting the commutation angles, and thus changing the direction of the conversion power flow [1, 2]. In SRM operation mode, the electronic power converter regulates the magnitude of the stator current to meet the torque and speed requirements of the mechanical load. In SRG operation, the power converter energizes the stator phases to support continuous conversion from mechanical energy to electrical energy by extracting it from the prime mover. Belonging to the class of doubly-salient reluctance machines, SRM/G together with its electronic power converter and controller has the advantages of simple and rugged brushless machine structure, no high switching frequency of the power converter, good reliability of the machine and power converter, as well as low inertia and fault tolerance capability. All these issues conspire to favour SRM/G in high-speed applications.

In recent years, there has been an increasing interest in using SRM/G as integrated starter-alternator for more-electric-aircraft or more-electric-car engines, to generate electric power and also to provide engine starting [3, 4]. This is because SRM/G has the potential of higher

reliability, less manufacturing cost and faster dynamic response than its permanent-magnet machine contender. However, SRM/G exhibits noticeable torque ripple and acoustic noise. The torque ripple is due to highly nonlinear and discrete nature of the torque production mechanism, which is significant at the commutation instants. Besides, traditional closed-loop current control scheme for SRM/G brings large acoustic noise due to variable switching frequency [5]. The control key in SRM/G operation is to precisely synchronize the stator-phase current pulses with the rotor position, in order to accomplish maximum machine efficiency with reduced torque ripple.

In this context, the aim of the present work is to determine the optimal turn-on and turn-off angles for torque ripple reduction of a three-phase SRM/G in 6 stator poles/ 8 rotor poles configuration (Fig.1).

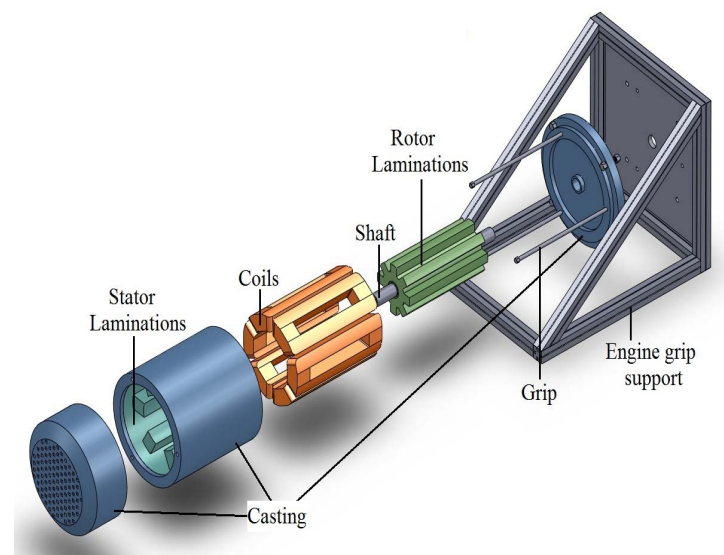


Fig. 1. Exploded view of the SRM/G under study

II. SRM/G SIMULATION MODEL

To solve the problem regarding torque ripple, an analytical model of SRM/G is implemented in MATLAB/Simulink environment, comprising calculus relations for the stator-phase voltages, inductances, electromagnetic torque and torque ripple.

A. Voltage computation

The applied voltage on the stator phase equals the sum of resistive voltage drop and time-derivative of the linkage flux:

$$V_1 = r_1 \cdot i_1 + \frac{d\phi_1}{dt}, \quad (1)$$

where ϕ_1 and i_1 are the magnetic flux and the current of phase 1, respectively.

If the mutual inductance between windings is neglected, the matrix form of stator-voltage equations for the considered three-phase SRM/G can be written as

$$\begin{bmatrix} v_1 \\ v_2 \\ v_3 \end{bmatrix} = [R_1 \quad R_2 \quad R_3] \cdot \begin{bmatrix} i_1 \\ i_2 \\ i_3 \end{bmatrix} + \begin{bmatrix} L_1 & 0 & 0 \\ 0 & L_2 & 0 \\ 0 & 0 & L_3 \end{bmatrix} \cdot \frac{d}{dt} \begin{bmatrix} i_1 \\ i_2 \\ i_3 \end{bmatrix} + \frac{d}{d\theta} \begin{bmatrix} L_1 & 0 & 0 \\ 0 & L_2 & 0 \\ 0 & 0 & L_3 \end{bmatrix} \cdot \begin{bmatrix} i_1 \\ i_2 \\ i_3 \end{bmatrix} \cdot \begin{bmatrix} \frac{d\theta_1}{dt} & \frac{d\theta_2}{dt} & \frac{d\theta_3}{dt} \end{bmatrix} \quad (2)$$

where $\frac{d\theta}{dt}$ is the rotor angular speed (rad/s), R the electrical resistance of each stator phase and $\frac{dL}{d\theta}$ the inductance slope.

B. Inductance computation.

An important step in writing the analytical model of the SRM/G is to compute the magnetic flux of one phase function of the current and the rotor position. By taking into consideration a perfectly aligned position between the stator and the rotor teeth (Fig.2a) the maximum inductance expression can be easily found below [7]:

$$L_M = \mu_0 \cdot \frac{N^2 \cdot l_a \cdot w_R \cdot D_{oR}}{2g}, \quad (3)$$

where N is the number of turns per phase winding, l_a the machine axial length, g is the air-gap, D_{oR} the outer diameter of the rotor and w_R the rotor pole-arc. The fringing and the end effects are neglected in (3).

For determining the value of the minimum inductance, L_m , corresponding to the unaligned position between stator and rotor teeth, the design parameters of a prototype

SRM/G were introduced in *JMAG-Designer* software, in order to build a finite-element (FE) field-analysis model (Fig.2). The rotor was gradually rotated until the rotor teeth reached the unaligned position of Fig.2, *b*. Further, the overlapped surface between stator and rotor teeth was measured, and using equation (3), but with the measured overlapping surface, the minimum inductance value was determined.

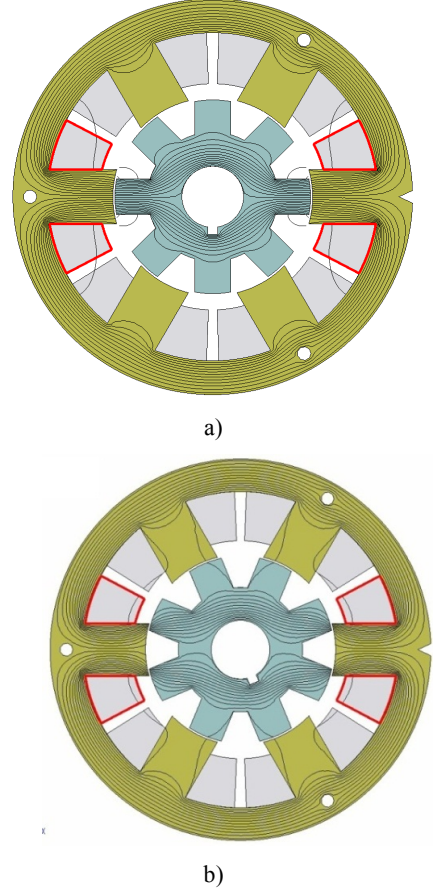


Fig.2. Magnetic flux distribution in the 6/8 SRM/G for aligned position (a) and unaligned position (b)

In Fig.3, inductance characteristics of the prototype three-phase SRM/G are represented for different current values, i.e. FE-computed inductance characteristics are marked by (red) squares, and experimentally-obtained (on prototype SRM/G) inductance characteristics are marked by (blue) triangles. The experimental determination of the maximum and minimum inductances of the SRM/G prototype has been performed by supplying one stator phase with different voltages, measuring the applied voltage, current and resistance values, and computing the inductance values by the following formula [10]:

$$L = \frac{1}{2\pi f} \sqrt{\left(\frac{U}{I}\right)^2 - R^2} \quad (4)$$

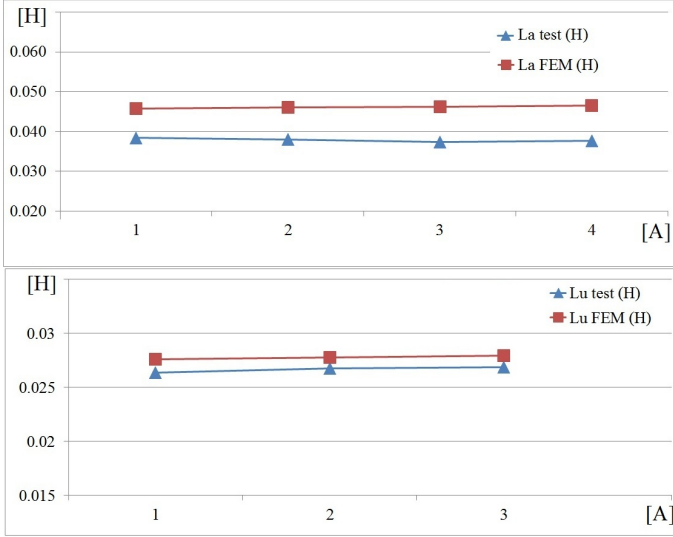


Fig.3. FE-computed and experimentally-obtained inductance characteristics of the prototype three-phase SRM/G, for aligned position (upper) and unaligned position (lower).

with the frequency of the power supply of 50 Hz and the value of the measured resistance of $R = 2.98 \Omega$ per phase. In Fig.4 is represented the ideal waveform of the inductance as function of rotor angular position [1].

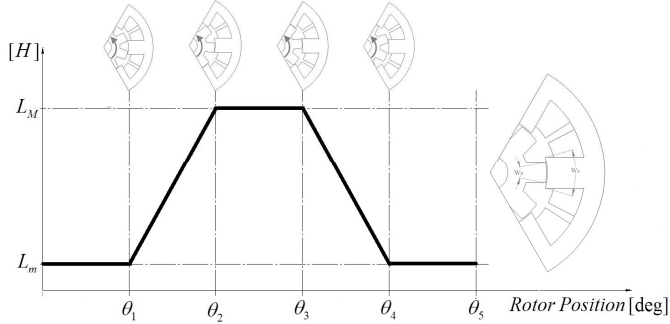


Fig.4. Idealized phase-inductance characteristic of the three-phase SRM/G as a function of rotor angular position

$$\theta_1 = \frac{1}{2} \left[\frac{2\pi}{N_R} - (w_S + w_R) \right] \quad (5)$$

$$\theta_2 = \theta_1 + w_R \quad (6)$$

$$\theta_3 = \theta_2 + (w_S - w_R) \quad (7)$$

$$\theta_4 = \theta_3 + w_R \quad (8)$$

$$\theta_5 = \frac{2\pi}{N_R}, \quad (9)$$

where N_R is the number of rotor teeth, w_S the stator-tooth width and w_R the rotor-tooth width.

To determine the θ_{on} angle (eq.5) for the SRM operating mode, the instant when the inductance starts to increase (when the rotor tooth starts to overlap the stator pole) must be known. The θ_{off} angle (eq.6) corresponds to the instant when the rotor tooth is perfectly aligned with the corresponding stator pole, i.e. when the proper stator-phase energizing must end.

For the SRG operation mode, the θ_{on} angle (eq.6) corresponds to the instant when the excitation of the proper stator-phase must occur, while the θ_{off} angle (eq.7) corresponds to the instant when the rotor exits the aligned position.

C. Electromagnetic torque computation

The calculus expression of the electromagnetic torque for a three phase machine can be written as

$$T_e = \frac{1}{2} \left\{ i_1^2 \frac{dL_1}{d\theta} + i_2^2 \frac{dL_2}{d\theta} + i_3^2 \frac{dL_3}{d\theta} \right\} \quad (10)$$

In the above relation, the SRM/G magnetic circuit saturation effect and the mutual inductances were neglected.

D. Torque ripple computation

The torque ripple is calculated by the following formula [10]:

$$T_{rip} = \frac{T_{max} - T_{min}}{T_{av}} \quad (11)$$

where T_{max} , T_{min} and T_{av} are the maximum, minimum and average values of the SRM/G developed torque, respectively.

The MATLAB/Simulink model for determination of SRM/G optimal commutation angles is presented in Fig.5.

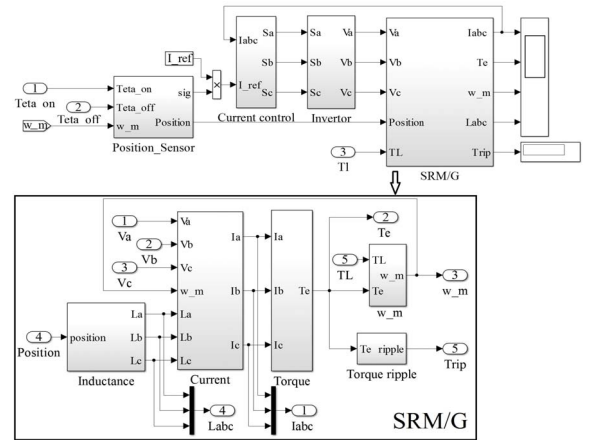


Fig.5. MATLAB/Simulink model of the SRM/G

In the SRM/G simulation model, hysteresis current control was implemented, sampling time of $\tau_s = 2 \cdot 10^{-5}$ s was used, and DC-source supply of 130 V was considered.

The outputs of the SRM/G simulation block are the current, torque and torque ripple, speed and inductance. The position-sensor block yields the rotor position (computed from rotor speed) for electronic switching of SRM/G and energizing its right stator phase at right time via the three-phase half-bridge asymmetrical inverter with the topology and power switches signals shown in Fig.6.

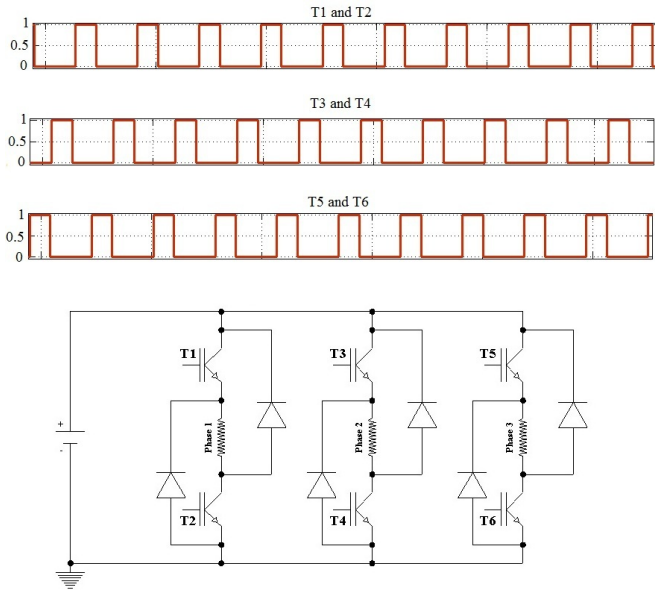


Fig.6. Three-phase half-bridge asymmetrical inverter

III. SRM/G OPTIMAL COMMUTATION ANGLES

In this section, SRM/G optimal commutation angles are determined for both motoring and generating operation modes.

The reference current is set to 4 A value, and theta-on and theta-off angles are chosen using equations (5) – (9).

To obtain the best switching angles 5 different rotor speeds/loads were used in order to get more accurate values of these angles. If we choose to use a smaller number of rotor speeds/loads (i.e. only two) other values for these angles are obtained, less accurate ones.

A. SRM optimal commutation angles

For the SRM operation mode, torque-ripple characteristics as a function of both theta-on and theta-off commutation angles are computed (Figs.7 and 8) at constant speed and constant mechanical load, respectively. For the turn-on angle, the band values are chosen between -1° and 2° with an increasing step of 0.2° ,

whereas for the turn-off angle, the band values are chosen from 17° to 24° with an increasing step of 0.5° .

In Fig.7, the surface characteristics of SRM torque ripple for 5 different constant values of the rotor speed (700, 1000, 1300, 1600 and 2000 rpm) are represented.

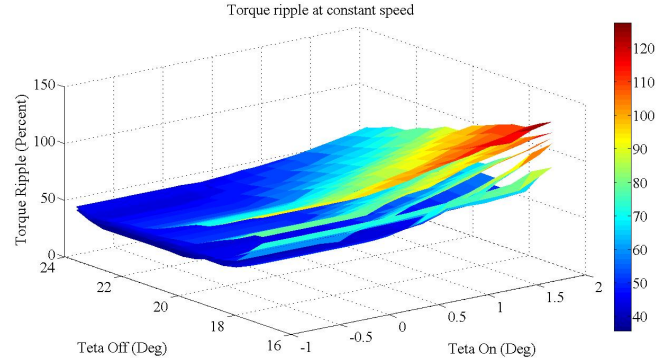


Fig.7. SRM torque-ripple characteristics as a function of both theta-on and theta-off commutation angles, at constant speed

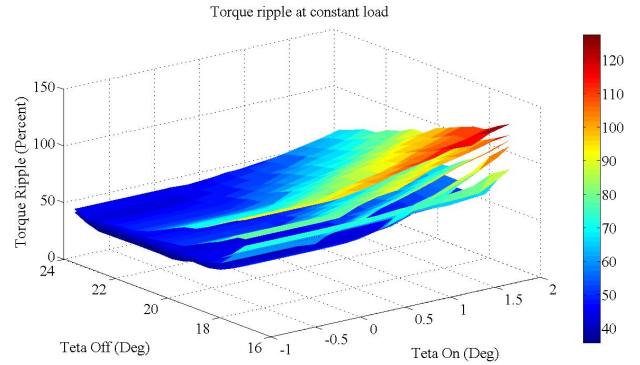


Fig.8. SRM torque-ripple surface characteristics as a function of both theta-on and theta-off commutation angles, at constant load torque

Fig.8 represents the surface characteristics of SRM torque ripple for 5 different mechanical loads, chosen so that the corresponding rotor speed is around of 700, 1000, 1300, 1600 and 2000 rpm, respectively.

To determine the SRM optimal commutation angles, that ensure the lowest torque ripple, the mean-value computation method was used: for each rotor speed and load torque value, respectively, the commutation angles were determined, such that the lowest torque ripple was obtained for each case; hence, 5 pairs of values for theta-on and theta-off angles were obtained, as recorded in Table 1; from these 5 paired-values for theta-on and theta-off angles, an average paired-value was obtained and considered as the best one, i.e. $\theta_{on} = 0.04^\circ$ and $\theta_{off} = 21.692^\circ$, for constant rotor speed and $\theta_{on} = -0.118^\circ$ and $\theta_{off} = 21.7^\circ$, for constant load torque, respectively (Table 3).

TABLE 1. SRM OPTIMAL THETA-ON AND THETA-OFF ANGLES FOR DIFFERENT VALUES OF ROTOR SPEED AND LOAD TORQUE

Speed	Theta -On	Theta -Off	Ripple Torque	Load Torque	Theta -On	Theta -Off	Ripple Torque
700	0	22.06	34.67	0.2	-0.16	19.82	35.66
1000	0	21.14	38.46	0.15	-0.16	22.64	39.6
1300	0	22.06	40.3	0.11	0.05	20.76	41.77
1600	0	20.22	43.03	0.06	-0.16	22.64	43.92
2000	0.2	22.98	42.47	0.001	-0.16	22.64	43.04

B. SRG optimal commutation angles

For the SRG operation mode, a prime mover is needed and the commutation angles must be shifted, so that the excitation stage occurs when the rotor tooth is perfectly aligned with the corresponding stator pole. If the prime mover displaces the SRG rotor from this aligned position, an opposite (negative) electromagnetic torque is developed by the machine, which thus operates as a generator.

Similarly to the motoring operation case, SRG torque-ripple characteristics are computed (using MATLAB) as a function of both theta-on and theta-off commutation angles (Figs.9 and 10) at constant speed and constant mechanical load, respectively. For the turn-on angle, the band values are chosen between 10° and 15°, whereas for the turn-off angle, the band values are chosen from 35° to 40° (with an increasing step of 0.25° in both cases).

In Fig.9, the surface characteristics of SRG torque ripple for 5 different constant values of the rotor speed (700, 1000, 1300, 1600 and 2000 rpm) are represented. Fig.10 represents the surface characteristics of SRG torque ripple for 5 different electromagnetic torques, chosen so that the corresponding rotor speed is around of 700, 1000, 1300, 1600 and 2000 rpm, respectively.

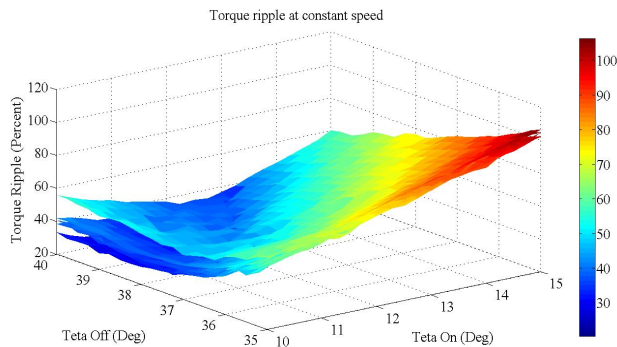


Fig.9. SRG torque-ripple characteristics as a function of both theta-on and theta-off commutation angles, at constant speed

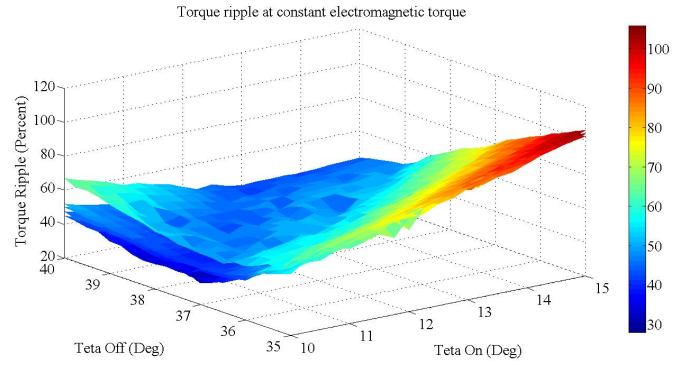


Fig.10. SRG torque-ripple surface characteristics as a function of both theta-on and theta-off commutation angles, at constant electromagnetic torque

Similarly to the SRM case, the mean-values computing method is used for determining the best commutation angles of SRG operation mode, from the 5 pairs of values for theta-on and theta-off angles recorded in Table 2. The obtained average paired-values, considered as the best ones, were $\theta_{on} = 12.25^\circ$ and $\theta_{off} = 40^\circ$, for constant speed and $\theta_{on} = 13.05^\circ$ and $\theta_{off} = 39.7^\circ$, for constant electrical load, respectively (Table 4).

TABLE 2. SRG OPTIMAL THETA-ON AND THETA-OFF ANGLES FOR DIFFERENT VALUES OF ROTOR SPEED AND LOAD TORQUE

Rotor Speed	Theta -On	Theta -Off	Ripple Torque	Elmag Torque	Theta -On	Theta -Off	Ripple Torque
700	12.75	40	21	-0.29	12	39.75	37.72
1000	12.25	40	20.81	-0.32	12.25	39.75	33.01
1300	12.25	40	21.03	-0.36	14.75	39.75	33
1600	11.5	40	20.29	-0.39	13.5	39.75	27.92
2000	13.75	40	30.34	-0.41	12.75	39.5	41.34

IV. SIMULATION RESULTS

A. Simulation results for SRM operation mode

Table 3 presents the SRM torque ripple values for the optimal commutation angles determined above by the average-values computation method, in comparison with the torque ripple values obtained for theoretical commutation angles. It can be found, that SRM torque ripple values

- are reduced (in average) by 22.07% for optimal commutation angles determined by the average-values computation method as compared to torque ripple values obtained for theoretical commutation angles, at constant rotor speed.

- are reduced (in average) by 23.18% for optimal commutation angles determined by the average-values

computation method as compared to torque ripple values obtained for theoretical commutation angles, at constant load torque.

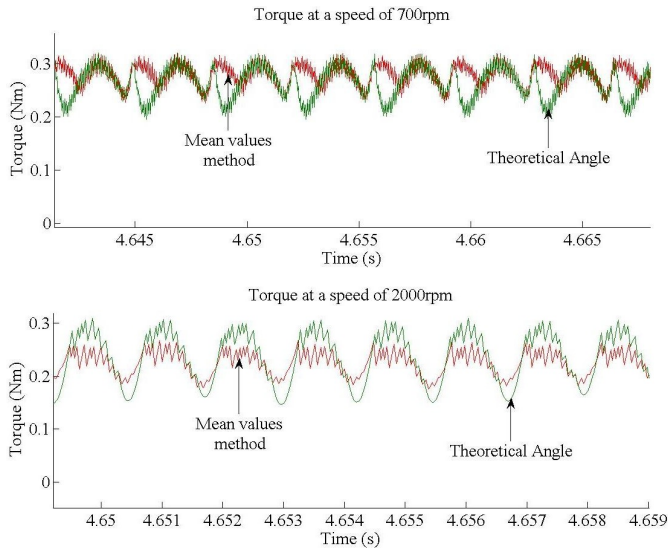


Fig.11. Torque behavior depending on the commutation angles at two different speeds.

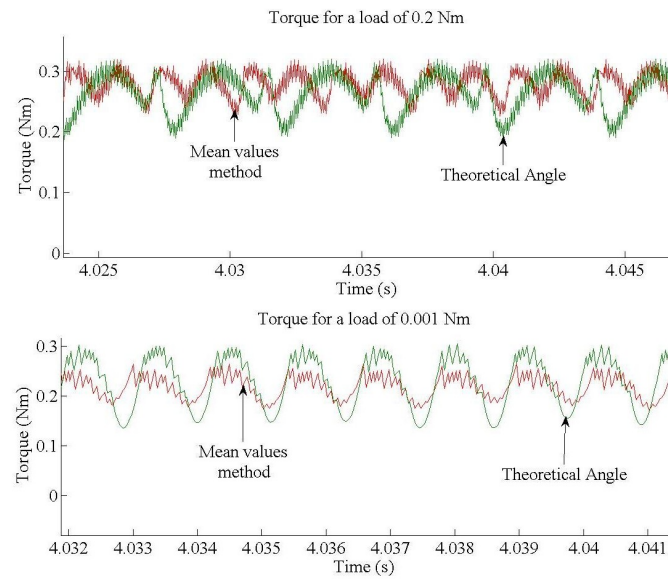


Fig.12. Torque behavior depending on the commutation angles for two different loads.

TABLE 3. COMPARATIVE SIMULATION RESULTS FOR SRM OPERATION MODE

Speed (rpm)	Ripple Torque (%)	Average Torque (Nm)	Commutation Angles (Deg)	Percentage reduction (%)
700	36.22	0.2794	Computed values by the average-value computation method	26.67
1000	40.17	0.2726		4.27
1300	43.49	0.262		12.30

1600	44.28	0.2472	$\theta_{on} = 0.04^\circ$	28.81
2000	47.17	0.2247	$\theta_{off} = 21.692^\circ$	38.28
700	49.39	0.2655	Theoretical values $\theta_{on} = -0.17^\circ$ $\theta_{off} = 17.94^\circ$	
1000	41.96	0.2648		
1300	49.59	0.2592		
1600	62.2	0.2513		
2000	76.43	0.2371		

Load Torque (Nm)	Ripple Torque (%)	Average Torque (Nm)	Commutation Angles (Deg)	Percentage reduction (%)
0.2	35.99	0.2786	Computed values by the average-value computation method $\theta_{on} = -0.118^\circ$ $\theta_{off} = 21.7^\circ$	31.59
0.15	40.75	0.2706		3.37
0.11	44.03	0.2587		5.19
0.06	44.9	0.2418		33.20
0.001	47.85	0.2183		42.56
0.2	52.61	0.2647	Theoretical values $\theta_{on} = -0.17^\circ$ $\theta_{off} = 17.94^\circ$	
0.15	42.17	0.2649		
0.11	46.44	0.2576		
0.06	67.22	0.2448		
0.001	83.31	0.2279		

In Fig.11 and 12 is represented the waveform of the electromagnetic torque for the smallest and the biggest load torque (Fig.12) and for the lowest and highest speed (Fig.11). For each case, the angles used were those obtained through the mean values method and the results were compared to the results obtained with the theoretical angle. The exact values of the used angles (Figs.11 and 12), of electromagnetic torque and ripple torque can be found in Table 3.

B. Simulation results for SRG operation mode

Table 4 presents the SRG torque ripple values for the optimal commutation angles determined above by the average-value computation method, in comparison with the torque ripple values obtained for theoretical commutation angles. It can be found, that SRG torque ripple values

- are reduced (in average) by 46.1% for optimal commutation angles determined by the average-values computation method as compared to torque ripple values obtained for theoretical commutation angles, at constant rotor speed.

- are reduced (in average) by 19.7% for optimal commutation angles determined by the average-values computation method as compared to torque ripple values obtained for theoretical commutation angles, at constant (negative) electromagnetic torque.

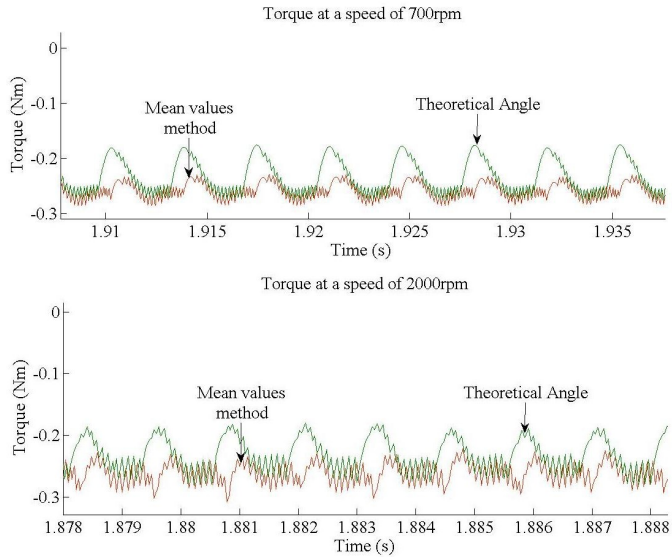


Fig.13. Torque behavior depending on the commutation angles at two different speeds

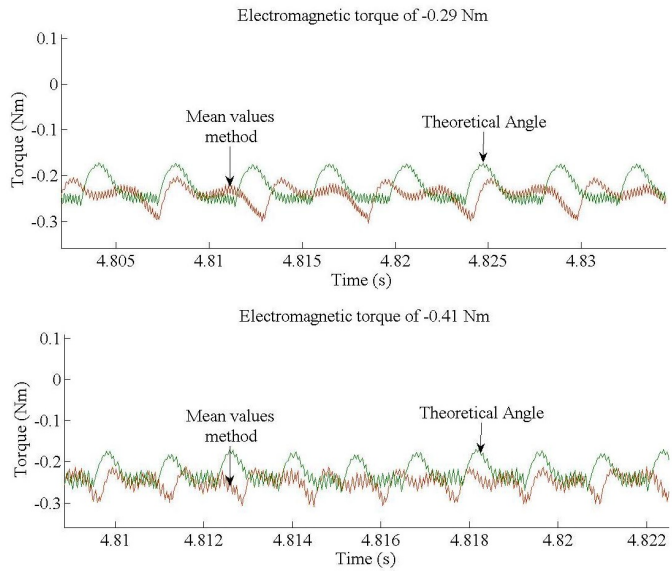


Fig.14. Torque behavior depending on the commutation angles at two different electromagnetic torque

Fig.13 and Fig.14 illustrate the waveforms of the electromagnetic torque for the generator mode. For the realization of Fig.13 the speed of the generator was chosen to be constant for the smallest value (700rpm) and the biggest value (2000rpm). In Fig.14 the electromagnetic torque was chosen to be constant for a value of -0.29 Nm and -0.41 Nm. In both figures (13 and 14) the chosen angles were the ones calculated with the method of mean values and the theoretical angle. The exact values of ripple torque and electromagnetic torque are shown in Table 4. As it can be noticed from Table 4, Fig.13 and Fig.14 the value of the electromagnetic torque varies with the angles, therefore not only the ripple torque

depends on the commutation angles but also the electromagnetic torque.

TABLE 4. COMPARATIVE SIMULATION RESULTS FOR SRG OPERATION MODE

Speed (rpm)	Ripple Torque (%)	Average Torque (Nm)	Commutation Angles (Deg)	Percentage reduction (%)
700	24.15	-0.258	Computed values by the average-value computation method $\theta_{on} = 12.25^\circ$ $\theta_{off} = 40^\circ$	48.98
1000	20.81	-0.258		57.00
1300	21.03	-0.259		57.06
1600	28.39	-0.258		45.62
2000	34.47	-0.259		22.00
700	47.33	-0.238	Theoretical values $\theta_{on} = 12.05^\circ$ $\theta_{off} = 37.15^\circ$	
1000	48.4	-0.236		
1300	48.98	-0.236		
1600	52.21	-0.2401		
2000	44.19	-0.2317		

Elmag Torque (Nm)	Ripple Torque (%)	Average Torque (Nm)	Commutation Angles (Deg)	Percentage reduction (%)
-0.29	40.54	-0.242	Computed values by the average-value computation method $\theta_{on} = 13.05^\circ$ $\theta_{off} = 39.7^\circ$	10.82
-0.32	35.69	-0.249		15.21
-0.36	35.3	-0.255		19.94
-0.39	29.12	-0.258		33.65
-0.41	43.38	-0.249		16.22
-0.29	45.46	-0.225	Theoretical values $\theta_{on} = 12.05^\circ$ $\theta_{off} = 37.15^\circ$	
-0.32	42.09	-0.23		
-0.36	44.09	-0.235		
-0.39	43.89	-0.2385		
-0.41	51.78	-0.2237		

V. CONCLUSION

The aim of this paper was the determination of optimal turn-on and turn-off angles for torque ripple reduction of a three-phase 6/8 SRM/G. An analytical model of SRM/G and a commutation-angle optimization technique for reducing the torque ripple were implemented in MATLAB /Simulink environment, for both motoring and generating operation modes over an extended speed range. Simulation-based performance analysis results for SRM/G with hysteresis current-control and commutation angles optimized to reduce torque ripple have been also provided and discussed.

REFERENCES

- [1] R. Krishnan, *Switched reluctance motor drives: modeling, simulation, analysis, design and applications*, CRC Press, Boca Raton, USA, 2001.
- [2] H. Chen, J.J. Gu, "Implementation of three-phase switched reluctance machine system for motors and generators," *IEEE/ASME Trans. Mechatron.*, vol.15, no.3, pp.421-432, 2010.
- [3] R. Hall *et al.*, "Design and initial testing of an outer rotating segmented rotor switched reluctance machine for an aero-engine shaft-line-embedded starter/generator", *Proc. IEEE Int. Electr. Mach. Drives Conf. – IEMDC 2005*, pp. 1870–1877.
- [4] B. Fahimi, A. Emadi, R.B. Sepe, Jr., "A switched reluctance machine-based starter/alternator for more electric cars", *IEEE Trans. Energy Convers.*, vol. 19, no. 1, pp. 116–124, 2004.
- [5] J. Sun *et al.*, "Implementation of a high-speed switched reluctance starter/generator system", *Proc. IEEE 15th Int. Conf. Electr. Mach. Syst. – ICEMS 2012*, 5 pp.
- [6] J. Sun *et al.*, "Torque ripple comparison of short-pitched and fully-pitched winding switched reluctance machine", *Proc. IEEE 15th Int. Conf. Electr. Mach. Syst. – ICEMS 2012*, 6 pp.
- [7] Muhammet Garip Yusuf Ozoglu Erkan Mese, "Static analysis of mutually coupled switched reluctance motor with finite element method", *UCTEA The Chamber Of Electrical Engineer.*
- [8] V.V. Prabhu, K.S. Mahesh, C. Renuka, "Simulation of switched reluctance motor/generator with optimum turn-on and turn-off control for the application of variable speed drives", *Proc. IEEE Int. Conf. Sustainable Energy Intell. Syst. – SEISCON 2011*, pp. 501-506.
- [9] C. Mademlis, I. Kioskeridis. "Optimizing performance in current-controlled switched reluctance generators". *IEEE Trans. Energy Convers.*, vol. 20, no. 3, pp. 556-565, 2005.
- [10] D. Ilea, F. Gillon, P. Brochet, M.M. Radulescu, "Comparative finite-element and permeance-network analysis for design optimization of switched reluctance motors", in: *"Computational methods for the innovative design of electrical devices"*, Springer-Verlag, Berlin, Germany, 2011, pp. 304-310.

Electromagnetic Design and Finite-Element Analysis of an Axial-Flux Permanent-Magnet Machine

Adrian Augustin POP

Department of Electroenergetics and Management
Technical University of Cluj-Napoca
Cluj Napoca, Romania
Augustin.POP@enm.utcluj.ro

Horia BALAN

Department of Electroenergetics and Management
Technical University of Cluj-Napoca
Cluj Napoca, Romania
Horia.Balan@enm.utcluj.ro

Mircea M. RADULESCU

Department of Electrical Machines and Drives
Technical University of Cluj-Napoca
Cluj Napoca, Romania
Mircea.Radulescu@emd.utcluj.ro

Mihai CHIRCA

Department of Electrical Machines and Drives
Technical University of Cluj-Napoca
Cluj Napoca, Romania
mihaichirca@mail.utcluj.ro

Valentin ZAHARIA

Department of Electrical Machines and Drives
Technical University of Cluj-Napoca
Cluj Napoca, Romania
Valentin.ZAHARIA@mae.utcluj.ro

Abstract— This paper approaches the electromagnetic design and finite-element analysis of an axial-flux permanent-magnet (AFPM) synchronous generator for small-scale wind turbines. The study is conducted to find a good-performance and cost-effective electric generator topology for micro-wind power application. The proposed double-sided two-stators-one-rotor AFPM synchronous generator with non-overlapping concentrated slotless-stator-winding and ironless PM-rotor disk could be the machine of choice in grid-connected or stand-alone small-scale wind energy conversion systems.

Keywords—axial flux; permanent magnet; wind energy;

I. INTRODUCTION

Despite their great potentials small-scale wind turbines reveal low penetration in the renewable-energy production market, as compared with large utility-size wind turbines, due to the following main reasons [1]: (i) micro-wind turbines operate mostly in low-wind-speed areas, experiencing self-starting problems, which have negative consequences on the energy yield; (ii) the cost per installed kW of current stand-alone micro-wind turbines is much higher than that for large wind turbines; (iii) micro-wind turbines require good technical skills and rather complex equipment in manufacturing and maintenance processes, which increase their installing and operational costs.

Many micro-wind turbine manufacturers use direct-driven generators [2], thus avoiding mechanical gear, reducing size of the entire system, lessening noises and lowering installation and maintenance costs. However, a direct-driven micro-wind

generator has to operate at very low speeds in order to match the wind turbine speed, and to produce electricity within a reasonable frequency range; hence, the micro-wind generator has a rather big size, and must be designed with a large number of poles.

Axial-flux permanent-magnet (AFPM) synchronous generators are increasingly being used in the last decade for direct-drive small-scale wind turbine applications [3, 4]. Compared with conventional radial-flux PM machines, the AFPM synchronous generators have the advantages of more compact structure due to the flat shape with short axial-length, larger power-to-weight ratio and torque density, more flexible PM-field and armature-winding design, better cooling and modular construction. The drawback of a low-speed direct-driven AFPM synchronous generator is that it requires larger diameter, which affects the material cost of the machine [5]. The double-sided two-stators-one-rotor AFPM synchronous generator topology with non-overlapping concentrated slotless-stator-winding and ironless PM-rotor disk is considered in this paper, which is organized as follows. In Section II, the preliminary electromagnetic design of the proposed double-sided internal-rotor AFPM synchronous machine for use as a direct-driven generator with small-scale wind turbines is addressed. Section III presents the 3-D finite-element field analysis and simulation results for the double-sided AFPM synchronous generator design evaluation. Conclusion is drawn in Section IV.

II. PRELIMINARY ELECTROMAGNETIC DESIGN OF THE AFPM SYNCHRONOUS GENERATOR FOR SMALL-SCALE WIND TURBINES

The considered AFPM synchronous generator has an inner PM-rotor with eight pole-pairs of axially-magnetized NdFeB-type magnets, which are accommodated in an ironless disk. External slotted stators may increase notably the airgap flux density due to the reduced clearance between rotor and stator. The required amount of rotor-PMs becomes smaller, thus lowering the global cost of the machine. On the other hand, the use of slotted-stator armature winding results in significant cogging torque and content of harmonics in the back-emf waveform. Such problems must be tackled efficiently from the electromagnetic design viewpoint.

References [6, 7] advocate the application of slotless-stator concentrated non-overlapping armature-winding in AFPM synchronous generators, since the winding process using prefabricated coils is cost-effective. Furthermore, the space needed by the end-windings and thus the copper losses are minimized.

The rated power of the AFPM synchronous generator under study is of 2.5 kW for the rotational speed of 200 rpm.

By applying the general sizing equation to the small AFPM synchronous generator under study, the outer surface diameter D_o is obtained as

$$D_o = \left[\frac{8 p}{\pi^2 f k_i k_p \eta (1 + \lambda) (1 - \lambda^2) (B_g)} \frac{P_{out}}{k_f} \right]^{1/3} \quad (1)$$

The total outer diameter of the machine is given by

$$D_{tot} = D_o + 2W_{Cu} \quad (2)$$

and the total axial length of the machine can be expressed as

$$L_{tot} = L_r + 2L_s + 2g \quad (3)$$

where the rotor axial length sums the rotor-core and rotor-PM contributions, i.e.

$$L_r = L_{r,core} + 2L_{PM} = B \frac{B_u}{B_{r,core}} \cdot \frac{\pi (1 + \lambda) D_o}{8 p} + \frac{\mu_{r,PM} B_g}{B_{rem} \frac{k_f}{k_d} B_g} g \quad (4)$$

with $B_{r,core}$ representing the flux density in the rotor-disk core; B_u , the attainable flux density on the surface of the rotor-PM; $\mu_{r,PM}$ and B_{rem} , the relative permeability and the remanent flux density of the rotor-PM material, respectively; k_d and k_f , the leakage flux factor and the peak-value-corrected radial-airgap flux-density factor of the machine, respectively; k_e , the back-emf factor, i.e. the armature-winding distribution factor; N_{ph} , the number of turns in series per armature-winding phase; f , the mains electrical frequency; p , the number of machine pole-pairs; D_i , D_o , the diameters of the inner and outer surfaces of

the machine, respectively; $\lambda = D_i / D_o$, the inner-to-outer diameter ratio; \hat{B}_g , the peak value of the magnetic flux density in the airgap (magnetic loading); g , the airgap axial length.

The stator axial length sums the stator-core axial length

$$L_S = L_{s,core} \quad (5)$$

where

$$L_{s,core} = \frac{B_g}{B_{s,core}} \cdot \frac{\pi \alpha_p (1 + \lambda) D_o}{4 p} \quad (6)$$

with $B_{s,core}$, the flux density in the stator core; α_p , the ratio of the average airgap flux density to the peak value of the airgap flux density; J_{slot} , the stator-slot current density; k_{Cu} , the copper-fill factor.

The analytical preliminary electromagnetic design has been used for determining the main data of rotor and stator components for the small three-phase AFPM synchronous generator, listed in Table I.

Table I Main design data of the small three-phase double-sided inner-rotor AFPM synchronous wind-generator

Design data	Value
Turns per stator-winding phase	2500
Turns per coil	312
Wire diameter [mm ²]	0.5
Slot-fill factor (gross)	0.5
Stator phase-winding resistance [Ω]	12
Rotor-PM thickness [mm]	20
Airgap clearance [mm]	2
Number of PM-rotor poles	16
Outer radius [mm]	295
Rated rotational speed [rpm]	200
Rated output power [W]	2500

III. 3-D FINITE-ELEMENT FIELD ANALYSIS OF THE AFPM SYNCHRONOUS GENERATOR FOR SMALL-SCALE WIND TURBINES

Due to rapid advances in computational methods, a number of 3-D finite-element (FE) field analysis software packages are now available, so that a given field problem may be solved by a judicious choice of the software tool. In this paper, the design evaluation of the small three-phase double-sided inner-rotor AFPM synchronous wind-generator is conducted by time-stepped 3-D FE field analysis using the commercial software JMAG-Studio.

The time-stepping FE field-circuit solution procedure entails the following steps: (i) build the geometric field model and the coupled circuit model of the AFPM wind-generator; (ii) build the sliding surface for time-stepping analysis; (iii)

select solver, boundary conditions and time increment; (iv) execute the program to obtain the FE field-circuit solution.

Rotor-PM flux-density distribution from 3-D FE analysis of the small double-sided inner-rotor AFPM synchronous wind-generator is presented in Fig. 1, which proves that magnetic saturation in the PM-rotor disks is not of concern.

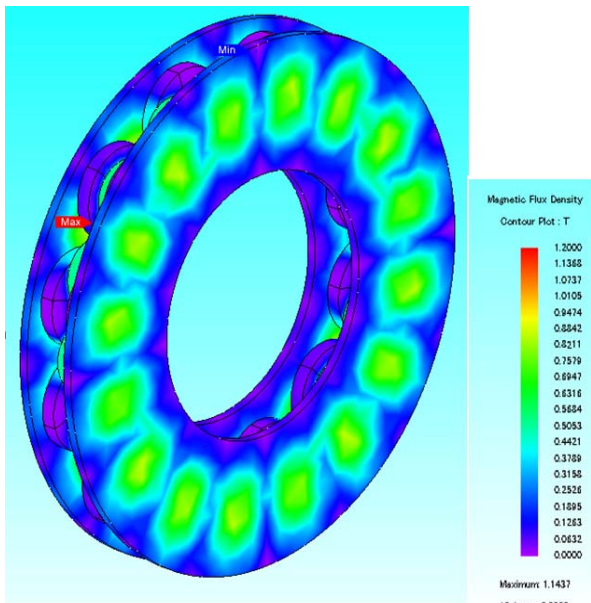
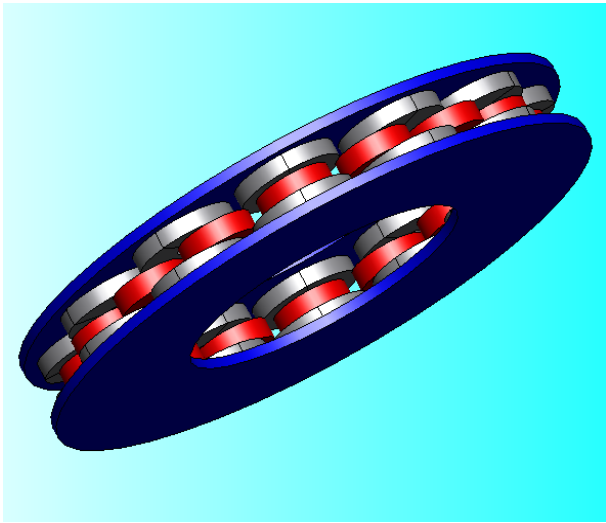


Fig. 1. Rotor-PM flux density distribution in the small double-sided inner-rotor AFPM synchronous wind-generator.

The induced back-emf waveforms under no-load (open stator-circuit) condition are computed in Fig.2, showing a rms-value of about 364 [V/phase].

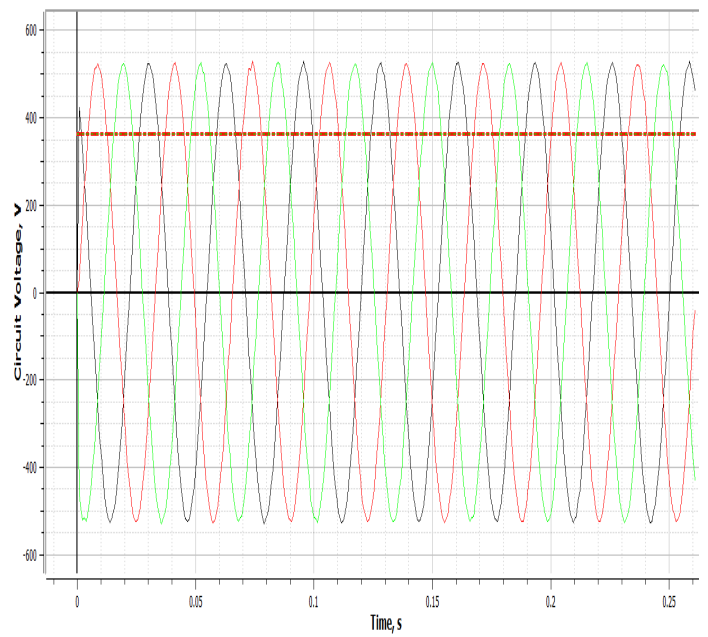


Fig. 2. FE-computed line back-emfs of the small double-sided inner-rotor AFPM synchronous wind-generator under no-load condition

The performance of the small double-sided inner-rotor AFPM synchronous wind-generator supplying an isolated, three-phase resistive load of 158 [Ω /phase] is computed using the 3-D FE time-stepping analysis. Fig. 3 presents the FE-computed dynamic electromagnetic torque. It can be seen that the mutual torque ripple caused by harmonic components of the developed electromagnetic torque is quite significant.

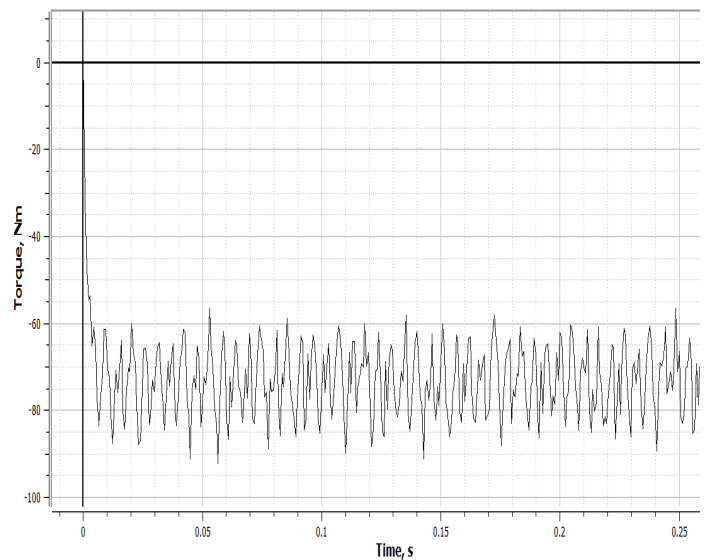


Fig. 3. FE-computed dynamic electromagnetic torque of the small double-sided inner-rotor AFPM synchronous wind-generator under resistive load condition.

Fig. 4 shows the FE-computed stator-winding line-voltage and line-current waveforms, which are practically sinusoidal. It is to be noted, that the computed waveforms have taken into account the geometry of the stator-armature winding coils.

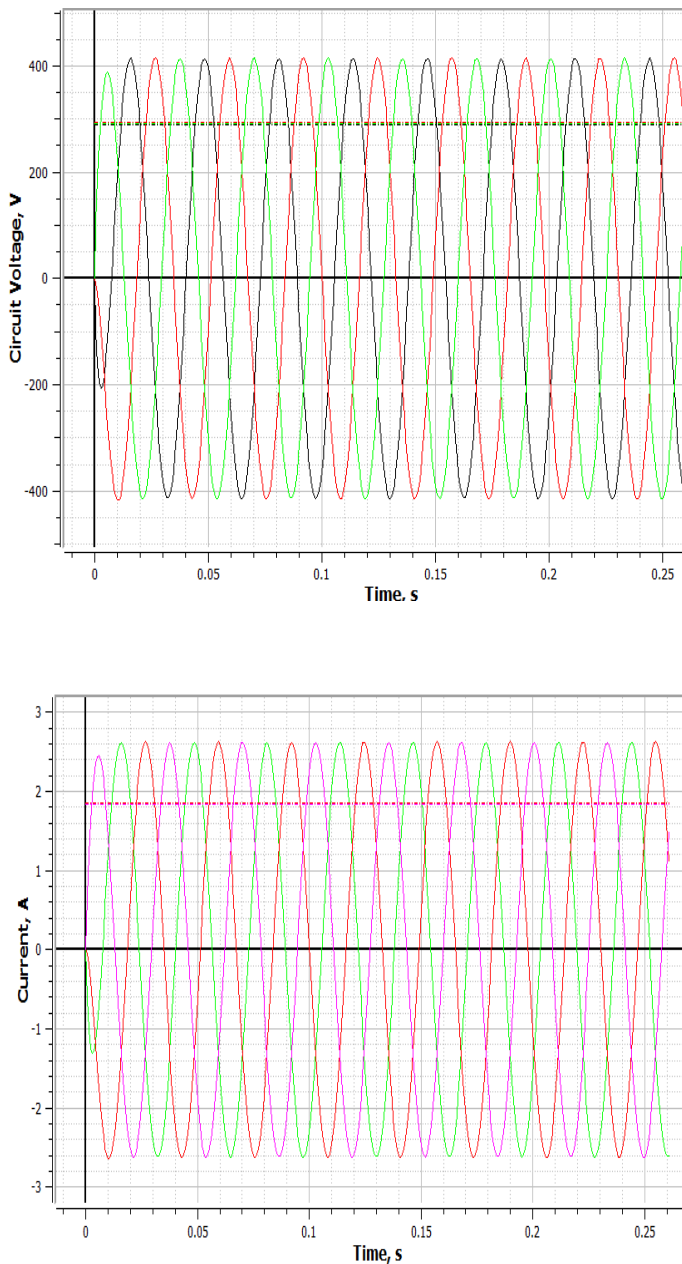


Fig. 4. FE-computed stator-winding line-voltage and line-current waveforms for the small double-sided inner-rotor AFPM synchronous wind-generator under resistive load condition.

The FE-computed results, as well as the active material masses from the design analysis of the small double-sided inner-rotor AFPM synchronous wind-generator are summarized in Table II.

Table II Design FE-analysis results for the small double-sided inner-rotor AFPM synchronous wind-generator

Design FE-analysis result	Value
Copper mass of the stator winding [kg]	25
Mass of rotor PMs [kg]	9.93
Iron mass of stators [kg]	25
Total mass [kg]	60
I_{rms} [A]	1.85
U_{rms} [V]	298
Stator-winding copper losses [W]	130
Torque [Nm]	75
Active materials estimated cost [Euro]	350
Manufacturing cost factor	1.5
Total estimated cost [Euro]	525

IV. CONCLUSIONS

Electromagnetic design of a small double-sided inner-rotor AFPM synchronous wind-generator has been addressed and discussed in this paper. Its two-stators-one-rotor topology with non-overlapping concentrated slotless-stator-winding and ironless PM-rotor disk makes this design well suited for low-speed micro-wind generator applications. The FE-based design analysis results have shown its good performances in output characteristics, electromagnetic torque and overall cost effectiveness.

V. ACKNOWLEDGEMENT

This work was supported by Romanian Executive Unit for Financing Higher Education, Research, Development and Innovation (UEFISCDI) from the research project with the code PN-II-PT-PCCA-2011-3.2-1519.

VI. REFERENCES

- [1] S.O. Ani, H. Polinder, J.A. Ferreira, "Comparison of energy yield of small wind turbines in low wind speed areas". *IEEE Transactions on Sustainable Energy*, vol. 4, no. 1, pp.42-49, 2013.
- [2] E. Spooner, A.C. Williamson, "Direct-coupled, permanent-magnet generators for wind turbines", *Proceedings IEE - Electric Power Applications*, vol. 143, no. 1, pp. 1-8, 1996.
- [3] J.R. Bumby, R. Martin, "Axial-flux permanent-magnet air-cored generator for small-scale wind turbine", *Proceedings IEE - Electric Power Applications*, vol.152, no.5, pp. 1065- 1075, 2005.
- [4] T.F. Chan, L.L. Lai, "An axial-flux permanent-magnet synchronous generator for a direct-coupled wind-turbine system," *IEEE Transactions on Energy Conversion*, vol. 22, no. 1, pp. 86-94. 2007.
- [5] J.F. Gieras, R.-J. Wang, M.J. Kamper, *Axial flux permanent magnet brushless machines*, 2nd edition, Springer-Verlag, 2008.
- [6] A. Mahmoudi, H.W. Ping, N.A. Rahim, "A comparison between the TORUS and AFIR axial-flux permanent-magnet machine using finite element analysis", *Proc. IEEE Int. Electr. Mach. Drives Conf. - IEMDC 2011*, pp.242-247, 2011.
- [7] Hanne Jussila *et al.*, "Concentrated winding axial flux permanent magnet motor for industrial use", *Proc. 19th Int. Conf. Electr. Mach. - ICEM 2010*, Rome, Italy, 2010.
- [8] A.A. Pop, M.M. Radulescu, F. Gillon, "Modelling and permanent-magnet shape optimization of an axial-flux machine", *Proc. 20th Int. Conf. Electr. Mach. - ICEM 2012*, Marseille, France, 2012.

Current control methods for grid-side three-phase PWM voltage-source inverter in distributed generation systems

I. Lar^{*}, M.M. Radulescu^{*}, E. Ritchie^{**}, A.A. Pop^{*}

^{*} SEMLET Group, Technical University of Cluj-Napoca, P.O. Box 345, RO-400110 Cluj-Napoca, (Romania)

^{**} Aalborg University, Pontopidanstraede 101, Aalborg, (Denmark)

E-mail: ionut.lar@gmail.com, mircea.radulescu@mae.utcluj.ro, aer@et.aau.dk, augustin.pop@mae.utcluj.ro

Abstract – A comparison between two current control methods for grid-side inverter, i.e. PI control and forward predictive control, is made. The PI current control is implemented in d-q synchronous frame, while the forward predictive current control is implemented in abc stationary frame. The paper presents both simulation and experimental results, which were made at a reduced scale (2.2 kW). The constant-power test showed that both methods have good results in respect to existing grid codes.

I. INTRODUCTION

The increase demand for electrical power, together with the rapid growth of DGS has produced a new mean of power generation. In grid-connected DGSs, three-phase pulse-width-modulation (PWM) voltage-source inverters are now mandatory for purposes of power conversion, grid interfacing and control optimization [1].

Existing grid codes, demand new control algorithms which gives possibility to regulate injected active and reactive power. The grid operator's main objective is to keep the grid balanced by controlling both active and reactive power flow [2].

There are many current control strategies, which were debated during the years. The most significant current regulating techniques for voltage-source inverters are hysteresis control, proportional-integral (PI) control and predictive control [3]. While the PI control needs a good tuning to match system parameters, and the hysteresis control leads to variable switching frequencies, the predictive control affords opportunities for more precise current regulation of grid-connected inverters.

Previous work [3] was done in order to improve predictive control strategy by implementing a direct digital predictive regulator. DGSs plant, usually is formed by an output filter and a distribution transformer. In this case the grid impedance is smaller in comparison to the equivalent impedance of the DGSs.

However, with good tuning of the current controller, the grid impedance variation can be avoided. Predictive current control family is divided in two main strategies:

(i) deadbeat control, which calculates the inverter's output voltage so that the current through inverter is forced to follow its reference; dead beat control was subject of debates for long time, thus becoming now a traditional current control strategy[2],[3];

(ii) forward predictive control modifies dead beat algorithm structure, i.e. instead of zero-current error at the beginning of the next switching period, the current error is half the difference of the previous two current errors; it was proven that the forward predictive control can improve the dead beat control performance.

The new robust forward predictive current control strategy has been developed in [2] as an improvement of existing Deadbeat Predictive control strategy. In this context, the present paper makes a comparative simulation and experimental study of the forward predictive current control and the commonly used PI current control for grid-side three-phase PWM voltage-source inverters in DGSs.

II. FORWARD PREDICTIVE AND PI CURRENT CONTROLS OF GRID-CONNECTED INVERTERS

A. Forward Predictive Current Control

Forward predictive current control assigns to the current error of the actual switching period half the difference of previous two current errors [2].

Fig. 1 shows the system raw scheme. In order to obtain inverter's load current expression, second Kirchhoff theorem is applied

$$U_{i_{abc}} - U_{g_{abc}} = L_e \cdot \frac{di_{m_{abc}}}{dt} - R_e \cdot I_m, \quad (1)$$

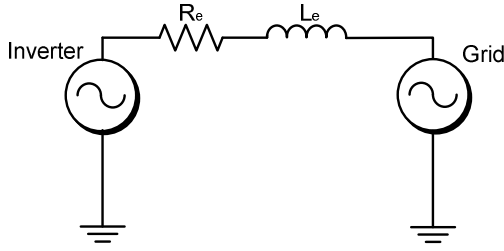


Fig. 1. System raw scheme.

where

- $U_{i_{abc}}$ - inverter output voltages
- $U_{g_{abc}}$ - grid voltages
- $I_{m_{abc}}$ - inverter load current trough each phase
- L_e - transformer and filter equivalent inductance
- R_e - transformer and filter equivalent resistance

For digital implementation of control scheme, (1) can be represented in discrete-time with the sample period of T_s as follows:

$$u_{i_a}^{av}[n] = u_{g_a}^{av}[n] + L_e \cdot \frac{i_{m_a}[n+1] - i_{m_a}[n]}{T_s}, \quad (2)$$

where

$u_{g_a}^{av}[n]$ - average grid voltage on phase A,

at sampling point n

$i_{m_a}[n]$ - measured inverter current, at sampling point n

$i_{m_a}[n+1]$ - measured inverter current, at sampling point $n+1$.

Considering that the change of the grid voltage is linear, their average values $u_{g_a}^{av}[n]$ can be predicted based on the actual ones:

$$u_{g_a}^{av}[n] = 1.5u_{g_a}[n] - 0.5u_{g_a}[n-1]. \quad (3)$$

Traditional predictive current control algorithm performs the computational operations for the next switching in the previous switching cycle.

According to [4], the computational time is insignificant compared to switching cycle time. Therefore, sampling point n was moved right behind controlling point " n " as shown in Fig. 2.

For small control periods when sampling and calculation time of the processor is significant compared to

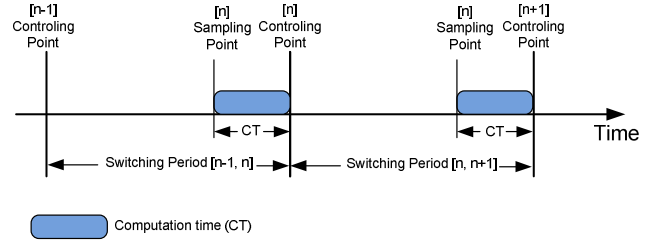


Fig. 2. Time schematic of sampling point and controlling point in forward predictive current control [5], [6].

control time, the command voltage $u_{i_a}^{av}[n]$, which should be loaded into the PWM generator at time $[n]$, will be delayed with one switching period. This will lead to lower control accuracy and poor stability margin. In order to compensate the control delay influence, a current observer can be derived from (2) and (3) for the switching period $[n-1, n]$:

$$i_{m_a}[n] = (u_{i_a}^{av}[n-1] - 1.5u_{g_a}[n-1] + 0.5u_{g_a}[n-2]) * \frac{T_s}{L_e} + i_{m_a}[n-1] \quad (4)$$

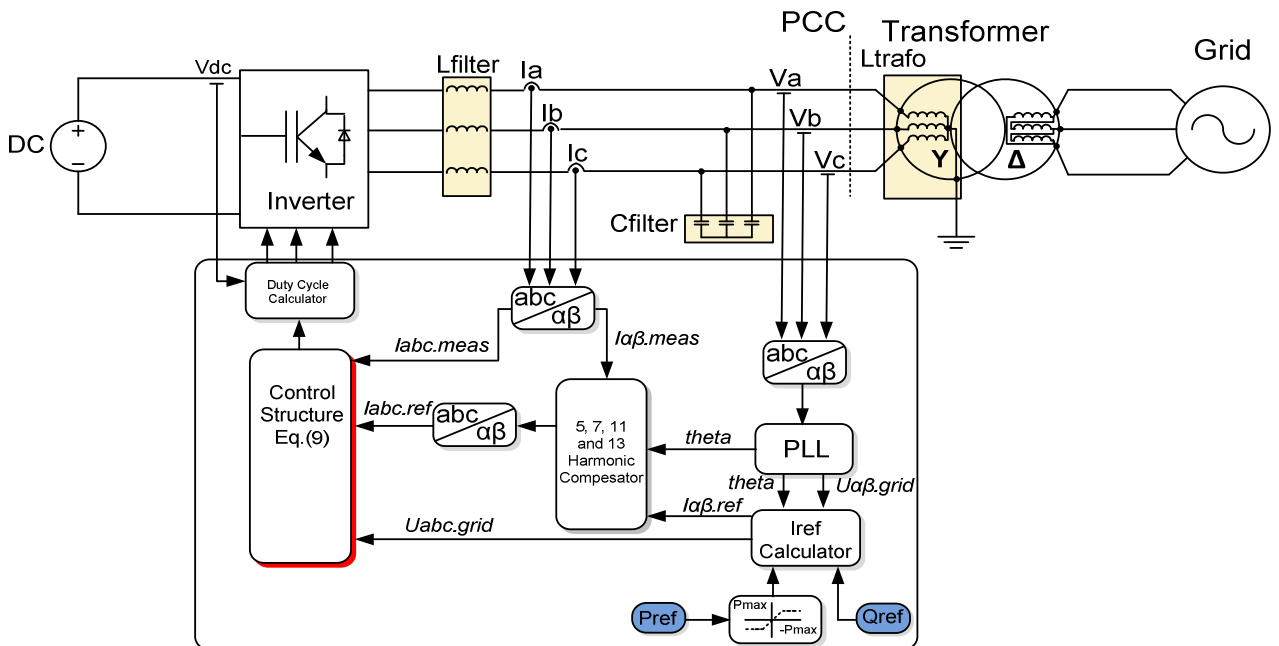


Fig. 3. Forward Predictive current control basic diagram

Starting from forward predictive control definition, one can write

$$i_{e_a}[n+1] = \frac{i_{e_a}[n] - i_{e_a}[n-1]}{2} \quad (5)$$

The current error represents the difference between the reference and the measured current:

$$i_{e_a}[n] = i_a^{ref}[n] - i_{m_a}[n]. \quad (6)$$

By substituting (6) for $i_{e_a}[n]$ and $i_{e_a}[n-1]$ in (5) for sampling points $[n]$ and $[n-1]$ the load current at sampling point $[n+1]$ can be forward predicted as

$$i_{m_a}[n+1] = i_a^{ref}[n+1] - 0.5(i_a^{ref}[n] - i_a^{ref}[n-1]) - i_{m_a}[n] + i_{m_a}[n-1] \quad (7)$$

Introducing the above expression of $i_{m_a}[n+1]$ in (2), the average output voltage can be evaluated:

$$u_{i_a}^{av}[n] = u_{g_a}^{av}[n] + \frac{L_e}{T_s}(i_a^{ref}[n+1] - 0.5i_a^{ref}[n] + 0.5i_a^{ref}[n-1] - i_{m_a}[n-1] - 0.5i_{m_a}[n]) \quad (8)$$

In order to compensate the control delay influence, the current observer from (4) and average grid voltage from (3) may give the final command voltage $u_{i_a}^{av}[n]$ as

$$u_{i_a}^{av}[n] = 1.5u_{g_a}[n] + 0.25u_{g_a}[n-1] - 0.25u_{g_a}[n-2] - 0.5u_{i_a}[n-1] + \frac{L_e}{T_s}\{i_a^{ref}[n+1] - 0.5i_a^{ref}[n] + 0.5i_a^{ref}[n-1] - i_{m_a}[n-1]\} \quad (9)$$

The control scheme of the forward predictive current control is shown in Fig.4.

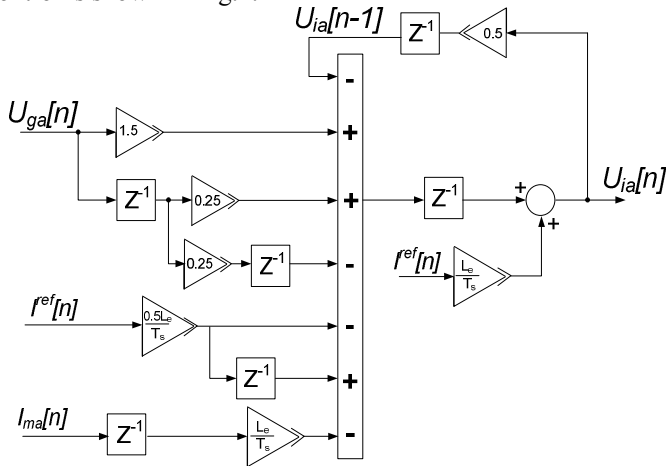


Fig. 4. Control scheme of the forward predictive current control.

Based on the approach presented in [6], the reference currents can be calculated from instantaneous active and reactive power as

$$i_{\alpha}^{ref} = \frac{u_{g_{\alpha}} P^{ref} + u_{g_{\beta}} Q^{ref}}{u_{g_{\alpha}}^2 + u_{g_{\beta}}^2} \quad (10)$$

$$i_{\beta}^{ref} = \frac{u_{g_{\beta}} P^{ref} - u_{g_{\alpha}} Q^{ref}}{u_{g_{\alpha}}^2 + u_{g_{\beta}}^2}. \quad (11)$$

B. Proportional-Integral (PI) Current Control

The PI control scheme (Fig.5) consists in two controllers, which regulates the output active and reactive power. This leads to reference currents generation which need to be tracked by internal controller. Ultimately this will lead to inverter switches commands

By adjusting the d-axis component of the current, an active power control is achieved. Identically, by regulating the q-axis current component a reactive power control is achieved. So, by setting the current in the quadrature axis to be null, the reactive power is also null, and thus the power factor becomes equal to unity.

The voltage feed forward and the decoupling component between the d and q axes are added after PI controller. Harmonic compensator component are being added to reference voltages before the duty cycles generator of the VSI.

In order to determine the system's stability an equivalent transfer function for the PI current controller along with the inverter, filter respectively plant is presented in Fig.6.

- PI transfer function:

$$G_{PI}(s) = K_p + \frac{K_i}{s}, \quad (12)$$

- Control Algorithm transfer function:

$$G_c(s) = \frac{1}{1+sT_s}, \quad (13)$$

where $T_s = 1/f_s$ and $f_s = 8kHz$ is sampling frequency;

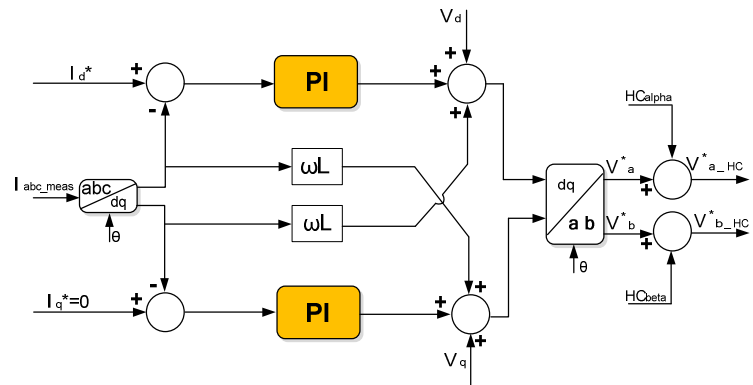


Fig. 5. Control scheme of the PI current control.

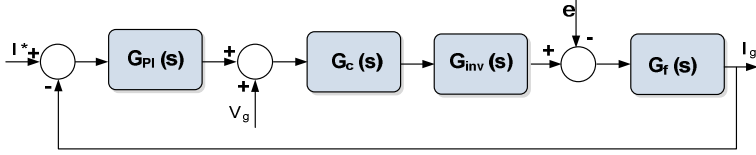


Fig. 6. Block diagram of the PI control scheme.

- Inverter transfer function:

$$G_{inv} = \frac{1}{1+0.5sT_{sw}}, \quad (14)$$

where $T_{sw} = 1/f_{sw}$, and $f_{sw} = 8\text{kHz}$ is the switching frequency.

The transformer is an important component in the design procedure of the controller. Joined at the existing converter LC filter forms an LCL filter. The capacitor and the transformer inductance as well as the grid inductance introduce two additional zeros and poles causing system instability. Therefore, a dumping resistance (R_d) is connected in series with the filter capacitor, as shown in Fig.7.

The equivalent transfer function of the block diagram from Fig.6 becomes:

$$G_{ech} = \frac{G_{PI}G_cG_{inv}G_f}{1+G_{PI}G_cG_{inv}G_f} \quad (15)$$

With

$$G_f(s) = \frac{1+R_dC_f s}{L_f L_t C_f s^3 + C_f(L_f R_d + L_t R_d + L_t R_f + L_f R_t) s^2 + (L_f + L_t + R_d C_f R_f + C_f R_f R_t) s + (R_f + R_t)} \quad (16)$$

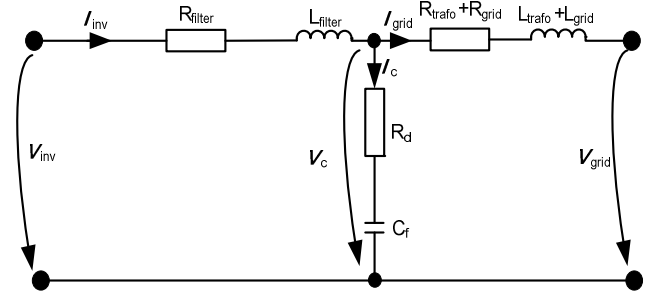


Fig. 7. LCL-filter equivalent electrical scheme.

The integral and proportional gains for the PI controller were determined as [7]

$$K_p = \frac{2(R_t + R_f)}{3T_d} K_i = \frac{K_p(R_t + R_f)}{L_t + L_f}. \quad (17)$$

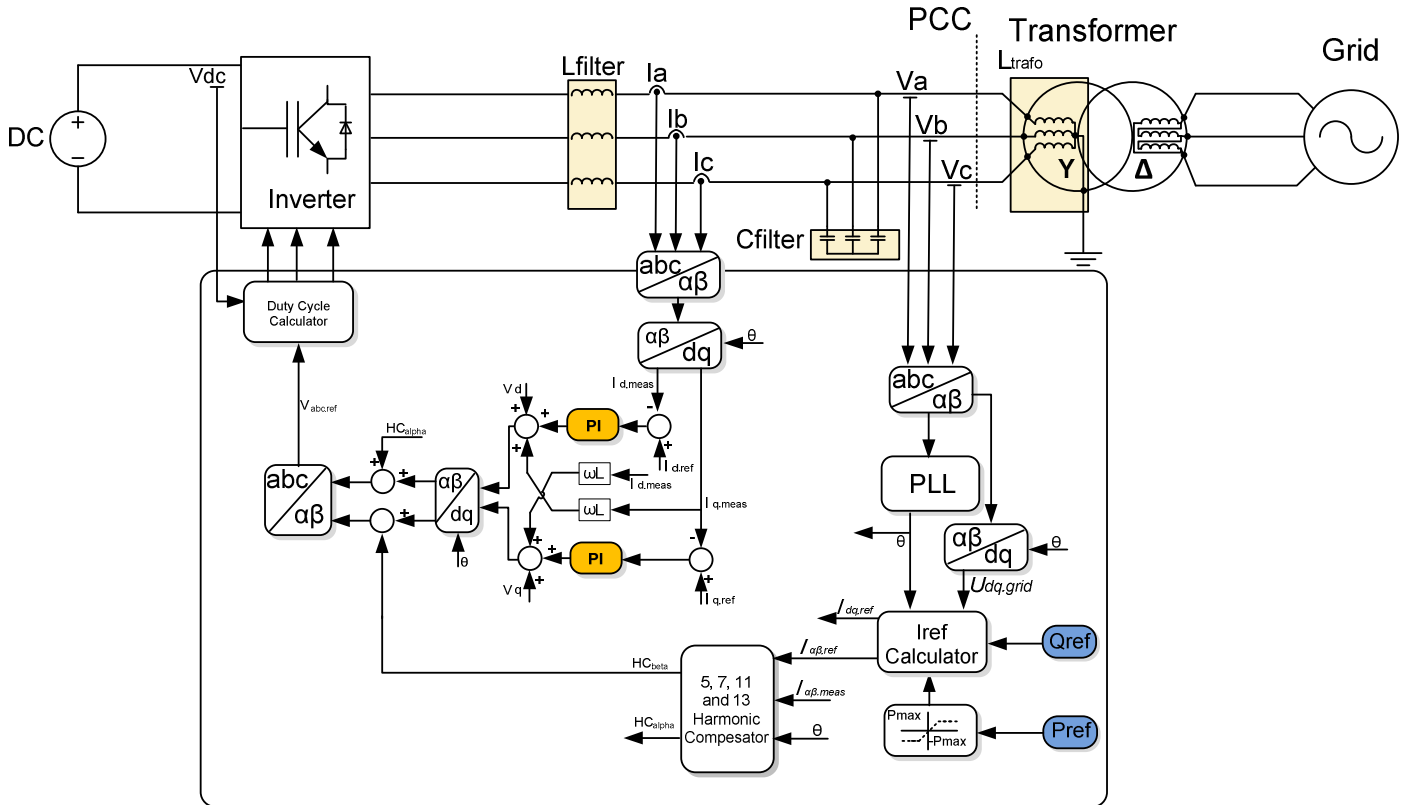


Fig. 8. Structure of the PI current control with harmonic compensator.

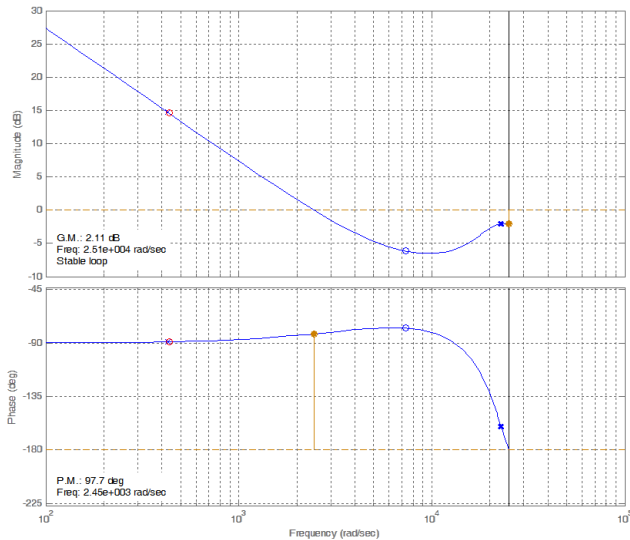


Fig. 9. Bode graph for the plant and PI current control open-loop system.

According to open loop bode graph it may be concluded that this design is robust and can tolerate a 2.11 dB gain increase or a large phase lag in the open-loop system without going unstable. ($G_m = 2.11$ dB(at $2.5e + 004$ rad/sec, $P_m = 97.7$ deg)

III. SIMULATION RESULTS

Computer simulations have been carried out using Simulink and PLECS, Matlab Toolbox's to comparatively assess the performances of both PI and forward predictive current control strategies. Constant power and step-change in power reference were tested in order to determine how fast the control system reacts.

A. Constant-power test simulation results

As shown by Table 1 and Fig.10, for steady-state constant-power simulated test both current control methods, present good results in current amplitude, wave shape and harmonics content.

Table 1. Harmonic-content results from constant-power simulation

	no harmonic compensation		with harmonic compensation	
	PI	FW. PCC	PI	FW. PCC
	THD [%]	THD [%]	THD [%]	THD [%]
P=500 W; Q=0VAr	33.25	24.83	13.84	9.42
P=1000 W; Q=0VAr	19.77	14.91	7.63	5.92
P=1000 W; Q=-1000VAr	11.75	8.05	6.52	4.44
P=1000 W; Q=1000VAr	15.81	10.83	6.76	4.6
P=1000 W; Q=-2000VAr	9.4	6.44	5.11	3.48

B. Power step-change test simulation results

Both current control strategies have been tested at various active- and reactive-power step-changes.

In Fig.11, a step-change of 500 W in active power has been applied in order to define how both current controls can adapt to any reference power changes. As can be seen, PI control follows more accurately the reference current at low power, but shows higher transients and twice the recovery-time during a step-change in power reference.

In Fig.12, a step-change of -1500 VAR in reactive power is simulated. It is pointed out that the forward predictive current control has better harmonic content and less recovery-time after transients.

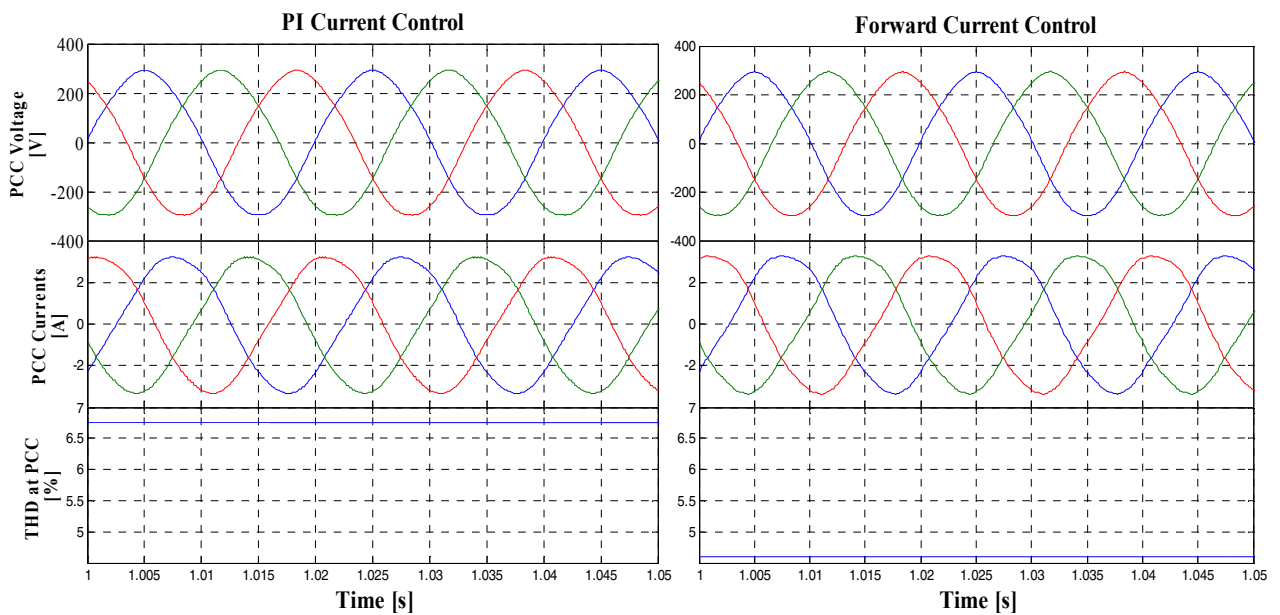


Fig. 10. Steady-state constant power (P = 1000 W and Q = 1000 VAR) test simulation results.

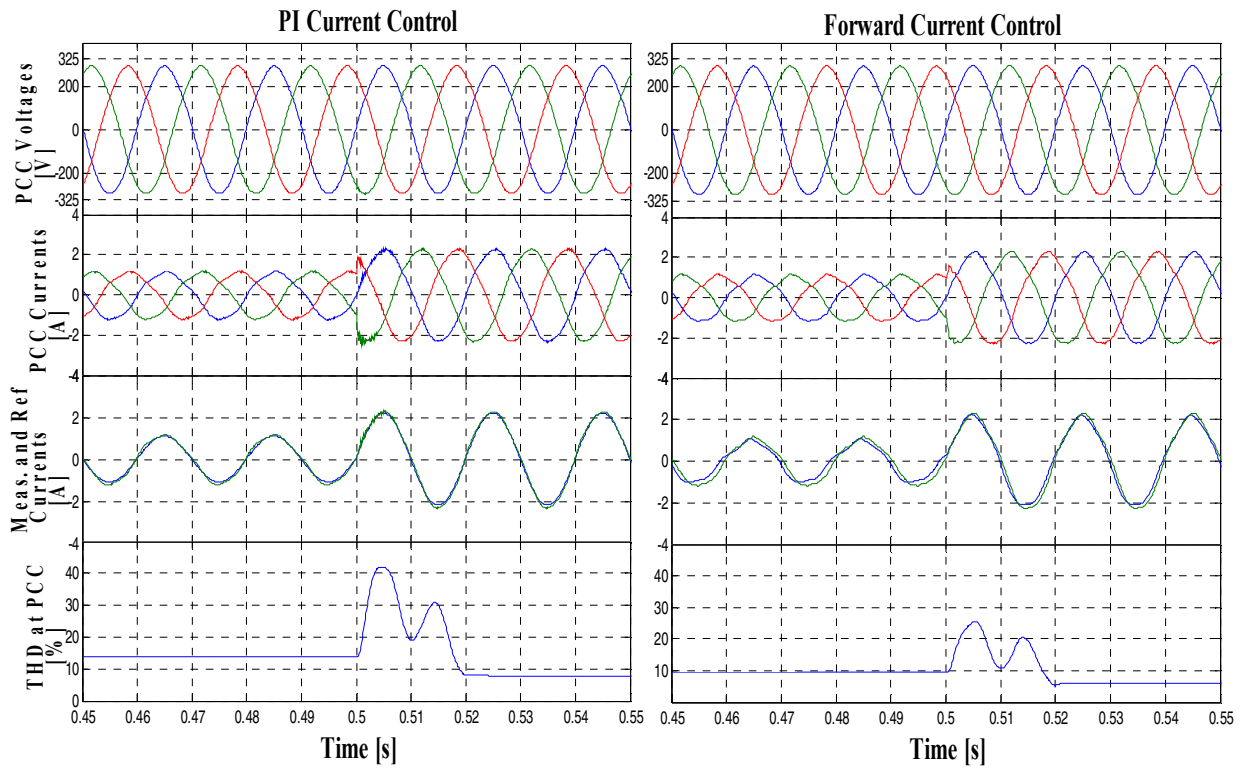


Fig. 11. Active power step-change (from $P_1 = 500 \text{ W}$ to $P_2 = 1000 \text{ W}$ and $Q = 0 \text{ VAR}$) test simulation results.

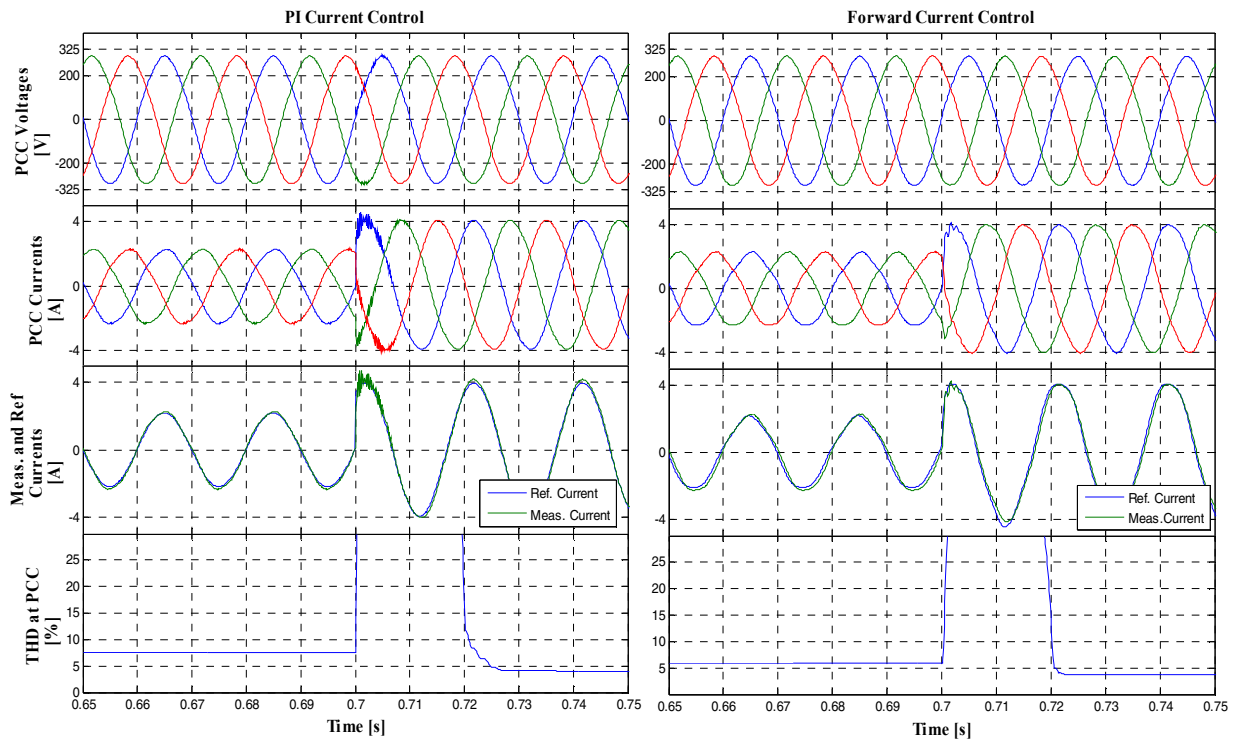


Fig. 12. Reactive power step-change (from $Q_1 = 0 \text{ VAR}$ to $Q_2 = -1500 \text{ VAR}$ and $P = 1000 \text{ W}$) test simulation results.

IV. EXPERIMENTAL RESULTS

Several experimental tests were carried out using the laboratory set-up of Fig.13 with dSPACE interface controlling the 2.2 kW, grid-connected three-phase PWM voltage-source inverter. The parameters of the hardware equipment are listed in Table 2.

The model configuration used for experimental work represents the main configuration on which the simulation model was built. Danfoss-type FC302 2.2 kW- 400Vac converter was used as a grid-side inverter, together with an LC sine-wave filter (Danfoss code No. 130B2443). The inverter is an IGBT-based converter, whose interface cards have been replaced by Interface and Protection Cards (IPC2). The dSPACE system delivers five signals for each IPC2 card: three duty cycles for the inverter switches, one enable and one reset signal. The voltage and current measurements are achieved through LEM modules.

Table 2. Hardware equipment parameters of the experimental set-up

Hardware parameters		
Fsw	Switching frequency	8000 Hz
Faq	Acquisition frequency	8000 Hz
C_filter	Filter capacitance	4.7 [μ F]
R_conv	Converter resistance	0.1 [Ω]
L_conv	Converter side filter inductance	1.8 [mH]
R_trafo	Transformer resistance	0.03 [Ω]
L_trafo	Transformer inductance	2 [mH]
L_mag	Transformer magnetization inductance	100 [mH]

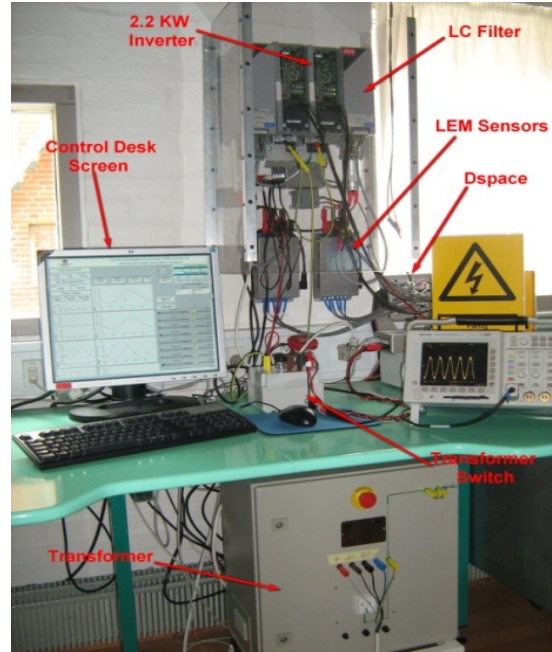


Fig. 13. Photograph of the experimental setup.

The experiments were conducted for the same value as the simulation in order to be able to compare them.

A. Constant-power test experimental results

Compared to simulations, experimental results for the forward predictive current control are quite similar, (Fig.14), excepting the smaller harmonics level shown for low power (Table 3).

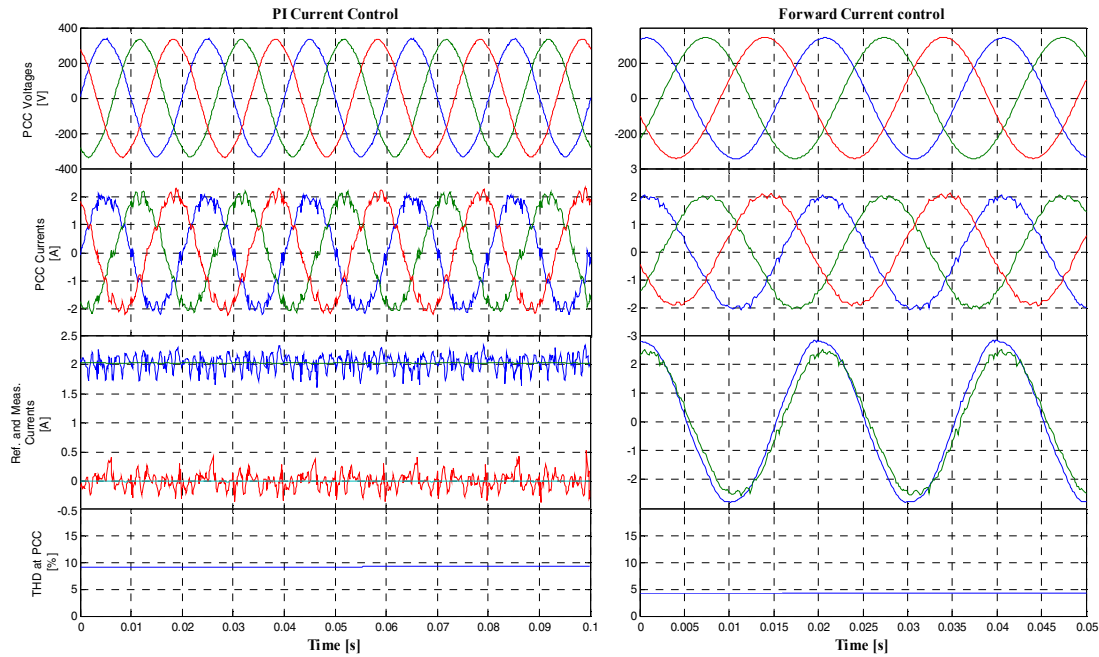


Fig. 14. Steady-state constant power ($P = 1000$ W and $Q = 1000$ VAR) test experimental results.

Table 3. Harmonic-content results from constant-power experimental test

	no harmonic compensation		with harmonic compensation	
	PI	FW. PCC	PI	FW. PCC
	THD [%]	THD [%]	THD [%]	THD [%]
P=500 W; Q=0VAr	35.96	22.98	14.67	6.795
P=1000 W; Q=0VAr	26.78	12.66	9.12	4.29
P=1000 W; Q=-1000VAr	14.94	6.18	4.49	2.895
P=1000 W; Q=1000VAr	11.79	8.847	3.38	3.25
P=1000 W; Q=-2000VAr	11.63	5.177	3.4	2.46

With harmonic compensation block, both current control strategies comply with IEEE 1547 and IEC 61727 standards in respect to current harmonics, in range of 30–100% of rated inverter power. For low power, the forward predictive control has significantly reduced harmonics level compared to PI control.

B. Power step-change test experimental results

The transient responses of both current control schemes to a step-change in active power and reactive power are shown in Fig.15 and Fig.16, respectively.

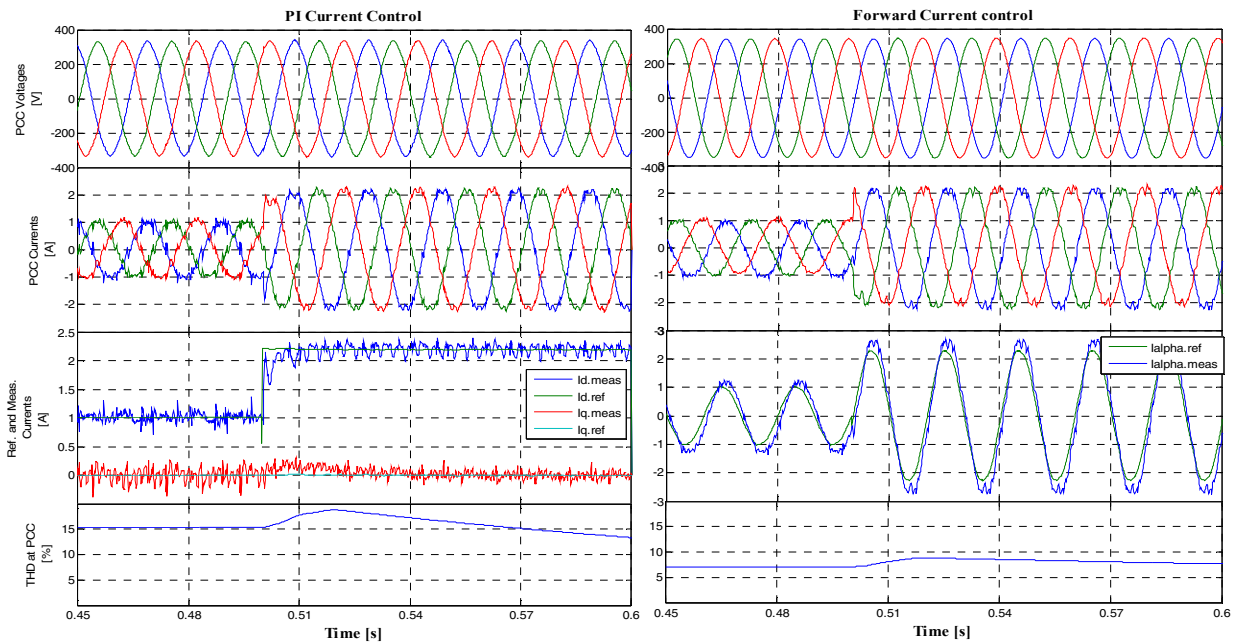


Fig. 15. Active power step-change (from P1= 500 W to P2=1000W and Q=0 VAR) test experimental results.

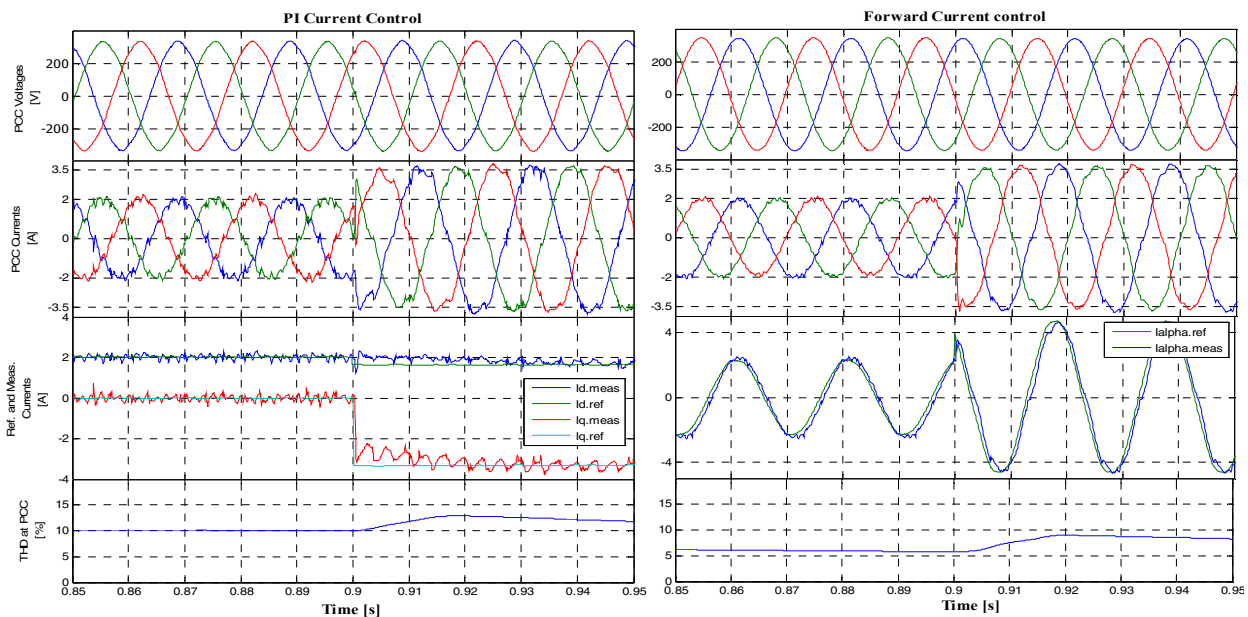


Fig. 16. Reactive power step-change (from Q1=0 VAR to Q2 = - 1500VAR and P = 1000 W) test experimental results.

V. CONCLUSIONS

Two current control schemes, i.e. forward predictive control and PI control, for grid-side three-phase PWM voltage-source inverter in DGSs have been presented. Those are suitable for practical implementation with good transient response and minimal harmonic distortion.

Simulation and experimental results have been presented to confirm the efficient operation of the new forward predictive current control algorithm. The constant power test showed that both current control methods have good results in respect to existing grid codes. The recovery time at power step-change and the harmonics content are smaller for the forward predictive control as compared with the PI control.

ACKNOWLEDGMENT

This paper was supported, in part, by the Romanian grant 'Doctoral Studies in engineering sciences for developing the knowledge based society (SIDOC)', POSDRU/88/1.5/S/60078, co-funded from European Social Fund through Sectorial Operational Program Human Resources 2007-2013.

The authors are grateful to ELECTROGRUP SA and Department of Energy Technology, Aalborg University, Denmark for providing laboratory facilities for the experimental work.

REFERENCES

- [1] Q.Zeng, L. Chang, Development of an SVPWM-based predictive current controller for three-phase grid-connected VSI, Conf. Rec. 40th IEEE IAS Annu. Meet.,2005, Vol. 4, pp. 2395-2400.
- [2] I. Lar, M.M. Radulescu, E. Ritchie, D.L. Irimie, Control strategies of grid-side PWM inverter for distributed power generation systems, Proc. Aegean Conf. Electr. Mach. Power Electron. - ELECTROMOTION Joint Conf., 8-10 Sept.2011, Istanbul, Turkey, pp. 605-610.
- [3] D.G. Holmes, D.A. Martin, Implementation of a direct digital predictive current controller for single- and three-phase voltage source inverters,Conf. Rec. 31st IEEE IAS Annu. Meet.,1996, Vol. 2, pp.906-913.
- [4]G.H.Bode et al., An improved robust predictive current regulation algorithm, IEEE Trans. Ind. Applicat.,Vol. 41 (2005), pp. 1720 - 1733.
- [5] H.M. Kojabadi et al., A novel DSP-based current-controlled PWM strategy for single phase grid connected inverters, IEEE Trans. Power Electron.,Vol. 21 (2006), pp. 985-993.
- [6] A.Nabae, T.Tanaka,A new definition of instantaneous active-reactive current and power based on instantaneous space vectors on polar coordinates in three-phase circuits,IEEE Trans. Power Deliv., Vol. 11 (1996), pp. 1238 - 1243.
- [7] M.Liserre, F. Blaabjerg, R. Teodorescu, Grid impedance estimation via excitation of LCL-filter resonance, IEEE Trans. Ind. Applicat.,Vol. 43 (2007), pp. 1401-1407.

Electromagnetic torque capabilities of axial-flux and radial-flux permanent-magnet machines

Adrian Augustin Pop
Department of Electrical Machines and Drives
Technical University of Cluj Napoca
Cluj Napoca, Romania

Mircea Radulescu
Department of Electrical Machines and Drives
Technical University of Cluj Napoca
Cluj Napoca, Romania

Horia Balan
Power Engineering and Managment
Technical University of Cluj Napoca
Cluj Napoca, Romania

Hristiyan Kanchev
Electrical Machines
Technical University of Sofia
Sofia, Bulgaria

Abstract— This paper aims to evaluate capabilities of axial-flux and radial-flux permanent-magnet machines. The comparison is done exclusively from an electromagnetic point of view. The electromagnetic design comparison of conventional radial-flux and axial-flux topologies is carried out in view of traction drive applications.

Index Terms—Axial-flux permanent-magnet machine, radial-flux permanent-magnet machine, electromagnetic design comparison

I. INTRODUCTION

The idea of comparing two different machines is a difficult task. Many researchers try to force the equality in comparison using subjective constraints. The end result is often that the constraints themselves favor one geometry over the other, leading to inconclusive results.

Small electronically-commutated (or brushless) axial-flux permanent-magnet (AFPM) machines have been under keen research interest in the last decade as an alternative to conventional radial-flux PM machines, particularly for low-speed direct-drive applications (e.g. wheel motors and wind generators), due to their advantages of flexible disk (pancake) shape, compact and rugged construction, adjustable flat (plane) airgap, high power density and high torque-to-weight ratio [1-3].

The paper presents a comparative analysis of electric motors with PM-excited radial, respectively axial, magnetic flux. The ability to develop the electromagnetic torque defines the comparison criterion. The analysis may serve for sizing / choosing small structures for electric traction and wind-power energy conversion applications.

The machines are compared in terms of electromagnetic torque and torque density capabilities with the overall volume, losses and flux density that are kept constants.

II. RADIAL-FLUX PERMANENT-MAGNET MACHINE

The design of a conventional three phase 6/18 RFPMM has been considered, leading to the configuration shown in Fig. 1.

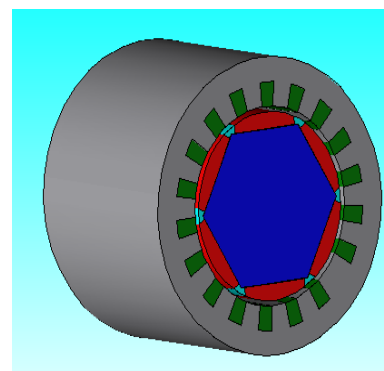


Fig. 1. Radial-flux permanent-magnet machine

For this machine the coils are wound around 18 stator teeth. The magnets are glued on the rotor skeleton.

The main advantage of the radial-flux machine is the standardized topology, which means lower production costs.

III. AXIAL-FLUX PERMANENT-MAGNET MACHINE

The simplest AFPM machine structure uses an annular, slotted (or slotless) stator, containing the radially-arranged armature windings, and a disk-rotor, carrying PMs that produce the axial flux. The AFPM machine has a larger diameter-to-active-length ratio compared to its radial-flux counterpart. As a consequence, when the number of poles increases, the AFPM-machine radial active part remains almost unchanged, while the axial length can decrease, so that the torque density increases.

The research work contained in this paper first refers to small brushless AFPM machines having surface-mounted NdFeB rotor-PMs and three-phase slotted-stator distributed armature windings, which are most suitable for low-speed direct-drive applications. The primary reasons are that, the fixture of external stators may be arranged easily, and the axial loading of bearings is rather small due to the internal rotor topology.

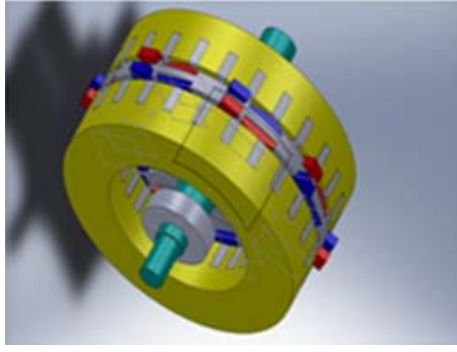


Fig. 2. Axial-flux permanent-magnet machine

Once with the advance in PM technology, the AFPM machine has born interest among the researchers in electric machines domain. The machines with axial airgap made the designers now to consider this solution a feasible one.

The AFPM machine considered in this paper [4] is a two-stators and one-rotor topology. The rotor with 4 pole-pairs is sandwiched between the two stators. The rated power is about 0.3 kW, and the rated rotational speed is 1500 rpm. The magnets are of high-energy NdFeB-type, and are glued on the solid-iron disc-rotor. The material of the stator core is a fully-processed electrical steel sheet M600-50A.

IV. COMPARATIVE ELECTROMAGNETIC DESIGN

Besides the technological and manufacturing differences, it seems interesting to compare AFPM and RFPM machines to understand when and where the first ones show potential advantages.

A general comparison of AFPM vs. RFPM machines is not possible due to the large number of possible technical solutions; thus the comparison is focused on two specific types of surface-mounted PM machines:

- the most common RFPM machine with one external stator and one internal rotor;
- the AFPM machine with two external stators and one internal rotor.

Both machines are compared in terms of electromagnetic torque and torque density for the same overall volume, losses and the flux density. The study is carried out in order to evaluate the comparative capabilities of both machines.

As explained in [5], the comparison between the machines is done using the ‘sizing equations’, which link the electromagnetic torque (T) to the active machine length (L) and the machine reference diameter (D):

$$T \sim D^2 \cdot L \quad (1)$$

Accordingly, one assumes that the elevation in temperature (ΔT) is due to Joule losses, and the heat transfer is only convective.

Thus, the heat transfer can be expressed as

$$\Delta\theta = \frac{RI^2}{hS_{ex}}, \quad (2)$$

where R is the electrical resistance of the stator winding, which takes into account also the effect of stator teeth, and $S_{ex} = \pi D \cdot L$ is the thermal exchange surface area.

By developing the expressions for R and S_{ex} in (2), the elevation in temperature is found to be constant if the current is proportional to the reference diameter :

$$I^2 = \frac{hS_{ex} \cdot \Delta\theta}{R} = const. \times D^2 \cdot \Delta\theta. \quad (3)$$

From classical equations of electric machine theory, the electromagnetic torque can be considered to be proportional to the useful airgap surface A_{gap} :

$$T \sim A_{gap} \quad (4)$$

The comparative geometry and electromagnetic torque expression for the RFPM and AFPM machines under study are given in Table I.

The ratio (K) in the torque expression depends only on the technology used to design the PM machines.

The width of the AFPM machine is supposed to be equal to $2a$. This corresponds to the double stator thickness of the RFPM machine, which is a quite realistic assumption.

Table I. Comparative geometry and electromagnetic torque expression for the RFPM and AFPM machines

	Radial	Axial
Bulk		
Area A_{exc} (m ²)		
Volume (m ³)	$V_R = \pi \cdot (r + a)^2 \cdot L$	$V_A = \pi \cdot \left(r_{mec} + \frac{L_A}{2} \right)^2 \cdot 2a$
Diameter (m)	$D_R = 2(r + a)$	$D_A = 2 \left(r_{mec} + \frac{L_A}{2} \right)$
Width (m)	$W_R = L$	$W_A = 2a$
Torque (Nm)	$T_R = K \cdot 2\pi \cdot \left(\frac{D_R}{2} - a \right)^2 \cdot W_R$	$T_A = K \cdot 2\pi \cdot \left(\frac{D_A}{2} - \frac{L_A}{2} \right)^2 \cdot L_A$

Both AFPM and RFPM machines develop the same torque if they have the same airgap area, i.e. $A_R = A_A$.

The two machines are equivalent if they develop the same electromagnetic torque, and have the same bulk dimensions, i.e. $W_R = W_A$ and $D_R = D_A$.

From Table I, the following torque relation is introduced:

$$T_R = \alpha \cdot T_A, \quad (6)$$

where α defines the torque ratio between the RFPM and AFPM machines. If α is bigger than 1, the RFPM machine structure is obviously preferred instead of an AFPM one.

From the same Table I, one may write :

$$L_A = \frac{D_A}{\beta} \quad 3 < \beta \leq \infty \quad (7)$$

where β represents the stack length in relation to the outer diameter for the AFPM machine structure. For machine building practical reasons, $\beta \geq 3$. If β equals 2, the inner diameter of the AFPM machine is null.

By introducing the torque expressions of Table I in (6), one obtains :

$$\left(\frac{D_R}{2} - a\right)^2 \cdot W_R = \alpha \cdot \left(\frac{D_A}{2} - \frac{L_A}{2}\right)^2 \cdot L_A. \quad (8)$$

By considering (7) and the same bulk dimensions of both RFPM and AFPM machines (i.e. $W_R = W_A$ and $D_R = D_A$), (8) leads to

$$\frac{\alpha}{\beta} \left(\frac{\beta - 1}{\beta}\right)^2 x^3 - x^2 + 2x - 1 = 0 \quad (9)$$

with the shape coefficient $x = \frac{D_A}{W_A} = \frac{D}{W}$.

An AFPM machine can be transformed around its mean radius into a RFPM machine. In such a transformation, the width is always two times smaller than the diameter, which means that $x \geq 3$.

In the particular case $\alpha = 1$, (9) becomes

$$(x - \beta) \left(x - \frac{\beta(2\beta - 1) + \beta\sqrt{4\beta - 3}}{2(\beta - 1)^2}\right) \times \left(x - \frac{\beta(2\beta - 1) - \beta\sqrt{4\beta - 3}}{2(\beta - 1)^2}\right) = 0. \quad (10)$$

Equation (10) shows that an AFPM machine is equivalent to a RFPM one with the same bulk dimensions if the shape coefficient x is equal to β .

To be efficient, the AFPM machine must have a high diameter for a small width. For example, if $\beta = 4$, the diameter must be, at least, four times higher than the width in order to have an AFPM machine structure instead of a RFPM one.

The expression of $\alpha(x, \beta)$ can be obtained from (9) as

$$\alpha(x, \beta) = \frac{(x - 1)^2 \cdot \beta^3}{(\beta - 1)^2 \cdot x^2} \quad (11)$$

If $\alpha > 1$, RFPM machine is preferred, while if $\alpha < 1$, AFPM machine is better. The above equations do not allow the machine sizing, but gives the answer whether the designed AFPM or RFPM machine is well chosen with reference to its bulk dimensions.

Fig. 3 shows the evolution of α as a function of x and β . When $\alpha < 1$, at the bottom of the figure, an AFPM machine structure is a good choice, otherwise a classical RFPM one should be preferred.

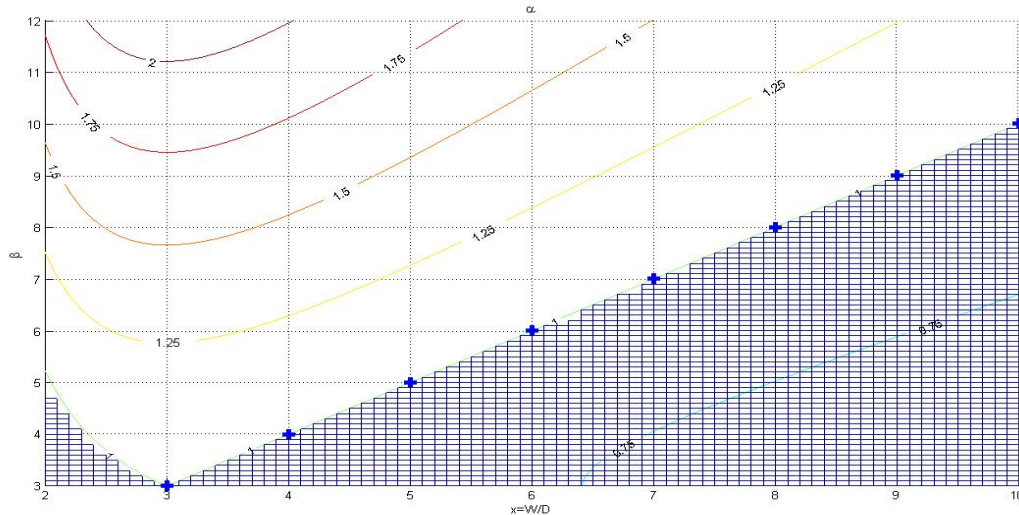


Fig. 3. Evolution of α as a function of x and β , for single airgap.

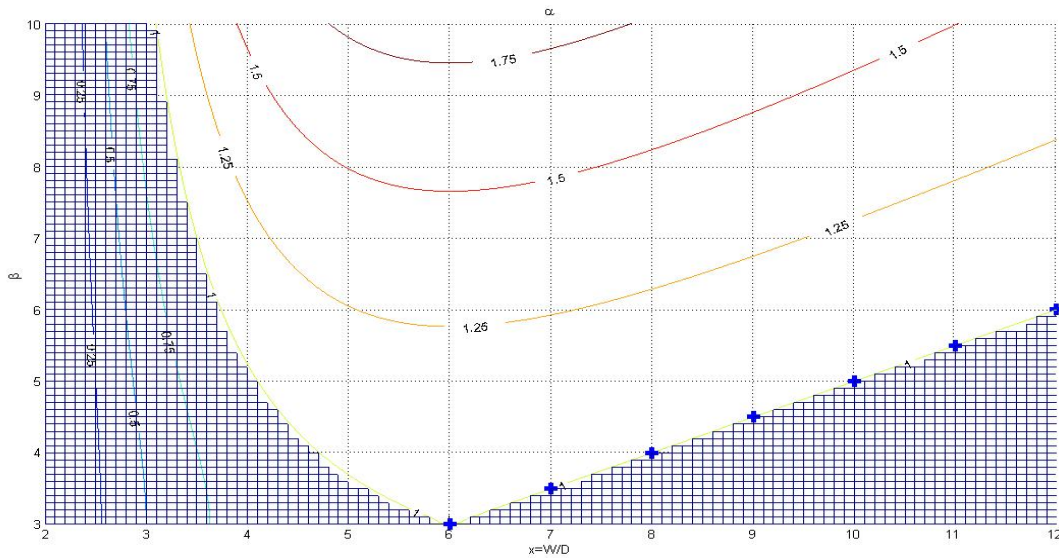


Fig. 4. Evolution of α as a function of x and β , for double airgap.

V. CONCLUSIONS

The reasoning process is similar if an AFPM machine with double airgap is studied; then, the width is $W_A = 4a$ and the electromagnetic torque becomes

$$T_A = 2K \cdot 2\pi \cdot \left(\frac{D_A}{2} - \frac{L_A}{2} \right)^2 \cdot L_A \quad (12)$$

Equation (10) is simply multiplied by 2. Fig. 4 shows the evolution of α as a function of x and β , for this case. The domain for preferential choice of an AFPM machine is increased.

If in the above torque expressions, one considers the machine diameter at the third power instead of the second one, one obtains again $x = \beta$ as a solution of (10), what means that the electromagnetic torque is also proportional to $D^3 L$, as reported earlier in [3].

It must be emphasize that the other two solutions, x_2 and x_3 , of equation (10) are always smaller than 3, and converge towards 1, as shown in Fig. 5.

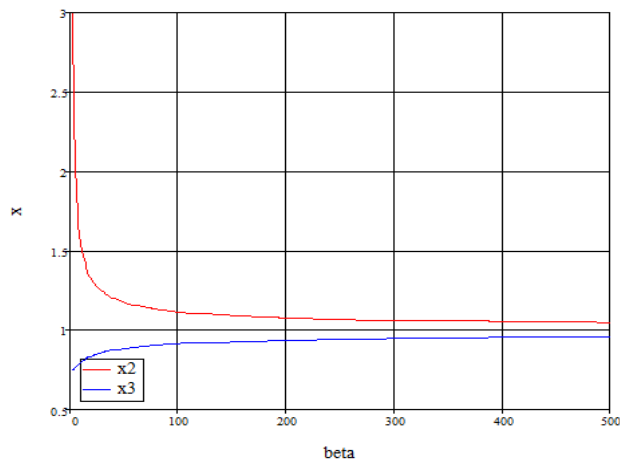


Fig. 5. Evolution of x_2 and x_3 as a function of β .

RFPM machines possess positive features for electric traction applications, such as simple structure, ruggedness, high torque density and wide-speed operation range. For a direct-drive topology, the AFPM machine provides higher torque-to-weight ratio, better heat removal, flexible compact shape and adjustable airgap, as compared to its RFPM counterpart.

The comparative electromagnetic design analysis developed in the paper for RFPM and AFPM machine topologies has shown that both are equivalent in torque and size, if the shape coefficient x is equal to the ratio β between the stack length to the outer diameter of the PM machine. Besides, there is a certain combination of coefficients x and β , for which the AFPM machine structure provides more torque capability than the classical RFPM one.

Since the PM machine output torque is proportional to the effective airgap area for constant electrical and magnetic loadings, the AFPM machine with double airgap reveals higher torque-to-weight ratio.

REFERENCES

- [1] J.F. Gieras, R.-J. Wang, M.J. Kamper, *Axial-flux permanent-magnet brushless machines*, 2nd Edition, Springer, The Netherlands, 2008.
- [2] K. Sitapati, R. Krishnan, Performance comparisons of radial and axial field, permanent-magnet, brushless machines, *IEEE Trans. Ind. Applicat.*, Vol. 37 (2001), No. 5, pp. 1219-1226.
- [3] A. Parviainen, *Design of axial-flux permanent-magnet low-speed machines and performance comparison between radial-flux and axial-flux machines*, Ph.D. Thesis, Lappeenranta University of Technology, Finland, 2005.
- [4] A.A. Pop, F. Gillon, M.M. Radulescu, *Modeling and permanent magnet shape optimization of an axial-flux machine*, Proceedings of International Conference on Electrical Machines – ICEM, 2012, Marseille, France, CD-ROM.
- [5] A. Cavagnino, M. Lazzari, F. Profumo, A. Tenconi, A comparison between the axial flux and radial flux structures for PM synchronous motors, *IEEE Trans. Ind. Applicat.*, Vol. 38 (2002), No. 6, pp. 1517-1524.

Diagnosis of Short Circuit and the Earthing of a Transformer Station

Traian Varodi

Power Engineering and Management
Technical University of Cluj-Napoca
Cluj-Napoca, Romania
tvarodi@gmail.com

Adrian Augustin Pop

Electrical Machines
Technical University of Cluj-Napoca
Cluj-Napoca, Romania
augustin.pop@mae.utcluj.ro

Horia Balan

Power Engineering and Management
Technical University of Cluj-Napoca
Cluj-Napoca, Romania
horia.balan@eps.utcluj.ro

Mircea Buzdugan

Building Services Engineering
Technical University of Cluj-Napoca
Cluj-Napoca, Romania
mircea.buzdugan@insta.utcluj.ro

Abstract—The paper presents the monitoring of the power quality of an underground electric line fed by a high voltage transformer station 110/10 kV and a subsequent earthing fault situation followed by a short circuit. The monitoring process was performed using a power quality analyzer. The analysis of the evolution in time of the phenomena highlights the variations of the voltage in the medium voltage bus of the transformer station during the failure situation.

Keywords— earthing system, short-circuit, overcurrent protection.

I. INTRODUCTION

The continuity of power supply and quality assurance of electricity, especially for the energy produced by renewable sources [1...7] imposes that the energy supplier takes all necessary precautions to maintain the electricity required parameters and to ensure the reliability of the electrical equipment in the national power grid system.

With respect to power equipments, it can be said that the best reliable solution is the use of a monitoring system. Currently, the utilization of predictive maintenance for equipments diagnoses, instead of preventive maintenance is more suitable.

It is well known that short circuits are connections having low impedance between two points of a circuit, normally being at different voltages values.

If a short circuit occurs far from the source, the short circuit current limitation is achieved by the short circuit equivalent impedance of the network [8, 9].

Power breakers represent the largest class of electric devices that must ensure the switching functionality, i.e. “connection” and “disconnection” in the circuits in normal operating conditions and under fault conditions as well.

The communication in the connection process but especially in the disconnection one is usually followed by priming, burning and electrical arc suppression [10].

In the disconnection process, the electric arc leads to thermal stress, mainly on the contacts of the electrical devices and on the elements of the extinguishing chamber, determining also a high dielectric stress due to commutation overvoltages [11, 12]. All these conduct to the idea that the power equipments in a transformer stations must be monitored. In the case of current short circuit occurrence, the monitoring system should provide the fastest possible disconnection so as the short circuit current interrupted by the power breakers would have a minimum value.

Monitoring the parameters during failure is a particular problem leading to the analysis of the protections functionality in order to detect the malfunctioning of these systems and of the switching processes.

The detection of the protection malfunctions [13] and switching processes in case of abnormal operation phenomena can affect the overall stability of the power system.

If not properly managed or neglected, these events may cause undesired operation and major disturbances in a high voltage transformer station.

II. THE SHORT CIRCUIT CURRENT COMPUTATION

In the electrical energy transmission and distribution systems different types of short circuits can occur between the three phases and earth [14, 15, 16]:

- earthing;
- short circuit between phases;
- three phase short circuit.

The first two types of short circuits are asymmetrical, and the third one could be placed in the symmetrical short circuit category.

The methods of calculating the equivalent impedance in low voltage networks, involve several steps.

From the wiring diagram, the schematic is done for each component, and for the equivalent circuit (Fig. 1.), for a single-phase short circuit (Fig. 2a, b) and for a symmetrical and an asymmetrical short circuit respectively.

In the situation in which the diagrams include multi-levels voltage interlinked with transformers, referring the impedance at the fault location is necessary. All impedances are referred to the same level of voltage, i.e. the line nominal voltage at short-circuit location. This aim of this referring method is to determine an equivalent circuit, powered from a single source.

Assuming a grid supplied by the voltage U , in case of a short circuit in a point having the voltage U_d , the current short circuit produces phase Joule losses $P=U^2/R$, where R is the real resistance of grid. Referring the circuit elements and sources must preserve the dissipated power. At the grid voltage the power dissipation equation is equivalent to:

$$P = \frac{U_d^2}{R_r} \quad (1)$$

Starting from this point the equations for the referred impedances at the fault location can be inferred also.

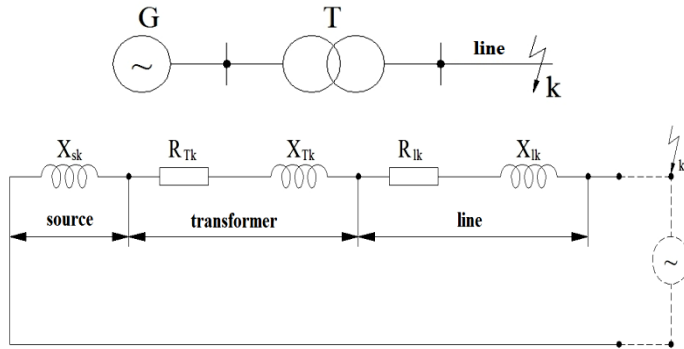


Fig. 1. Transformation through equivalent diagrams

In order to calculate the symmetrical and asymmetrical short circuit currents it is necessary to determine the parameters of the elements contained in the structure of the equivalent diagram: electrical lines, transformers, reactance coils, synchronous machines, etc.

For three-phase systems having neutral conductor, there are different ways of treating the neutral in order to reduce the short circuit current [17]. As it was stated above, the three-phase short circuit is a symmetrical one, while the two-phase and single-phase short circuits are asymmetrical and they are calculated using the method of symmetrical components. For example, in the case of single-phase short-circuit with the neutral point connected to the ground through the impedance Z_n , Fig. 2, the conditions at fault location are:

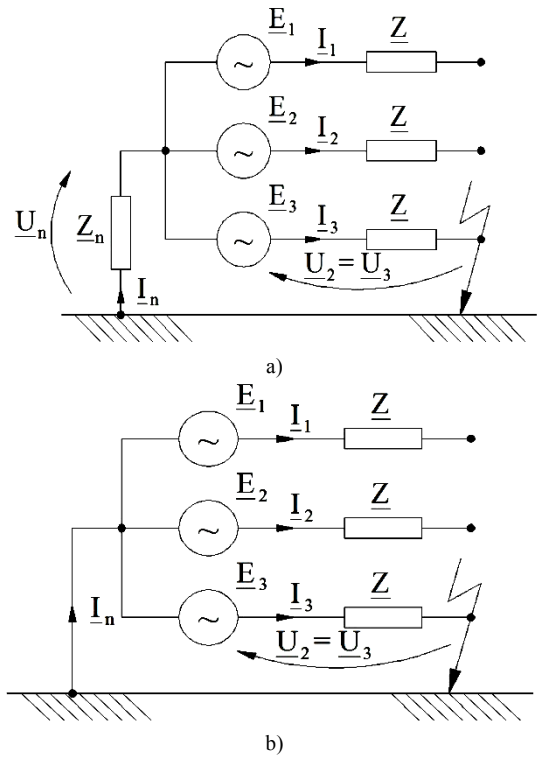


Fig. 2. One phase short circuit. a) neutral earthed by the impedance Z_n , b) neutral solidly grounded.

$$\underline{I}_1 = 0 \quad (2)$$

$$\underline{I}_2 = 0 \quad (3)$$

$$\underline{I}_3 = \underline{I}_n \quad (4)$$

$$U_3 = U_n \quad (5)$$

resulting in:

$$\underline{I}_h + \underline{I}_d + \underline{I}_i = 0 \quad (6)$$

$$\underline{I}_h + a^2 \underline{I}_d + \underline{I}_i = 0 \quad (7)$$

$$\underline{I}_h + a \underline{I}_d + a^2 \underline{I}_i = 0 \quad (8)$$

$$\underline{U}_h + a \underline{U}_d + a^2 \underline{U}_i = 3 \underline{Z}_n \underline{I}_h \quad (9)$$

Using the following equations

$$\underline{E}_1 = \underline{E}_d = \underline{Z}_d \underline{I}_d + \underline{U}_d \quad (10)$$

$$\underline{E}_i = 0 = \underline{Z}_i \underline{I}_i \quad (11)$$

$$\underline{E}_h = 0 = \underline{Z}_h \underline{I}_h + \underline{U}_h \quad (12)$$

results in:

$$\underline{I}_d = \frac{\underline{E}_1}{\underline{Z}_d + \underline{Z}_i + \underline{Z}_h} \quad (13)$$

$$\underline{I}_k = a \underline{I}_k; \underline{I}_i = \underline{I}_d \frac{1-a^2}{a-1} \quad (14)$$

and the value of fault current becomes:

$$I_3 = 3 \frac{E_1}{Z_d + Z_i + Z_h} \quad (15)$$

If the neutral of the network is solidly connected to the ground and assuming

$$Z_n = 0 \quad (16)$$

the fault current is given by (15) and if the following simplified hypothesis is used:

$$Z_h = Z_d = Z_i = Z \quad (17)$$

the current through the faulty phase is

$$I_3 = \frac{E_3}{Z} = \frac{E_1}{Z} \quad (18)$$

having therefore an identical value like in the case of a three phase short circuit.

III. THE COMPONENTS OF THE TRANSFORMER STATION

The station where the case study was performed is a transformation station 110/10 kV, where is a 10 kV distribution in the area, made with double bar system and transversal coupling. 110 kV bar separators are CLP type. 10 kV line cells are provided with overcurrent protection and reserve, made either with classic relay or digital relay. In the transformation station on the 110KV bar, the current transformers are mounted, CESU type.

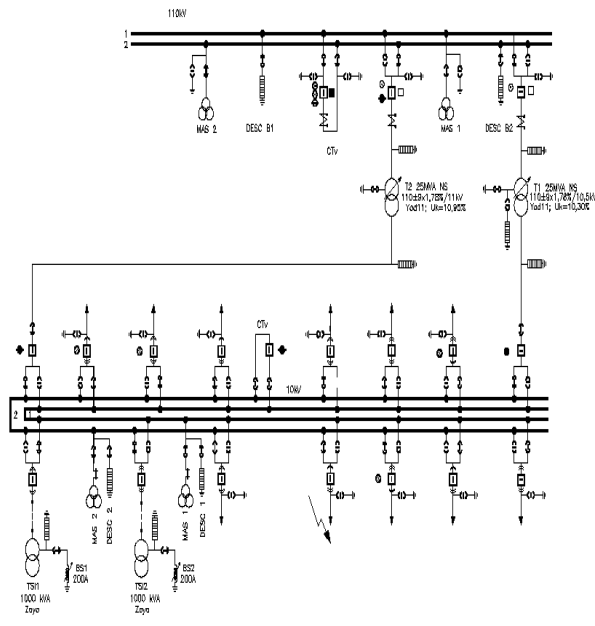


Fig. 3 The schematics of the high voltage transformer station.

The transformer station switches 110 kV -STE and STEP are manually controlled. IO switches- 110 kV with small quantity of oil for indoor and outdoor installations are constructed by interconnecting two extinguishing rooms. The V assembly is placed on a column composed of a 110 kV insulator.

The transformer station is provided with the medium voltage breakers type IO 10-15-20/630, 1250, 2500, 4000, IUP - 25 and IUP-M10-20/630, 1000. These are opening and closing devices for high voltage circuits, in the presence of the working currents and automatic opening of these circuits in the moment of current overload occurrence with unacceptable values, as well as for short circuits cases.

The breakers must have a sufficient breaking capacity in order to interrupt high short-circuit currents in a short time interval.

The connecting/disconnecting switches used in the medium voltage station cells are interior type TNS-10 and STIP-10.

Current transformers, type CIRS, CIRT1, CIRTO or CESU, are mounted also in medium voltage stations.

The neutral point handling in medium voltage is performed using extinguishing coils, the neutral point of the transformer being earthed via an extinguishing coil. Suppression coils of capacitive currents are AC electric devices providing the inductive currents required for the suppression of the capacitive currents at the fault location when phase earthing faults occur.

The adjustment of suppression coil is achieved by electric command and performed after any connection or disconnection procedure of the underground electrical line or after any change in the grid configuration.

The 110/10 kV station works in normally operating situation, with transformer T1 operating on the 110 kV bus no. 2 and on the 10 kV bus no. 2, transformer T2 in reserve on 110 kV bus 2 and 10 kV bus 2, with the non-spinning reserve canceled, the transversal coupling between 10 KV bus no. 1 and no. 2 is connected. The underground electrical line of 10 kV is supplied from the 10 kV bus no. 2 of this station.

IV. MEASUREMENTS AND EXPERIMENTS

The monitoring equipment, power quality analyzer Mavowatt 70 [18], has been used to record the events succession for a single-phase earthing short circuit. Events are detailed shown in Figs. 4 – 10.

Draw-View 8.9.00 HASP : 962026390 (388EC12En)

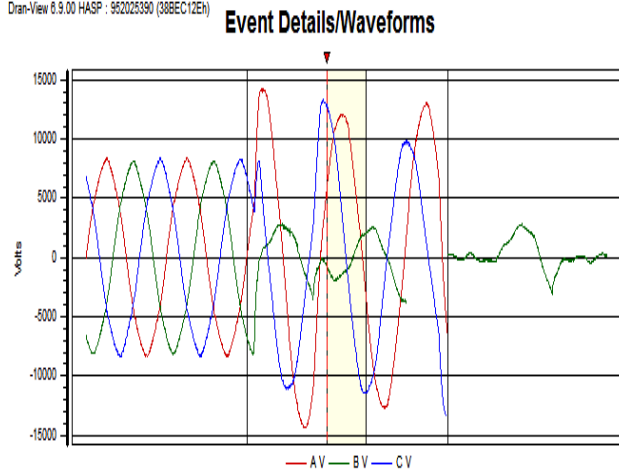


Fig. 4 Waveforms recorded at the occurrence of a single fault in phase B.

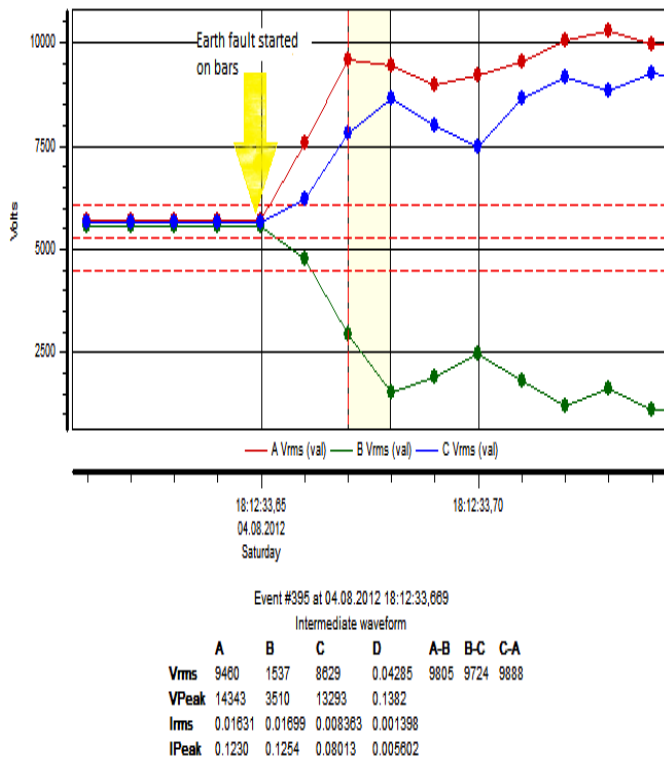


Fig. 5 RMS voltage values versus at the occurrence of a single phase fault.

From the recorded oscillograms it can be noticed the amplitude versus time characteristics of the voltages of the medium tension bus. Based on these results one can observe the evolution of the line and phase voltages in the very short period of occurrence of the events in the medium voltage network supplied from the transformer station.

These faults lead to high variations in the amplitude of phase and line voltages versus time on the medium voltage bus of the 110/10 kV transformer station.

From the time evolution of the phase voltage amplitude on the medium voltage bus, the phase earthing failure instant may be observed. The phase belongs to a medium voltage underground line supplied by one medium voltage bus.

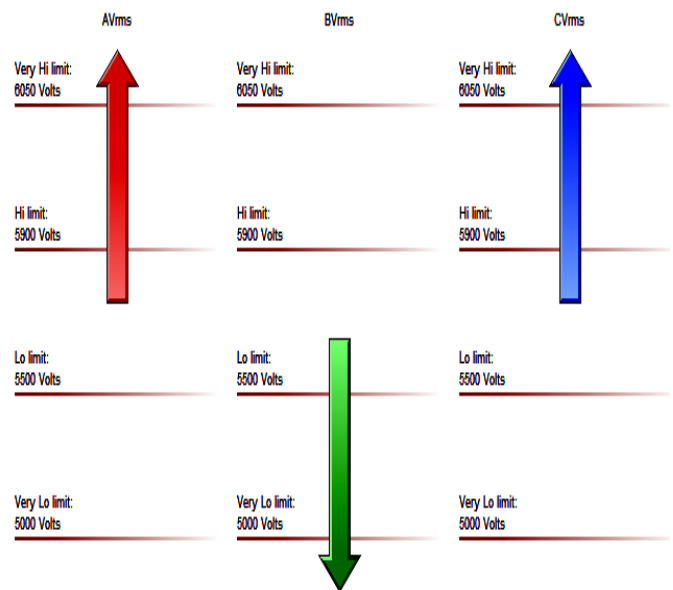
Fig. 5 highlights the earthing failure time of phase B at one time instant (i.e. 18:12:33.65 p.m.). The rms value of the voltage in phase B drops below 2.5 kV, while in phase A the rms value of the voltage reaches 14.3 kV and in phase C reaches 13.2 kV.

In the time interval corresponding to B phase earthing, the rms values of the voltages values are shown in Table I.

Fig. 8 highlights that after 39 ms (at 18:12:34.04 p.m.), phase B is isolated, while in the same time the earthing of phase C occurs. After 7 ms (at 18:12:34.11 p.m.) the earthing of phase A occurs also. In this moment, the two phase short circuit appears and the rms value of the voltage in phase A and C drop below 2KV.

After another 24 ms (at 18:12:34.34 p.m.) a three-phase short circuit occurs, as shown in Fig. 10.

Event Details/Waveforms



Event #403 at 04.08.2012 18:12:34,000
AVrms, BVrms, CVrms Voltage Journal Trigger Several

	AV	BV	CV					
Threshold crossed (Volts)	6050	5000	6050					
Magnitude (Volts)	7483	4807	6897					
	A	B	C	D	A-B	B-C	C-A	TOT
Vrms	9880	1527	8741	0.04350	9795	9717	9882	
VDC	14.04	15.73	14.91	0.007685				
VRmsDev	1647	1595	1644	0.05889				
VPeak	14562	3962	13555	0.1382				
Vphi-Fnd	10.53	245.4	104.8	86.46	30.00	270.0	150.0	
Vunb(DevAvg)	18.24	27.21	8.969					27.21
VZeroSeqCmp								1774
VPosSeqCmp								6200
VNegSeqCmp								111.7
Vunb(NegSeq)								1.801
Vunb(ZeroSeq)								28.62
Freq								50.01

Fig. 6 The set limits of the phase voltages

TABLE I. VOLTAGE VALUES ACCORDING TO FIG. 5.

Voltage	phase A [kV]	phase B [kV]	phase C [kV]
Effective value	9,88	1,52	8,74
Peak value	14,56	3,96	13,55

V. CONCLUSIONS

The maximum short-circuit current corresponds to a fault in the close proximity of downstream terminals of the protection device, and the short-circuit current of minimum value corresponds to a fault at the far end of the protected line.

In any case, the protection device must disconnect the fault within a time interval that must protect the conductor in terms of thermal and dynamic stress.

Event Details/Waveforms

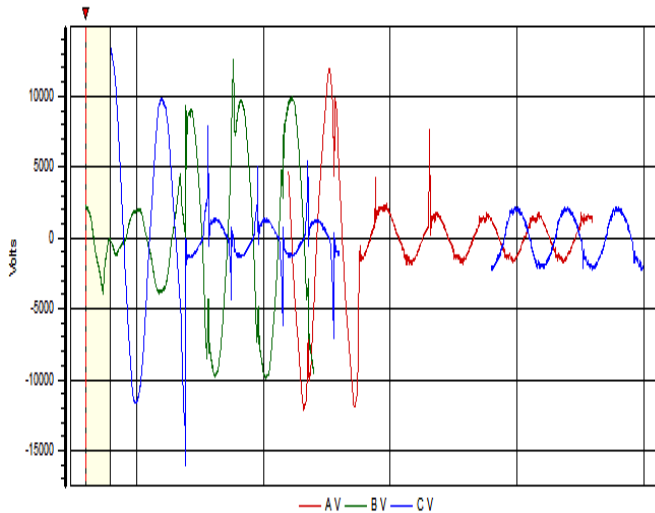


Fig.7 Waveforms recorded at the breakdown of phases A and C.

Event Details/Waveforms

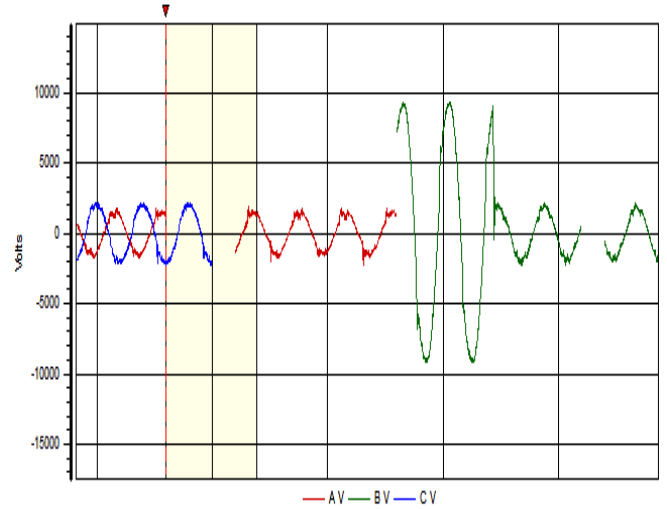


Fig.9 Waveforms of the phase voltages recorded on medium voltage bus. Three phase short circuit occurrence.

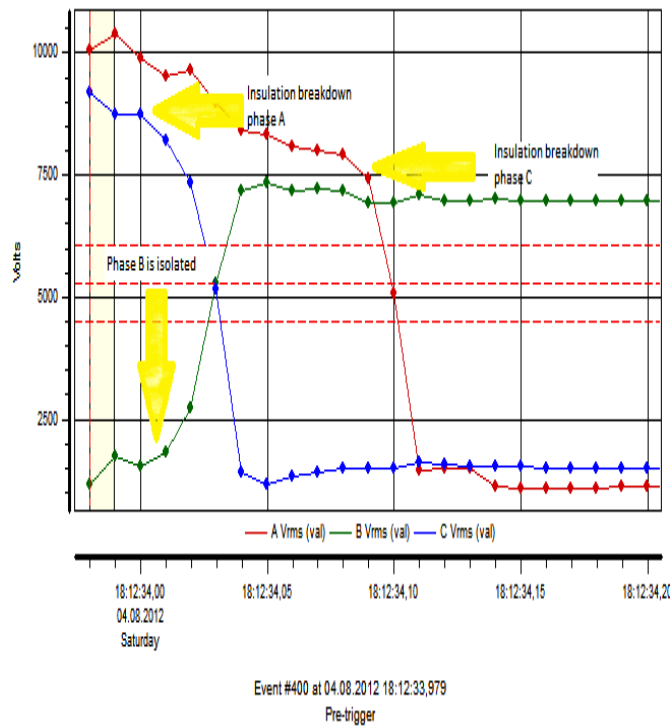


Fig. 8 Amplitude time characteristics of the phase voltages on medium voltage bus. A and C phase breakdown

It is very important that the protection system has as a component the measuring circuit which detects rapidly the short-circuit current. Thus the power breaker will disconnect at a lower level value of the short circuit current [19, 20].

The experimental results presented in the section III highlights that between the moment of the earthing fault and the moment of the three phase short circuit occurrence, approximately 24 ms are passed. This permits the developing of a maximum level of the short circuit current on the affected phases.

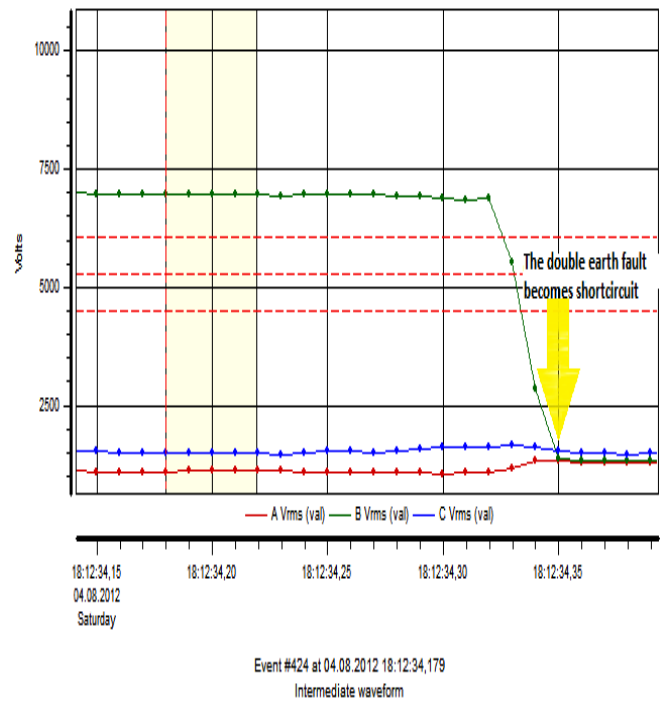


Fig.10 Amplitude time characteristics of the phase voltages on medium voltage bars. Three phase short circuit occurrence.

Using a monitoring system provided with power quality analyzers is not a solution, since the time of disconnection of power breaker permits the development of the maximum level of short circuit current.

One possible solution to avoid this situation is to use static commutation switches that are much faster than electromechanical circuit breakers, in the condition of using a rapid measuring system for the current.

Also using a monitoring system and comparing the measured values with the actual short-circuit current can

significantly reduce the time of disconnection and the value of short-circuit current in the power breaker.

REFERENCES

- [1] D. Salomonsson, L. Soder, and A. Sannino, "Protection of low-voltage dc microgrids," *IEEE Trans. Power Del.*, vol. 24, no. 3, pp. 1045-1053, Jul. 2009.
- [2] X. Yang, M.-S. Choi, S.-J. Lee, C.-W. Ten, and S.-I. Lim, "Fault location for underground power cable using distributed parameter approach," *IEEE Trans Power Sys.*, vol. 23, no. 4, pp. 1809-1816, Nov. 2008.
- [3] D.T.W. Chan, X. Yibin, "A Novel Technique for High Impedance Fault Identification", *IEEE Transaction on Power Delivery*, Vol. 13, No. 3, July 1998, pp. 738 – 744.
- [4] M.-S. Choi, S.-J. Lee, D.-S. Lee, and B.-G Jin, "A new fault location algorithm using direct circuit analysis for distribution systems," *IEEE Trans. Power Del.*, vol. 19, no. 1, pp. 35-41, Jan. 2004.
- [5] G. T. Wrate, I. K. Tasinga, S. S. Low, D. J. Melvold, R. S. Thallam, D.W. Gerlach, and J. Y. Chang, "Transient overvoltages on a three terminal dc transmission system due to monopolar ground faults," *IEEE Trans. Power Del.*, vol. 5, no. 2, pp. 1047-1053, Apr. 1990.
- [6] M. Aucoin, B.D. Russell, "Detection of Distribution High Impedance Faults using Burst Noise Signals Near 60 Hz", *IEEE Transaction on Power Delivery*, Vol. 2, No. 2, Apr. 1987, pp. 342 – 348.
- [7] A.V. Marnishev, B.D. Russell, C.L. Benner "Analysis of High Impedance Faults using Fractal Techniques", *IEEE Transactions on Power Systems*, Vol. 11, No. 1, Feb. 1996, pp. 435 – 440.
- [8] A. Greenwood, "Electrical Transient in Power System", John Wiley and Sons, USA, 1991.
- [9] B.D. Russell, C.L. Benner, "Arcing Fault Detection for Distribution Feeders. Security Assessment in Long Term Field Trials", *IEEE Transaction on Power Delivery*, Vol. 10, No. 2, Apr. 1995, pp. 676 – 683.
- [10] B.D. Russell, C.L. Benner, "Arcing Fault Detection for Distribution Feeders. Security Assessment in Long Term Field Trials", *IEEE Transaction on Power Delivery*, Vol. 10, No. 2, Apr. 1995, pp. 676 – 683.
- [11] R. P. P. Smeets, V.Kertész, "A newarc parameter database for characterization of short-line fault interruption capability of high-voltage circuit breakers," Paris, France, Rep. A3-110, 2006, CIGRE.
- [12] B.D. Russell, C.L. Benner, "Arcing Fault Detection for Distribution Feeders. Security Assessment in Long Term Field Trials", *IEEE Transaction on Power Delivery*, Vol. 10, No. 2, Apr. 1995, pp. 676 – 683.
- [13] P. M. Anderson, "Power system protection", New York, IEEE Press, 1999.
- [14] S. Ebron, D.L. Lubkeman, M. White: A Neural Network Approach to the Detection of Incipient Faults on Power Distribution Feeders, *IEEE Transaction on Power Delivery*, Vol 5, No. 2, Apr. 1990, pp. 905 – 914.
- [15] M. J. Mousavi and K. L. Butler-Purry, "A novel condition assessment system for underground distribution applications," *IEEE Trans. Power Sys.*, vol. 24, no. 3, pp. 115-1125, Aug. 2009.
- [16] R. P. P. Smeets, V.Kertész, S. Nishiwaki, K. Suzuki, "Performance evaluation of high-voltage circuit breakers by means of current zeroanalysis," *IEEE/Power Eng. Soc. T&D Conf. Asia Pacific*, Yokohama, Japan, 2002.
- [17] R. P. P. Smeets, V. Kertész, S. Nishiwaki, T. Koshizuka, K. Suzuki, "Short-Line fault interruption assessment of High-Voltage circuit breakers by means of current zero analysis," *CIGRE Colloquium, Sarajevo, Paper 20*, 2003.
- [18] Mavowatt 70. User Manual, Gossen Metrawatt.
- [19] R. P. P. Smeets, A. H. Eenink, V. Kertész, "A new high-resolution high-frequency current-zero measuring system," *ERA Conf. Meas. and Cal. in High-Voltage Testing*, Paper 1.2, 1998.
- [20] R. P. P. Smeets, V.Kertész, "High-resolution current-zero measurements during short-circuit current interruption by SF₆ and vacuum circuit breakers," *Proc. 10th Int. Conf. Short Circuit Currents in Power Systems*, Lodz, Poland, 2002, pp. 101–108.

Flux-density space-harmonics minimization for an axial-flux permanent-magnet machine

Adrian Augustin Pop
Department of Electrical Machines and Drives
Technical University of Cluj Napoca
Cluj Napoca, Romania

Horia Balan
Power Engineering and Management
Technical University of Cluj Napoca
Cluj Napoca, Romania

Mircea Radulescu
Department of Electrical Machines and Drives
Technical University of Cluj Napoca
Cluj Napoca, Romania

Abstract –The content of flux-density space-harmonics in axial-flux permanent-magnet machines (AFPMMs) is an important concern to the machine designer due to its impact on machine performances. In AFPMMs, the space-harmonics are related to the flux-density and the MMF distributions in the airgap, which are mainly determined by the PM excitation. This paper proposes two different approaches to study the flux density in the airgap. The finite-element and analytical methods are jointly developed in order to model and compare the flux density waveforms. Many optimization methods have been proposed in order to optimize the design of PM machines. In this paper, the authors investigate the optimal PM design in order to minimize the space-harmonics distribution using the sequential quadratic programming (SQP) optimization algorithm. By selecting the appropriate PM shape and size, it is possible to remove the undesirable harmonics. Using the SQP, the PM shape is optimized, and the harmonics content is notably reduced. The optimal solutions given by the FE model are then validated.

Index Terms-- axial-flux permanent-magnet machine, finite-element modeling and analysis, total harmonic distortion, design optimization

I. INTRODUCTION

Axial-flux permanent-magnet machines (AFPMMs), also called disc-type PM machines, are an attractive alternative to cylindrical radial-flux permanent-magnet machines (RFPMMs) due to their higher torque and power density, compact construction and lower noise, and thus have gained popularity in recent years [1]. The AFPMM possesses another beneficial feature, i.e. the axial length is small compared with the classical RFPMM.

The AFPMM considered in this paper is a two-stators and one-rotor topology for light electric traction applications. The PM rotor has 4 pole-pairs, and is sandwiched between the

two stators. The rated power of this machine is about 0.3 kW, and the rated rotational speed is 1500 rpm. PMs are of high-energy NdFeB-type, and are glued on the solid-iron disc-rotor. The material of the stator core is a fully-processed electrical steel sheet M600-50A. The stator has a particular construction being constituted from 25 slots. The rotor-PM arrangement is shown in Fig.1. It can be seen that there are 16 magnets glued on the rotor body. There are two separated PMs for each pole. The first PM has a rectangular geometry, and the second one is an arc-shaped magnet. Due to this PM arrangement, the flux density distribution reveals an unusual waveform [2].

The torque developed by the AFPMM is affected by harmonics of various origins, such as:

- space-harmonics caused by the stator slots;
- space-harmonics of the magnetomotive force (MMF) due to the non-sinusoidal distribution of the armature-phase windings [3];
- time-harmonics related to the power electronic supply, and affecting the stator-armature current.

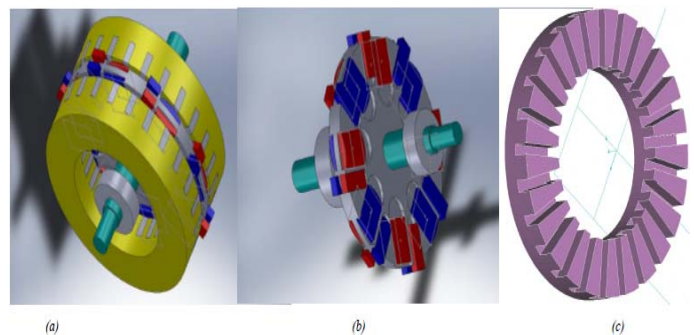


Fig. 1. (a) 3D representation of AFPBPM (b) The rotor with permanent magnets (c) One of the two stators.

II. INFLUENCE OF MAGNETIC PARAMETERS ON TORQUE COMPUTATION

Torque pulsations in permanent magnet machines are due to the interaction between electromotive force harmonics and current:

$$T_e = \frac{3}{2} \cdot \frac{E_1 I}{\Omega} + \frac{3}{2} \cdot \frac{I}{\Omega} \cdot \sum_{k=1}^3 (E_{6k-1} + E_{6k+1}) \cos 6k\theta. \quad (1)$$

I is the phase current, E represents the phase electromotive force (EMF), and Ω , the angular rotor speed. The stator-phase currents are considered perfectly sinusoidal.

The space-harmonics distribution and its interaction with the torque is the objective of the present work. Minimizing the space harmonics distribution of flux density will improve the electromagnetic torque, as clearly emphasized by (1).

Supposing ideally distributed stator windings, the back-emf results as

$$e = n \frac{\partial \varphi}{\partial t} = n \frac{\partial \int B dS}{\partial t} = n \frac{\partial \int BLR d\theta}{\partial t} = nB(\theta)LR\Omega \quad (2)$$

where φ is the flux density in the airgap, R , the radius of the rotor and L , the length of the machine.

If ignoring the winding effect, the harmonics of the EMF are those of the flux density. Hence, reducing these harmonics will permit to reduce the harmonics of the EMF.

An interesting method in controlling the spatial flux repartition and total harmonic distortion (THD) is to modify the shape of rotor PMs.

III. OPTIMAL ROTOR-PM DESIGN TO MINIMIZE FLUX-DENSITY SPACE-HARMONICS

A. Flux-density modeling using finite element method

In order to evaluate quickly the performance of the AFPMM, the 2-D finite-element (FE) field analysis is a time- saving solution compared to the 3D FE analysis. Hence, using the 2D FE field model, the airgap flux density distribution is obtained (Fig. 2).

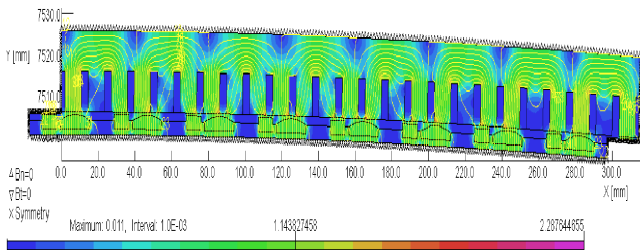


Fig. 2. 2-D representation of the AFPMM.

In Fig. 3, the FE simulation is performed for a slotless machine, therefore the stator-slotting impact on the flux density repartition is not taken into account. Accordingly, Fig. 3 only reveals the airgap flux density repartition generated by the two PMs of a single rotor-pole.

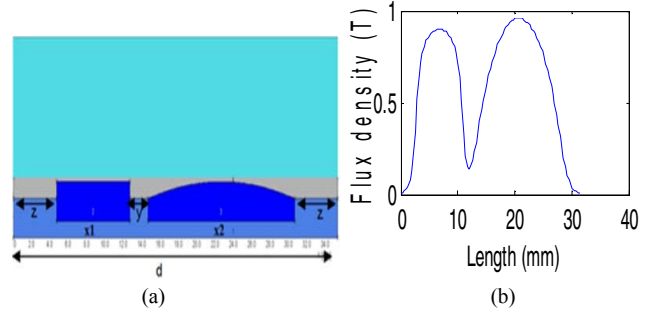


Fig. 3 (a) One-pole representation of the AFPMM; (b) Flux-density distribution for one half-period.

This first simulation of the AFPMM was made under open-circuit stator condition in order to monitor the airgap flux pattern. This technique considers the time-space distribution of electromagnetic quantities, so that it enables to identify the cross-coupling between different spatial and temporal field components. Therefore, it provides a very interesting insight into the correlation between different design variables and machine performances.

The airgap flux-density harmonics representation can be obtained by using the Fourier-series development :

$$B(\theta) = \sum_{n=1}^{\infty} (a_n \cos(n\theta) + b_n \sin(n\theta)) = \sqrt{a_n^2 + b_n^2} \cdot e^{j\varphi} \quad (3)$$

where $n = 1$ corresponds to the fundamental component.

B. Flux-density modeling using analytical method

The second flux-density model considered here is represented by the analytical model of Eq. (4), which allows further reducing the computation time as compared to the FE method. The analytical model is developed in MATLAB by means of trigonometric functions and nonlinear regression.

The results obtained from the FE and analytical models are now compared in order to verify the field computation accuracy. In Fig. 4, the airgap flux-density distribution obtained using both models is shown, emphasizing their satisfactory agreement.

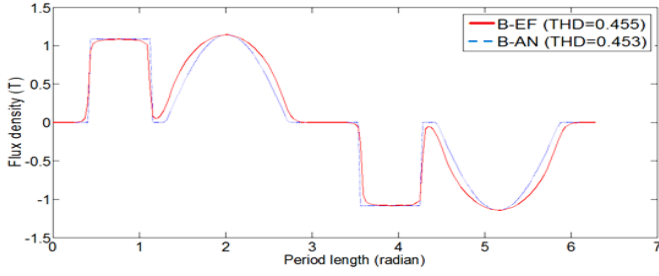


Fig. 4. Airgap flux density distribution of the AFPMM.

Improving the rotor-PM shape enables the minimization of key harmonic components that exist in a given design. Furthermore the optimization will be carried out using FE and analytical field models and modifying the rotor-PM geometry.

C. Flux-density harmonics optimization using FE model

In order to reduce undesired flux-density harmonics, several steps have to be executed. In Fig. 5, the information flux between the optimization algorithm (SQP) and the FE (Opera 2D) model is emphasized. The roles of different modules in Fig. 5 are specified in Table I.

The AFPMM optimization process starts with step (1) within MATLAB. The SQP algorithm makes regular calls to the FE field model of the AFPMM, throughout a MATLAB developed interface. The AFPMM model evaluation is carried out using the commercial FE optimization software Opera 2D.

Table I. Role of different modules in AFPMM optimization process

Module	Role
(1)SQP optimization	perform optimization on a low-budget of FEM evaluations
(2)Opera 2D	perform FE-based evaluation (pre, post-processing and analysis)
(3)Analyzer	launch FE evaluation, recombine the flux density signal and export the results to THD computation block
(4)THD computation	Fast Fourier Transformation (fft-Matlab) and THD computation

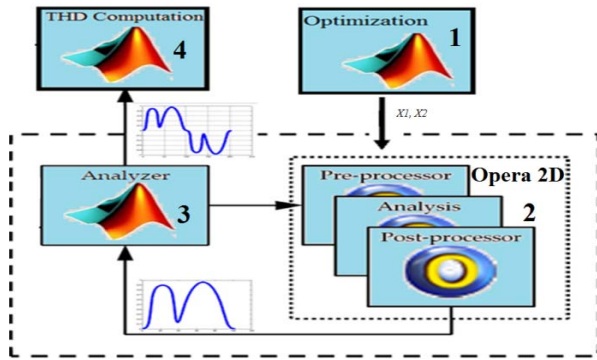


Fig. 5. Flux-density harmonics optimization process for the AFPMM using FE field model.

The FE model evaluation implies three distinct phases: *pre-processing* (FE mesh is generated for the given geometrical configuration), *analysis* (static analysis (ST) is performed for the model, generating a results file) and *post-processing* (FE results are extracted and made available to the MATLAB model launching function by MATLAB–Opera interface). Depending on the geometrical configuration, one FE model evaluation (pre-processing, analysis and post-processing) takes about 15 seconds.

The MATLAB model launches the function then exports the results to the Analyzer. The flux-density signal is recomposed for entire period. Then the signal passes to the THD computation block. Here, the signal is subject to Fast Fourier Transformation (FFT). The THD is now computed. Once the optimization process is finished, the optimization results are handled and analyzed in MATLAB.

a) Optimization

The first block represents the optimization algorithm implementation. $X1$ represents the length of the rotor-pole first PM (Fig.3) and $X2$, the length of the rotor-pole second PM. The values of this variable are optimized in order to reduce the THD. Concerning the PM shape optimization, the classical SQP (Sequential Quadratic Programming) optimization algorithm is used. This algorithm is applied within MATLAB.

The SQP algorithm attempts to approximate the objective function using a quadratic model and the constraint functions using a linear model of the optimization variables. SQP has excellent local convergence properties, and is faster than most other gradient based optimizers on a large set of test problems [4].

The SQP is used to speed-up the search process and obtain an improvement in the objective function value as quickly as possible.

b) FE field model

FE field model of the AFPMM has been developed using the commercial FE software Opera 2D. The model construction through command lines allows the automated modification of device parameters within an optimization process. The FE mesh of the geometry is also parameterized, depending on different values of the geometrical parameters for a given AFPMM configuration.

FE-based software consists of three parts, i.e. ‘pre-processor’, ‘processor’ and ‘post-processor’.

- The pre-processor

The pre-processor is used to draw the geometry of AFPMM, to define materials and model borders. Here a parameterized

model is realized in order to use it in optimization process. The model of AFPMM is composed of three tasks:

- a) Draw: here, one-pole representation of AFPMM was built for slotless stator.
- b) Materials: the physical characteristics of the geometrical areas previously drawn in their specific properties (magnetic linear, nonlinear) were assigned.
- d) Boundary conditions: normal, tangential and symmetric conditions were applied to the external lines of the AFPMM geometry.

- The processor

In the “processor”, the partial differential equation is solved in discrete form. It solves a linear system by a given method of resolution. For the nonlinear problem, the processor solves in an iterative way until the required precision is reached. The processor makes possible to find magnetic potential-vector values in each node. When this variable is found, the magnetic flux density distribution can be determined, which is the main objective for the optimization problem.

- The post-processor

The “post-processor” is the element where the results are analyzed. A visualization aspect is often useful for the comprehension of the results. The role of this block is to visualize the airgap flux density and then to be redirected to an output file.

c) Analyzer

The analyzer is used for recomposing the flux density signal for an entire period. This block also serves to interface FE model and MATLAB. The computation results are then exported to the THD block.

4. THD computation

Like the conventional synchronous machines the sinusoidal flux density waveform is desirable for many PMM applications. Due to the low PM permeability, which is comparable to that of air, the shape of the airgap flux density depends not only on the airgap length, but also on the shape and dimensions of the PM itself.

The THD of a signal is a measure of the harmonic distortion, and is defined as the ratio of the sum of the powers of all harmonic components to the power of the fundamental frequency:

$$THD = \frac{\sqrt{\sum_{h=3,5,7,\dots,13} B_h^2}}{\sqrt{B_1^2}} \quad (4)$$

Accordingly, an optimization method is introduced that allows improving the rotor-PM shape and dimensions in order to minimize key harmonic components that exist in the given design. The analysis deals with the rotor structure, especially the rotor-PM shape, as described in Fig. 6.

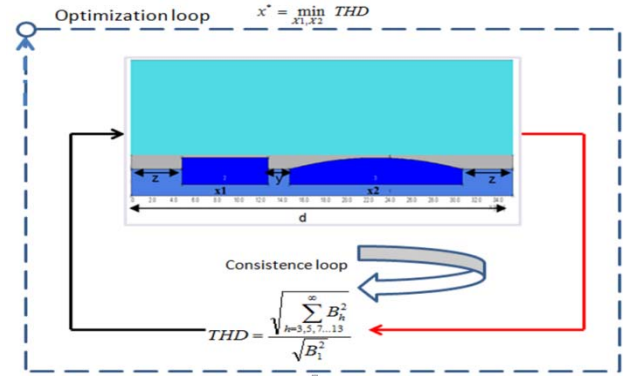


Fig. 6 Mono-objective optimization problem

The mono-objective optimization problem is formulated as follows :

$$\begin{cases} \min THD(x_1, x_2) \\ x_{1\min} \leq x_1 \leq x_{1\max} \\ x_{2\min} \leq x_2 \leq x_{2\max} \end{cases} \quad (5)$$

A. Optimization results

Numerical optimization method has been applied to identify optimal rotor-PM design for the AFPMM under study, in order to reduce the THD. In Table II, the optimization results are presented.

Table II. Mono-objective optimization results

Parameters	Rated values	Variation interval	Optimized values	Units
x_1	8	$2 < x_1 < 19$	2	mm
x_2	16	$3 < x_2 < 10$	19	mm
y	1.95	1.95	constant	mm
z	computed	computed	computed	mm
d	31.41	31.41	constant	mm
THD	0.455	-	0.27	-

The length X_1 of the rotor-pole first PM is reduced to 2mm, whereas the length X_2 of the rotor-pole second PM is increased

to 19 mm. It can also be seen that the THD is minimized to 0.27 for the FE model used in the optimization process.

In Fig. 7, the influence of $X1$ and $X2$ variables to THD computation is presented. As can be seen, the optimization process is trying to minimize the length of the rotor-pole first PM and to maximize the rotor-pole second PM. The blue regions represent the optimum solutions while the red regions, the undesirable solutions.

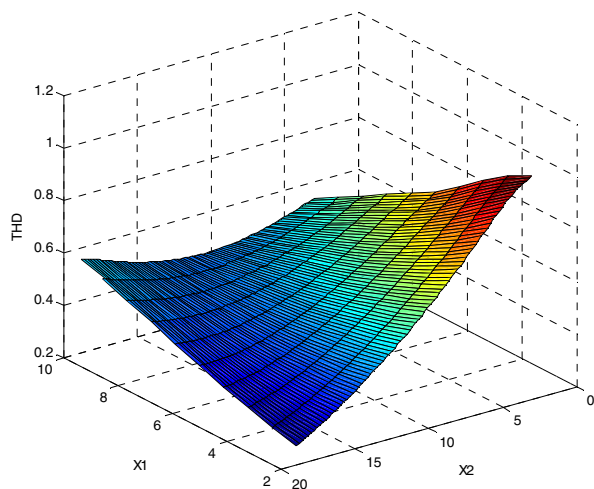


Fig. 7. THD 3-D representation as a function of $X1$ and $X2$ variables for the FE field model used in the optimization process.

IV. CONCLUSIONS

In this paper, a small double-sided AFPMM has been presented. FE model was developed in order to predict the airgap flux-density distribution.

The possibility of reducing the harmonic content of the airgap flux-density waveforms in AFPMM has been presented. The approach was primarily formulated from the mathematical point of view, and then transposed into a minimization problem. Optimization technique was applied to systematically modify a composite function of odd- harmonics content.

REFERENCES

- [1] Patterson, D.J. *et al.*, "A comparison of radial and axial flux structures in electrical machines," *Proc. IEEE International Electric Machines & Drives Conference – IEMDC 2009*, pp.1029-1035, 2009.
- [2] Pop, A.A.; Gillon, F.; Radulescu, M.M., "Modeling and permanent magnet shape optimization of an axial-flux machine", *Proc. Int. Conf. Electr. Mach. – ICEM 2012*, Marseille, France, CD-ROM.
- [3] Nguyen, T.D.; Tseng, K.J.; Chi Zhang; Shao Zhang; , "Loss study of a novel axial flux permanent magnet machine," *Proc. IEEE International Electric Machines & Drives Conference – IEMDC 2011*, pp.1143-1148, 2011.

[4] Tiwari, S.; Fadel, G.; Koch, P.; Deb, K., "Performance assessment of the hybrid archive-based Micro Genetic Algorithm (AMGA) on the CEC09 test problems," *Evolutionary Computation, 2009. CEC '09*

[5] Zhai Guofo; Wang Qiya; Ren Wanbin , "An Output Space-Mapping Algorithm to Optimize the Dimensional Parameter of Electromagnetic Relay," *IEEE Trans. Magn.*, vol.47 (2011), no.9, pp.2194-2199.

Wavelet Analysis in Monitoring and Diagnosis of Power Circuit Breakers.

Radu Adrian Munteanu
Electrical Engineering and Measurements
Technical University of Cluj-Napoca
Cluj-Napoca, Romania
radu.a.munteanu@ethm.utcluj.ro

Horia Balan
Power Engineering and Management
Technical University of Cluj-Napoca
Cluj-Napoca, Romania
horia.balan@eps.utcluj.ro

Adrian Augustin Pop
Power Engineering and Management
Technical University of Cluj-Napoca
Cluj-Napoca, Romania
augustin.pop@mae.utcluj.ro

Mircea Buzdugan
Building Services Engineering
Technical University of Cluj-Napoca
Cluj-Napoca, Romania
mircea.buzdugan@insta.utcluj.ro

Abstract—Monitoring of electrical equipment is a direction of current development in the maintenance domain. The method aims to establish the operation state of the monitored equipment. Fault diagnosis existing on power circuit breakers is very important aspect in emergency situations, when it must be interrupted by high current circuit breakers. This paper presents a model of vibration monitoring using Wavelet–Morlet transform. Here are reviewed theoretical problems of using Wavelet–Morlet transform, signal processing techniques and experimental results that highlight the difference between faulty equipment and one in a proper working condition.

Keywords—monitoring, power switches, analysis, diagnosis.

I. INTRODUCTION

Power circuit breakers are devices that perform switching functions in the system. Is a complex device that performs mechanical and electrical functions. The maintenance methods are essential for the proper functioning because is ensure the equipment reliability. The analysis of power circuit breakers, by monitoring, requires the development of data processing methods received from transducers. In the standard power circuit breaker is defined as a device able to break working or faulty currents, which require reliability in normal operation or in faulty mode, situation when the equipment fulfills the protection functions.

Equipment monitoring is determined by the proper functioning condition throughout all life cycle of the equipment. Depending on the measurements results of the equipment status through data analysis which indicate the damage trends are required for maintenance activities.

The advantages of this predictive strategy are obvious, improving the reliability and reducing the maintenance costs. The monitoring requires a data acquisition module and a data processing module.

Fig. 1 [4] is an example of monitoring the status of the circuit breaker type IUP-M20/630.

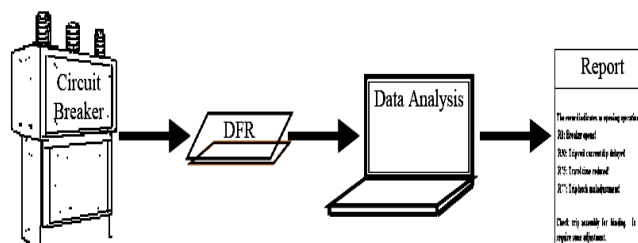


Fig. 1. Condition monitoring system for circuit breaker

The system comprises a power switch, a digital fault recorder, DFR, used to collect data and a portable computer which dispose of a software for data processing. The analysis is finally materialized by a test report. Digital fault recorder, DFR is a data acquisition device widely used in the system. They are used to record transient regimes and system changes acquired from control and communication equipment.

In the domain of vibration signals processing the use of analysis methods in time and frequency domain, is widespread mainly due to their simplicity. However, these methods in the case of non-stationary signals analysis, generates a series of errors that can have sometimes an important effect.

Considering the nonlinear functioning characteristic of power circuit breakers it is necessary to take into account the advanced methods of signal processing. For non-stationary signal the spectrum is changing in time from here appeared the necessity for time-frequency analysis.

Signal processing techniques in the time-frequency domain should highlight the non-stationarity of the analyzed signal. Physical significance of time-frequency representations is the spectro-temporal energy density.

The level of development reached today in computer field enables the successful implementation of mathematical algorithms. These algorithms although appeared for some time ago, had little practical application.

In the domain of signal vibration processing the use of analytical methods is widespread especially in time and frequency domain mainly due to their simplicity. However, these methods in the analysis of non-stationary signals, generates a number of errors that can sometimes become important.

Taking into account the linear operating characteristic of the power switches, it is necessary to evaluate some advanced signal processing methods.

II. WAVELET ANALYSIS

Study and Wavelet analysis shows undeniable advantages compared to Fourier analysis [1]. Wavelet function is defined according to the relation [2]:

$$\Psi_{a,b}(t) = \frac{1}{\sqrt{a}} \Psi\left(\frac{t-b}{a}\right) \quad (1)$$

with

- a the dilatation parameter and
- b the translation parameter.

Continuous Wavelet transform, TWC of a finite energy signal $x(t)$, with the analysis function $\Psi(t)$ is the convolution of signal $x(t)$ with the parent function Wavelet, scaled and conjugated Ψ^* :

$$W_x(a,b) = \frac{1}{\sqrt{a}} \int_{-\infty}^{+\infty} x(t) \cdot \Psi^*\left(\frac{t-b}{a}\right) dt \quad (2)$$

The decomposition of the function $\Psi(t)$ must be fast enough in order to ensure the analysis in time / space and in frequency.

Also, the Wavelet function must satisfy the following condition [3]:

$$C_\Psi = \int_0^{+\infty} \frac{|\Psi(\omega)|^2}{\omega} d\omega < \infty \quad (3)$$

Where $\Psi(\omega)$ is the Fourier transform of the Wavelet function $\psi(t)$ and C_Ψ is a constant that depends on which Wavelet function we use.

In contrast to sine functions, Wavelet functions are a class of asymmetric functions, which are not described by any analytical expression.

They have a finite period of time and the average value is always equal to zero, the eq. (4). With the help of calculated Wavelet coefficients, it is possible to reconstruct the original signal $x(t)$.

$$|\Psi(0)| = \int_{-\infty}^{+\infty} \Psi(t) dt = 0 \quad (4)$$

Since Wavelet coefficients considers the similarity between the signal $x(t)$ and Wavelet function $\Psi_{a,b}(t)$, the main problem in applying the continuous Wavelet transform, is the appropriate selection of the parent Wavelet function.

There are some basic features that can be used as parent function for Wavelet transform (Fig. 1), but for using them effectively, particular details should be considered for the application which uses Wavelet Transform.

Specialized literature [4] proposed to use the Wavelet Morlet function for detecting periodic impulses which are corresponding to power failures breakers.

Through Wavelet Morlet function, Fig. 1(f), the corresponding correlation between $x(t)$ the finite energy signal and $\Psi(t)$ the Wavelet function is achieved. The Wavelet Morlet function shape is similar to the pulse from Fig. 2.

The continuous Wavelet transform has quite high accuracy, but in practice the discrete Wavelet transform is more often used due to reduced computational time.

Continuous Wavelet transform is a powerful tool for evaluation of the nonlinear systems parameters problem of extracting their specific values.

Discrete Wavelet transform is a simplified version of the continuous Wavelet transform. The advantage of this transform consists on the simplicity implementation, reducing execution time and a lower level of necessary resources.

In discrete Wavelet transform, the signals are analyzed using a set of basic functions that perform a simple scaling and translation.

The transform is determined by successive analysis with low pass and high-pass filters of the oscillogram provided by the Wavelet analysis of the signal $x(t)$.

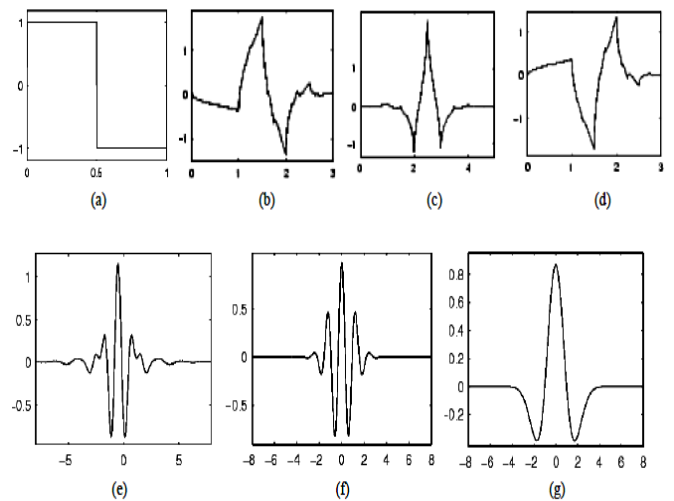


Fig. 2. Wavelet signals examples: (a) Haar, (b) Daubechies4, (c) Coiflet, (d) Symlet, (e) Meyer, (f) Morlet, (g) Mexican Hat.

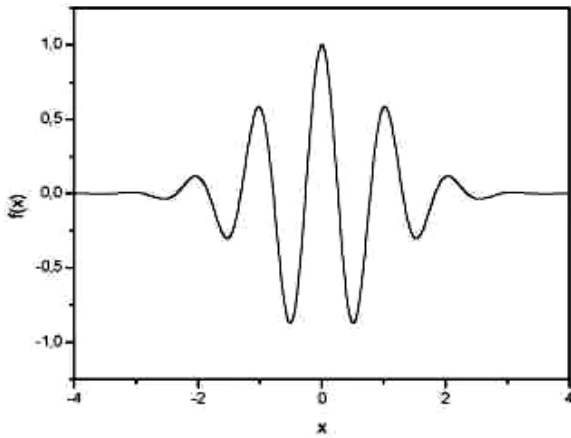


Fig. 3. Real part of Morlet function

The analysis filter of the oscillogram provided by the Wavelet analysis, decomposes the $x(t)$ signal into two signals $c(t)$ and $d(t)$. The signal $c(t)$ consists in the low frequencies of the signal (the approximated part), and the signal $d(t)$ consists in the high frequency (detailed part) of the signal $x(t)$ (Fig. 3).

Each level of approximation contains all the information available at the previous level, plus an additional component named detail component.

The discrete Wavelet transform produces a multiscale representation of the input signal and is implemented by iterating the analysis filter benches of the oscillogram provided by the Wavelet analysis.

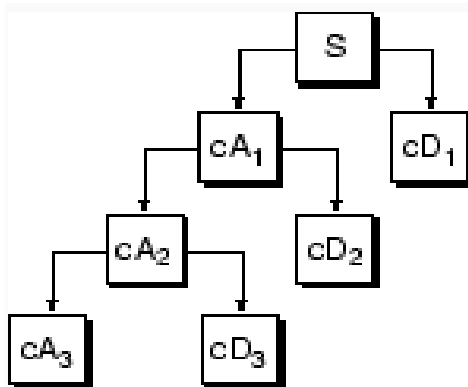


Fig. 4. The Wavelet decomposition [5].

The filters that split the band in two parts produce a signal that is occupying only half of the band. The filtering will continue until it reaches the desired level, the maximum number of decomposition levels depending on signal strength.

The total number of decomposition levels can be calculated using the equation:

$$N_n \geq \frac{\log f_s / f}{\log 2} + 1 \quad (5)$$

where N_n is the number of levels, and f_s is the sampling frequency.

The reconstruction of the original signal, based on discrete coefficients of Wavelet transform is the reverse process of decomposition and this is obtain with the help of synthetic filters benches.

DWT transform assumes that the noise affects only parameters from certain scale of representation corresponding to fine detail components.

Discrete Wavelet transform is superior to the solution based on the use of Fourier transform, which is incapable of maintaining the intervals unaltered when sudden changes are arising in the amplitude of analyzed signal.

Filtering noise using Wavelet thresholding technique involves the following steps [6]:

- Calculating the coefficients corresponding to the discrete Wavelet transform (separating low and high signal frequency components);
- Applying a soft or hard thresholding to the resulted coefficients and eliminating those factors with very small value, retaining only those coefficients greater than a limit.

Typically, the individual threshold values are selected for each scale as part;

The hard thresholding technique applied to a signal produces large oscillations near the points of discontinuity in comparison with thresholding soft technique.

Soft thresholding is an extension of the hard thresholding technique, firstly by setting to zero those elements whose absolute value is less than the limit imposed, then decreasing the non-zero coefficients which tend to zero.

Setting the threshold λ can be made according to eq. 6, through the global technique of thresholding for all levels of decomposition [6]:

$$\lambda = \sqrt{2 \cdot \log n} \quad (6)$$

In [7] the authors performed a comparison between the three algorithms in order to eliminate noise (Universal, MinMax and SURE) using Wavelet transform.

The authors demonstrate that the algorithm SURE (Stein's unbiased Risk Estimate) using the hard thresholding technique provide better performances than other algorithms used for the synthesis of signals.

The universal algorithm using the soft thresholding technique determines better results for real signals when using Wavelet Daubechies function of fifth order. In the study presented in [7] the functions Haar Wavelet, Coiflet 5 and Symmlet 5 are also used.

III. POWER SWITCHES FAULT DIAGNOSIS USING WAVELET ANALYSIS

The inconveniences determined by the use of analytical methods mentioned above can be overcome by using the Wavelet analysis.

For the implementation of the Wavelet analysis the following steps must be taken into account:

- noise removing from the signal acquired;
- filters and Wavelet functions designing for vibration signals;
- the application of continues Wavelet transform;
- scalogram plotting.

Noise elimination from the signal acquired was performed using a thresholding Wavelet technique which involves the following steps:

- low and high frequency components separating for the acquired signal;
- separating low and high frequency components for the acquired signal;
- applying on the resulting coefficients the soft or hard thresholding;
- elimination of low value coefficients and keeping the coefficients above the set threshold;
- signal reconstruction.

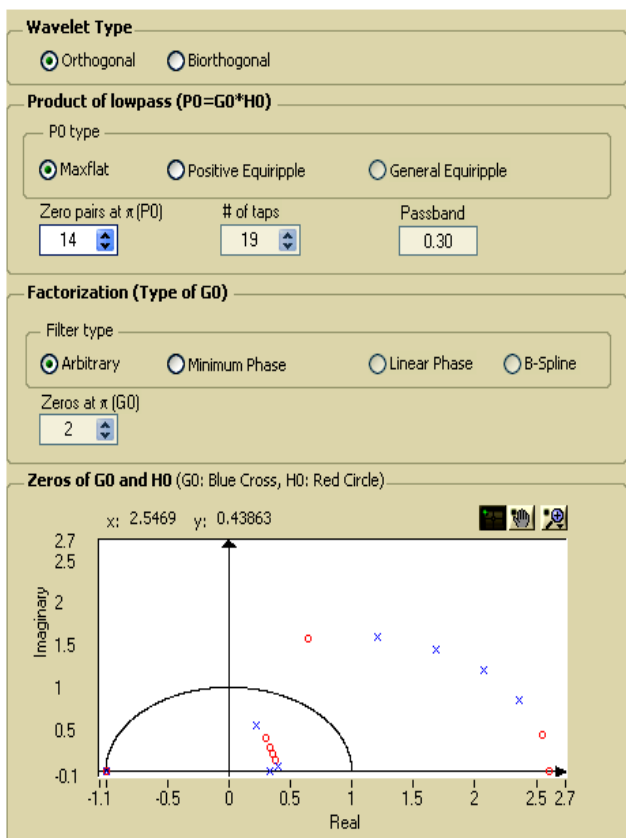


Fig. 5. Design parameters of Wavelet filters

The steps described above have been implemented using virtual instrument "WA Denoise VI" available in Labview library. This virtual instrument uses for signal decomposition into low and high frequency components the discrete Wavelet transform.

Within this virtual instrument the user can set the parameters for the threshold limit on Wavelet decomposition.

In this field one of the following SURE (Stein's unbiased Risk Estimate) variants can be chosen Universal, Hybrid or Min Max.

For noise reduction is indicated to use the "Universal" variant by which the threshold is set to value $\sqrt{2 \cdot \log L_s}$, relationship in which L_s is the length of the signal.

By setting the parameter "rescaling method" to "Multiple Levels", specifies that the noise estimation is performed at each level independently.

Regarding thresholding method is preferable to choose hard thresholding technique that produces large oscillations in the pulse proximity. This technique consists of setting to zero the coefficients whose absolute value is less than the threshold. Analysis and synthesis filters for the discrete Wavelet analysis are designed using virtual instrument "Wavelet Design". In Fig. 4 the parameters used for designing filters and Wavelet function are presented.

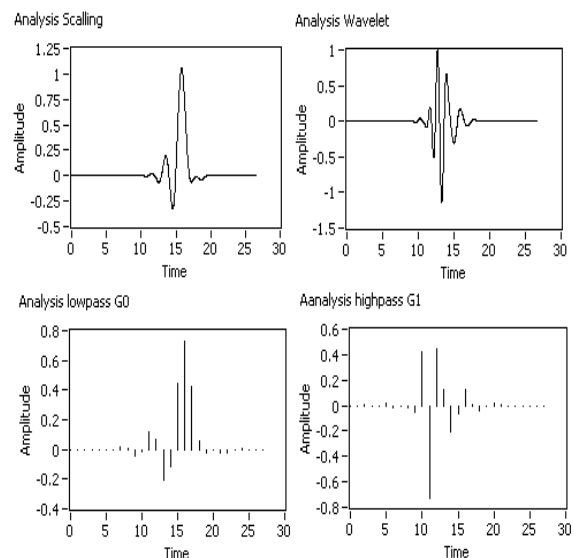


Fig. 6. The set of analysis filters

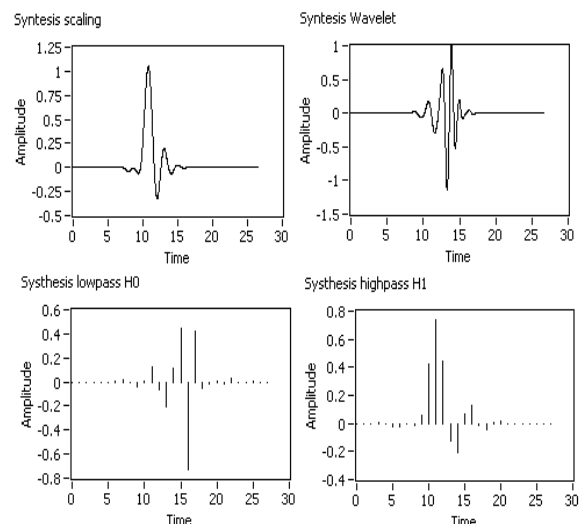


Fig. 7. Synthesis filters

In the designing of Wavelet filters the following steps are compulsory:

- selection of the type of the Wavelet transform;
- designing of an lowpass filter P_0 , which represents the product of the analysis G_0 and synthesis H_0 lowpass filters;
- selecting the type of factorization for the decomposition of P_0 in G_0 and H_0 .

After designing lowpass G_0 analysis filter and the synthesis lowpass filter H_0 , the virtual instrument "Wavelet Design" automatically generates a high-pass analysis and synthesis filter: G_1 and H_1 respectively (Fig. 5 and Fig. 6).

III. EXPERIMENTAL RESULTS

In Figure 8 the signals arising from the noise removal process are shown.

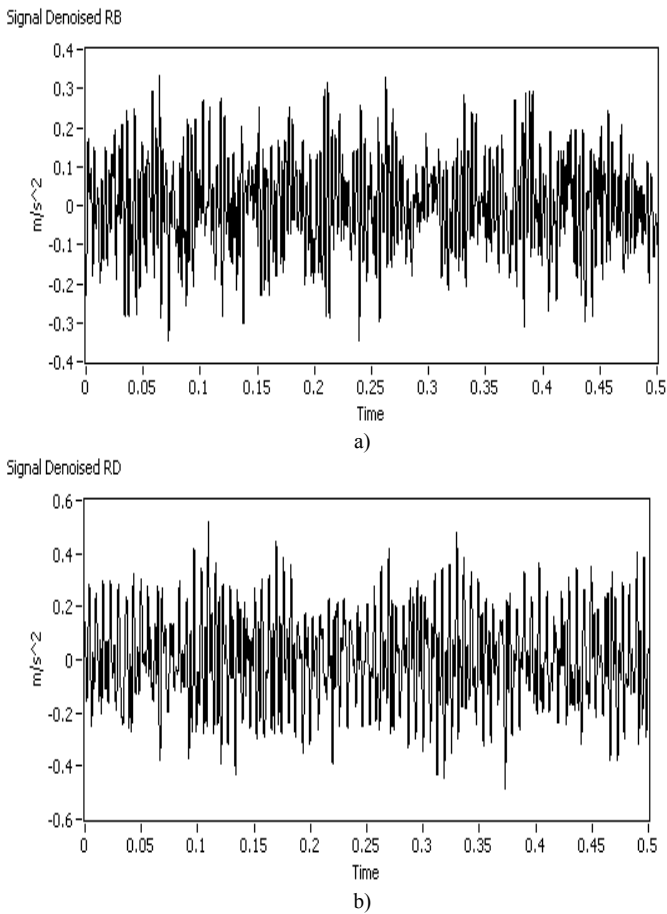


Fig. 8. The vibration signal with eliminated noise: a) breaker in functioning condition; b) defective circuit breaker.

The signals shown in Fig. 8 were analyzed using continuous Wavelet transform.

The Wavelet analysis is implemented using virtual instrument "WA Continuous Transform VI" which computes the coefficients of the continuous Wavelet transform.

The continuous Wavelet transform must be discretized in order to be applied to the acquired signals.

This discretization is achieved through dyadic sampling of the time-frequency (scale) plane based on a ratio equal to 2 between consecutive values of the translation and scaling parameters.

Fig. 8 shows the high values corresponding to low frequency scales and the small scales to high frequency. The continuous Wavelet transform gives good frequency resolution for high frequencies (small scales) and a good time resolution for low-frequency (large scale).

The scalogram from Fig. 9 was generated using Labview application where the block diagram is shown in Fig. 10. It can be observed that the magnitude of the vibrations and in particular their high frequency spectrum (Fig. 9b) makes the difference between a faulty breaker and a normal operating one (Fig. 9a)

It can be concluded that using continuous Wavelet transform, the power faulty breaker can be detected with better resolution and easily than using other techniques such as STFT power spectrum or cepstrum analysis, for faults of non simultaneous contacts break. The only drawback of this analysis method is that it requires large computing time for processing very large signals.

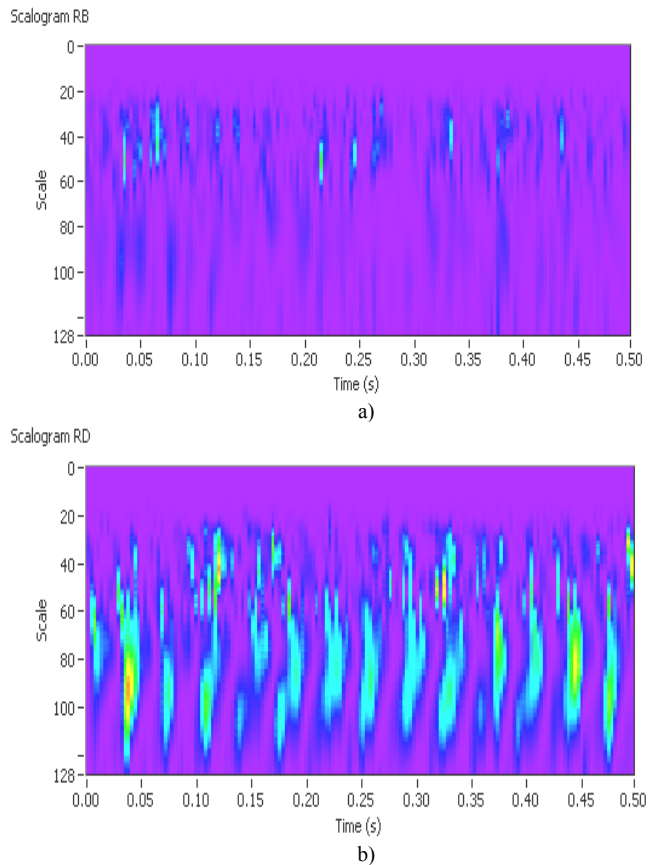


Fig. 9. The Wavelet analysis: a) good breaker b) defected breaker.

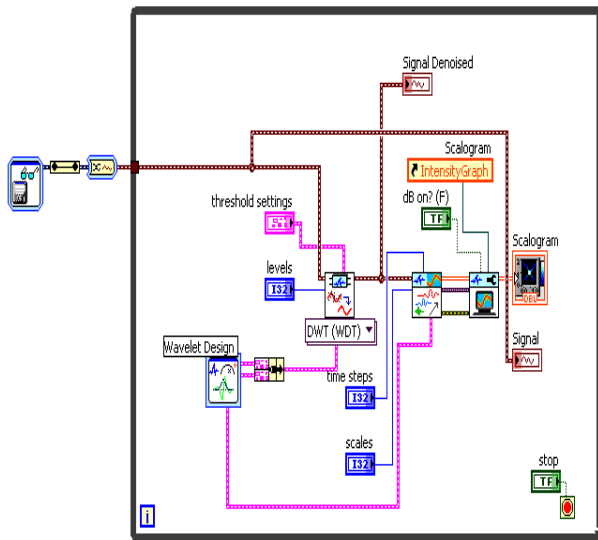


Fig. 10. The block diagram used for the Wavelet analysis

IV. CONCLUSIONS

Nowadays the vast majority of the applications used in vibrations monitoring call as diagnosis parameter the total square mean value. Computing these values on each cycle of the analyzed signal adds a supplementary detail to the analysis.

The linearity or the lack of linearity of the waveform is tied related to the amplitude variation of the analyzed signal. Therefore a sudden variations signal will be characterized by an irregular waveform, similar to that presented in Fig. 9b, while a signal having less significant variations of amplitude will be characterized by a quasi linear waveform.

Wavelet analysis depicted in Figs. 9a and 9b highlights that in the case of the faulty breaker, the waveform (Fig. 9b) presents large and irregular variations, while the scalogram of a normal operating breaker (Fig. 9a) tends to a horizontal asymptote.

Due to the use of power circuit breakers as switching equipment, most equipment manufacturers have not given importance to operational reliability study.

Efficiency is one of the most important parameters which must be taken into account in the operation of power circuit breakers, and this parameter depends, principally, on three factors:

- Energy prices passed through the breakers;
- The elapsed time between two successive disconnections;
- Operating and maintenance cost.

The first two factors cannot be changed, the energy prices being regulated by national regulatory organizations. The time elapsed between two successive disconnections depends on the specific breakdowns in the system, but the operating cost can be influenced using the correct and effective monitoring strategies.

The development and implementation of monitoring systems for power circuit breakers is a necessity due to their high rate of failure.

Currently the monitoring and diagnosis systems of the breakers status are using vibration signals, temperature measurement and also oil particles analysis in order to achieve the diagnosis of equipment operational status.

The monitoring systems have the following advantages:

- obtaining information regarding the faults or interruptions that might occur;
- the maintenance costs are significantly reduced by increasing the duration between two interventions and simplifies the diagnosis process;
- the life of equipment is extended;
- maximizing the investment profitability and reducing the operation costs.

REFERENCES

- [1] Unser, Michael and Thierry Blu, "Wavelet Theory Demystified." IEEE Transactions On Signal Processing, Vol. 51, No. 2, February 2003.
- [2] P. S. Addison, "Low-Oscillation Complex Wavelets", Journal of Sound and Vibration (2002) 254(4), 733-762.
- [3] Shie Qian, "Introduction to Time-Frequency and Wavelet Transforms", Upper Saddle River, New Jersey: Prentice Hall PTR, 2001.
- [4] Lin J., "Feature extraction of machine sound using wavelet and its application in fault diagnostics", NDT&E International, 34, 25-30, 2001.
- [5] Ioan Cozorici, Ioan Vădan, Horia Balan, "Condition Based Monitoring And Diagnosis Of Rotating Electrical Machines Bearings Using FFT And Wavelet Analysis", *Acta Electrotehnica*, volume 53, number 4, pg. 350-354, ISSN 1841- 3323, Ed. Mediamira Science Publisher, Cluj-Napoca, 2012.
- [6] C. Taswell, "The Why, How, and Why of Wavelet Shrinkage Denoising", Computing in Science and Engineering, June 2000, <http://www.toolsmiths.com/docs/CT199809.pdf>
- [7] M. C. E. Rosas-Orea, M. Hernandez-Diaz, V. Alarcon-Aquino, and L. G. Guerrero-Ojeda, "A Comparative Simulation Study of Wavelet Based Denoising Algorithms", CONIELECOMP 2005, ISBN: 0-7695-2283-1, pp: 125 – 130.

Performances Optimization and Characteristics of the Voltage Generated by Multilevel Inverters

Horia Balan

Power Engineering and Management
Technical University of Cluj-Napoca
Cluj-Napoca, Romania
horia.balan@eps.utcluj.ro

Adrian Augustin Pop

Power Engineering and Management
Technical University of Cluj-Napoca
Cluj-Napoca, Romania
augustin.pop@mae.utcluj.ro

Mircea Buzdugan

Building Services Engineering
Technical University of Cluj-Napoca
Cluj-Napoca, Romania
mircea.buzdugan@insta.utcluj.ro

Radu Adrian Munteanu

Electrical Engineering and Measurements
Technical University of Cluj-Napoca
Cluj-Napoca, Romania
radu.a.munteanu@ethm.utcluj.ro

Abstract—Several fixed frequency applications of multilevel converters require a very low level of distortion factor of the output voltage. Bringing the output voltage to a form as close as possible to a sine wave is usually done through linearization methods of the Newton-Raphson algebraic equations. The method proposed in section III uses for the waveforms optimization a genetic algorithm, having a positive impact on the total harmonic distortion reduction. Experimental validation of the method is performed using a programmable source which drives an induction motor.

Keywords—*distorsion factor, multilevel converter, genetic algorithm.*

I. INTRODUCTION

It is well known that the main applications of DC – AC voltage conversion at a fixed frequency and amplitude are:

- injection into the system of the energy provided by renewable energy sources;
- energy supply through uninterrupted power sources;
- DC power transmission at high voltage.

The most important issue of the conversion is that the injected alternative voltage needs to have a as low as possible total distortion factor and thus the harmonic content injected have to be decreased to minimum values. AC-DC voltage conversion is achieved through inverters. Inverter topologies research was influenced by the development of the "off-shore" renewable energy sources. At the same time energy transmission and injection into the power system is another issue relevant for research.

Energy produced from "off-shore" renewable sources is converted to DC, transported to the mainland and converted afterwards into AC voltage before being delivered to the power system. In these successive conversions, the most important issue is obviously the commutation process.

Commutation can be "soft", if the waveforms are synthesized by the control circuits through pulse width modulation (PWM) or "hard", if the waveforms are synthesized by the command of static commutation devices through a diagram topology used in the inverter power circuit.

In general, it is desired to avoid commutation on high voltage side, but for several applications it can't be avoided. Semiconductor devices are usually limited by the reverse voltage at values lower than 10 kV, so in transmission of the DC high voltage (HVDC) above 100 kV, a proper commutation is achieved by connecting semiconductor devices series connected or using multilevel converters.

The simplest topology that can be used for this conversion is the two-level inverter consisting of four switches. Each switch is provided with diode, antiparallel connected, since the configuration needs reverse current diode.

The multilevel inverter is a power electronic system that synthesizes a sinusoidal output voltage from several DC sources, which can consist in batteries, solar cells or capacitors.

Multilevel inverter operation is based on a number of switches series connected in order to deliver important values of sinusoidal voltage and current.

Since multiple switches are series connected, the commutation angle is an important value for multilevel inverters, since all the switches have to be operated so as the output voltage and current present a minimum harmonic distortion.

Total harmonic distortion (THD) is reduced by increasing the number of levels. It is obvious that an output voltage with a minimum total harmonic distortion is desirable, but increasing the number of levels requires more commutation devices complicating therefore the command and the control circuits. A trade off is also compulsory between price-weight-

complexity of an output voltage having a minimum total harmonic distortion.

Previous works in the area of multilevel inverters have focused rather on THD and on inverter commutation model. The vast majority is focused on obtaining a sinusoidal output voltage and current with minimum THD using different commutation models.

The commutation angles in multilevel inverters are highly important because they can affect the shape of the output voltage and the THD of the current.

There are several studies on different methods of harmonics elimination, which are related to commutation angle calculation [1]. The newest method used in order to eliminate the harmonic content is the resultant theory which summons the computation of the commutation angles.

Some papers have focused on different uses of multilevel inverters, while others are relating to different topologies, application dependent.

Paper [1] for instance compares the H-bridge multilevel inverters in the case of high power electric motors.

II. THE WAVEFORM OPTIMIZATION THROUGH HARMONIC ANALYSIS

The optimization of the voltage waveform provided by multilevel converters has as objective the reduction of total harmonic distortion. This can be performed by using mathematical equations with several parameters [2], but this method leads to complicated nonlinear equations. If the variable parameter is the commutation angle, solving the equations system is a quit difficult task.

In [3] there are presented the waveforms having a reduced degree of modulation, but showing a higher total harmonic distortion (THD). In [4] is proposed a method for THD reduction using harmonics elimination.

The concept of selective harmonics elimination [5] is combined with the one of symmetrical waveform and the elimination of inferior to 2 rank harmonics [2]. In general for multilevel converters mounted in cascade it is desired to optimize the commutation angles in order to minimize the THD.

Connecting in series a number of s H bridges the resulting output voltage will be the sum of the individual ones:

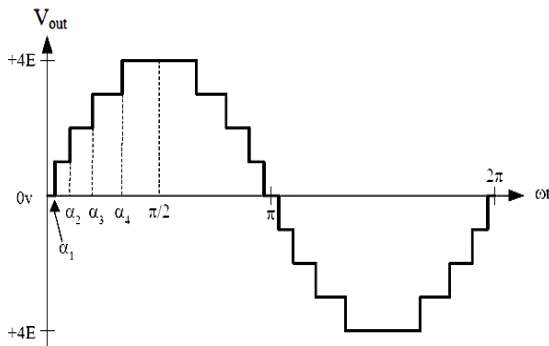


Fig. 1. The output voltage for a 9 steps inverter.

$$V_{out} = V_{dc1} + V_{dc2} + \dots + V_{dcs} \quad (1)$$

Determining the command angles has an interesting impact and it can be computed by eliminating the s-1 harmonics, different from the fundamental. It results in a system of transcendent equations, difficult to be solved analytically. The specific literature [4] offers numerical solutions, which uses Newton-Raphson method for solving the nonlinear equations system.

The procedure depicted in this section is a successive approximation method for solving the equations system [4].

Fig. 2 presents the function $y=f(\alpha)$ and the problem of solving the equation $f(\alpha)=k$ is brought to the foreground.

In the point α^j of the abscise axis, the tangent to the curve $y=f(\alpha)$ and the intersection with the line $y=k$ determines another point on the abscise, having the value α^{j+1} . The iteration is repeated from this point until the solution of the equation $f(\alpha)=k$, is obtained with the desired approximation.

As an example, in order to generate a 9 levels voltage per half cycle, determining the commutation angles $\alpha_1, \alpha_2, \alpha_3$ and α_4 is needed. Using a modulation index of $M=85$, the 3, 5 and 7 order harmonics are cancelled.

In the conditions imposed above, the system of nonlinear equations becomes:

$$\begin{aligned} \cos \alpha_1 + \cos \alpha_2 + \cos \alpha_3 + \cos \alpha_4 &= \frac{0.85 \cdot 3\pi}{4} \\ \cos 3\alpha_1 + \cos 3\alpha_2 + \cos 3\alpha_3 + \cos 3\alpha_4 &= 0 \\ \cos 5\alpha_1 + \cos 5\alpha_2 + \cos 5\alpha_3 + \cos 5\alpha_4 &= 0 \\ \cos 7\alpha_1 + \cos 7\alpha_2 + \cos 7\alpha_3 + \cos 7\alpha_4 &= 0 \end{aligned} \quad (2)$$

In order to implement the algorithm, the Matlab-Simulink platform is used and the values of the commutation angles expressed in radians obtained for the final iteration of the eqns. (2) are:

$$\alpha_1=5.2538; \alpha_2=28.1201; \alpha_3=46.3876; \alpha_4=84.0989 \text{ [4].}$$

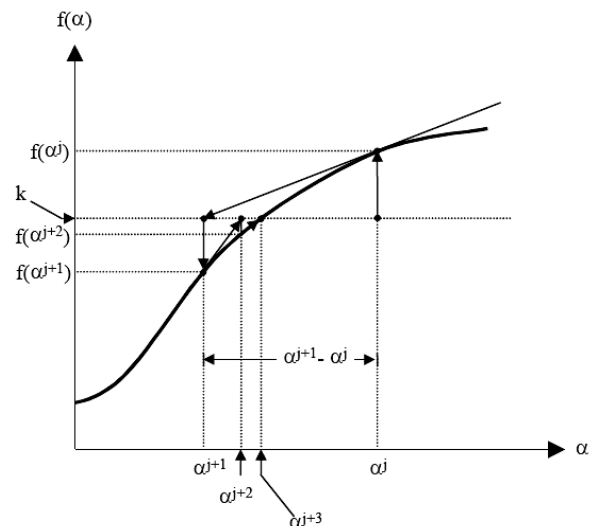


Fig. 2. The linearization technique

In a synthesized waveform using these angles, the 3rd, 5th and 7th harmonics are eliminated, the first harmonic component of voltage which appears in the output voltage of the multilevel inverter being the 9th order harmonic component.

The total harmonic distortion is defined by:

$$THD = \frac{\sqrt{\sum_{n=2}^{\infty} H_n^2}}{H_1}, \quad (3)$$

where H_n is the amplitude of rank n harmonic, and H_1 the fundamental amplitude.

Equation (4) defines the amplitude of the n^{th} order harmonic, generated by the multilevel inverter in a quarter of a cycle of symmetrical waveform:

$$h_n = \frac{4E}{n\pi} \sum_{k=1}^s \cos(n\alpha_k) \quad (4)$$

and substituting it in equation (3), the THD becomes:

$$THD = \frac{\sqrt{\sum_{n=2}^{\infty} \left(\frac{1}{n} \sum_{k=1}^s \cos(n\alpha_k) \right)^2}}{\sum_{k=1}^s \cos \alpha_k} \quad (5)$$

This is the computation procedure of the THD and taking into consideration the first 63 harmonics, eq. (5) becomes:

$$THD = \frac{\sqrt{\sum_{n=2}^{63} \left[\frac{1}{n} (\cos n\alpha_1 + \cos n\alpha_2 + \cos n\alpha_3 + \cos n\alpha_4) \right]^2}}{(\cos \alpha_1 + \cos \alpha_2 + \cos \alpha_3 + \cos \alpha_4)}, \quad (6)$$

The THD computed in [4], by taking into account the harmonic components having orders below 63 is 12.73%.

III. SYNTHESIS OF WAVEFORMS USING GENETIC ALGORITHMS

In order to implement a genetic optimization algorithm of the operation mode of a multilevel inverter, in order to reduce the harmonic content, the Matlab Simulink software platform is used.

The development of a proper function having the role of optimization based on genetic algorithms is compulsory. The implemented function has as initial data the level of multilevel inverter voltage and the number of iterations of the optimization process. The output data are the amplitude and the impulse period which are necessary for the reconstruction of the voltage waveform and at the same time of the THD introduced by the new optimized inverter.

The implemented genetic algorithm using the Matlab Simulink platform function started from a population of 100 randomly generated, each of them representing a possible set of functional parameters of the studied multilevel inverter.

In order to obtain the feasible function for the implemented genetic algorithm for each set of possible functional parameters the mean square error is determined. The error is determined as a difference between the waveform

produced by the converter and the desired sinusoidal waveform.

Within the iterative optimization process, in order to determine the inverter optimal configuration, the set of possible solutions from an initial population is subjected to an iterative process consisting in the following steps:

- Step 1: determining the value of optimization function for each possible configuration of converter from the starting population of the genetic algorithm;
- Step 2: from the current population, two possible solutions shall be randomly selected, which will become the subject of a crossing process in order to form two new possible solutions;
- Step 3: repeat step 2 until a set of 80 potential new solutions is obtained;
- Step 4: a process of mutation applied randomly to the current population, respectively to the set of descendents formed by the crossing process leads to a set of 20 new possible solutions (mutants solutions);
- Step 5: on the basis of the optimization function evaluated for each possible new solution the top 15 best possible inverters configurations plus 85 other possible solutions which are transferred to the next iteration are determined.

This iterative optimization process is repeated several times and the results are provided as a called parameter of the developed function until the value of the corresponding function associated to the best solution falls below a predefined value.

The studies conducted by the authors of the present paper have shown that a total of 5000 iterations will be sufficient to determine the best configuration for any type of multilevel convertor.

The results thus obtained were considered superior to those depicted in section II [4]. It should also be noted that they are compliant to the standard SR EN 50160/2011, which requires a THD value below 8%. The convergence graphs of THD values for a 9 steps inverter is presented in Fig. 3.

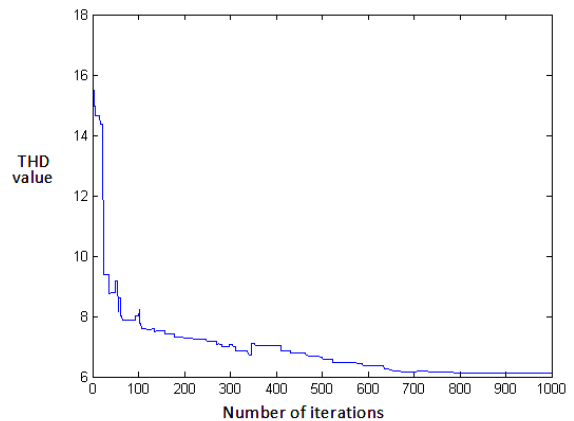


Fig. 3. The convergence graph for the 9 step inverter.

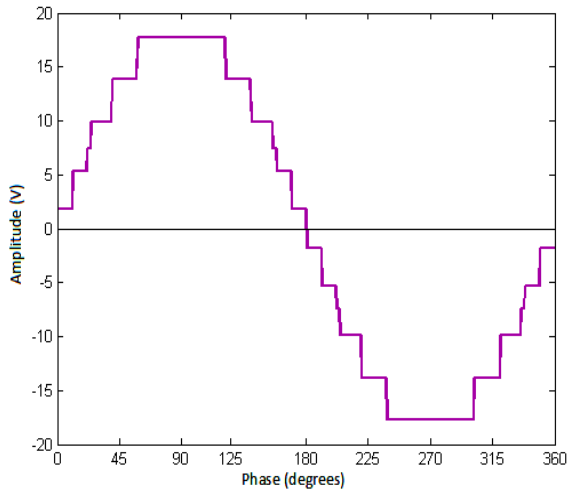


Fig. 4. The waveform shape for the 9 steps inverter

The goal of the algorithm was to obtain a waveform using a specified number of steps, having an as low as possible value of THD, in order to be stored into a programmable source. What makes the presented algorithm to outperform other methods [4] is the fact that in the case of a 9 steps waveform, there are 14 variables, width and height of each step voltage. Thus, the three waveforms width must satisfy the condition that their sum must be equal to $\pi/2$, and by testing a number of values which satisfy the basic conditions to get the best solution having the lowest THD.

The waveforms thus obtained are plotted in Fig. 4 (the abscise axis is denoted in sexagesimal degrees). It must be noticed that these waveforms have to be processed in order to be stored in the programmable source.

Analyzing the waveforms, it can be seen that, what makes them different from most of those depicted in the literature is the variability of steps, not only with respect to the voltage level but also to the value of switching angle. At the same time, the obtained waveform doesn't start from zero as the majority of the waveforms presented in the literature and available in the library of programmable source. The values of the THD thus obtained are superior to those obtained by other methods.

IV. GENERATION OF MULTILEVEL CONVERTERS VOLTAGES IN PROGRAMMABLE SOURCES

The influence of distorted regime can be highlighted experimentally using programmable sources.

Due to the nonlinear characteristics of multilevel converters in the distributed generation systems, the current and voltage harmonic are obviously present, having negative effects on loads and leading to the reduction of energy parameters.

Medium power nonlinear loads, usual in energy systems have an important contribution in the total harmonic pollution; therefore to decrease this kind of pollution becomes a very important issue.

Examples of such equipment are: adjustable drives with AC and DC motors, uninterruptible power supplies, digital automatic control, etc.

For a waveform measured using a digital instrument, Fig. 5, the harmonic analysis is shown in Fig. 6, where the harmonic levels are shown as a percentage in relation to the fundamental harmonic.

Knowing the amplitudes and phases of the harmonic components the waveform can be reconstructed using the software developed for CTS 15003iX California Instruments Programmable source (Figs. 7 and 8).

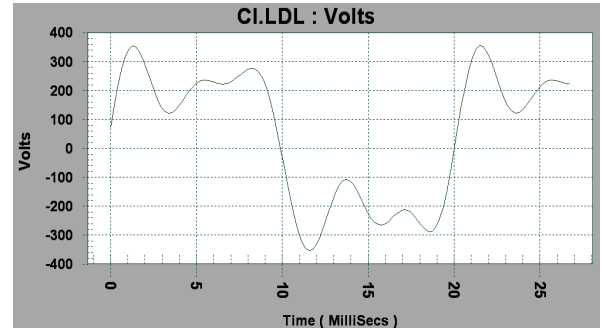


Fig. 5. The waveform of the absorbed voltage by a nonlinear consumer

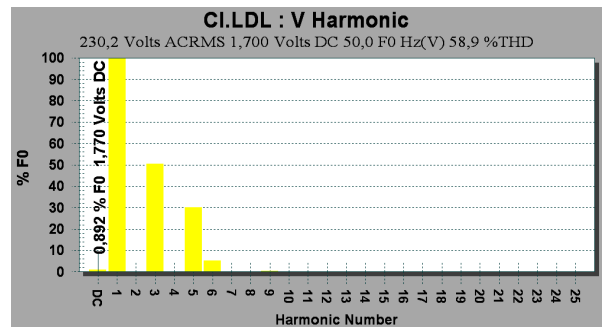


Fig. 6. The harmonic analysis of the absorbed voltage by a nonlinear consumer

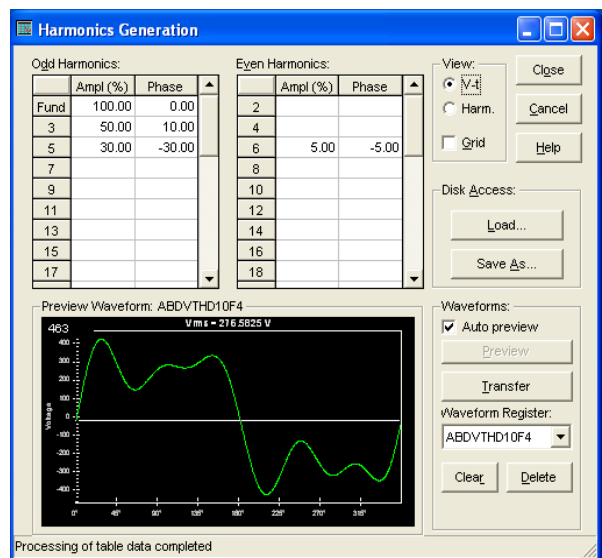


Fig. 7. The waveform generated by CIGui32 software.

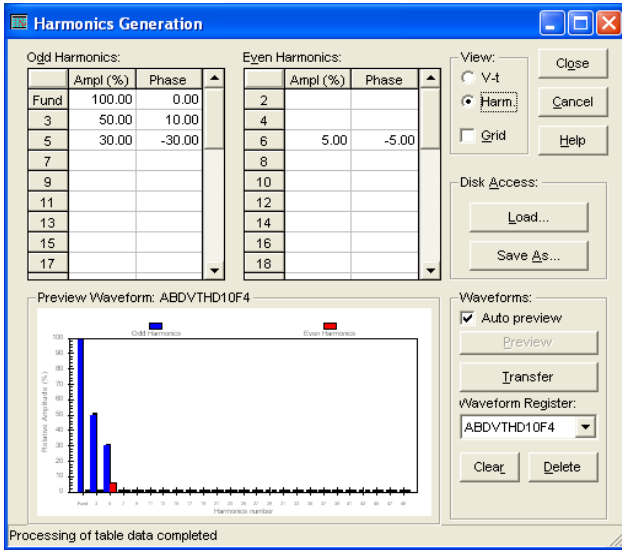


Fig. 8. The harmonic analysis of generated voltage with CIGui32 software.

V. EXPERIMENTAL RESULTS

The performance of the waveforms generated by the genetic algorithm must be compared with the one obtained through the Newton-Raphson linearization method and with the performance of a waveform with an identical number of voltage steps with constant voltage step levels and pulse duration [6 - 11].

In Fig. 9 is depicted the waveform obtained using the genetic algorithm. The waveform is stored in a programmable source for the case of an inverter with 9 voltage levels.

In load operation, the waveform deviates from the ideal form shown in Fig. 9; the resulting waveform of the voltage is presented in Fig. 10. It can be noted that it has the same shape of the waveform, but there is an additional ripple caused by the nonlinearities of the load.

In Fig. 11 is shown the waveform available for the command of the same type of inverter in the programmable source library.

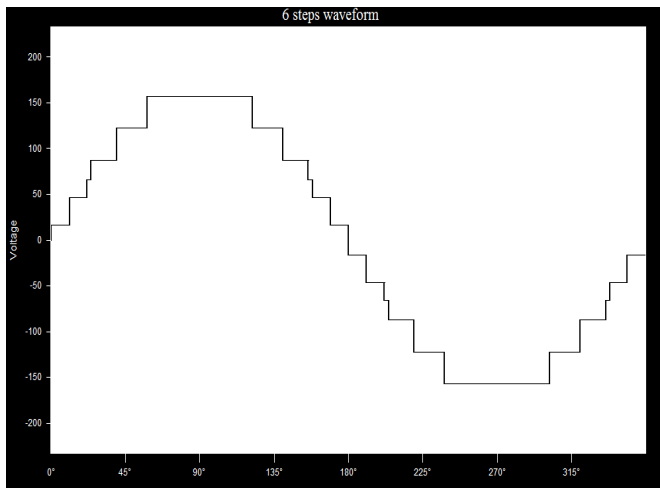


Fig. 9. The ideal waveform of 9 level multilevel inverter.

The voltage supplied by the programmable power source, Fig. 12, is characterized by voltage steps of constant amplitude and equal switching angles.

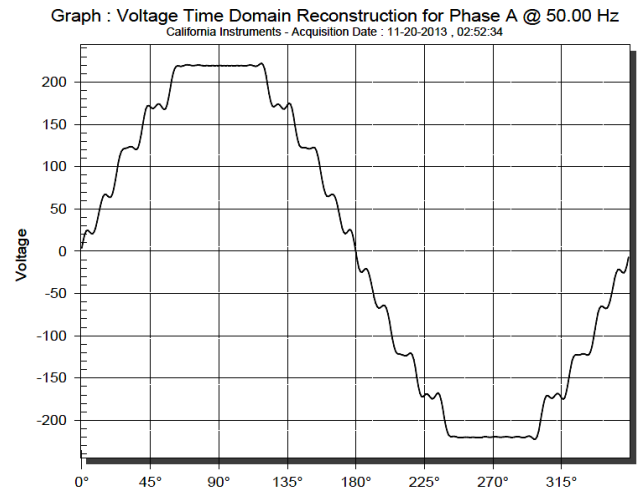


Fig. 10. The waveform obtained through genetic algorithm for the 9 level inverter in load operation mode.

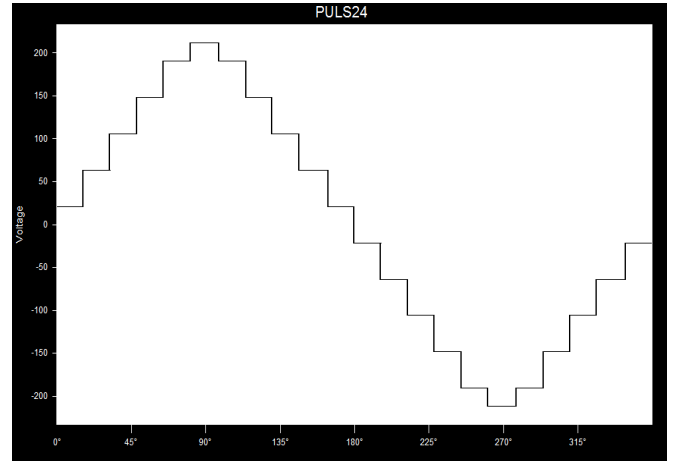


Fig. 11. The waveform available in the programmable source library for the 6 level inverter in no load operation mode

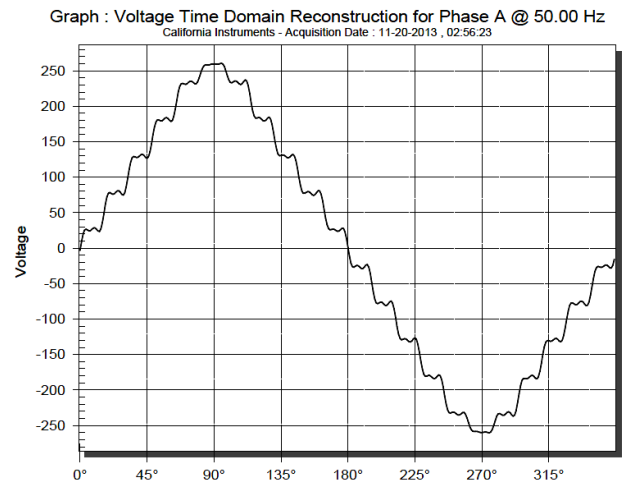


Fig. 12. The voltage waveform generated by programmable source, in load operation mode.

The above experimental results were obtained using a programmable source as an emulator for the multilevel inverter.

The waveforms generated by the unloaded programmable source coincide with the waveforms stored in the programmable source library (Figs. 9 – 11).

The waveforms obtained by the programmable source supplying an induction motor are depicted in Figs. 10-12. The programmable source is provided with a measuring block manufactured by National Instruments, connected via a RS 485 interface with the software CIGui 32 of the programmable source, which allows the measurement of the output electrical values.

VI. CONCLUSIONS

The experimental results depicted above, compare the waveforms of the electrical values supplying the load with the same waveforms provided by the genetic algorithm (Fig. 10) and those provided by the programmable source library (Fig. 12).

TABLE I. HARMONIC LEVELS

Acquisition Date : 11-20-2013 California Instruments THD Voltage = 5.85 %				Acquisition Date : 11-20-2013 California Instruments THD Voltage = 11.77 %			
	rms.	rel. (%)	Phase		rms.	rel. (%)	Phase
Fund	229.310	100.00	0.00	Fund	228.030	100.00	0.00
3	2.760	1.20	8.70	3	22.120	9.70	181.30
5	1.640	0.72	173.90	5	6.040	2.65	353.10
7	3.400	1.48	358.80	7	0.740	0.32	179.30
9	4.250	1.85	177.00	9	0.650	0.29	44.60
11	0.530	0.23	359.20	11	0.210	0.09	101.80
13	0.940	0.41	358.60	13	0.470	0.21	75.70
15	2.780	1.21	175.30	15	1.460	0.64	177.00
17	4.120	1.80	358.10	17	1.360	0.60	335.70
19	4.760	2.08	358.00	19	2.800	1.23	192.10
21	4.730	2.06	177.80	21	8.740	3.83	359.30
23	4.460	1.94	178.70	23	8.920	3.91	0.10
25	1.630	0.71	1.30	25	2.340	1.03	200.40
27	2.160	0.94	2.80	27	1.150	0.50	334.50
29	2.870	1.25	3.90	29	0.390	0.17	357.10
31	3.590	1.57	5.10	31	0.390	0.17	62.30
33	1.280	0.56	8.70	33	0.180	0.08	93.90
35	1.810	0.79	8.50	35	0.340	0.15	97.10
37	2.780	1.21	9.40	37	0.780	0.34	186.50
39	0.800	0.35	186.80	39	0.460	0.20	323.80
41	1.900	0.83	190.80	41	1.060	0.46	222.30
43	1.040	0.45	15.10	43	3.000	1.32	14.40
45	1.120	0.49	16.10	45	3.790	1.66	16.80
47	0.150	0.07	191.40	47	1.290	0.57	232.90
49	0.050	0.02	155.10	49	0.690	0.30	337.50

Table 1 presents the levels of harmonics up to order 49 for two situations, namely the waveforms provided by the genetic

algorithm and the waveforms of the library. It can be seen that through the developed genetic algorithm, the third harmonic is reduced from 9.70% to 1.20%, which significantly increases the efficiency of motor operation (lowering its operating temperature).

On the other hand, compared with the case of 3 levels inverter, the fifth harmonic is lower, being reduced from 2.65% to 0.72% the growth appears only for the seventh harmonic, which increases from 0.32% to 1.58%, and the ninth harmonic from 0.29% to 1.85%. Taking into account the fact that the harmonics 5 and 7 determine the negative sequence component, may cause oscillations in the operation mode, only the 7th harmonic needs to be filtered.

VII. REFERENCES

- [1] L.M. Tolberg, F.Z. Peng, "Multilevel Converter for Large Electric Drives", IEEE Transactions on Industry Applications, Vol. 35, No. 1, Jan./Feb. 1999, pp. 36-44.
- [2] P.M. Bhagwat, V.R. Stefanovic, "Generalized Structure of a Multilevel PWM Inverter," IEEE Transactions on Industry Applications, Vol.IA-19, No.6 Nov./Dec., 1983, pp.1057-1069.
- [3] F. Z. Peng, J. S. Lai, "Dynamic Performance and Control of a Static Var Generator Using Cascade Multilevel Inverters," IEEE Transactions on Industry Applications, Vol.33, No.3, May/June, 1997, pp.748-755.
- [4] S., Sirisukprasert, "Optimized Harmonic Stepped-Waveform for Multilevel Inverter", Master's Thesis, Virginia Polytechnic Institute and State University, URN: etd-100899-000251, 1999.
- [5] H. S. Patel, R. G. Hoft, "Generalized Techniques of Harmonic Elimination and Voltage Control in Thyristor Inverter: Part I-Harmonic Elimination," IEEE Transactions on Industry Applications, Vol.IA.9, No.3, May/Jun., 1973, pp.310-317.
- [6] IEEE Standard. 519-1992 - IEEE Recommended Practices and Requirement for Harmonic Control in Electrical Power Systems – IEEE Industry Applications Society/ Power Engineering Society.
- [7] Horia Balan, Mircea I. Buzdugan, Cristina Chiorean, Ana Iacob, Petros Karaisas, "A Passive EMI Filter for the Reduction of ActiveFilter Generated Network Distortions", Annals of the University of Craiova, No. 36, 2012, ISSN 1842-4805, pg. 235-241
- [8] H. Balan, M. I. Buzdugan, C. Chiorean, P. Karaisas, "Reduction of the distortion current factor of the current drawn by the electromagnetic vibrators supplied at variable frequency", *Materials Science Forum Vol. 721 (2012) pp 275-280 Online available since 2012/Jun/04 at www.scientific.net*
- [9] H. Balan, Cristina Chiorean, P. Karaisas, Testing Electronic Equipment using Waveforms Generated with Programmable Sources, Buletinul AGIR, anul XVII, nr. 4/2012, octombrie-decembrie 2012, ISSN-L 1224 – 7928, ISSN (online) 2247 – 3548, pg. 73-78.
- [10] Cristina Chiorean, Mircea Rădulescu, „Testing the Performance of EMI Filters Used in Connecting Renewable Energy Sources to the Power Grid”, Acta Electrotehnica, Special Issue, Proceedings of the 5th International Conference on Modern Power Systems MPS 2013, 28-31 May 2013, Cluj-Napoca, Romania, Mediamira Science Publisher, pp 87-92
- [11] Electromagnetic compatibility "(EMC) – Part 2-12: Environment – Compatibility levels for lowfrequency conducted disturbances and signalling in public medium-voltage power supply systems", IEC 61000-2-12.

Loss Analysis of Small Three-Phase Cage-Induction Motors under Sinusoidal and PWM Voltage Supply

Dan L. IRIMIE

Department of Electrical Machines and Drives
Technical University of Cluj-Napoca
Cluj Napoca, Romania
Dan.irimie@mae.utcluj.ro

Adrian Augustin POP

Department of Electroenergetics and Management
Technical University of Cluj-Napoca
Cluj Napoca, Romania
augustin.pop@enm.utcluj.ro

Mircea M. RADULESCU

Department of Electrical Machines and Drives
Technical University of Cluj-Napoca
Cluj Napoca, Romania
Mircea.Radulescu@emd.utcluj.ro

Andreea Laczko

Department of Electrical Machines and Drives
Technical University of Cluj-Napoca
Cluj Napoca, Romania
Andreea.laczko@mae.utcluj.ro

Abstract – Loss analysis of small induction motors is conducted in order to show the differences by supplying with sinusoidal and PWM voltage. In the first part of the analysis, under sinusoidal voltage supply, the motor was tested according to the Canadian CSA C390–98 standard (based on IEEE 112B). These results are the reference for finite element-based and analytical loss calculations. In the second part of the analysis, the same procedure for determining the iron losses is carried out for the PWM voltage-fed induction motor. The obtained waveforms are comparatively studied, and an analytical approach is made to account for the increase of iron losses.

Keywords—loss analysis; induction motor; PWM voltage supply;

I. INTRODUCTION

While oil price is rising every day, greater attention is paid to alternative cheaper solutions using the electricity. Bearing in mind, that a photovoltaic panel, a wind turbine or a hydro plant generates electricity from renewable sources (light, wind and water fall potential) the systems based on fossil fuels will become history. From the consumer point of view, the desire is to make a specific task with less effort and, after cost analysis, to decide whether one should get a cheaper tool with poorer efficiency or an expensive system with higher efficiency.

For the particular example of electrical machine, the average life span is about 20 years and, for this reason, taking into account the price of the electrical machine and the cost of the electricity, everyone agrees that the former is much greater. In order to cut off these costs, engineers thought that improving the machine efficiency will result in a smaller cost during the life cycle of the electric machine.

Designers of electric machines need to accurately estimate the machine efficiency, thus to compute the losses by three different ways: practical, analytical or using finite element method (FEM). Since, in the design stage, practical tests

cannot be carried out, other solutions for loss determination have to be used, i.e. analytical or FEM-based calculations.

Although all machine manufactures indicate the energy efficiency in catalogues, data bases or the machine plate under sinusoidal supply, often in industry, the power electronic inverter supply is used. This has many advantages, the greatest being the mechanical angular speed variation.

Inverters convert constant-frequency, constant-amplitude voltage into a variable (controllable) frequency-variable (controllable) amplitude voltage. The variation of power frequency supplied to the motor leads to the variation of rotating-field speed, which modifies the mechanical angular speed of the machine. Considering a constant-torque load, and varying proportionally amplitude and frequency of the voltage supplied to the motor results in constant flux and, therefore, constant torque, while the current remains unchanged. So, the motor provides continuous adjustments of speed and torque according to the mechanical load [1]. The main drawback of this solution is the increase of iron losses, which inevitably will alter the energy efficiency.

Some authors made an analysis, in which the real PWM-waveform voltage supply is considered, showing that, at rated voltage, the iron losses are with 73% higher, in the teeth, and with 3% higher, in the yoke, in respect to sine-waveform voltage supply. This is achieved by measuring the real PWM waveform and then, on an Epstein frame, the obtained waveform is reproduced [2]. Other authors [3] suggest the use of the PWM-voltage form factor, which affects the eddy-current losses and the excess losses. In [4] and [5], a new formula is introduced, that requires voltage average and RMS values. Comparative results for the methods described in [3] and [4] are reported in [6].

Most difficult losses to predict are the iron losses and stray load losses. As iron losses are about 26% from the total losses, for small cage-induction motors considered here, while stray load losses are about 0.5-2%, the present paper is focused on iron losses analysis. These losses are difficult to predict, since

they are dependent on many factors, like nonlinearity of the magnetic material, supply frequency, geometrical parameters etc. Iron losses are composed of eddy-current losses and hysteresis losses, and both do not follow the same determination procedure because of their different origin. Besides, due to manufacturing processes, iron losses are higher than predicted. Empirical coefficients are then used to take into account the losses in teeth and yoke.

II. LOSS ANALYSIS UNDER SINUSOIDAL VOLTAGE SUPPLY

In electrical machine domain, there is not a unified solution regarding the losses. Surveying the literature, one can find practical tests (induction motor), the European standard (IEC 60034-2-1), the American standard (112B), the finite element method and some analytical methods. Before approaching the practical tests issues, the induction motor under study is presented; it has 36-slot stator, 44-bar aluminum-squirrel-cage rotor (Fig.1), 2.2kW output power and energy efficiency of about 72% [7].

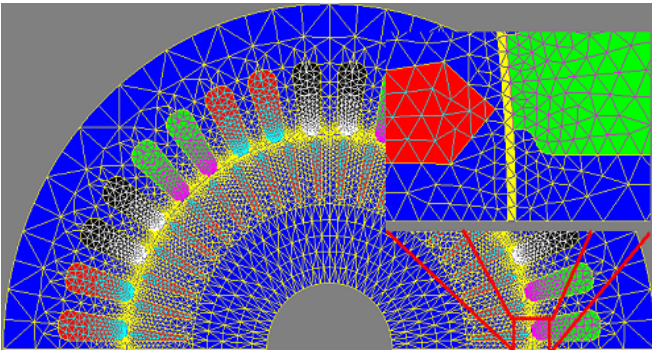


Fig. 1. Finite-element discretization of the half cross-section of the small three-phase cage-induction motor under study.

CSA C390–98 standard [8] is a general guideline for determining the energy efficiency of electrical machines, based on the IEEE 112B standard. It contains the so called ‘input-output method with indirect measurement of the stray-load loss and direct measurement of the stator winding, rotor winding, core and windage-friction losses’, which establishes some basic steps in order to determine the tested motor efficiency.

After all the measurements are carried out, the total losses are obtained, as in the numerical example of Fig.2 for the small three-phase cage-induction motor under study. One can see, that as part of the results, the iron losses are 216 W. According to this standard, the input power is consumed on stator Joule losses, iron losses and mechanical losses.

As suggested in [4], the mechanical losses under no-load conditions can be cancelled, when driving the induction motor by a synchronous motor with the same synchronous speed as the induction motor. Moreover, into the input power there are also some additional losses at no-load conditions, like the Joule losses in the squirrel-cage bars due to m.m.f. harmonics produced by the stator no-load current; but, for the time being,

this formulation from the international standard is taken into account.

The stator winding loss at no-load condition is calculated as:

$$P_{ws} = 3R_s I_s^2, \quad (1)$$

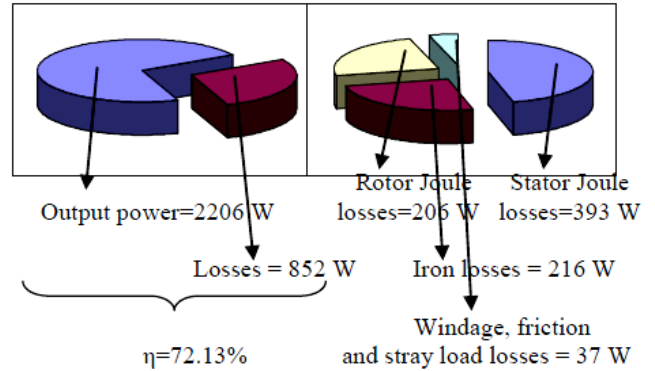


Fig. 2. Output power and loss components, as experimentally obtained from the CSA C390 – 98 for the small three-phase cage induction motor under study.

where I_s is the measured rms value of the stator-phase current, and R_s is the stator-phase resistance, which is determined from the cold-measured stator resistance and temperature, the winding load temperature and a coefficient depending on the conductive material of stator windings [8].

For different voltages, this procedure was carried out, and by subtracting these losses from the measured no-load input power, one gets the core loss and windage loss.

The last voltages from the no-load test are squared, and plot-ted vs. calculated core and windage losses, and where the extrapolated curve intercepts the losses axis, one can find the friction losses; further subtracting these losses from previous obtained losses, one can find the iron losses [8].

From an analytical field distribution, using geometrical data, BH characteristic and winding design data provided by the manufacturer, iron losses are computed. In the literature, there are two analytical methods for calculating the iron losses. The first and the oldest one is the Steinmetz formulation, which is used in this paper; the other, is the dB/dt method given in [9].

In practice, the effect of the punching process on iron losses is also taken into account.

Due to the larger area for the punching processes in teeth as compared to yoke, the iron losses including both eddy-current losses and hysteresis losses are separately calculated for teeth and yoke, as [10]

$$\begin{aligned} P_{Fe,d} &= K_{Vd} \left(\frac{B_{d,1/3}}{1.0} \right)^2 v_{10} m_d, \\ P_{Fe,y} &= K_{Vy} \left(\frac{B_{y,s}}{1.0} \right)^2 v_{10} m_y, \end{aligned} \quad (2)$$

where $P_{Fe,d}$, $P_{Fe,y}$ denote the iron losses in teeth and yoke, respectively; $B_{d,1/3}$ is the flux density at one-third distance from the airgap to the stator outer diameter; K_{Vd} , K_{Vy} are punching-related coefficients for teeth and yoke, respectively, which increase both the eddy-current and hysteresis losses; m_d and m_y denote the mass of teeth and yoke, respectively, and \mathcal{U}_{10} is the mass density of iron losses in the so-called ‘Epstein frame’ at 1 T [4]; here, K_{Vd} and K_{Vy} can be chosen as follows: $K_{Vd} = 1.8-2$, $K_{Vy} = 1.3-1.5$; for the greatest values of coefficients, one can get 95.86 W for overall iron losses.

In the above statement, the iron losses are proportional to the square of sinusoidal airgap flux density. In fact, the magnetic flux density is not sinusoidal due to saturation and discrete conductor position in slots. Therefore, the real flux-density waveform has to be reconstructed analytically, accounting for these effects.

The flux density curve follows the m.m.f. curve, which is described by a step distribution function [4]:

$$\Theta_{step} = z_{Q1} \cdot I_1, \quad (3)$$

where z_{Q1} is the number of conductors placed in a slot. Summing the characteristics for all three phases, taking into account the current amplitudes and using the expression :

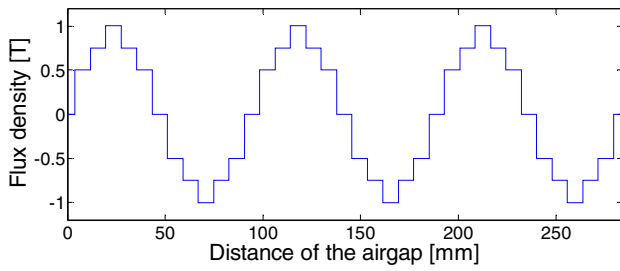


Fig. 3. Step distribution of the flux density in the airgap.

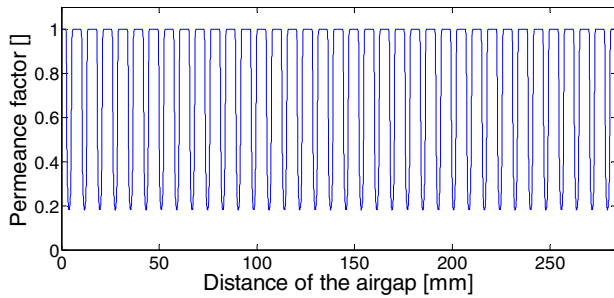


Fig. 4. Permeance factor for the 36-slot stator.

$$B(\alpha) = \frac{\mu_0 \Theta(\alpha)}{\delta}, \quad (4)$$

one can obtain the flux density in the airgap shown in Fig.3.

The flux-density waveform due to slotting is estimated using [11]. There are 36 stator slots, and underneath each stator slot-opening the permeance factor is decreased to about 0.18, as illustrated in Fig.4.

According to the effect of step distribution, the flux density waveform is derived in Fig.5.

Due to saturation, the peak value of flux density tends to be flattened, i.e. the value decreases with the degree of saturation expressed by the ratio B_{max} / B_{av} in stator tooth and airgap.

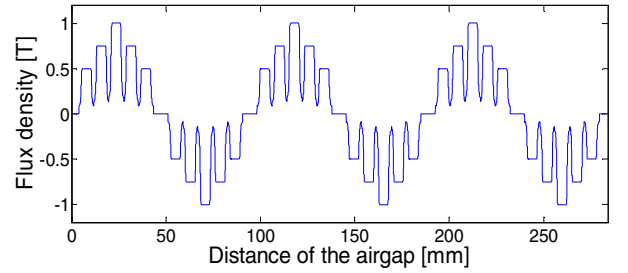


Fig. 5. Airgap flux-density distribution with influence of stator slots.

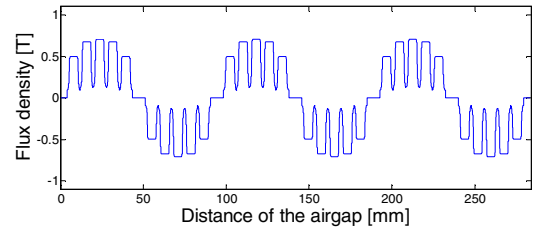


Fig. 6. Airgap flux-density distribution under saturation and stator-slotting effects.

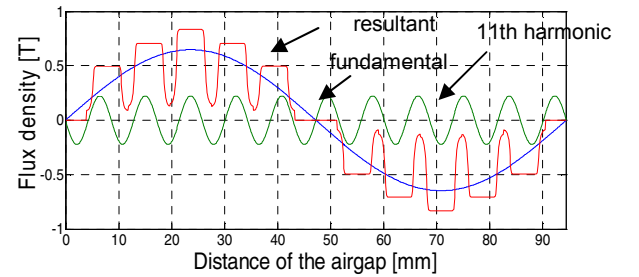


Fig. 7. Airgap flux-density distribution along two poles.

Hence, it can be seen that the peak value of B is 0.84 T (Fig.7) instead of about 1 T (Fig. 6).

The waveform of the airgap flux density being a periodic function, it can be decomposed in harmonics of different amplitudes and frequencies by Fourier analysis. These harmonics contribute to iron losses. Along the first two poles, the flux-density fundamental and 11th harmonic (which is dominant) are plotted in Fig.7, showing amplitudes of 0.648 T and 0.224 T, respectively.

For the fundamental amplitude (50Hz) the iron losses are found to be of 95.86 W. However, iron losses consist of eddy-current losses, which are dependent on the square of both frequency and flux density, and magnetic hysteresis losses, which are proportional to the frequency and the square of the flux density.

At high frequencies, eddy-current reaction must be considered. Along the steel sheet width, the flux density will

decrease from the edge to the center of the sheet. This fact is accounted for by

$$k_w = \frac{3}{\zeta} \cdot \frac{\sinh \zeta - \sin \zeta}{\cosh \zeta - \cos \zeta},$$

$$\zeta = \frac{b_{sh}}{d_E}, d_E = 1 / \sqrt{\pi f \mu \kappa}. \quad (5)$$

The permeability of electrical steel is not constant, but variable with the magnetic field strength. Therefore, harmonics with amplitude less than 0.5 T are not accurately taken into account in calculation of eddy-current losses. Considering just the fundamental and the 11th harmonic in the stator teeth (1.83T and 0.63 T, respectively) with the data provided by the steel manufacturer, one obtains the results listed in Table 1.

TABLE 1. Iron losses of the small induction motor under study

	Lower coefficients		Higher coefficients	
	teeth	yoke	teeth	yoke
Punching coefficients	1.8	1.3	2	1.5
Fundamental	25	20.5	25	20.5
11 th harmonic	47.9	9.71	47.9	9.71
Iron losses / region	131.22	39.27	145.8	45.31
Iron losses	170.47		191.11	

Since at rated speed, the frequency of rotor-induced currents is very low (i.e. 4.75 Hz), the rotor iron losses are negligible.

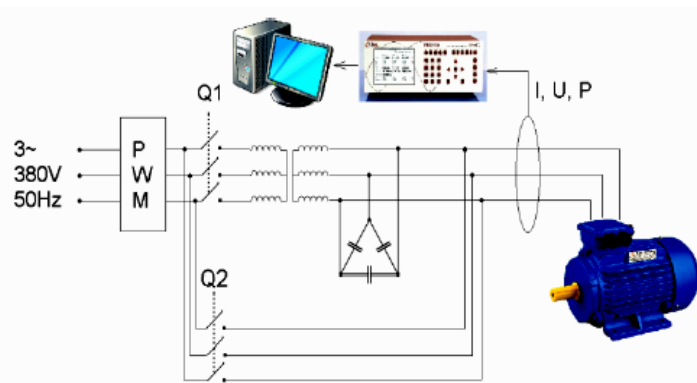


Fig. 8. Experimental set-up for no-load test: Q1-closed, Q2-open, sinusoidal voltage supply; Q1-open, Q2-closed, inverter-fed voltage.

The comparison of the analytically-determined iron losses for higher coefficients of Table 1 with those obtained from no-load test leads to a relative error of 13%.

III. LOSS ANALYSIS UNDER PWM VOLTAGE SUPPLY

Taking into account that the main influence of the PWM voltage waveform influences the iron losses, that part of the CSA C390-98 standard, which leads to the iron losses

determination is conducted under inverter-fed voltage. The schematic experimental set-up is depicted in Fig.8.

Actually, the transformer with the ratio 1:1.2 is used in order to conduct the test at nominal voltage, 400V. In the second test, when just Q2 is switched on, the transformer is moved between the grid terminals and the inverter module in order to compare the results of the test (Table 2):

TABLE 2. Test results according to CSA C390-98 standard

	Sinusoidal supply	PWM Supply
Voltage [V]	399.6	402.1
Current [A]	4.82	4.93
P _{abs} [W]	446	456.33
R _{stator@temp} [Ω]	6.745@101.6°C	6.197@74.3°C
P _{iron} [W]	216	235

- The test includes 11 voltage points: two above rated voltage and eight under the rated voltage.
- The last (smallest) voltages are squared and plotted against the input power. The extrapolation of this line gives us the mechanical power.
- The mechanical power under sinusoidal test procedure was used in the PWM test procedure.

Under these circumstances a method for predicting the loss differences is chosen between the methods presented in the last part of the introduction. The method for deriving the growth of iron losses under PWM voltage supply is based on [5].

There is a relation between the voltage waveform and the magnetic induction. So, using Steinmetz formula for the losses, one can identify a relation between voltage waveform and losses, since both eddy-current and hysteresis losses are proportional to B squared.

Therefore, the iron losses with any voltage waveform can be determined as

$$P_{ir} = \eta^x P_{h,sin} + \chi^2 P_{ec,sin}, \quad (6)$$

where $P_{h,sin}$ and $P_{ec,sin}$, represent the hysteresis and eddy-current losses, respectively, for sinusoidal supply; η and χ are coefficients depending on mean rectified and RMS values. From the data provided by the material manufacturer the iron loss segregation could be done in order to get the eddy-current and hysteresis losses for sinusoidal waveform.

For the special case of PWM voltage waveform [5] the above equation reduces to

$$P_{ir,PWM} = P_{h,sin} + \chi^2 P_{ec,sin}, \quad (7)$$

so that the increase of hysteresis loss component is nullified under PWM voltage supply.

With Kinetiq PPA2530 precision power analyzer, the components of χ factor (RMS values of real and fundamental voltages) can be determined, for each voltage point from the practical test; for the rated voltage this factor is 1.178.

In conclusion, the eddy-current losses under PWM voltage supply are 1.388 higher than under sinusoidal voltage supply.

By introducing this factor into the iron loss calculation procedure for the results presented in Table 1, the new outcome is presented in Table 3.

TABLE 3. Iron losses under PWM voltage supply

	Lower coefficients		Higher coefficients	
	teeth	yoke	teeth	yoke
Punching coefficients	1.8	1.3	2	1.5
Fundamental	31.7	38.1	31.7	38.1
11 th harmonic	62.3	74.9	62.3	74.9
Iron losses / region	169.2	146.9	188	169.5
Iron losses	316		357	

IV. CONCLUSIONS

Taking as reference the practical test, the iron losses of the small three-phase cage-induction motor under study increase under PWM voltage supply as compared to the sinusoidal voltage supply from 216 to 235 W.

An analytical method for iron loss determination of small cage-induction motors has been proposed, starting from the Steinmetz equations and using Fourier analysis of the airgap magnetic induction waveform. The proposed method takes into account magnetic saturation and stator-slotting effects. However, the empirical factors used and the 11th harmonic calculation method may introduce some errors into the analytical determination of iron losses.

The iron loss analysis results have shown good agreement with experimental tests according to international standards.

REFERENCES

- [1] Induction motors fed by PWM frequency inverters, (<http://catalogo.weg.com.br/files/wegnet/WEG-induction-motors-fed-by-pwm-frequency-converters-technical-guide-guide-028-technical-article-english.pdf>).
- [2] Cester, C., Kedous-Lebouc, A., Cornut, B., Iron loss under practical working conditions of a PWM powered induction motor, *IEEE Trans. Magn.*, September 1997.
- [3] Amar, M., Kaczmarek, R., A general formula for prediction of iron losses under non-sinusoidal voltage waveform, *IEEE Trans. Magn.*, September 1995.
- [4] Boglietti, A. *et al.*, A general model to predict the iron losses in inverter-fed induction motors, *IEEE Energy Conversion Congress and Exposition – ECCE 2009*, 20-24 September 2009.
- [5] Boglietti, A. *et al.*, Predicting iron losses in soft magnetic materials with arbitrary voltage supply: an engineering approach, *IEEE Trans. Magn.*, March 2003.
- [6] Boglietti, A. Cavagnino, A., Iron loss prediction with PWM supply: an overview of proposed methods from an engineering application point of view, *Conference Record of the 2007 IEEE 42nd IAS Annual Meeting*, 23-27 September 2007.
- [7] Irimie, D.L., Radulescu, M.M., Saint-Michel, J., Peltier, F., Comparative loss analysis of small three-phase cage induction motors, *19th International Conference on Electrical Machines – ICEM 2010*, 6-8 September 2010.
- [8] *CAN/CSA C390-98 Energy Efficiency Test Methods for Three-Phase Induction Motors*, Canadian Standards Association, 01-Dec-1999.
- [9] Fiorillo, F., Novikov, A., An improved approach to power losses in magnetic laminations under nonsinusoidal induction waveform, *IEEE Trans. Magn.*, May 1990.
- [10] Binder, A., *Energy Converters – CAD and System Dynamics*, Lecture Notes, Darmstadt University of Technology, Germany, 2009.
- [11] Freeman, E.M., *The calculation of harmonics, due to slotting, in the flux-density waveform of a dynamo-electric machine*, The Institution of Electrical Engineers, UK, Monograph No. 523, June 1962.

Analysis of multilevel converters operation through programmable source emulators

Balan Horia
Technical University of Cluj
horia.balan@eps.utcluj.ro

Pop Adrian Augustin
Technical University of Cluj
augustin.pop@mae.utcluj.ro

Buzdugan Mircea
Technical University of Cluj
mircea.buzdugan@insta.utcluj.ro

Berinde Ioan
Technical University of Cluj
ioan_berinde@yahoo.com

Abstract- This paper presents state-of-the-art elements in the context of energy increasing efficiency and of the development of various renewable energy sources. The utilization of power electronic converters gives proper answer to this goal regarding the transport and distribution of electrical energy. For multilevel converters, the synthesized waveform is experimentally tested using a programmable source as emulator.

Index Terms—energy efficiency, multilevel converter, emulator.

I. INTRODUCTION

The classical electric networks were built in order to transfer electrical energy from a relatively small number of large units of electricity production, centralized by a large number of distributed loads. The power flows are generally unidirectional from the central generator to the distributed load. Currently, relatively small units of distributed generation (DG) were connected to distribution networks, even if they were not designed to work with conventional generators. In this new configuration of the power system, the power fluxes are not unidirectional. Numerous studies confirm that electric networks can support without problems 10-15% penetration level of distributed generation electricity without the need of major structural changes in the system, but the integration must be controlled.

Three tendencies confirm the possibility of applying the DG of electricity:

- restructuring of utilities providers, which will allow free access to the market;
- policy of growing the use of renewable energy sources that are more suitable for distributed use than for the concentrated utilization;
- technical progress.

The integration of renewable energy sources represents the connection (adding) distributed electricity producers to the grid.

Integration problems are related to:

- protection systems;
- connection standards;
- power electronics;
- problems regarding the quality of electrical energy.

The distributed generation units may be independent of the network in parallel with the network or a combination of these two options. In the latter case, the distributed generation unit operates normally in parallel with the network, but when a fault occurs, the unit is disconnected from the grid, and continues to operate independently, in insulated mode. A typical method for connecting the source of distributed generation to the medium voltage network, through the main transformer is shown in Figure 1. The generator connection/disconnection is performed by the power transformer circuit breaker (the main switch). Depending on the importance and size of installation the transformer separator can be replaced by a switch.

From the electrical point of view, there are three types of DG sources:

- with synchronous generator;
- with asynchronous generator;
- with power electronic inverter.

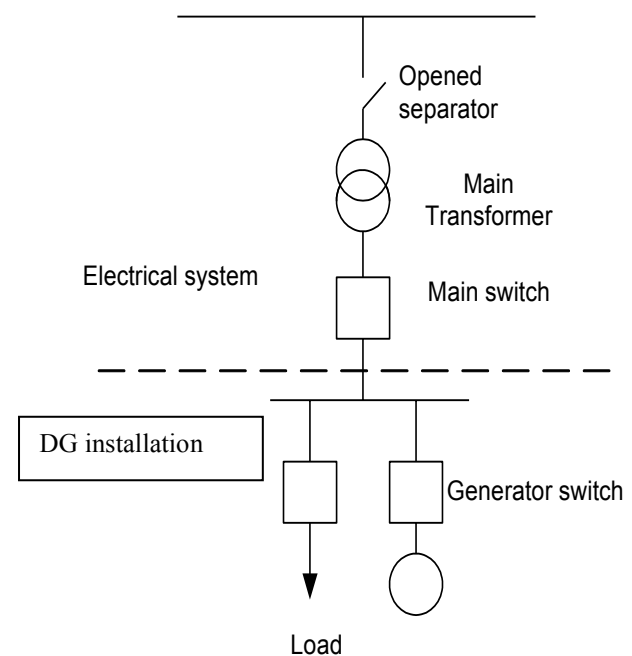


Fig. 1. Grid connection of distributed sources.

The general diagram shown in Figure 1, illustrates the interconnection technologies for the installations, which are using synchronous and asynchronous generators. Other types of DG technologies require the use of slightly different interconnection schemes. In all cases, due to the voltage level of the interconnection point, it is necessary to use a transformer. The small power units can be directly connected to the low voltage network.

The first two distributed generation sources are common technologies which are using rotating machinery, while the third variant uses a wide range of power electronic converters. In terms of interconnection, these three types have different impacts on the distribution network.

Applications of static converters in distributed generation are the conversion of AC-DC-AC voltage at fixed voltage and industrial frequency.

The AC-DC-AC electricity conversion has components and applications that are not necessarily related to DG, as follows:

- the DC to AC voltage conversion supplied by renewable energy sources provided by wind farms or photovoltaic parks;
- DC to AC conversion of the voltage stored in the equipments batteries of UPS (uninterruptible power source);
- AC-DC conversion carried by DC high voltage lines.

II. MULTILEVEL CONVERTERS IN THE SYSTEMS USED ON ENERGY CONVERSION

As it is known, the application of DC voltage-AC voltage conversion at fixed frequency and amplitude are:

- the injection into the system of energy provided by renewable energy sources;
- energy supplying by interruptible power sources;
- DC power transmission at high voltage.

The most important problem of the conversion is the fact that the alternative voltage injected need to have a minimal distortion factor and so the harmonics injected are decreased to minimum values. AC-DC voltage conversion is achieved through inverters. Inverter topologies research was influenced by the development of "off-shore" renewable energy sources. The energy transport and energy injection into the power system was another problem studied by the researchers.

The energy produced from renewable sources "off-shore" is converted to DC, transported to the mainland, where it is converted into AC voltage and delivered to power system. At the conversion elements, the most important issue is the commutation.

The commutation can be "soft" when the waveform is synthesized by the control circuits through pulse width modulation (PWM) or "hard" when the waveform is synthesized by the command of static commutation devices through diagram topology used in the inverter power circuit.

In general, it is desired to avoid commutation on the inverter force side, but for mentioned applications, this cannot be prevented.

Semiconductor devices are usually limited by the reverse voltage at values lower than 10 kV, but on the transport of DC high voltage (HVDC) the 100 kV switching voltage is exceeded and the commutation is achieved by connecting a series of semiconductor devices or using multilevel converters. The simplest topology that can be used for this conversion is the two-level inverter which is made of four switches. Each switch consists of an antiparallel diode, since the configuration needs reverse current diode.

The multilevel inverter is a power electronic system that synthesizes a sinusoidal output voltage from several DC sources. DC sources can be batteries, solar cells or capacitors.

Multilevel inverter operation is based on a number of switches connected in series in order to obtain on the output voltage and sinusoidal current.

Since multiple switches are connected in series, the angle of commutation is important for multilevel inverters, because all switches would be operated in such a way that the output voltage and current to have minimum harmonic distortion.

Total harmonic distortion (THD) is reduced by increasing the number of levels. It is obvious that an output voltage with a minimum of total harmonic distortion is desirable, but increasing the number of levels requires more commutation devices and so complicates the command and control circuits.

The compromise necessity appears for price-weight-complexity for an output voltage with minimum of total harmonic distortion. Previous work in the area of multilevel inverters focused more on THD and on inverter commutation model. The majority were focused in order to obtain at the output a sinusoidal voltage and a current with minimum THD using different commutation models.

The commutation angles in multilevel inverters are so important because they can affect the shape of the output voltage and the THD of current.

There are several studies on different methods of harmonics elimination, which are related to commutation angle calculation [1]. The newest method used to eliminate harmonics is the resultant theory. The harmonics elimination in a multilevel converter using this method focuses on the resultant theory in order to calculate the commutation angles. Some papers have focused on different uses of multilevel inverters, while others relate to different topologies depending on the electricity application for which are used. The papers [2,3] compares the H-bridge multilevel inverters in the case of high power electric motors.

The most common multilevel inverter topologies are:

- diode-clamped multilevel inverter (DC-MLI);
- flying capacitor multilevel inverter (FC-MLI);
- cascaded H-Bridge Multilevel Inverters (CHB-MLI).

When the number of levels is larger than three for DC-MLI inverters, the number of clamped diodes and the complexity of the scheme are increased.

FC-MLI inverters are based on voltage balancing and can generate different waveforms at the output. It also requires a phase balancing capacitors and leads to increased complexity by increasing the number of capacitors. They are defined as different combinations of capacitors allowing the charging or

discharging of the individual flying capacitors in order to produce the same phase leg voltage.

Among these three types of usual multilevel inverters topologies, the cascade inverter has the smallest number of components for a given number of levels. Cascade multilevel inverters are made up of a number of cells of H-bridge type in order to synthesize the required voltage from several separated direct voltage sources (SDCS), which may be batteries or fuel cells.

All these properties of cascade inverters allow the using of various control strategies using pulse width modulation (PWM) for a more accurate control. In addition for the previously mentioned technologies specific control techniques have been developed for multilevel inverters such as selective harmonic elimination PWM (SHE-PWM), sinusoidal PWM (SPWM), space-vector PWM (SVM) and modulation techniques derived thereof. The modulation methods used for the multi-level inverters can be classified according to the commutation frequency

Optimizing the output voltage waveform for the multilevel inverter has as aim the reduction of total harmonic distortion.

This can be done by minimizing the mathematical expression of the total harmonic distortion, depending on various parameters [5]. Applying this way of solving the problem leads to a system of linear equations, system difficult to resolve when the variable parameter is the control angle.

In [6], waveforms with a low degree of modulation are presented, but here the THD is higher.

In [7], a method for eliminating harmonics in order to decrease the THD is proposed by combining the concept of selective harmonic elimination [8], with the concept of symmetric waveform and elimination of lower order harmonics [5].

In general, for CHB-MLI, the orientation was to optimize the switching angles so that the total harmonic distortion is minimized.

As is known, by linking in series of n switching circuit, connected to a DC voltage source, the summing of the output voltage is achieved and thus the inverter output voltage being V_{out} :

$$V_{out} = V_{dc1} + V_{dc2} + \dots + V_{dcn} \quad (1)$$

With n bridge switches [1], connected in series a $2n + 1$ levels output voltage can be synthesized.

The voltages are provided by n sources V_{dc1} , V_{dcn} that provides the same or different value of DC voltage.

The waveform optimization may take into account another variable element, the switching angles.

There are three possibilities to optimize the waveform of multilevel inverters, depending on variable parameters, namely:

- Constant-voltage steps and variable switching angle;
- Variable-voltage steps and constant switching angle;
- Variable-voltage steps and variable switching angle.

Another element to take into account in synthesizing the waveform is related to the slope of a sinusoidal function at the origin, which can be synthesized according to:

- N switching circuits connected in series;
- $2n$ -level output voltages, when the voltage at the inverter output doesn't contain 0 Volts voltage step;
- $2n + 1$ output voltage level when the output voltage contains the zero voltage steps.

The synthesis of multilevel waveform has been addressed in the literature by various mathematical methods [4, 5, 6, 7, 8, 9]. The articles permit a synthesis of the step waveform for the best approximation of the output sine wave and are based on Fourier series and Wavelet transform.

The obtained properties create a mathematical tool that could be applied in the design of multilevel inverters. The obtained waveforms can be generated through programmable sources.

III. EMULATORS FOR MULTILEVEL CONVERTERS

An accurate electric power supply implies rms voltage and frequency limits according to standards and admissible distortion thresholds for the voltage and current waveforms. Harmonic currents affect the power system due to their flow from the load to the source and in low voltage affect the VSD systems interposed between the interference source and the low voltage transformer substation. Equipment produces more current disturbances than it used to do. Both low- and high-power equipment are more and more powered by simple power electronic converters which produce a broad spectrum of distortion.

The voltage and current waveforms distortion are mainly due to

- static converters commutation process;
- harmonic components generated by nonlinear loads;
- flicker due to fluctuating loads;
- converter operation when the firing angle is increasing;
- resonances because of compensating capacitors, which along with the grid impedance act as resonant circuits.

The equipment has become less tolerant of voltage quality disturbances, production processes have become less tolerant of incorrect operation of equipment, and companies have become less tolerant of production stoppages.

These were several reasons for adopting conducted interferences test standards and the development of specific test equipments which perform tests according to conducted immunity and emission standards.

In order to better study and solve such problems, we have used as precompliance equipment the CTS 15300iX programmable source (Fig.2) produced by California Instruments [10], [11].

The programmable source used for testing is an instrument from CTS series produced by California Instruments, which provides an efficient test solution in terms of value for money, which aims to verify the product compliance with a large number of testing standards in AC and DC.



Fig. 2. California Instruments CTS-15003iX.

The CTS Series of testing system offers the following advantages:

- single-phase and three-phase systems for a wide range of power debited on the load;
- data acquisition system with direct access to the PC bus provides high resolution and high sampling rate for accurate measurement and high transfer speeds, even in three phase mode, unlike other IEC test systems that provide a rate transfer limited by the IEEE-488 interface;
- test software PC-based for harmonics and flicker that offers real-time data color update and continuous monitoring of PASS / FAIL type;
- support for European and Japanese standards;
- simple utilization under Windows offering IEC test setup, data analysis, display and test reports in MS Word format;
- high resolution, no gap acquisition data storage to disk in ASCII format for post-acquisition analysis and reporting;
- resumption of recorded test data step or fast - Fast Forward;
- single Step and Fast Forward replay of recorded test data.

Available for power levels ranging from 1250 VA to 30,000 VA, CTS Systems cover the complete range of single and three phase products that need testing to conform with existing and pending IEC standards.

All iX Series AC sources meet IEC requirements for low voltage distortion and offer arbitrary waveform generation, precision measurements, and waveform analysis capabilities for load voltage and current.

AC power source real distortion is measured in real time during harmonics testing and any distortion is indicated that

could affect the test results. All iX Series based CTS systems support full compliance IEC 61000-4 AC immunity test as well (certain options may be required).

The 1251RP source based on CTS system which can be used for realizing complete harmonics tests and flicker test with low power load and with an peak coefficient of the maximum current.

IV. EXPERIMENTAL RESULTS AND CONCLUDING REMARKS

As load was used an induction motor (asynchronous) single-phase squirrel cage, with the following characteristics: $U_n=230$ Vac; $P=460$ W; $\cos\phi=0.8$; $\eta=0.8$.

The load has been provided from the programmable source CTS-15003iX, with the waveforms generated through the genetic algorithm. The waveforms used for controlling the multilevel inverters are also generated from the programmable source library.

Using the developed software tool we performed the conversion of voltage levels and the waveforms format obtained from genetic algorithm at the levels and format required for supplying the load.

In Fig. 3, the waveform thus obtained and placed into the programmable source.

In load operation the waveform deviates from the ideal form presented above, as shown in Fig. 4. The same allure waveform can be noticed, less the existence of a ripple caused by the nonlinearity of the motor.

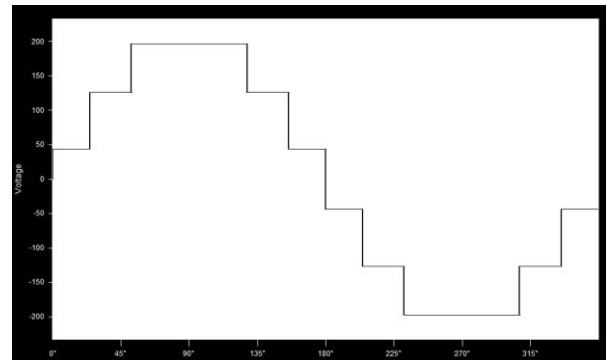


Fig.3. Ideal waveform of three-step inverter under no-load operation.

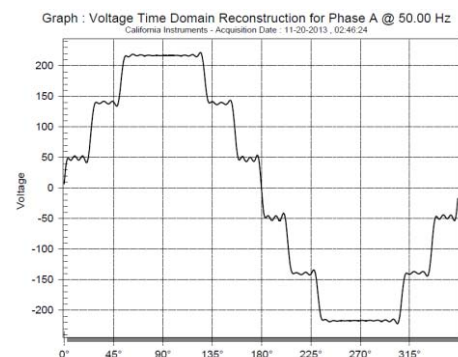


Fig. 4. Waveform obtained through the genetic algorithm of the three-step inverter under load operation.

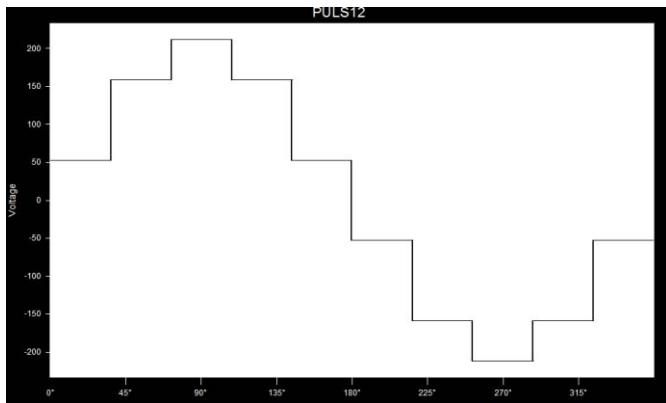


Fig. 5. Waveform generated from the programmable source library of three-step inverter under no-load operation.

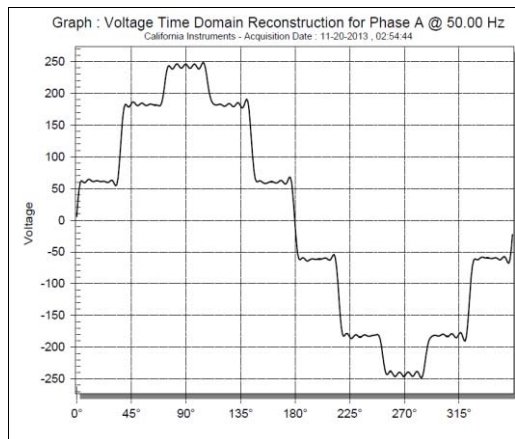


Fig. 6. Waveform generated from the programmable source library of the three-step inverter under load operation.

In Fig.5, the waveform generated by the programmable source library for the same type of inverter is shown.

Fig. 6 presents the experimental result for the motor supplied by the waveform of Fig.5.

In Table 1, the levels of harmonics up to order 49 for supplying the two waveforms are presented.

It can be seen that through the developed genetic algorithm, the third harmonic is reduced from 4.95% to 0.68%, which significantly increases the motor operation efficiency (decreasing its operating temperature).

On the other hand, there is an increase in the level of the fifth-order and the seventh voltage harmonics.

Fifth order harmonic increases to 1.68%, while the seventh order increases to 2.83%.

In view of the fact that the two harmonic components determines the negative sequence and may result in oscillation operation, it is important that the harmonic components to be filtered by means of harmonic filters.

Also the use of programmable source as waveform emulator can allow the spectral analysis for the waveforms from library source and also for the waveforms obtained based on genetic algorithm.

TABLE I

THE HARMONICS LEVEL

Acquisition Date : 11-20-2013
California Instruments
THD Voltage = 11.45 %

	rms.	rel. (%)	Phase
Fund	227.890	100.00	0.00
3	1.560	0.68	17.80
5	3.820	1.68	176.00
7	6.450	2.83	358.40
9	6.160	2.70	176.30
11	2.270	1.00	170.00
13	15.930	6.99	358.00
15	14.360	6.30	358.10
17	1.920	0.84	5.40
19	1.170	0.51	4.60
21	2.240	0.98	359.40
23	3.090	1.36	177.10
25	1.810	0.79	175.70
27	5.830	2.56	2.10
29	5.980	2.62	3.60
31	1.460	0.64	9.70
33	1.610	0.71	8.80
35	1.550	0.68	9.30
37	2.000	0.88	185.90
39	1.510	0.66	187.40
41	2.860	1.25	12.90
43	3.180	1.40	15.10
45	1.080	0.47	21.20
47	1.640	0.72	20.60
49	1.390	0.61	22.50

Acquisition Date : 11-20-2013
California Instruments
THD Voltage = 16.85 %

	rms.	rel. (%)	Phase
Fund	225.840	100.00	0.00
3	11.170	4.95	175.70
5	0.290	0.13	97.30
7	4.410	1.95	169.40
9	24.900	11.03	358.60
11	20.040	8.87	358.10
13	2.550	1.13	164.20
15	0.290	0.13	94.20
17	1.530	0.68	158.10
19	10.590	4.69	358.70
21	9.300	4.12	359.30
23	1.390	0.62	159.80
25	0.260	0.12	95.60
27	0.820	0.36	154.00
29	6.090	2.70	3.40
31	5.530	2.45	5.10
33	0.960	0.43	161.20
35	0.240	0.11	100.10
37	0.550	0.24	156.20
39	4.040	1.79	11.20
41	3.780	1.67	13.60
43	0.760	0.34	165.70
45	0.210	0.09	106.00
47	0.450	0.20	162.40
49	2.950	1.31	20.80

REFERENCES

- [1] F. Blaabjerg, R. Teodorescu, M. Liserre, and A. V. Timbus, "Overview of control and grid synchronization for distributed power generation systems," *IEEE Trans. Ind. Electron.*, vol. 53, no. 5, pp. 1398–1409, Oct. 2006.
- [2] R. Teodorescu, F. Blaabjerg, J. K. Pedersen, E. Cengeli, S. U. Sulistijo, B. O. Woo and P. Enjeti, "Multilevel Converters-A Survey" *European Conference on Power Electronics and Applications*, 1999.
- [3] M. Veenstra, and A. Rufer, "Non-Equilibrium State Capacitor-Voltage Stabilization in a Hybrid Asymmetric Nine-Level Inverter: Nonlinear Model-Predictive Control", *European Power Electronics and Drives Association (EPE) Journal*, Vol. 15, No. 1, February 2005, pp. 28-35.
- [4] Nabae, I. Takahashi, H. Agaki, "A New Neutral-Point Clamped PWM Inverter", *IEEE Transaction on Industry Applications*, Vol. IA-17, No. 5, Sep./Oct., 1981, pp. 518-523.
- [5] P.M. Bhagwat, V.R. Stefanovic, "Generalized Structure of a Multilevel PWM Inverter," *IEEE Transactions on Industry Applications*, Vol.IA-19, No.6 Nov./Dec., 1983, pp.1057-1069.
- [6] F. Z. Peng, J. S. Lai, "Dynamic Performance and Control of a Static Var Generator Using Cascade Multilevel Inverters," *IEEE Transactions on Industry Applications*, Vol.33, No.3, May/June, 1997, pp.748-755.
- [7] S., Sirisukprasert, "Optimized Harmonic Stepped-Waveform for Multilevel Inverter", Master's Thesis, Virginia Polytechnic Institute and State University, URN: etd-100899-000251, 1999.
- [8] H. S. Patel, R. G. Hoft, "Generalized Techniques of Harmonic Elimination and Voltage Control in Thyristor Inverter: Part I-Harmonic Elimination," *IEEE Transactions on Industry Applications*, Vol.IA.9, No.3, May/Jun., 1973, pp.310-317.
- [9] S.R. Bowes, "New Sinusoidal Pulse Width-Modulated Inverter", *Proceedings IEEE*, Vol. 122, No. 11, Nov. 1975.
- [10] *** California Instruments CTS15003iX, "*Compliance Test System, User Manual, CTS 3.0*";
- [11] *** California Instruments CTS15003iX, "*AC Power Source, User Manual*";

Modeling and Simulation of Current Digital Relays

Balan Horia
Technical University of Cluj
horia.balan@eps.utcluj.ro

Buzdugan Mircea
Technical University of Cluj
mircea.buzdugan@insta.utcluj.ro
Pop Adrian Augustin
Technical University of Cluj
augustin.pop@mae.utcluj.ro

Berinde Ioan
Technical University of Cluj
ioan_berinde@yahoo.com

Abstract- Optimal setting of current relays is a crucial issue in the protection of power systems. The paper depicts an algorithm for the optimal coordination of these relays. The algorithm was tested for a grid supplied at one end. The novelty of the paper consists in the modeling and the simulation of the coordination of the overload relays.

Index Terms—modeling, current relay, simulation.

I. INTRODUCTION

A very important issue of the a.c. power grids consists in defining the command, control and protection strategy, meant to assure the normal, safe and stable operation of the system.

There are several elements which must be considered in the choice of the protection system. The design and the choice of a protection system implies the knowledge of the faults that may appear in electric grids. From the point of view of the effects, immediate or delayed in time, these faults may be of a greater or lesser intensity. Current relays represent the primary protection in the distribution systems. The development of electronic devices, replaced the old electromechanical technology, used in the first generations of protective relays, with the static technology. However, static relays present several drawbacks, since analog circuits are very sensitive to electromagnetic interference. On the other hand the magnitudes of the voltage and the currents are limited in analog circuits, affecting the relay sensitivity.

Embedding a microprocessor in the architecture of a relay, which emulate the function and the logic of a relay date from the early eighties. Digital relays included an analog-digital converter used for sampling the signals from the instrumentation transformers, the microprocessor being used in defining the relay's logic. Digital relays determined also an improvement of accuracy and control of the input signals, using higher complexity algorithms and performing extra tasks and functions.

Digital relays represent sophisticated equipment, having multiple uses and having the possibility of recording signals during the fault duration, monitoring and communicating with other relays in the grid. Digital relays use microprocessors dedicated for processing digital signals, being therefore more rapid and efficient and maintaining in the same time their economic advantage.

Most of situations, it is impossible to investigate the above mentioned in a real case of a system, due to different economic, functional or security impediments. Therefore, several approaches and equipment have been developed, in

order to overcome these deficiencies: e.g. real time digital simulators (RTDS), reversible real time digital simulators and software packages for modeling protective relays [1].

Digital models of the protective relays offer an economic and reliable alternative in the analysis of relays performance and of the protection systems. At the same time, they permit the detailed analysis of the performance at the level of each internal module. Implementation of new algorithms is improved using modeling, which offers the possibility of settings and corrections, before testing the prototypes and launching the production itself. For specific problems, the use of the models offers the possibility of new solutions, if the usual configurations are not satisfactory.

II. DIGITAL PROTECTION RELAYS ARCHITECTURE

Fig. 1 depicts the block diagram of a digital protection relay.

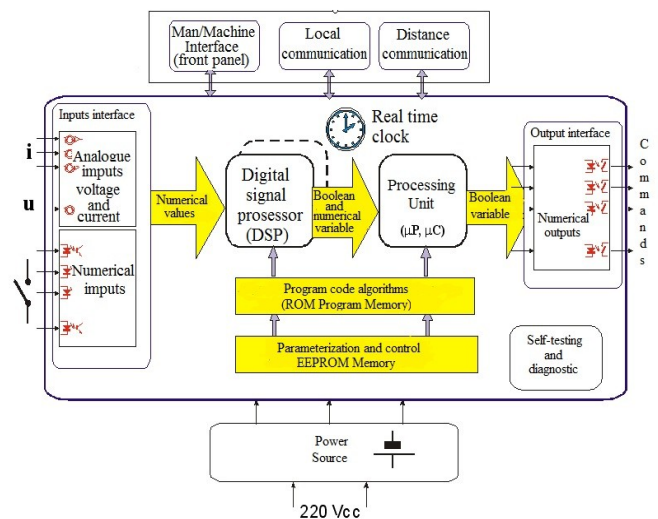


Fig. 1. Digital relays architecture.

The main parts of the digital relay are:

- intermediary current and voltage transformers, which take the values from the instrumentation transformers;
- analog-digital converters and memory circuits, storing the data to be processed;
- data processor, running the computational algorithm and survey the input values;

- central processing unit, that controls the logic sequences of the protection and provides the communication with the interface;
- interface, having digital input output circuits.

The digital relay detects any modification in the protected system, through terminals connected to the current and voltage transformers or from different monitored states through digital inputs. Data are processed in real time using a microprocessor, which, function of the data received, makes decisions and send control commands to the output interface and to the breakers, if tripping is needed. Digital relay settings are performed through communication ports, SCADA or other specific software of the relay. Algorithms, settings and recording performed by the microprocessor are stored in the memory of the digital relay.

III. CURRENT PROTECTION

The principle, consisting in the protection of the overcome of the limit values of the current, was the basis of the early protection systems. Starting from this basic principle, step maximum current protection systems have been developed. For an accurate operation of these relays, one must know the fault currents in each element of the grid [2].

The compulsory data for the relay settings are:

- the wiring diagram of the protected system, which consists of protection relays and the associated current transformers;
- the impedances of the system's elements (generators, transformers, transmission lines);
- minimum and maximum value of the short circuit currents in each protection location;
- starting currents of electric motors;
- maximum load current in each protection location;
- the decay curves of the fault current supplied by the generators;
- current transformers characteristics.

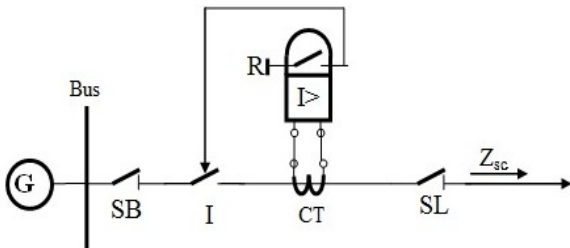


Fig. 2. Maximum current protection schematics.

The current relay setting must be checked for the maximum value of the short circuit current in the first instance. The reaction time must be minimum. Afterwards, the operation of the relay for minimum short circuit current must be checked. The reaction time must be satisfactory.

The wiring diagram of a maximum current protection for a radial network power system is depicted in Fig. 2, where the bus isolator is denoted by SB, the line isolator, by SL, the

breaker by I, the current transformer by TC and finally by I> the maximum current relay.

The main devices composing this protection system are the maximum current relays and the current transformers.

The tripping condition of the relay is

$$I_c > I_p \quad (1)$$

where I_c represents the current in the surveyed circuit and I_p the tripping value of the relay, relative to the primary winding of the current transformer. Note that this protection acts in a short circuit situation (instantaneous tripping with breaking) and doesn't fit for protection against overloads. The overload protection is also a current protection, but a delayed one. The delay is needed for discriminating between transient and permanent overloads, the overloads effects on the system's elements being delayed in time.

Fig. 3 depicts a schematic of overload protection using relays.

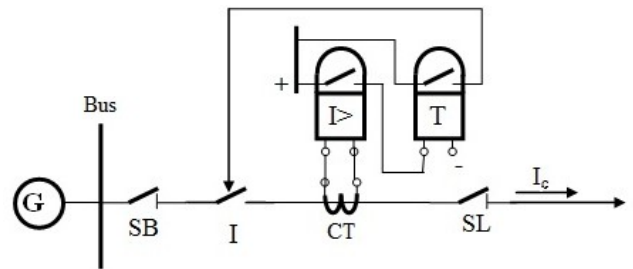


Fig. 3. Overload protection relay schematics.

Note that the contacts of the both relays, the maximum current relay I> and the time relay perform an logic AND function. Consequently, the tripping of the breaker appears only if the current in the circuit overcome the setted value I_p and the duration t_c exceeds the delay time t_p :

$$(I_c > I_p) \text{ and } (t_c > t_p) \quad (2)$$

Maximum current relays may present an independent characteristic curve, when the tripping time does not depend on the magnitude of the fault current, or a dependent one, when the tripping time depends on the magnitude of the surveyed circuit (which is a multiple of the set current). Consequently, this type of protection is characterized by the bellow features:

- the maximum current protection is the simplest and the cheapest protection (minimum number of components);
- the settings are pretentious and difficult to achieve in applications;
- readjustments and even relocating are needed in case of system's modifications.

Protection must be selective in order to isolate the faulty area, leaving unaffected the rest of the system. The protection device located nearest the faulty location must trip (i.e. the nearest fuse or breaker).

The correct coordination and the selectivity of the current protection may be achieved using several methods. The main

possibilities in achieving selectivity are based on the following discrimination methods:

- discrimination by time;
- discrimination by current;
- discrimination fault direction;
- discrimination by both time and direction;
- discrimination by both time and current.

IV. MODELING OF DIGITAL PROTECTION RELAYS

Relays models are used in designing new algorithms and prototypes and also in verifying and optimizing the relays performance already operating in power systems [4, 5, 6].

The manufacturers created relays models in order to assess their performances. The models are following the process, by replacing the input values in equation modeling the relays, in order to verify if the output values obtained are acceptable. The characteristics of the current protection relays represented the beginning of the modeling in this area. Mathematical models have been performed using algebraic equations in order to represent in current-time coordinates the overload relay characteristics. The first model of the operation in a transitory regime of a distance relay was developed using a nine order mathematical model in the state space of a “mho” element [3].

Simulation programs of transitory regime are software packages that simulate the transitions occurring in multiphase systems, their use being wide spread and unanimously accepted. They are power tools in study and analysis.

The current-time characteristic curve of a current relay is depicted in Fig. 4.

Curve A-B represents the time inverse characteristics of the relay and is used for high currents, larger than the rated values and lesser than the short circuit currents, but larger enough to determine the fault of certain equipment if they last a sufficient period of time.

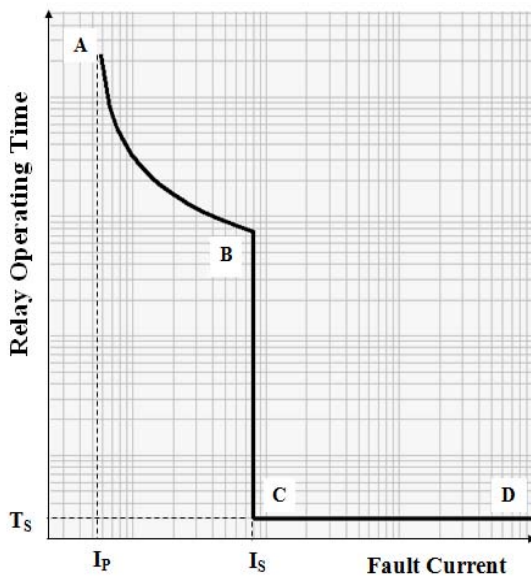


Fig. 4. The characteristics current-time of the relay.

Curve B-C-D is used for the instantaneous and fast clearing of the very large short circuit currents ($>I_s$), by reducing the tripping time to the value T_{di} .

The general shape of the inverse characteristics of an overload relay corresponds to equation 3:

$$T = \frac{K}{I_d^n - 1}; 1 < I_d < \frac{I_s}{I_p} \quad (3)$$

where T is the tripping time of the relay, I_d ($I_d = I_c/I_p$), the faulty normalized current set at the magnitude I_c , I_p the starting current of the tripping and I_s the short circuit current. K and n are constants denoting: K is the a constant depending on the relative operating time and n depending on the inverse time characteristics of the relay.

According to the values of these constants (standardized in IEC 255), the type of the relay's characteristics is determined (Table I).

TABLE I
THE VALUES OF THE CONSTANTS INVOLVED IN THE INVERSE TIME CHARACTERISTICS OF THE RELAY

No.	Types of characteristics	n	K
1.	standard inverse	0,02	0,14
2.	very inverse	1,00	13,50
3.	extremely inverse	2,00	80,00
4.	long time inverse	1,00	120,00

Equation (3) becomes in case of fault:

$$T = \frac{K}{I_d^n}; I_p < I_d < I_s \quad (4)$$

Choosing appropriate values for the constants n and K , any desired curve may be obtained. For the instantaneous portion of the relay curve, its tripping time is defined in relation (5):

$$T = T_{di}; I_c > I_s, \quad (5)$$

where T_{di} is the instantaneous tripping time.

Fig. 5 depicts the logic diagram of implementing the inverse current-time characteristics and Fig. 6 depicts the schematic diagram of the current protection tripping.

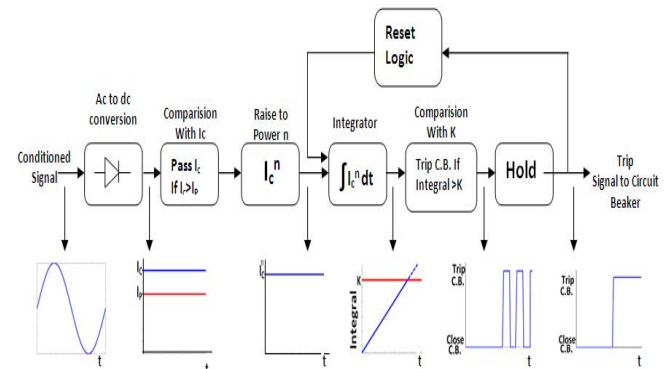


Fig. 5. The logic diagram for the implementation of the inverse current-time characteristics.

The rms value of each measured phase current is compared to the set magnitude of the tripping current.

If the rms value of one of the currents overcomes the set value a tripping command for the main breaker is made.

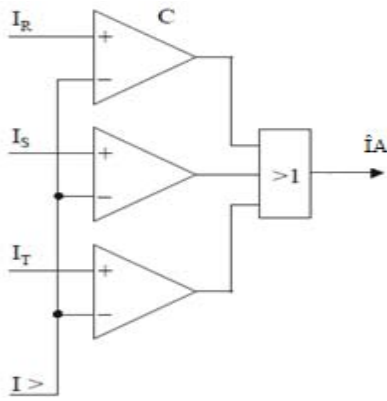


Fig. 6. Block diagram for the current protection tripping.

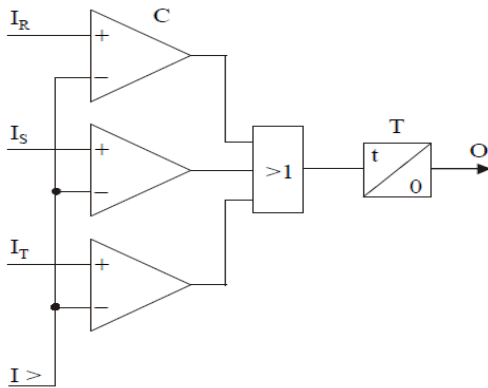


Fig. 7. Block diagram with delay.

In case of overload, the schematic diagram with delay, depicted in Fig. 7, is used. In this situation the tripping is performed only if the fault persists after the set delay time duration.

V. SIMULATION OF THE PROTECTION RELAY MODEL

Matlab is a high-level language and environment for numerical computation and statistical analysis, allowing matrix calculus, function visualization, development of algorithms, creating interfaces, enable to interact with different applications.

Matlab is a matrix/vector high level language which includes control loop instructions, functions, data structures, input/output commands and object oriented programming. Matlab permits both rapid programming of small scale applications and detailed programming in order to develop complex high level software. It contains additional packages, one of them being Simulink, an environment permitting several simulations. Dynamic systems can be easily simulated.

Simulink is a graphic environment offering a set of block libraries, permitting development, simulation, implementing and testing different time variable systems.

Every module is interconnected with the others through exchange variables, representing subsystems inputs/outputs. The input data of the system's elements are included in m-

files. In order to run a simulation, the m-file is executed first; afterwards the information is loaded in a workspace. Afterwards the model simulation is performed.

Simulink is a software package used in modeling, simulating and analyzing dynamic systems, for linear, nonlinear, continuous or discrete and hybrid systems, having several sampling periods. It provides a graphical user interface (GUI) for creating models as diagrams built up of blocks, using the click-and-drag technique. Therefore, drawing diagrams is simple and intuitive. Moreover the thorough and tedious mathematical formulation is avoided.

At the same time, Simulink offers a vast library of sources, loads, linear and nonlinear components, connectors, etc. that permit drawing diagrams and building user's specific blocks.

Once the model created, simulation could be performed using different integration methods from the Simulink menus or Matlab commands. Using oscilloscope type blocks or other different display devices one can observe the results even during the simulation process. At the same time the values of the parameters may be modified in order to observe immediately their effects. The results can be exported in the Matlab workspace for future manipulations or visualizations. Fig. 8 presents the Simulink library.

Simulink offers also advanced integration and functions analysis algorithms which provide quick and accurate simulation results, e.g.:

- seven integration methods
- interactive simulation with real time display of results
- Monte-Carlo type simulations
- stability calculation
- linearization

The open architecture of Simulink permits the extent of the simulation environment, i.e.:

- build up of special blocks and block libraries having specific icons, interfacing with the user through Matlab, Fortran or C;
- combining Fortran and C programs in order to take over the already validated models;
- generation of a C code using Simulink models with the optional generator C code of Simulink.

The implementation of the protection relay was performed using Matlab/Simulink. There were considered several blocks for every main component of the relay. Besides, particular blocks for the different types of protections of the digital relay have been built up.

Fig. 9 depicts the block diagram of the implement of the microprocessor for current protection.

One may see that from the power system, passing by the current transformer, the information is converted by the analog-digital converter. Afterwards the signal passes through a filter, and then into the block which calculates the peak current. In the relay logic the magnitude of the current is compared with the set value, the result of the comparison being the tripping decision in case of fault in the system.

The metering block of the peak value of the current is depicted in Fig. 10, and in Fig. 11, the block diagram of the implementation of the instantaneous characteristics of the relay.

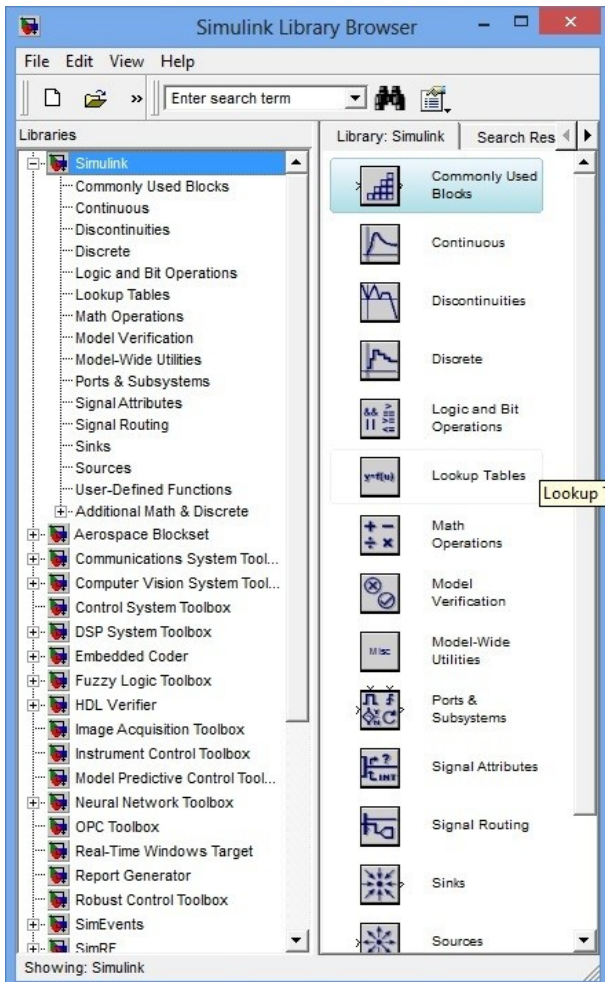


Fig. 8. Simulink library.

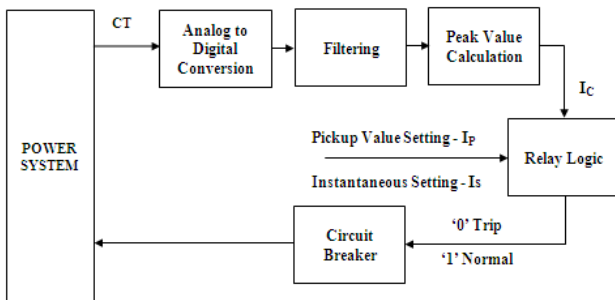


Fig. 9. Block diagram for the implementation of the current protection microprocessor.

The current I_c is compared to the set current I_s . If the magnitude of the current in the circuit is larger than the set value of the current a tripping command is transmitted, with a delay generated by the delay element.

If the magnitude of the current in the circuit is maintained larger than the set current for a time greater than the delay duration, the tripping command is transmitted to the power breaker.

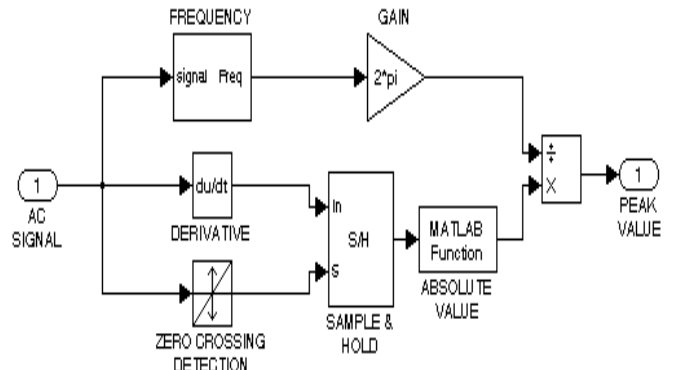


Fig. 10. Metering block of the peak value of the current.

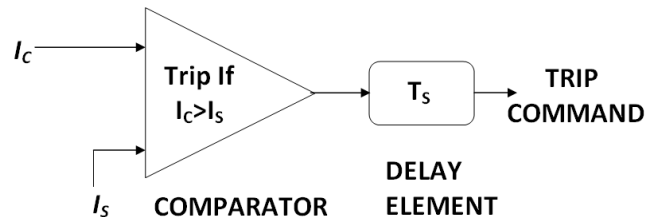


Fig. 11. Block diagram for the implementation of the instantaneous characteristics of the current.

Fig. 12 depicts the block diagram of the implementation of a current digital relay.

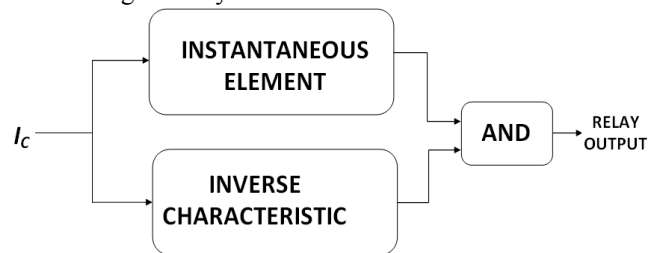


Fig. 12. Block diagram of the implementation of a digital current relay.

The simulation conditions have been set for a case study of mono-phase short circuit at a power of 0.75 kW, and the obtained waveform in the simulation process is depicted in Fig.13.

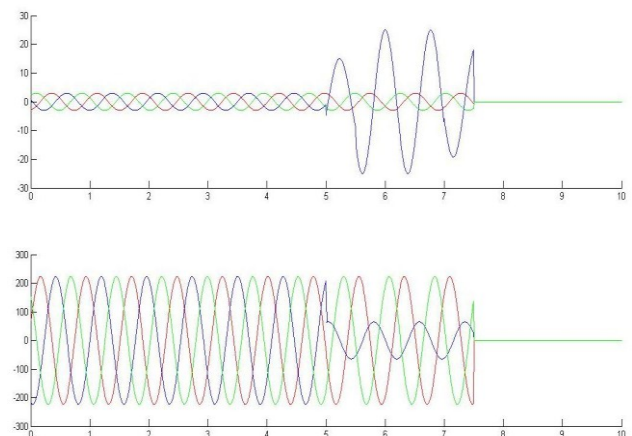


Fig. 13. Short circuit current's waveform.

VI. CONCLUSIONS

The results of the simulation were verified experimentally by generating the waveform transmitted to the relay in the conditions imposed by the simulations. As generator, Mentor 3V2I equipment was used and the recorded values are depicted in Fig. 14.

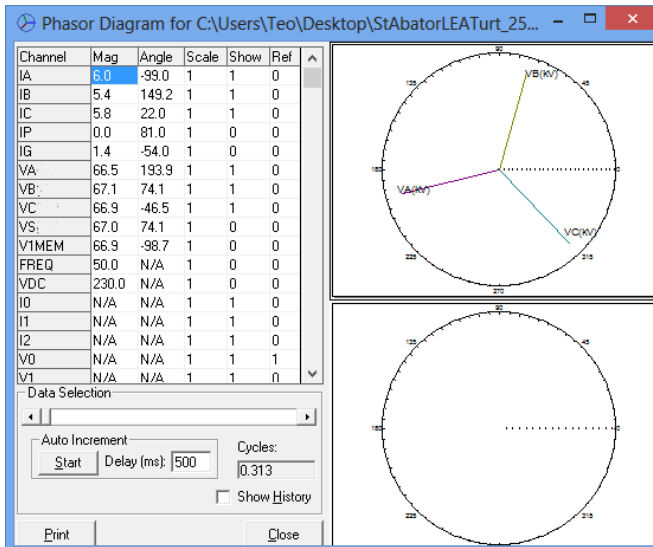


Fig. 14. Recorded values of the voltage and the current

It is important to notice that the shortcircuit on phase B leads to the sudden increase of the current. Using the data recorded of the digital relay, using an appropriate software package a harmonic analysis of the voltage and current may be performed.

The results obtained after simulation and experimental tests being very close, draw to the conclusion that the simulated model is validated.

REFERENCES

- [1] Q.H. Wu · Z. Lu · T.Y. Ji, *Protective Relaying of Power Systems Using Mathematical Morphology*, Springer-Verlag London Limited, ISBN 978-1-84882-499-7, 2009.
- [2] J. L. Blackburn, T. J. Domin, *Protective Relaying - Principles and Applications*, Taylor & Francis Group, LLC, ISBN 978-1-57444-716-3, 2007.
- [3] A. F. Sleva, *Protective Relay Principles*, Taylor & Francis Group, LLC, ISBN 978-0-8247-5372-6, 2009.
- [4] D. G. Dumitrascu, F. Balasoiu, H. Balan, S. Gadola, "How Can Synchrophasors Improve the Romanian Network Operation", *Protection, Automation & Control World Conference 2012*, 25-26 June 2012, Budapest, Hungary, paper ID: OPO 46, On CD.
- [5] Dumitrascu Daniel-George, Balan Horia-Cornel, "Using Artificial Neural Networks for the Detection of Power System Oscillations", *Acta Electrotehnica*, volume 54, number 5, pg. 179-184, ISSN 1841- 3323, Ed. Mediamira Science Publisher, Cluj-Napoca, 2013.
- [6] Dumitrascu Daniel-George, Hosu Ciprian, Barburas Ioan, Petrovan Tudor, Balan Horia-Cornel, "Synchrophasors Used for Islanding Detection – A Real Case Study", *Acta Electrotehnica*, volume 54, number 5, pg. 185-189, ISSN 1841- 3323, Ed. Mediamira Science Publisher, Cluj-Napoca, 2013.

Buck-Boost Corrector Implementing for Compact Fluorescent Lamp Applications

P.D. Teodosescu¹, M. Bojan¹, A.A. Pop¹, R. Marschalko¹
¹Technical University of Cluj-Napoca, Faculty of Electrical Engineering
400114 - Cluj-Napoca, Memorandumului Street, No.28, Romania
E-mail: petre.teodosescu@edr.utcluj.ro

Abstract-This research paper presents a method to improve the power factor of a compact fluorescent lamp through the deployment of a buck-boost pre-converter which operates at a fixed frequency and duty cycle. The used buck-boost pre-converter is a classic one switch topology characterized by reverse output voltage. This type of active power factor correction seems to have many advantages upon the classic boost PFC. The possibility to have a smaller or a greater voltage level than the input value, makes this type of topology a good option for a common half-bridge self oscillating CFL ballast. The results obtained following the use of the above-mentioned pre-converter are being analyzed through computer simulation as well as practical measurements.

I. INTRODUCTION

The Compact fluorescent lamp (CFL) represents a device that could be a good successor of the classical incandescent light bulb. By understanding the new trends in energy efficiency, the incandescent bulb is not coping with a good overall efficiency that the actual standards require. CFL represents a better option for Edison type bulbs because of the energy saving and longer lifetime but also presents some negative aspects when compared to the classical bulb. So it has a 4-5 times smaller energy consumption, an 8-10 times bigger functioning time period, while the output lighting energy is the same. It also presents some negative aspects such as a higher cost, a poor light quality for low cost devices (often found on east European countries). Another important disadvantage [1],[2],[3] that will be highlighted in this paper is the poor power factor and input current high harmonic distortion of this type of lighting device. As shown in [4], the good quality CFL has a power factor no more than 0.6 while the total harmonic distortion factor (THD) is higher than 70%.

II. ACTIVE POWER FACTOR CONVERTERS

Commonly, for active power factor correction classical buck, boost, buck-boost converters can be used. Depending on the control method, these converters could work in either continuous conduction mode (CCM) or discontinuous conduction mode (DCM).

In order to analyze the performances for these types of converters under power factor correction function, we need to highlight the way the converter receives the energy and the

way this energy is brought to the output. These 3 topologies use an inductor as temporary energy storage.

For the buck and boost converters [5],[6] as shown in (1) and (2), in order to obtain a resistive behavior, we need to have an input voltage a lot bigger than the output voltage for the buck topology and an output voltage a lot bigger than the input voltage for the boost topology. From (3) it can be easily seen that the buck-boost topology is the best solution because the input current is not depending on the output signal.

$$I_{in(Buck)} = \frac{D^2 T}{2L} (U_{in} - U_{out})$$
$$\Rightarrow R_{in(Buck)} \approx \frac{2L}{D^2 T} \text{ if } U_{in} \gg U_{out} \quad (1)$$

$$I_{in(Boost)} = \frac{D^2 T}{2L} \left(\frac{U_{in} U_{out}}{U_{out} - U_{in}} \right)$$
$$\Rightarrow R_{in(Boost)} \approx \frac{2L}{D^2 T} \text{ if } U_{in} \ll U_{out} \quad (2)$$

$$I_{in(Buck-Boost)} = \frac{D^2 T}{2L} U_{in} \Rightarrow R_{in(Buck-Boost)} = \frac{2L}{D^2 T} \quad (3)$$

Where: I_{in}, U_{in}, R_{in} - input current, voltage and resistance; I_{out}, U_{out} - output current and voltage; D -duty cycle; T -period; L -coil inductance.

III. POWER FACTOR CORRECTION FOR CFL BALLAST

For the CFL ballast associated with the fluorescent tube, seen as a load, the increase of the power factor and also limiting the input line harmonics could be done with quite good results with passive filters [9],[10] and with active methods [11]. In most cases, when an active power factor correction has been applied for a CFL lighting device the usual solution was to implement a boost preconverter. The ballasts that are suitable for this type of action were controlled by a dedicated IC as presented in Fig.1.

After analyzing some CFL electronic schematics of the most commonly found models on the market, the topology of the electronic ballast was the self-oscillating half-bridge

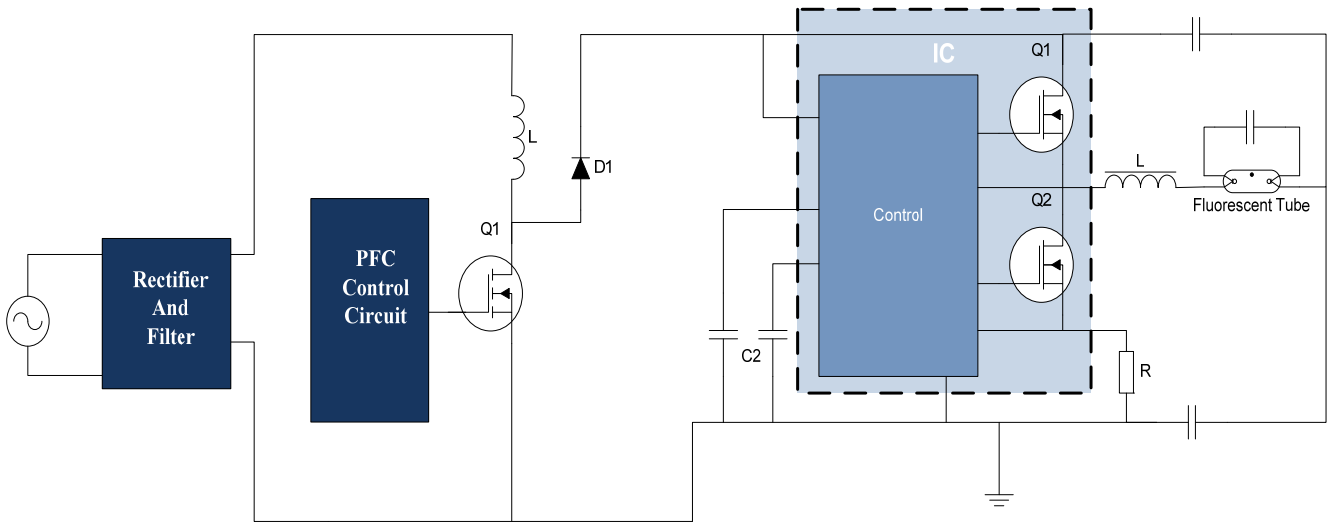


Fig. 1. Boost PFC for a IC controlled CFL ballast

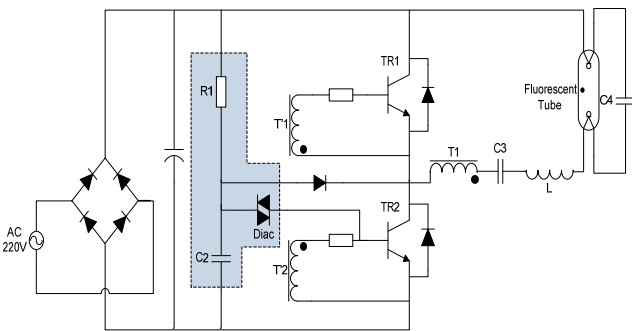


Fig. 2. Self-oscillating half-bridge CFL ballast

ballast presented in Fig.2. For manufactures this seems to be the best solution, all this because is a simple configuration and this affects the cost in a positive way. Besides this advantage it seems that this topology has passed the time test (over 10 years of presence on the market) which means that the industry has plenty of experience in this field and the lighting devices are at the optimum in terms of efficiency and expected lifetime.

It is well known that the boost topology converter, according to the name, has the particularity that the output voltage is bigger than the input voltage. The power factor correction with the help of the boost converter can be easily applied on the IC controlled CFL ballasts, but for the commonly found ballast that has a self-oscillating half-bridge topology this type of action is not the best solution because of the output voltage of near 400V. Usually, self-oscillation half-bridge ballast is working with an input voltage around 200V.

In order to make this ballast to work under 400V, some modifications of the schematics and electronic components need to be made at the inverter level so that it could work under this new condition. This modification could affect the level of performance and maturity of the technology that the

industry has achieved for this type of device. Under these considerations, in this paper we propose a method that can improve the power factor without affecting by any means the good performance and reliability achieved for this device in years of research. This could be possible if the inverter performances and parameters are not modified. This is done by using the original configuration of the inverter circuit associated with a DC voltage around 200V.

IV. BUCK-BOOST PFC FOR A CFL

In this paper we will focus on the implementation of the new way of active power factor correction by using a buck-boost preconverter applied on classic self-oscillating half-bridge CFL ballast as presented in the electronic schematic in Fig. 3.

The buck-boost topology converter has the particularity to have an output voltage lower or higher than the input voltage. This advantage could be well suited for our application where it can be programmed to have an output voltage around 200V. By using this topology it is possible to generate the optimal voltage for the inverter.

In terms of power factor improving capabilities from (3) the buck-boost topology is an interesting solution because of the total separation of the load from the power supply. This means that we can extract energy from the input line in a linear way with the help of the buck-boost converter and transfer it as needed to the load. The working principle for the preconverter is in DCM, which leads to a bigger EMI input filter.

If we can consider that the sub-assembly inverter-fluorescent tube is acting like a constant load (not having dimming capabilities) this makes the control circuit of the buck-boost converter to be very simple with constant frequency and duty cycle. If the performances of the lighting

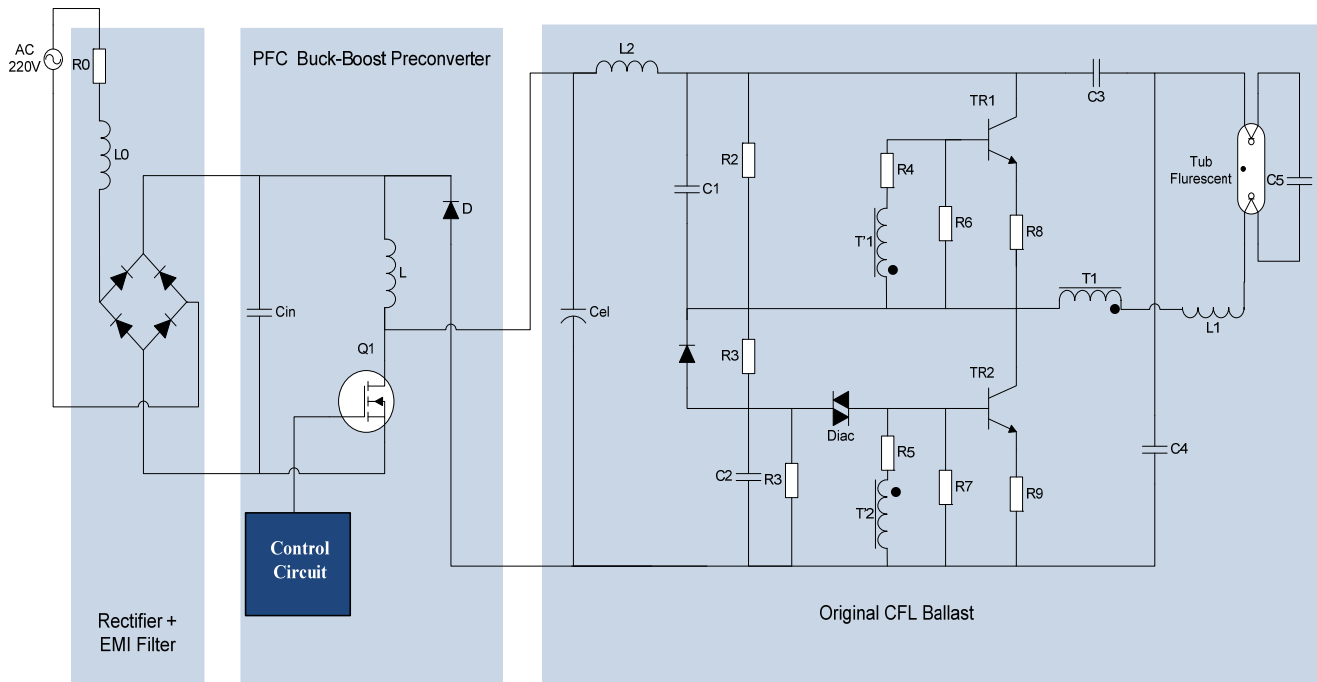


Fig. 3. Buck-boost PFC pre-converter in series with self-oscillating half-bridge CFL ballast

device need to be higher, then a PWM control could be applied for dimming capabilities.

In this paper the main goal is to transform this lighting device in a line-friendly one, with good power factor and low level of the input current harmonics. The performances of the CFL lighting system will be presented by means of practical experiments and software Orcad/PSpice simulations.

V. PARAMETER CALCULATION OF THE BUCK-BOOST PRECONVERTER

For implementing the presented solution we need to establish the level and the functioning limitations of the new electronic components introduced. In order to obtain a voltage around 200V at the output level of the buck-boost preconverter, the calculation is concerning the duty-cycle of the control circuit. Also, in order to obtain a good performance in terms of power factor correction, the working principle is based on DCM. The electronic components of the original inverter are kept the same, while some input considerations are taken into account like:

1. Working frequency of the preconverter will be 57KHz
2. The coil L will have a inductivity of 0.5mH
3. Input voltage of 230V
4. Output voltage of the buck-boost preconverter and also the input voltage of the inverter is 200V
5. To establish the output load R_S for the preconverter the equivalent impedance will be calculated around the proposed resistive behavior of the sub-assembly inverter-florescent tube [7].

From [8] the duty cycle and related time of conduction of the transistor Q is calculated for a Buck-Boost topology converter working in DCM with the help of the following expressions:

$$U_{out} = -U_{in} \frac{D}{\sqrt{\frac{2L}{R_S T_S}}} \quad T_S = \frac{1}{f}; \quad D = \frac{T_{on}}{T_s} \quad (4)$$

In order to choose the coil L, the transistor Q and the diode D, in terms of power handling the most important parameter is the maximum current during a commutation period:

$$I_{max} = DT_S \frac{U_{in}}{L} \quad (5)$$

The maximum current computed was 1.1A and the duty cycle was set to 14%.

VI. ORCAD/PSPICE SIMULATION AND EXPERIMENTING OF THE OVERALL SYSTEM

Under the calculation carried out in the previous chapter, an ORCAD/PSPICE model and an experimental test bench have been implemented in order to highlight the good performances in terms of improving the power factor that could be achieved using this type of solution. The analyzed performances of the overall system are divided into 3 categories:

1. The analyses of the working performances of the buck-boost converter.

2. The analyses of the electrical parameters of the unmodified sub-assembly inverter-fluorescent tube.
3. The analyses of the input behavior of the CFL lighting system.

In the first stage in Fig.4 and Fig 5 we present the working performances of the buck-boost preconverter working with a special load represented by the inverter –fluorescent tube sub-assembly. The practical measurement and simulated results obtained could conclude the fact that the model is performing like the experimental one.

The analysed electric parameters are:

- U_C - control voltage of transistor Q1
- U_{DS} - Transistor Q1drne-source voltage
- I_{Q1} - Transistor Q1current
- I_D - Diode D current
- I_L - Inductor L current
- U_D - Diode D commutation voltage

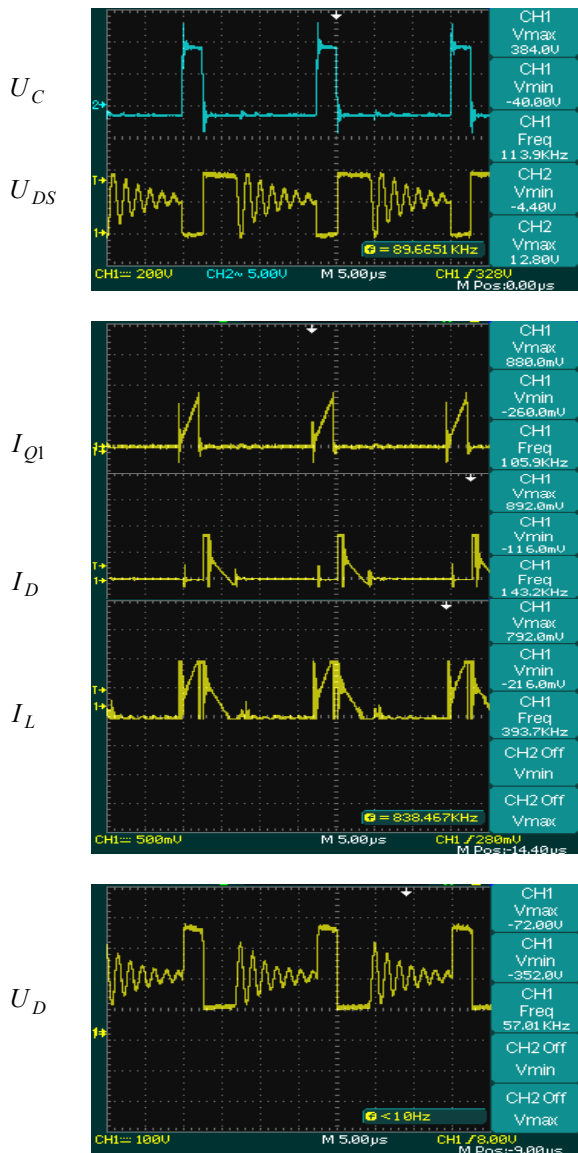


Fig. 4. Measured results for the buck-boost preconverter used for active power factor correction of CFL ballast.

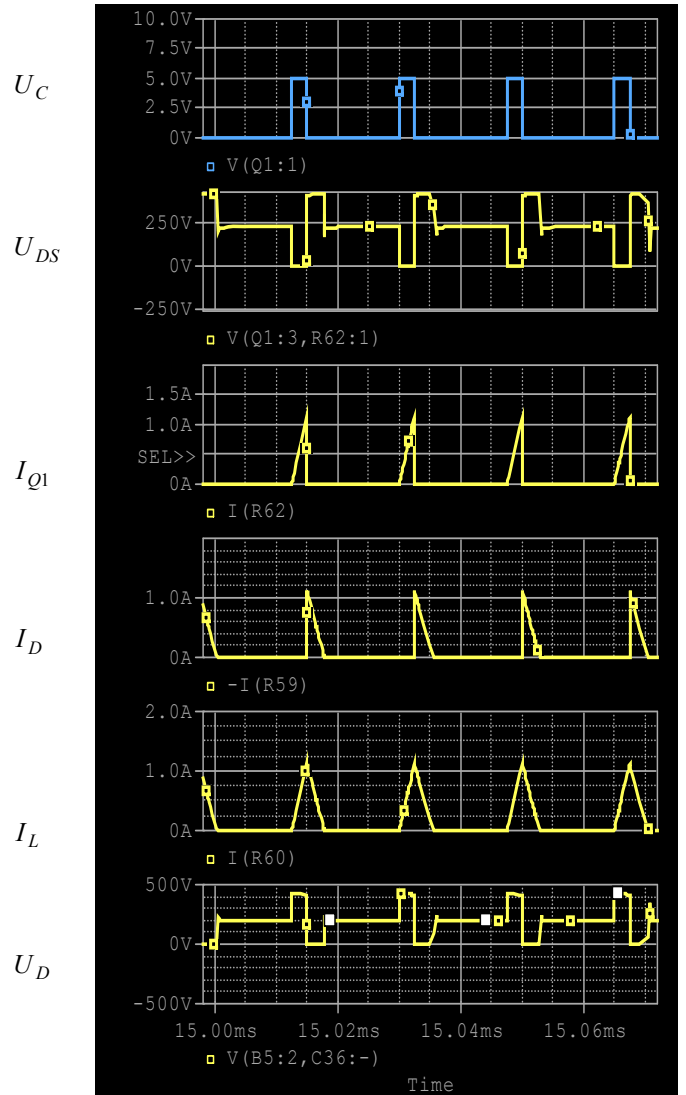


Fig. 5. Orcad/PSpice simulated results for the buck-boost preconverter used for active power factor correction of CFL ballast.

The steady state waveforms obtained with the help of practical measurements and software simulations highlight the typical behavior of this type of converter for DCM. By analyzing the waveform of the transistor drain current we observe that it has a linear increase during the period when the transistor is open, while on the period when it is blocked the current falls almost instantaneous to zero. At this moment begins the second stage when the energy captured in the magnetic circuit of the inductor L is laid out to the load with the help of the diode D. This aspect could be observed on the diode current waveform. The inductor L will behave like a temporarily energy storage device, accumulating energy when the transistor is opened and is outputting the energy when transistor is blocked. Because the energy transfer supports two stages of transformation from electric energy to magnetic energy, a small part of the energy is lost in the form of heat and this aspect is decreasing the efficiency of the system. For the simulated results in the waveform of the

inductor current this power loss is not present because of the ideal components being used.

The control circuit of the transistor Q1 consists of a well known 555 IC based oscillator circuit that delivers an rectangular impulse at a fixed frequency and constant duty cycle. This rectangular signal is the control signal U_c of the Q1 transistor. The schematics of this circuit are not presented because it is a well know path.

In the second stage of analyzing the behavior of the proposed lighting system, we will focus on the electric parameters of the inverter and fluorescent tube. This is very important so that we can observe if the implementation of the buck-boost PFC is affecting by any means the performances of the original circuit. The most important parameters that show this are the inverter working frequency, the fluorescent tube current value and ripple and also the tube voltage, as shown in Fig 6.

This representation indicates that the inverter working frequency is around 56 kHz while for the original circuit it was 57 kHz. The crest factor of the fluorescent tube current for the circuit with buck-boost system is 1.43, compared to 1.5 for the original circuit. We can conclude in this stage that the implementation of the buck-boost preconverter is not negatively affecting by any means the good performances of

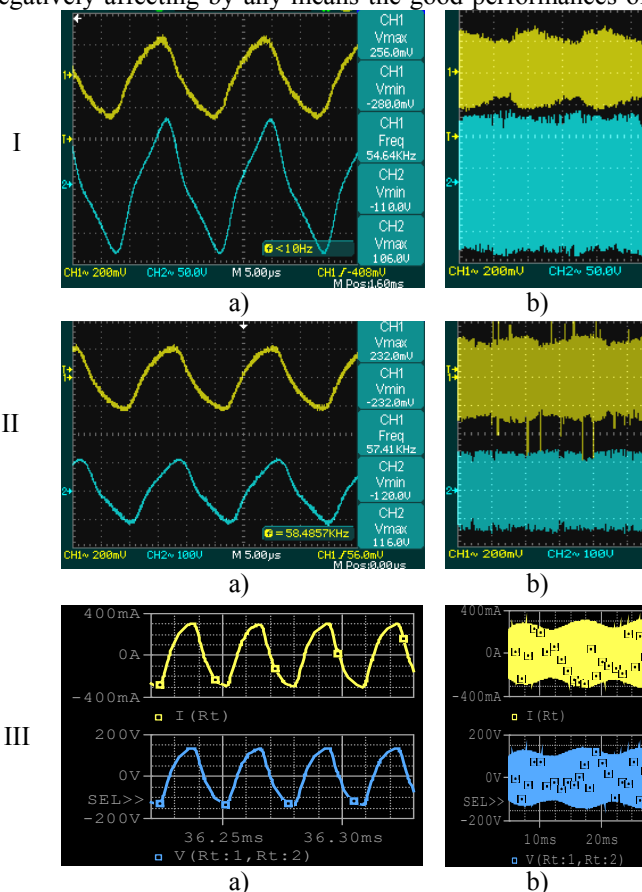


Fig. 6. Fluorescent tube current and voltage waveforms; a) High frequency current (yellow) and voltage (blue); b) Low frequency tube current and voltage ripple

- I) Measured results for the original circuit.
- II) Measured results for the circuit with buck-boost PFC preconverter.
- III) Orcad/PSpice simulated results for the circuit with buck-boost PFC preconverter.

the original circuit, even more it is decreasing the tube current ripple. This could have a positive effect on the expected working lifetime.

In Fig. 7 and Fig. 8 are presented, by simulated results, that the inverter input voltage with the buck-boost PFC has the same effective value as the inverter input voltages for the original circuit.

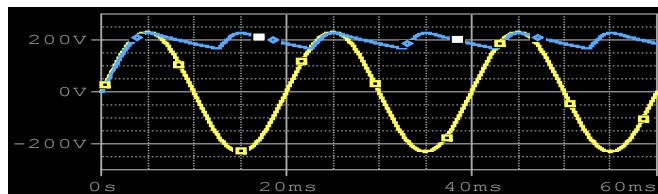


Fig. 7. Original CFL ballast input voltage (yellow) and inverter input voltage (blue)

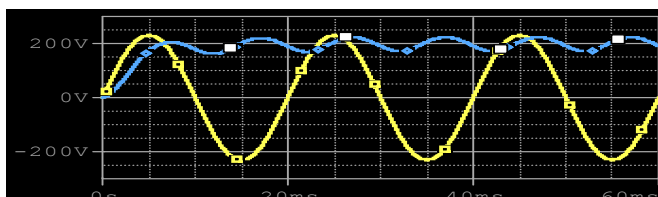


Fig. 8. CFL ballast with Buck-boost preconverter input voltage (yellow) and inverter input voltage (blue).

The last analyzing stage (Fig.9) will be focused on the impact of the buck-boost PFC implementation, on the behavior of this system in terms of power factor and line harmonics. The main objective of this paper was to transform the CFL non-linear load into a line friendly device. All in all we will analyze the power factor and total harmonics distortions of the proposed system from Fig.3, which is composed by the input filter, rectifier, buck-boost PFC, original inverter and fluorescent tube.

For the proposed circuit the input voltage is the reference

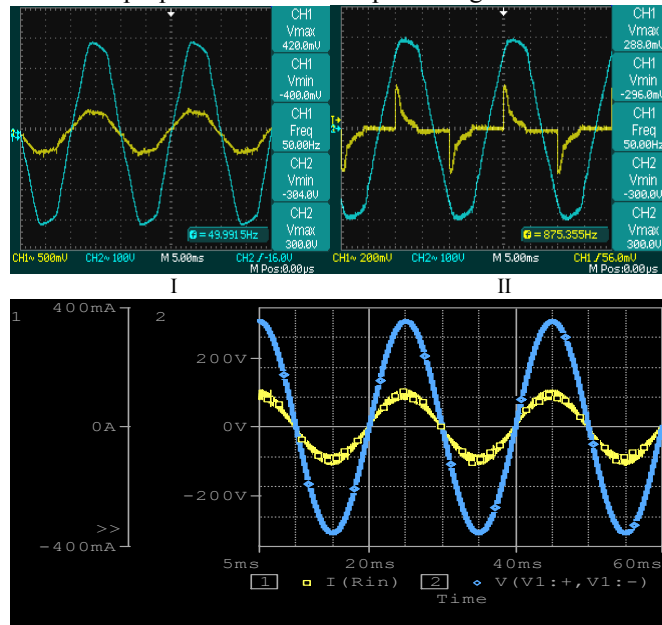


Fig. 9. Input current and voltage; I) Results for the electronic ballast with buck-boost PFC circuit; Measurements results; II) Results for the original CFL electronic ballast; Measurements results; III) Results for the electronic ballast with buck-boost PFC circuit; Orcad/PSpice simulated results .

signal. If the waveform of the input voltage is distorted, the input current will also be distorted. If the voltage is closer to a sinusoidal waveform also, the THD of the input current will be closer to 0.

The input current for the original circuit and for the proposed solution has been studied through Fourier analysis with the help of the Orcad/PSpice models (Fig. 10) and practical measurements (Fig.11).

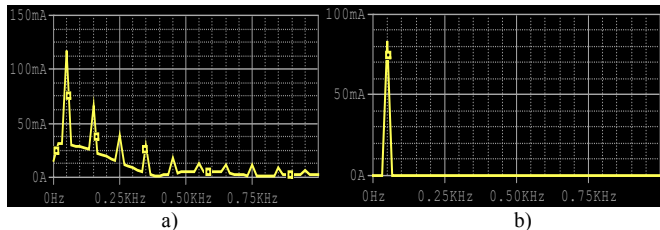


Fig. 10. Fourier analyses of the input current; a) Original circuit; b) Original circuit with Buck-Boost PFC.

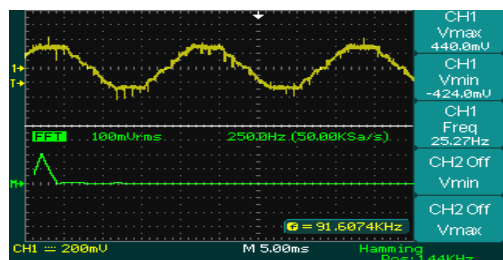


Fig. 11. Fourier analyses of the input current for the electronic ballast with buck-boost preconverter. Practical measurements.

The results confirm that the proposed circuit has a THD not more than 2.18% compared to 79.40% for the original circuit. The power factor computed was 0.99 while the measured one was near unity.

VII. CONCLUSION

In this paper we proposed a solution to improve the power factor of electronic ballast mainly used in compact fluorescent lamps by implementing a buck-boost PFC. This solution is one with great potential, in terms of power factor correction. The proposed circuit has a low complexity and low number of added electronic components which leads to a low cost of implementation. This aspect is one of great importance because in order to have a good solution for real market implementation, the cost component is very important and it needs to be as low as possible.

The results obtained for the input behavior of this solution are presenting this device as a linear one so, the power line is sensing this as a simple resistive load. This lighting device does not inject high frequency current harmonics in the grid and as a result we can consider this type of CFL a good replacement for the incandescent lamp with well know advantages, such as low energy consumption and long expected lifetime.

In Table 1 we illustrate a comparative analysis of the overall efficiency for different types of active power factor correction strategies applied on self-oscillating half-bridge CFL ballast.

TABLE I

Circuit	Overall efficiency
Ballast with IC (L6562) controlled Boost converter	86.3%
Ballast with Boost converter with simple control (fixed frequency, fixed duty cycle)	77.7%
Proposed Buck-Boost circuit	83.8%

The disadvantages of this circuit are the lower efficiency because of using two stages and the buck-boost topology. Also, it is characterized by a bigger complexity compared to the original circuit and presents a higher implementation cost. These disadvantages could be negligible compared to the negative effect of millions of these nonlinear loads on the power grid when the incandescent bulbs will be totally rejected from the market (2015). Because of the fast growing number of the small new nonlinear electrical and electronic equipments, in the near future we could have new legislative limitations also for these type of loads (<25W). Last but not least, this solution could be also fitted in the existing CFL Edison type enclosure.

ACKNOWLEDGMENT

This paper was supported by the project "Doctoral studies in engineering sciences for developing the knowledge based society-SIDOC" contract no. POSDRU/88/1.5/S/60078 project co-funded from European Social Fund through Sectorial Operational Program Human Resources 2007-2013.

REFERENCES

- [1] R.I. Sasaki, "The impact of electronic ballast compact fluorescent lighting on power distribution systems", Purdue University School of Electrical Engineering.
- [2] National Electrical Manufacturers Association, "Power Quality Implications of Compact Fluorescent Lamps in Residences", April 16, 1999.
- [3] F Giezendanner, J. Biela, J.W. Kolar, S Zudrell-Koch, "EMI Noise Prediction for Electronic Ballasts"
- [4] P. D. Teodosescu, M. Bojan, I.C. Vese, R.Marschalko "Study of the improvement of a CFL's power factor by using a valley fill filter, Acta Electrotehnica, Mediamira Science Publisher, Cluj, Vol. 53, No. 1, pp.74-80, 2012.
- [5] C.K. Tse, "Circuit theory of power factor correction in switching converters", International Journal of Circuit Theory and Applications, Volume 31, Page(5): 157-198, 2003.
- [6] Kübrich, D., Schmid, M., Dürbaum, T." A fast calculation tool for the design of PFC converters-method and application", Proceedings of the 32nd Annual Conference of the IEEE Industrial Electronics Society, 2005, 6-10 Nov. 2005, Page(s): 6 pp.
- [7] E. D. Edward, "Negative incremental impedance of fluorescent lamps", California Institute of Technology, 1995
- [8] Texas Instruments, "Understanding Buck-Boost Power Stages in Switchmode Power Supplies", Application Report, March 1999
- [9] P.N. Wood, "Fluorescent Ballast Design Using Passive P.F.C. and Crest Factor Control", International Rectifier Corporation
- [10] C. Contenti, P. Green, T. Ribarich, "A new Circuit for Low-Cost Electronic Ballast Passive Valley Fill with additional Control Circuits for Low Total Harmonic Distortion and Low Crest Factor", International Rectifier, Application Note AN-1074, 2004
- [11] ST semiconductors, "Electronic ballast with PFC using L6574 and L6561", Application note AN993, July 2009.

Insulation Resistance Testing Procedures

Antoniu TURCU

Electroenergetica si Managment
Technical University of Cluj-Napoca
Cluj-Napoca, Romania
antoniu.turcu@eps.utcluj.ro

Adrian Augustin POP

Electrical Machines
Technical University of Cluj-Napoca
Cluj-Napoca, Romania
augustin.pop@mae.utcluj.ro

Horia BALAN

Electroenergetica si Managment
Technical University of Cluj-Napoca
Cluj-Napoca, Romania
horia.balan@eps.utcluj.ro

Silviu STEFANESCU

Electroenergetica si Managment
Technical University of Cluj-Napoca
Cluj-Napoca, Romania
Silviu.Stefanescu@eps.utcluj.ro

Abstract—This paper refers to the testing procedures regarding the insulation resistance. The factors that have a negative influence upon the insulation resistance will be analyzed as well as the principles of the measurement of the insulation resistance. Through the process software Tera-Link, the tester used for experimental determinations Metrel MI 3200 TeraOhm 10kV emphasis the insulation resistance parameters of the tested equipment. The Metrel MI 3200 TeraOhm 10kV equipment, from the Electrical Equipment lab of the Technical University in Cluj-Napoca, allows taking the following tests and determinations for the electrical equipments insulation: determining the insulation resistance through the “spot reading” method, determining the „polarization index” (PI), through the „absorption test” procedure, determining the „dielectric absorption ratio” (DAR), the possibility of taking the dielectric discharge test and the possibility of measuring the insulation resistance tests with step voltage method. It is very interesting to notice the facility of portable equipment of the MI 3200 tester, the fast completion of the testing operations and the ease in interpreting results with Tera-link software.

Keywords—insulation resistance, absorption test, polarized index

I. INTRODUCTION

Before taking a decision about the tests which are made on the electrical equipment's, to detect the electrical faults, must be studied the reasons which conduct to these faults. Is important to know the insulation class, the insulation aging process and typical failure scenarios. Only then can decide over the tests which are made and if the high voltage test can be used.

The insulation represent the constructive part of electrical equipment's that separate conductive pathways at different potential, and the insulation material can be solid, liquid or gaseous, and, also, the vacuum. Without a perfect insulation, a given current is drained through the insulation. This current [1] can have low values, but represent the basic element which must be determined in attempts of insulation testing's. The

insulation is chosen as a design phase all the way as to withstand the life of the equipment, producer guaranteed, but should be considered the electrical equipment's are degraded over time because of different voltages between current ways, reducing the equipment service time. Must be mentioned that the electrical equipment's functional abnormal situations and which have the consequence an accelerate aging process, reduce the insulation lifetime. From that reason, a good practice suppose the insulation periodically tests, which identify the appearance of aging process, the cause of this phenomenon, followed to identify the necessary measurements to remedy.

The electrical equipment insulation system consists in ground insulation, the insulation between phases and the insulation between turns. Weakest link of insulation system is often the insulation between turns, if these exist in electrical equipment's. For an appropriate test of insulation system, must be made the different tests. The ground insulation can be tested with a Mega-Ohmmeter, in order to determine the insulation resistance values and to perform the polarization index test to evaluate the insulation elasticity. Also, must be performed a high continuous voltage test, to determine the insulation dielectric resistance [9] until the default level. The insulation between phases can be tested using one of the known methods and if the electrical equipment in disconnected. In most predictive maintenance scenarios, the complete disconnection of electric engine is not possible and the insulation between phases must be tested in the same way like the insulation between turns, with an overvoltage test. Are important to know the contributing factors to the insulation resistance deterioration, namely:

- *Contamination*: chemical deposit on the power lines, which cause the insulation damage;
- *The mechanical factors*: vibrations of actuators, which damage the insulation system;
- *The normal aging*: insulation time deterioration;

- *The premature aging* caused by the excessive temperatures, which leads to insulation damage;
- *Overvoltage spikes* lightning or caused by the static convertors.

All of the mentioned factors can be considered which building up a testing program. Usually, is considered a normal thermal process of insulation aging and the modality through the insulation aging is influenced by the mechanical factors, premature aging and overvoltage.

The insulation resistance testing principles taking account that the testing must be made without damaging insulation. During the test, must be considered the following principles:

- Testing voltage must be applied and gradually discharged. Therefore, applying and discharging of voltage steps must be realized with reasonable slopes;

- If through the test is applying a high voltage, the insulation gaps will be electrostatically charged. In situation which the equipment is suddenly reconnected to the supply system, can occur penetrations because of charged gaps. If even the insulation not failed, the time life of this is reduced. To avoid this situation, the testing equipment must realize the electrostatically load discharge to the final of the test sample, in a time period from 1 to 5 of insulation test time;

- The Testing cables must be in good condition;
- The measurement equipment's must be in the checking period;

- During the test, the wire guard and the testing cables do not touch. Also, the tested equipment must not be pressed in any way by the tester;

- The testing cables must not touch each other or with other equipment's, because these touches create supplementary leakages;

- To equipment's that shows sharp metallic accessories, they must be removed before testing, to avoid the Corona leakage;

- The tested equipment's used plugs must be specially built, to avoid the unwanted leakages between plugs;

- For precision measurements, should use wire guard;
- The testing sequences should follow the testing procedure;

- For tested equipment discharge should use the standard sticks from epoxide resin;

- After the test, all the values must be corrected for 20°C. Tables of correction factors or field rule of thumb may be used that the insulation resistance will halve for each 10°C rise and vice versa for apparatus containing immersed oil insulations. For apparatus containing solid insulations, the insulation resistance will halve for every 15°C rise in temperature and vice versa. In oil-immersed transformers, temperature of the top oil and in dry type transformers, ambient temperature is taken as the insulation temperature;

- The humidity will not affect, in generally, the insulation resistance, excepting the case which temperature is very low, near by the dew point, and form condensation on or in insulation.

II. THE INSULATION RESISTANCE TESTING PRINCIPLES

According with Ohm's Law, the current does not depending on time, but, a simple insulation resistance

measurement will show the current-time dependence. The reasons of this dependence are determined by the various phenomena which occurring after applying a voltage in the insulator. An insulation model is presented in figure no. 1:

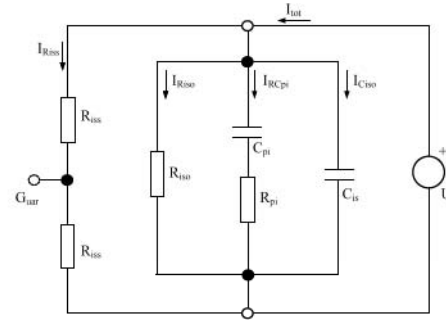


Fig. 1. The insulation model

where:

U – applied testing voltage;

R_{iss1} and R_{iss2} : leakage surface resistance;

R_{iso} : insulation resistance;

C_{iso} : insulation capacitance;

R_{pi} : polarization resistance;

C_{pi} : polarization capacitance.

The total current I_{tot} it consists of 4 components:

I_{Riss} : the leakage current on the surface;

I_{Riso} : the current through the insulation;

I_{Rcpi} : the absorbed polarization current;

I_{Ciso} : the capacitive charging current.

The leakage current on the surface I_{Riss} move to the insulation surface between the voltage applying points, causing an error in the insulation resistance measurement and can be limited using the guard terminal. As shown in the figure no. 1, this current passes the R_{iss1} and R_{iss2} resistors and does not depend on time.

$$I_{Riss} = \frac{U}{R_{iss1} + R_{iss2}} \quad (1)$$

The insulation leakage current I_{Riso} flow through the insulation, which presents the R_{iso} resistance (Fig. 1.) and has no dependence on time:

$$I_{Riso} = \frac{U}{R_{iso}} \quad (2)$$

The absorbed polarization current I_{Rcpi} is capacitor loading current C_{pi} . Initially, the capacitor is discharged, and the current has the U/R_{pi} initial value. Capacitor begins to charge and loading current decrease. At the final, the capacitor is fully loaded and the loading current is cancelled. The absorbed polarization current depends by the time, as shown from the next relation:

$$I_{Rcpi} = \frac{U}{R_{pi}} \cdot e^{-\frac{t}{R_{pi} \cdot C_{pi}}} \quad (3)$$

The other currents could distort the absorbed polarization current, so, the polarization current measurement can be problematic.

Often is easy to measure the opposite process: dielectric discharge. In this case, the measurement begins with the C_{pi} load capacitor. The connection cables are short-circuited and are measuring the depolarization current.

The $I_{C_{iso}}$ capacitive current load the C_{iso} capacitor which represents the capacity between the connected to the entrance plugs of the measuring instruments which are separated with tested insulation. $I_{C_{iso}}$ is limited only by the instrument internal resistance.

$$I_{C_{iso}} = \frac{U}{R_{int}} \cdot e^{-\frac{t}{R_{int} \cdot C_{isc}}} \quad (4)$$

where R_{int} is supply internal resistance and with this, the I_{tot} total current is:

$$I_{tot} = I_{R_{iss}} + I_{R_{iso}} + I_{RC_{pi}} + I_{C_{iso}} \quad (5)$$

Figure no. 2 present the current diagram based on the standard insulation model:

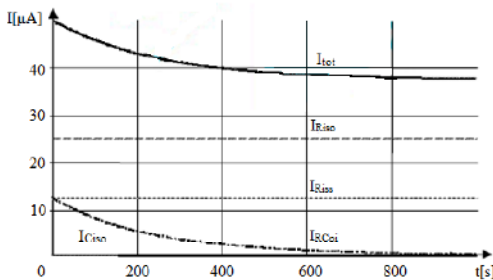


Fig. 2. The current diagram for an ideal voltage source

III. INSULATION TESTING PROCEDURES

To determine the insulation characteristics it was developed the various testing methods. Diagnostic insulation DC tests electrically simulate the insulation and measure the response. Dependent upon that response, we can draw some conclusions about the condition of insulation. These tests are:

- Spot Test;
- Time-Resistance Test such as: Polarization Index (PI) and Dielectric Absorption Ratio (DAR);
- Step Voltage Test;
- Discharge based Tests such as: Dielectric Discharge Test, EDA Test and Isothermal Relaxation Current Test (IRC Test);
- DC High Potential Test;
- Surge Test.

The „spot reading” testing method is the simplest and quickest insulation resistance determination method. Using this method can be qualitatively determined how good or how bad is the insulation. In this testing method, the measuring

instrument is connected along of tested instrument insulation. A test voltage is applied for a period of time. Usually, reading is made after 1 minute, as shown in the figure no. 3.

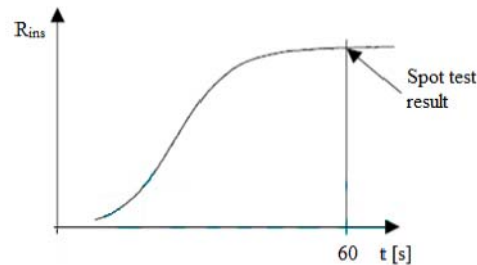


Fig. 3. Resistance-time diagram for „Spot reading” testing method

This testing method can be used when the insulation temperature is bigger than dew-point temperature. The insulation temperature is a very important measure because the reading can be corrected function of working temperature. Tested insulation working temperature is, usually, bigger than ambient temperature and, for the safety reasons, the resistance must be corrected function of working temperature. Resistance corrected readings must be recorded in a database to be compared during the time. Dust and humidity determine a decrease of insulation resistance. A sudden decrease of insulation resistance indicates the equipment damage, because of insulation. As has been mentioned, this method offer general information's about the insulation resistance. A simple and efficient method to establish the inferior limit of insulation resistance is the „mega-ohm” procedure. Under this procedure, the insulation resistance must be at least $1M\Omega$ for each kV of operation voltage, but not less than $1M\Omega$. for instance, a motor with 5kV nominal voltage should have minimum resistance equal with $5M\Omega$. An inappropriate insulation causes a decrease of R_{iso} resistance and the growth through the insulation of $I_{R_{iso}}$ current. The absorption current is lower, relative with leakage current, which have an approximately constant value. Insulation resistance is lower. (Figure no. 4). A good insulation will result a continuous increasing of insulation resistance for a period of time. This thing is determined by the absorption and is highlighted in figure no. 4. The absorption effect is much higher than the required time for insulation capacitance loading.

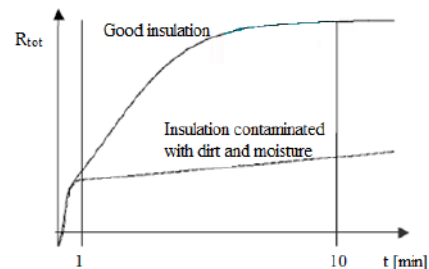


Fig. 4. Time diagram for an appropriate and an inappropriate insulation

Obtained results through this method not depend on temperature and offer the conclusive results without comparing results with those previously. The measuring making with this

method not offer the data about insulation resistance but only the report between two different readings. The temperature influence is the same for both of measuring's; therefore the temperature has no effect over the results. This method is known named "absorption test" and the measuring results is "polarization index".

„Polarization index" (PI) is defined as a ratio between two resistances, measured in two different moments. The frequent ratio is 10 minute to 1 minute, for insulation resistance continuous measurement, but this ratio is not a rule

$$PI = \frac{R_{tot}(10 \text{ min})}{R_{tot}(1 \text{ min})} \quad (5)$$

An appropriate insulation present a low leakage current and the total current decrease slowly. Therefore the appropriate insulation polarization index is big. A damaged insulation has a low polarization index, because the leakage current is higher and constant. The general values of polarization index are presented in Table I.

TABLE I. POLARIZATION INDEX SPECIFIC VALUES

PI	Tested material status
1 to 1,5	Unacceptable (old type of insulations)
2 to 4 (usually 3)	Good insulation (old types)
4 (very high insulation resistance)	Good insulation (new types)

The polarization index measurement is useful to test the old insulation types, like soaked oil paper, when the measured resistance at one minute with previous method is relatively small. If the insulation resistance measured at one minute is bigger than 5000 MΩ then the polarization index may not be considered. „Dielectric absorption ratio" (DAR) is similar with polarization index, the only one difference being the reading results time period. Periods are shorter and first results are obtained at 30 s and the second at 1 min.

$$DAR = \frac{R_{tot}(1 \text{ min})}{R_{tot}(30s)} \quad (6)$$

General values for dielectrically discharge are presented in Table II.

TABLE II. DAR INDEX SPECIFIC VALUES

DAR	Tested material status
<1	Damage insulation
1 ≤ DAR ≤ 1.25	Acceptable insulation
>1.4	Very good insulation

When the polarization index for an ordinary insulation is 2 or smaller even for new materials, can be used the DAR test. The minimum value required for DAR index is 1.25, while for PI index, minimum value is 2. Another used method is insulation resistance measuring with step voltage steps. As shown from figure no. 2 and 3, the insulation resistance is not

depending by the voltage. Practically, the insulation resistance depends by the testing voltage. Testing the insulation, with much smaller than nominal voltage, often the measuring results are influenced by the humidity and dust, while the aging effects are mechanical damage or a clean and dry insulation cannot be determined on low voltage. The local defects influence is reduced to low voltage, but their influence growth quickly in the same time with test voltage growth. This thing is indicated by the rapid decreasing of insulation resistance. Measuring through voltage steps is relatively simple. The tested apparatus is subjected to different voltage steps. Is starting with the lowest voltage level and is growing with some good defined steps until the highest voltage level. Figure no. 5 present a testing example in 5 steps with equal time periods. Recommended ratio for this testing type is 1 to 5. For each step, the test voltage should be applied to the same period, usually 60 seconds. The measuring result is a curve which show the resistance dependence reported to the testing voltage.

The curve form shows the insulation quality:

- the damage insulation resistance will decrease quickly;
- a good insulation will have an approximately constant resistance for every voltage steps.

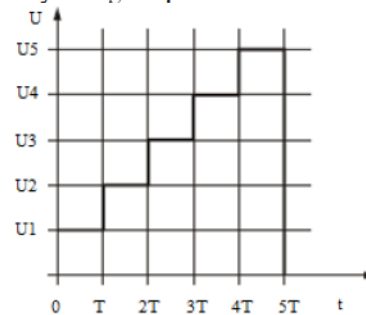


Fig. 5. Typically measuring method with voltage steps

The increased voltage test is one of the based tests, used for insulation resistance diagnose. The principle is the simple one: the increased voltage is applied to the tested apparatus for a certain period of time or to the insulation damage (Figure no. 7). The voltage growth grade, the maximum voltage and applying time of maximum voltage are very important and depend by the tested apparatus type. These parameters are defined in standards. The insulation damage is indicated by the suddenly growth of current over the predefined limits.

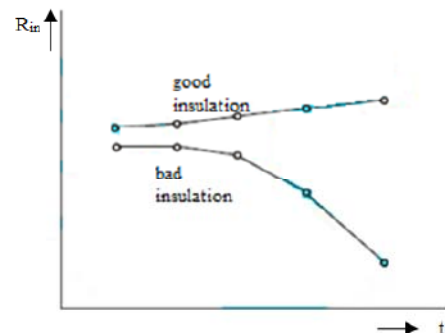


Fig. 6. Voltage steps method typically results.

The curve form shows the insulation quality:

- the damage insulation resistance will decrease quickly;

- a good insulation will have an approximately constant resistance for every voltage steps. The increased voltage test is one of the based tests, used for insulation resistance diagnose. The principle is the simple one: the increased voltage is applied to the tested apparatus for a certain period of time or to the insulation damage (Figure no. 7). The voltage growth grade, the maximum voltage and applying time of maximum voltage are very important and depend by the tested apparatus type. These parameters are defined in standards. The insulation damage is indicated by the suddenly growth of current over the predefined limits.

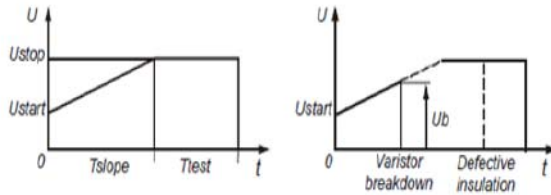


Fig. 7. Increase voltage method measuring procedure

This procedure can be made through two methods:

First procedure consists in voltage maintaining voltage for a predefined period of time. The tested apparatus must resist to this voltage without insulation to yield. In this case, the voltage slope up must be small enough to prevent the damage of insulation. Testing time with a predefined voltage is usually 1 minute and from 2 seconds until 10 seconds for routine tests. Testing the breakdown voltage of a voltage suppressor. This test is similar with the first one, except that the voltage test increases until the tested object deterioration. The nominal voltage of a more voltage suppressors is defined like being corresponding in volt-ammeter characteristics for a 1mA threshold current.

IV. EXPERIMENTAL DETERMINATIONS

The measurements was made for three cables, with $U_n=220kV$, with 300 m aproximative length, according with PE 114 normative.

In Table III are presented the step voltage measuring results on the R phase. Although steps have been set from 2 kV up to 0 kV, as you can see, the voltage was not increase more than 2727 V. Must be mention that the measurements

was performed between the cable shield and grounding ring which supports are connected by cables that have been laid.

TABLE III. MEASURING RESULTS ON THE R PHASE

001	STEP VOLTAGE	$R > 10.0 T\Omega m$ $U = 2536 V$ $I = 0.06 mA$ $C = 80.3 nF$ $E(U_{n1}) = 18.7 G\Omega m$ $E(U_{n2}) > 4.0 T\Omega m$ $E(U_{n3}) = 4.25 G\Omega m$ $E(U_{n4}) = 11.8 G\Omega m$ $E(U_{n5}) > 10.0 T\Omega m$	$U_n = 10000 V$ timer = 05min00s $U1 = 2000 V$ $U2 = 4000 V$ $U3 = 6000 V$ $U4 = 9000 V$ $U5 = 10 kV$	07.Sep.2010 15:50
		$U1 = 2057 V$ $U2 = 2511 V$ $U3 = 2727 V$ $U4 = 2485 V$ $U5 = 2536 V$		

As shown in Table IV, insulation resistance at 10 kV could not be measured because $U = 4758 V$ voltage and $I = 4.32 mA$ current through insulation, was produced the insulation saturation phenomenon, measured resistance at this voltage being $R = 1.1 M\Omega$.

TABLE IV. VOLTAGE AND CURENT VALUES FOR SATURATION PHENOMENON

002	INSULATION RESISTANCE	$R = 1.10 M\Omega m$ $U = 4758 V$ $I = 4.32 mA$ $C =$ $D_{max} =$ $R_{min} =$	$U_n = 10000 V$ timer = 01min59s	07.Sep.2010 15:54

In Table V are presented the increased voltage measuring results on the three phases. As can be seen, the 10 kV voltages could not be reached on any phases even if the trigger current it was set from 3 (on the R phase) to 5mA.

According with PE114 normative, the 10 kV voltage maintaining time had to be 1 minute, but was impossible because around 7500V was produced the breakdown on every phase.

TABLE V. THE INCREASED VOLTAGE ON THE PHASES

		WITHSTANDING VOLTAGE	$U = 7672 V$ $I = 1.526 mA$	$U_{nstart} = 2000 V$ $U_{nstop} = 10000 V$ $T_{trig} = 3.000 mA$ $T_{step} = 00min02s$ $T_{end} = 01min00s$ $T_{reax} = 00min00s$	07.Sep.2010 16:11
R					
R		WITHSTANDING VOLTAGE	$U = 7946 V$ $I = 3.427 mA$	$U_{nstart} = 2000 V$ $U_{nstop} = 10000 V$ $T_{trig} = 5.000 mA$ $T_{step} = 00min01s$ $T_{end} = 05min00s$ $T_{reax} = 00min00s$	07.Sep.2010 16:24
S		WITHSTANDING VOLTAGE	$U = 7622 V$ $I = 2.633 mA$	$U_{nstart} = 2000 V$ $U_{nstop} = 10000 V$ $T_{trig} = 5.000 mA$ $T_{step} = 00min01s$ $T_{end} = 05min00s$ $T_{reax} = 00min00s$	07.Sep.2010 16:31
T		WITHSTANDING VOLTAGE	$U = 7650 V$ $I = 3.352 mA$	$U_{nstart} = 2000 V$ $U_{nstop} = 10000 V$ $T_{trig} = 5.000 mA$ $T_{step} = 00min01s$ $T_{end} = 05min00s$ $T_{reax} = 00min00s$	07.Sep.2010 16:44

TABLE VI TEST REPORT FOR THREE CABLE MEASUREMENTS

n	Location	Function	Results	Parameters	Date Time
1	001	STEP VOLTAGE	R > 10.0 T0hm U = 2326 V I = 0.00 mA C = 80.2 nF R(Jrn1) = 18.7 G0hm R(Jrn2) > 4.0 T0hm R(Jrn3) = 4.25 G0hm R(Jrn4) = 11.8 G0hm R(Jrn5) > 10.0 T0hm U1 = 2097 V U2 = 2511 V U3 = 2727 V U4 = 2485 V U5 = 2526 V	Un = 10000 V timer = 0.5min00s U1 = 2000 V U2 = 4000 V U3 = 6000 V U4 = 8000 V U5 = 10 kV	07.Sep.2010 15:50
2	002	INSULATION RESISTANCE	R = 1.10 M0hm U = 4758 V I = 4.32 mA C = _____ Pmax = _____ Pmin = _____	Un = 10000 V timer = 0.1min59s	07.Sep.2010 15:54
3	003	STEP VOLTAGE	R = 720 k0hm U = 3122 V I = 4.31 mA C = _____ R(Jrn1) = 3.75 G0hm R(Jrn2) = 3.90 G0hm R(Jrn3) = 3.25 G0hm R(Jrn4) = 559 k0hm R(Jrn5) = 720 k0hm U1 = 2092 V U2 = 4182 V U3 = 6313 V U4 = 2459 V U5 = 3122 V	Un = 10000 V timer = 0.5min00s U1 = 2000 V U2 = 4000 V U3 = 6000 V U4 = 8000 V U5 = 10 kV	07.Sep.2010 16:01
4	004	WITHSTANDING VOLTAGE	U = 7672 V I = 1.525 mA	Unstart = 2000 V Unstop = 10000 V Trig = 3.000 mA Tstep = 0.0min02s Tend = 0.1min00s Tmeas = 0.0min00s	07.Sep.2010 16:11
5	005	WITHSTANDING VOLTAGE	U = 7946 V I = 3.427 mA	Unstart = 2000 V Unstop = 10000 V Trig = 5.000 mA Tstep = 0.0min01s Tend = 0.5min00s Tmeas = 0.0min00s	07.Sep.2010 16:24
6	006	WITHSTANDING VOLTAGE	U = 7622 V I = 2.833 mA	Unstart = 2000 V Unstop = 10000 V Trig = 5.000 mA Tstep = 0.0min01s Tend = 0.5min00s Tmeas = 0.0min00s	07.Sep.2010 16:31

V. CONCLUSIONS

The Metrel MI 3200 TeraOhm 10kV equipment, from the Electrical Equipment lab of the Technical University in Cluj-Napoca [7], allows taking the following tests and determinations for the electrical equipment's insulation:

- determining the insulation resistance through the "spot reading" method;
- determining the „polarization index” (PI), through the „absorption test” procedure;
- determining the „dielectric absorption ratio” (DAR);
- the possibility of taking the dielectric discharge test;
- the possibility of measuring the insulation resistance tests with step voltage method.

It is very interesting to notice the facility of portable equipment of the MI 3200 tester, the fast completion of the testing operations and the ease in interpreting results with Tera-link software.

Analyzing the measurements that were taken, presented in tables 3, 4 and 5, we notice:

- the insulation resistance determined through the spot reading method borders within the values imposed by the standards [8].

REFERENCES

- [1] M. Hanif, "Principles and Applications of Insulation Testing with DC", IEP-SAC Journal 2004-2005, pp. 53-67.
- [2] *** Metrel, *Guide for Modern Insulation Testing* Version 1.1, Code No. 20 750 784, Horjul, Slovenia, 2008;
- [3] Schump, David E., *Predict Motor Failure with Insulation Testing*, Plant Engineering Magazine, September, 1996;
- [4] Zotos, Peter A., Member IEEE, *Motor Failures Due to Steep Front Switching Surges: The Need for Surge Protection User's Experience*, "IEEE Transactions on Industrial Applications, Volume 30, Number 6, Nov/Dec 1994;
- [5] *** Metrel, TeraOhm 10kV MI 3200 *User Manual* Version 2.2 Code No. 20 751 097;
- [6] PE 116-94 Normativ de incercari si masuratori la echipamente si instalatii electrice;
- [7] Balan H., Buzdugan M., Munteanu A. R., Botezan A., Cozonici I., Avram V., Karaisas P., "Insulation Resistance Testing of the Medium Voltage Switches" *Annals of the University of Craiova*, No. 34, 2010, Vol. I, ISSN 1842-4805, pg. 142-147.
- [8] IEEE 43-2000: Recommended Practice for Testing Insulation Resistance of Rotating;
- [9] Rodica Creț, Laura Dărăbant, Turcu A.C., *Dielectrici și materiale magnetice*, Editura Mediamira, Cluj-Napoca, 2008, ISBN 978-973-713-204-8

Monitoring 110/10kV Power Stations. A Case Study

Traian VARODI, Horia BALAN

Power Engineering and Management
Technical University of Cluj-Napoca
Cluj-Napoca, Romania

tvarodi@gmail.com, horia.balan@eps.utcluj.ro

Adrian Augustin POP

Electrical Machines and Drives
Technical University of Cluj-Napoca
Cluj-Napoca, Romania

augustin.pop@mae.utcluj.ro

Abstract—The paper presents an earthing fault situation followed by a short circuit of the underground electric lines that is fed from a transformer station 110/10 kV, monitored by a power quality analyzer Mavowatt 70. With this method an analysis of the time evolution can be made, highlighting the voltages variations in the bars of medium voltage in the transformer station during the failure situation.

Keywords—*earthing system, short circuit, wiring diagram*

I. INTRODUCTION

The continuity of power supply and quality assurance of electricity, especially for the energy produced by renewable sources [1, 2, 3] requires distributor (Electrica), to take measures to maintain the electricity supply parameters and to ensure the reliability of the electrical equipments in the national power grid system.

When referring to commutation equipments, we can say that the best reliable solution is the monitoring system. Currently, the utilisation of predictive maintenance for equipments diagnoses, instead of preventive maintenance is more suitable.

By short circuit we understand a connection with low impedance between two points of a circuit, which are normally at different voltages values.

If a short circuit occurs at a long distance from source, the short circuit current limitation is achieved by the short circuit equivalent impedance of the network.

Electrical devices commutation represents the largest class of electric devices which must ensure the switching functionality like “connection” and “disconnection” in the circuits where it is included in normal operating conditions and under fault conditions.

The communication in connection but especially in disconnection is usually followed by priming, burning and electrical arc suppression.

At disconnection, the electric arc leads to thermal stress, mainly on the contacts of electrical devices and on the elements of the extinguishing chamber, and also it leads to dielectric stress due to commutation overvoltages.

The above leads to the idea that the commutation equipments from transformer stations must be monitored. In the case of current short circuit appearance the monitoring system should provide the fastest possible disconnection so as

the current short circuit interrupted by the commutation equipments to be minimal.

Monitoring the parameters during failure is a particular problem and may lead to the analysis of the protections operation in order to detect the malfunctioning of power protections and switches.

The protection malfunctions and switches detection in case of electrical grid abnormal operation phenomena occurrence can affect the overall stability in a power system.

If not properly managed, these events can not be neglected as they may cause undesired operation at the occurrence of major disturbances in a transformer station.

II. THE COMPUTATION OF CURRENT SHORT CIRCUIT

In the electricity transport and distribution systems different types of short circuits can occur between the three phases and earth:

- earthing;
- short circuit between phases;
- three phase short circuit.

The first two types of short circuits are asymmetrical, and the third type could be placed in the symmetrical short circuit category.

The methods of calculating the equivalent impedance in low voltage networks, involves the following steps:

From the connection diagram, the schematic is made for each component and also its equivalent diagram (Fig. 1.) for a single-phase, for both symmetrical and asymmetrical short circuits.

Reporting the impedance at the fault location, in the situation where the diagrams include multi-levels voltage interlinked with transformers. All impedances refer to the same level of voltage, the line nominal voltage at short-circuit location. Impedance reporting at the fault location has as a purpose the determination of an equivalent circuit, powered from a single source. This reporting is made at the installation operating voltage, at the short-circuit place. Assuming a grid supplied by voltage U , in case of a short circuit in a point with the voltage U_d , the current short circuit produces phase Joule losses $P=U^2/R$, where R is the real resistance of grid. Reporting of the circuit elements and sources must preserve the dissipated power. At the grid voltage the power dissipation is $P=U^2/R$, this relation is equivalent to:

$$P = (U^2 \cdot U_d^2) / (R \cdot U_d^2) = U_d^2 / R, \quad (1)$$

where we can deduct the impedances reporting relation at the fault location;

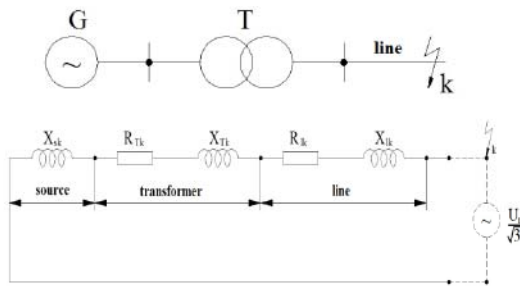


Fig. 1. Transformation through equivalent diagrams

To calculate the symmetrical and asymmetrical short circuit currents is necessary to determine the parameters elements that compose the equivalent diagram structure: electrical lines, transformers, reactance coils, synchronous machines, etc.

For three-phase systems with neutral conductor, in order to reduce the short circuit current, there are different ways of treating the neutral. The three-phase short circuit is symmetrical, the two-phase and single-phase short circuits are asymmetrical and they are calculated using the method of symmetrical components. For example, in the case of single-phase short-circuit with the neutral point connected to ground through the impedance Z_n , figure 2, the conditions at fault location are:

$$\underline{I}_1 = 0, \quad (2)$$

$$\underline{I}_2 = 0, \quad (3)$$

$$\underline{I}_3 = \underline{I}_n, \quad (4)$$

$$\underline{U}_3 = \underline{U}_n, \quad (5)$$

resulting:

$$\underline{I}_h + \underline{I}_d + \underline{I}_i = 0, \quad (6)$$

$$\underline{I}_h + a^2 \cdot \underline{I}_d + \underline{I}_i = 0, \quad (7)$$

$$\underline{I}_h + a \cdot \underline{I}_d + a^2 \cdot \underline{I}_i = 3\underline{I}_h, \quad (8)$$

$$\underline{U}_h + a \cdot \underline{U}_d + a^2 \cdot \underline{U}_i = 3 \cdot \underline{Z}_n \cdot \underline{I}_h, \quad (9)$$

Using the relations:

$$\underline{E}_1 = \underline{E}_d = \underline{Z}_d \cdot \underline{I}_d + \underline{U}_d, \quad (10)$$

$$\underline{E}_i = 0 = \underline{Z}_i \cdot \underline{I}_i, \quad (11)$$

$$\underline{E}_h = 0 = \underline{Z}_h \cdot \underline{I}_h + \underline{U}_h, \quad (12)$$

resulting:

$$\underline{I}_d = \frac{\underline{E}_1}{\underline{Z}_d + \underline{Z}_i + \underline{Z}_h}, \quad (13)$$

$$\underline{I}_h = a \cdot \underline{I}_d, \quad \underline{I}_i = \underline{I}_d \cdot \frac{1-a^2}{a-1}, \quad (14)$$

and the value of fault current is:

$$\underline{I}_3 = 3 \cdot \frac{\underline{E}_3}{\underline{Z}_0 + \underline{Z}_i + \underline{Z}_d}, \quad (15)$$

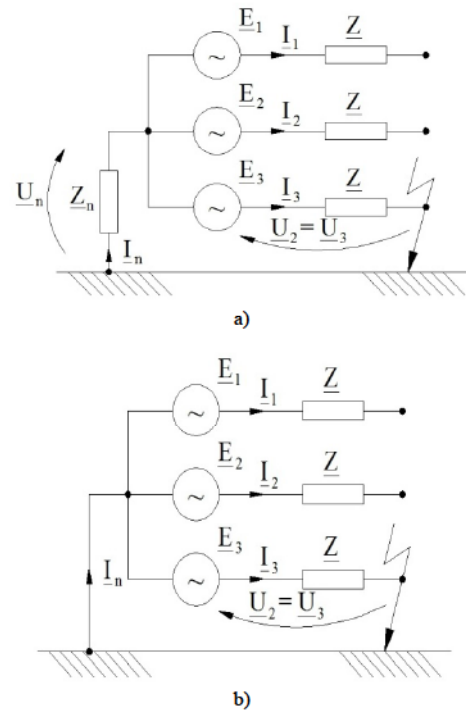


Fig. 2. One phase short circuit. a) the neutral earthed through the Z_n impedance, b) the neutral placed directly on ground.

If the neutral of the network is rigidly connected to the ground, assuming $\underline{Z}_n = 0$, the fault current is given by 1.37. and if we use the simplified hypothesis $\underline{Z}_d = \underline{Z}_h = \underline{Z}_i$ the current through the faulty phase is $\underline{I}_3 = \frac{\underline{E}_3}{\underline{Z}} = \frac{\underline{E}_1}{\underline{Z}}$, therefore identical value as in the case three phase short circuit.

III. THE COMPONENT OF TRANSFORMING STATION

The station where the case study was performed is a transformation station 110/10 kV, where is a 10 kV distribution in the area, made with double bar system and transversal coupling. 110 kV bar separators are CLP type. 10

kV line cells are provided with overcurrent protection and reserve, made either with classic relay or digital relay. In the transformation station on the 110KV bar, the current transformers are mounted, CESU type.

The station separators 110 kV -STE and STEP are manually controlled. IO switches- 110 kV with small quantity of oil for indoor and outdoor installations are constructed by interconnecting two extinguishing rooms. The V assembly is placed on a column composed of a 110 kV insulator. In stations the medium voltage switches utilized are IO 10-15-20/630, 1250, 2500, 4000, IUP - 25 and IUP-M10-20/630, 1000. These are opening and closing devices for high voltage circuits, in the presence of the working currents and automatic opening of these circuits in the moment of current overload occurrence with unacceptable values, as well as for short circuits cases. The switch must have a sufficient breaking capacity in order to interrupt high short-circuit currents in a short time interval. The separators which are used in the medium voltage station cells are inside separators of medium voltage- type TNS-10 and STIP-10. In medium voltage station, the CIRS, CIRTI, CIRTO or CESU current transformers are mounted. The neutral handling on medium voltage is made using extinguishing coils, and the transformer neutral is earthed through extinguishing coil. Suppression coils of capacitive currents are AC electric devices which provide inductive currents required to suppress the capacitive currents at failure location, when phase earthing defects appear.

The adjustment of suppression coil is made with the electric command and is executed after any connection or disconnection maneuver of an LES or after any change in the grid configuration.

The 110/10 kV station works in normal situation, with Transformer 1 operating on the 110 kV bar 2 and on the 10kV bar 2, Transformer 2 in reserve on 110 kV bar 2 and 10kV 2 bar, with the AAR canceled, the transversal coupling between 10KV bar 1 and 2 working. LES 10 kV is supplied from 10kV bar 2 from this station.

IV. EXPERIMENTAL MEASUREMENTS

The monitoring equipment, power quality analyzer Mavowatt 70 [4] is the element which has recorded the events succession in a single-phase earthing short circuit with events shown in Fig. 4, Fig. 5, Fig.6, and Fig. 7.

V. CONCLUSIONS

From the recorded oscillograms it can be noticed the amplitude-time characteristics of the voltages from the medium tension bars. Based on these results we can observe the evolution of the line and phase voltage in the very short period of appearance of the events that occurred in the medium voltage network supplied from the transformer station.

These defects are founded in the variation of the amplitude of phase and line voltage depending on time on medium voltage bars of the transformer station 110/10KV.

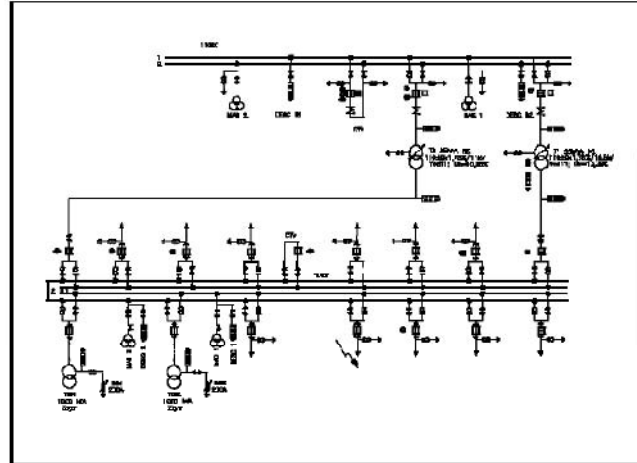


Fig. 3. Transforming station

From the phase voltage amplitude evolution on the medium voltage bars, the phase earthing failure moment can be observed. The phase belongs to a medium voltage underground line supplied from medium voltage bars.

Figure 4 highlights the earthing failure time of phase S at 18:12:33,65. The voltage amplitude of S phase drops below 2.5 KV, on R phase the amplitude reaches 14.3KV, and on T phase the voltage reaches 13.2KV.

In the time interval corresponding to phase S earthing the voltage values at 18:12:34 are shown in Table I:

Figure 6 highlights the fact that at 18:12:34, 04, after 39 ms, the S phase is isolated, while in the same time the earthing of T phase have been occurred. Further at 18:12:34 and 11 hundredths, after 7 ms the earthing of phase R appears. In this moment, the two phase short circuit appears and the effective voltage value of R of T phase reach below 2KV.

After another 24 ms (18:12:34 of 34 hundredths) three-phase short circuit occurs, as shown in Fig. 7.

The maximum short circuit current corresponds to a defect which is in the close proximity of downstream terminals of the protection device, and the short-circuit current of minimum value corresponds to a defect at the far end of the protected line.

TABLE I. VOLTAGE VALUES ACCORDING TO FIG. 5.

Voltage	R phase [KV]	S phase [KV]	T phase [KV]
Effective value	9,88	1,52	8,74
Peak value	14,56	3,96	13,55

In any case, the protection device must disconnect the defect within a time interval protecting the conductor in terms of thermal and dynamic stresses.

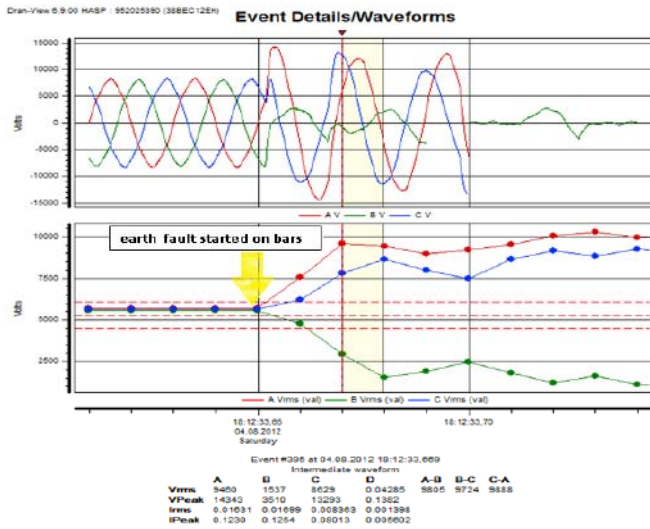


Fig. 4. Amplitude time characteristics of the phase voltages on medium voltage bars. S phase earthing.

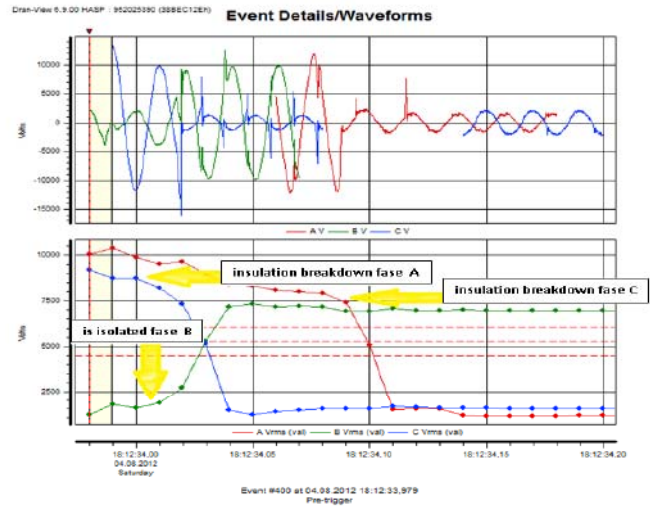


Fig. 6. Amplitude time characteristics of the phase voltages on medium voltage bars. R and T phase breakdown

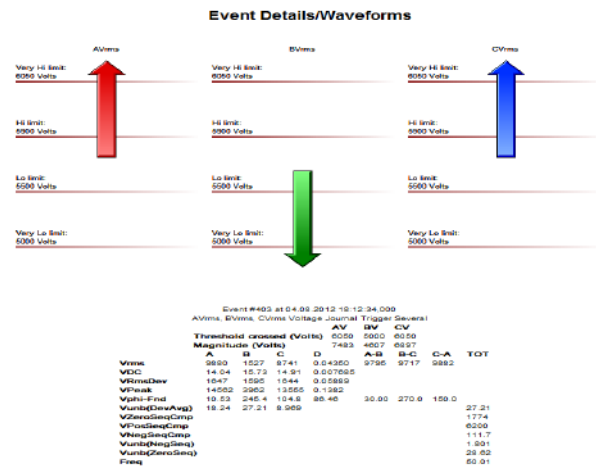


Fig. 5. Exceeding the established limits, set for the phase voltages

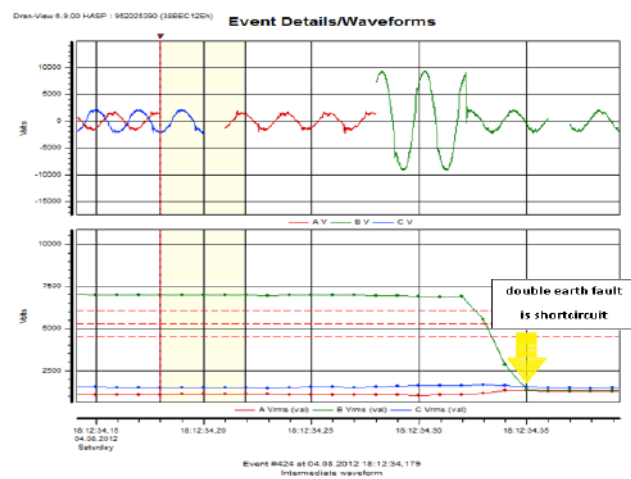


Fig. 7. Amplitude time characteristics of the phase voltages on medium voltage bars. Three phase short circuit appearance

REFERENCES

- [1] Florina Leach, Radu Adrian Munteanu, Ioan Vadan, Dan Capatana "A LabView Based Instrumentation System for Wind-Hidro Hybrid Power Rtation", The 14th Conference CAEE, Poznan, Poland, 20-22 April 2009, pp. 141-142, ISBN 978-83-89333-24-7.
- [2] Florina Leach, R. A. Munteanu, I. Vadan, D. Capatina, "Didactic Platform for the Study of Hibrid Wind-Hidro Power Plants", The 8th International Symposium Electromotion, Lille, France, 1-3 july 2009, paper ID OS 12, ISBN 978-2-915913-25-5.
- [3] Florina Cozorici, Ioan Vadan, Radu A. Munteanu, Ioan Cozorici, Petros Karaisas, "Design and Simulation of a Small Wind-Hydro Power Plant", ICCEP 2011 - International Conference on Clean Electrical Power, Ischia Italy, Jun 14-16, ISBN 978-1-4244-8929-9, pp 308-311.

Mavowat 70. User Manual

Reducing Short-Circuit Current in Continuous Voltage Networks Through Hybrid Commutation

Horia BALAN, Mircea BUZDUGAN, Adrian Augustin POP, Cristina CHIOREAN

Technical University of Cluj-Napoca

Cluj-Napoca, Romania

horia.balan@eps.utcluj.ro, mircea.buzdugan@insta.utcluj.ro, augustin.pop@mae.utcluj.ro, Cristina_chiorean@yahoo.com

Abstract— Continuity of the electric energy supply is chiefly affected by short circuits, which represent a very important issue in power systems, both in transmission and in distribution. A high value of the short circuit currents, exceeding the dynamic stability limits, may lead also to the damage of the commutation equipment and not only. Direct current grids are commonly used in electric tractions systems. The paper deals with typical problems encountered in classical circuit breakers, highlighting the mitigation of the short circuit current. Due to their high switching rate, solid state devices can be used for breaking short circuit currents at lower levels. An alternative, using hybrid switching in direct current grids is presented.

Keywords— *direct current breakers, zero crossing voltage switching, zero crossing current switching*

I. INTRODUCTION

It is well known that a short circuit represents a low impedance path, connecting two points of a grid, being normally at different voltages. If a short circuit occurs far from the source, the short circuit current limitation is due to the equivalent short circuit impedance of the grid. Near-to-generator, the stator reaction to the short circuit is relatively low, so the voltage at the moment immediate after the fault remains practically the same as before the fault. The most frequent reasons determining short circuits are: following lightning strokes into phase-conductors of overhead lines and damages of cables due to earth construction works as well as internal faults, generally due to ageing of insulation and misconducts.

Short circuits consequences depend on the type, the duration and the location of the fault and the current value is determined by the power of the sources supplying the short circuit, the distance between the source and the fault, the equivalent short circuit impedance, the operating time of the protection devices, the total breaking time and the type of the short circuit (mono, bi or three phase short circuit).

The consequences of the short circuit currents are: the electric arc at the fault location – insulation damages, cables are melting due to the high value of the current density. In the line supplying the short circuit, high potential differences occur, perturbing the normal operation of the connected loads and the isolation of the faulty devices, which generally collapse.

The commutation equipment is highly stressed (thermal and dynamical) by the short circuit current drawn and in some cases it definitively damages. High potential differences and dynamic instability of generators determine perturbations into the near grids [1].

Closing of a switching device can be done in normal or in short circuit operation. In the latest case it's important that the waveform of the short circuit current to be known, along with the model of the faulty grid, the circuit parameters limiting the short circuit current, the type of the short circuit and the calculating methods of the steady state components.

The analytic calculation relationships are based on a simplified calculation, which take into account the longitudinal parameters of the overhead electric lines (resistance and reactance), the transversal impedances being neglected. In the same time, the resistance of the transformers and electric machines are neglected, due to their highly inductive character. In the case of asymmetric short circuits, the direct and inverse sequence reactances are assumed to be equal, leading to an under-evaluation of the short circuit power. In the same time, the component elements of the grid are considered to be symmetric and the electromotive forces of the generators supplying the inductive, the grid becoming actually the load. Taking into account the maximal short circuit current values (10-20). In, or, in certain situations even higher, the schematic depicted in Fig. 2 represents the model of the short circuit fault that occurs in a simple R, L alternating current. In the equivalent circuit, the infinite bus is modeled by an ideal supply source. That condition is emulating a far short circuit, when the reactance of the generator represents maximum 10-15% from the total reactance at the short circuit location [1]. Short circuit are equal in magnitude and phase, being characterized only by the direct sequence component; the circuit elements are considered linear, having lumped parameters and permitting the application of the principle of superposition and consequently the representations of the sub-grids using equivalent impedances. The electric arc in the fault location is neglected, the short circuit being considered a solid one.

In Figs. 1 and 2 are depicted the equivalent schematics in normal operation and in short circuit [1]. The above assumptions lead to the under-estimation of the generators contribution, the short circuit being characterized by the fault at the load location. Thus, the short circuit load becomes highly

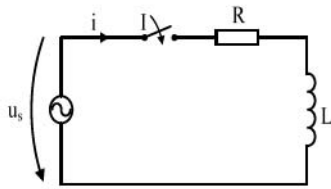


Fig. 1. Equivalent schematic in normal operation

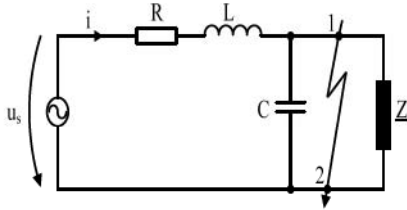


Fig. 2. Equivalent schematic of the short circuit

II. COMMUTATION IN DIRECT VOLTAGE

The commutation issue of direct current breakers is quite different in direct current from the commutation in alternating current [1]. Generally, the commutation refers to connecting and disconnecting the switching devices. Since in the closing process, the electrical, the thermal and the dynamical stresses are less important, the following analysis deals with the disconnection of the contacts. Fig. 3 depicts the direct current switching issue [2].

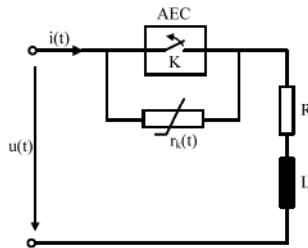


Fig. 3. A simplified schematic of the commutation for a direct current breaker

As an example, a direct voltage $u(t)=U$, that supplies an inductive load in steady state regime is taken into consideration. According to Fig. 3, during the disconnection of the contact, the process can be modeled by a variable resistance $r_k(t)$, presenting a fast increase versus time (eq. 1) [1]:

$$r_k(t) = r_{k0} \cdot \left(\frac{t}{t_0} \right)^p \quad (1)$$

where r_{k0} represents the initial resistance of the contact K of the switching device at $t = t_0$, t_0 representing the moment of the disconnection of the contacts, and p a over-unity exponent.

Due to the increase of the distance between contacts, disconnection of the contact K before the electric arc initiation could be considered as a variable capacitance. This effect is important, mainly in ultrafast disconnecting processes [1].

In Fig. 4 is depicted the equivalent resistance according to eq.1. In an ideal switching process, it can be assumed that the resistance variation is a unit step function versus time jumping instantaneously to the value R_{kmax} that characterize the open circuit. In the case of the mechanical switching that uses the mechanical breaking of the contact, a degree of switching γ can be defined, representing the ratio between the maximum resistance of the contact after disconnection and the resistance of the close contact:

$$\gamma = \frac{R_{kmax}}{r_{k0}} \quad (2)$$

In the very moment of the disconnection of the contact pieces, corresponding to the ideal commutation, the current value in the circuit drop down practically instantaneous to zero, without secondary switching phenomena. The disconnection of the direct current circuit can be modeled by the following differential equations [1]:

$$\begin{cases} L \cdot \frac{di}{dt} + [R + r_k(t)] \cdot i = U \\ i(0) = I_n \end{cases} \quad (3)$$

The voltage developed across the two pieces of the contact is defined by eq. (4):

$$U_K(t) = r_k(t) \cdot i(t) \quad (4)$$

If the instantaneous value of the current exceeds a certain limit, a switching electric arc will occur and will last for a certain duration time t_a . The electric arc extinction is the only one that actually confirms the disconnection of the circuit.

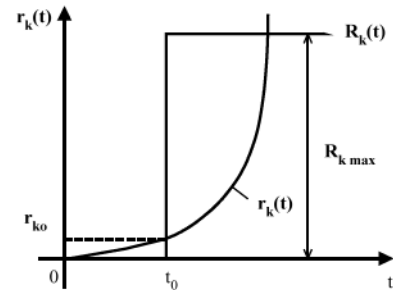


Fig. 4. Equivalent switching resistance

The real disconnection of the direct current circuits lasts for a total disconnecting time t_d that includes the arc duration t_a , considered from the moment of the disconnection command, till this command is validated, actually always with a certain delay. During this delay time, in the contacts area, an amount of energy (W_{com}) is dissipated (eq.5) [1]:

$$W_{com} = \int_0^{t_d} U_K(t) \cdot i(t) \cdot dt \quad (5)$$

For better performances of the switching devices, it is important that the disconnecting time and the dissipated energy should be as low as possible. Obviously, the performances depend on the constructive principle of the extinction room and of the circuit parameters.

In the moment of the disconnection, the electric arc leads mainly to thermal stress on the contacts and on the elements of the extinction room, but also to dielectric stress, due to switching voltages that occur consequently to the arc extinction. The design of the direct current breakers has to take into account the general aspects of the electric arc in the connection and the disconnection of the circuit and especially in short circuit conditions, as follows [3].

The evolution of the arc voltage versus time, for a certain waveform of the current, determines the maximum power extracted from the electric arc. In short circuit operation, it is compulsory to reduce the disconnecting duration of the breaker t_a , using ultrafast switching and to assure a convenient waveform of the limited current.

It is also desirable that the Joule integral reduction should be done by reducing the current peak value instead by reducing the disconnecting duration t_d . A lower value of the disconnecting time implies a higher value of the current rate di/dt , determining high overvoltages at the moment $t = t_0$. A reduced value of the disconnecting time and a higher value of t_d can be obtained only in the case of a convenient arc voltage. The arc voltage increases in the very first moments afterward remaining to value that does not exceed the supply voltage. Thus, the limiting ultrafast circuit breakers should be optimized from the point of view of the cinematic mechanism, especially the contacts and the mobile parts and from the point of view of the disconnection in short circuit conditions.

III. CLASSICAL COMMUTATION METHODS FOR DIRECT VOLTAGE CIRCUITS

In literature, [4], are proposed mainly three methods for breaking a direct current circuit, namely: the generation of a reverse voltage, the oscillation of the divergent current and the method of the reverse current injection. Fig. 5 depicts the typical waveforms of the current and of the voltage, during a direct current breaking for the three methods mentioned above.

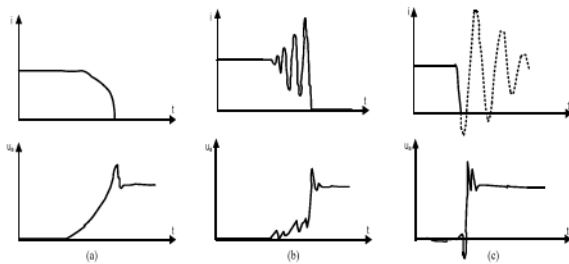


Fig. 5. Typical waveforms during a direct current breaking. (a) – generation of a reverse voltage; (b) – divergent current oscillation; (c) - reverse current injection

The method of generating a reverse voltage reduces the current to zero by creating an arc voltage exceeding the supply voltage. Due to the high arc voltage and to the energy that must

be dissipated, in the case of the high direct voltage systems the use of this method in practice is quite difficult. In the vast majority of the applications, part of the energy is dissipated by commutating the current through a resistor and/or capacitor and the other part through the electric arc. This disconnecting method is known as the current switching method.

The method of the divergent current oscillation creates a zero point by amplifying the magnitude of a high frequency current oscillation. This method uses the variation of the current versus the voltage of the electric arc (Fig. 6), which determines an increasing oscillating current in the circuit formed by the electric arc, the capacitor C and the inductance L.

A small rise in the arc voltage determines an increase of the current flowing through the capacitor, resulting in a corresponding drop down of the current flowing through the arc, which induces a supplementary rise of the voltage, due to the negative slope of the arc characteristics. If the time constant of the arc T_a is lower than a critical value T_c [5]:

$$T_a < T_c = -\frac{1}{2} \cdot r \cdot C + \sqrt{\frac{1}{4} \cdot r^2 \cdot C^2 - \frac{r}{R_a} \cdot L \cdot C}, \quad (6)$$

the amplitude of the oscillating current will increase.

In eq. 6, R_a represents the resistance of the arc in the stable operating point and r the dynamic resistance of the electric arc. If the dynamic resistance has a negative value, the oscillating current amplitude will increase. Alternative current circuit breakers could be also used in such cases, but only with constructive adjustments, in order to minimize the role of the parallel capacitor. This technique is considered a version of the switching current method [4].

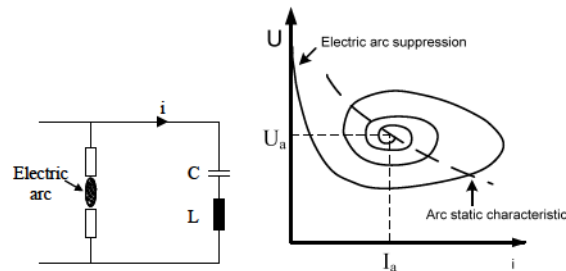


Fig. 6. Electric arc instability

The method of the reverse current injection creates a zero point by superposing a high frequency reverse current generated by the discharge of a previously charged capacitor, over the direct current. The conventional alternating current breakers may be also used, but the ancillary circuit configuration tend to be much more complicated comparing with other methods.

IV. DIRECT VOLTAGE STATIC SWITCHES

Power electronic switches have been taken into consideration from their early appearance, due to the advantages of semiconductors fast switching process, the

absence of the electric arc which implicitly determines a safer operation and a lower maintenance costs.

The main drawbacks of power electronic switches in comparison with the electromechanical circuit breakers are the following: the current slope and the limited operating voltage of the solid state device, high conduction losses and the occurrence of the leakage current.

Both types of breakers present advantages that might be exploited using in the same time the benefits of the solid state devices and of the mechanical contacts. Thus, the drawbacks of the electromechanical fault current limiters, such as the occurrence of the electric arc and the frequent maintenance issues could be removed. In the case of hybrid switches, other switching techniques are often used, i.e. switching techniques at zero crossing voltage and switching techniques at zero crossing current.

Nowadays, hybrid limiters using zero crossing voltage and current are developed and applied to the electromechanical fault current limiters. This symbiosis between the static and electromechanical switching techniques eliminates several drawbacks, resulting in a better reliability of the power current path of the hybrid breaker and in a lower maintenance cost.

Recent researches on hybrid switching technique, using new circuit topologies [6], are oriented towards diminishing the drawbacks of the hybrid commutation, their results highlighting that the ageing duration of the contacts for a hybrid switch is twice to three times lesser than in the case of a conventional circuit breaker [7]. However, in the case of hybrid switches the failure of the contacts material is due mainly to the occurrence and the duration time of the electric arc (50-100 ms).

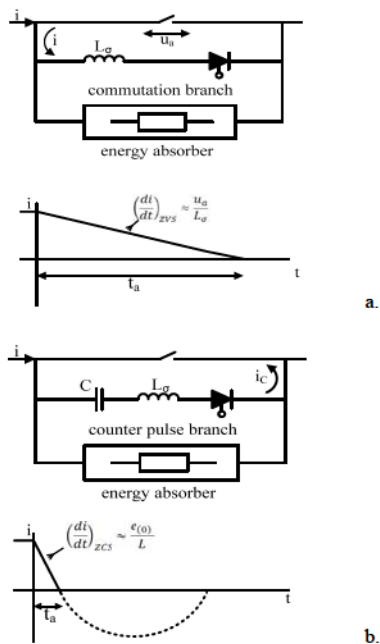


Fig. 7. Hybrid switching technique: a) commutation at zero voltage – zero voltage switching ZVS, b) commutation at zero current – zero current switching ZCS.

This is one of the major drawbacks of hybrid breakers with mechanical contacts, since the occurrence of the electric arc couldn't be avoided. The maximum duration time of the arc together with the rate of the current, di/dt , can be analyzed in order to get a maximum value of the duration till the current drop down to zero. This limit value could be useful as a design criterion for the hybrid switches [8].

In hybrid commutation, two main techniques are used, namely: switching at zero crossing of the voltage (ZVS) and switching at zero crossing current (ZCS), meant to reduce the electric arc duration and to extend the operating time of the electromechanical breaker. The voltage generated across the contacts at the end of the extinction process, depends on the voltage across the supply lines, on the value of the fault current in the faulty path and on the circuit or grid topology and structure. In general, the reduction of the power developed by the electric arc has also effects on reducing the electromagnetic interference (EMI), due to the lower recovery oscillating voltage. Alleviating the influence of the electric arc can be performed by introducing parallel supplementary circuitry across the mechanical contacts, as depicted in Fig. 7.

Prior to the development of high power semiconductor devices (gate turn off thyristors – GTO's or insulated gate bipolar transistors – IGBT's), embedded thyristors in forced switching commutation circuits have been used [9]. Despite their complexity, these topologies have been used for a long period of time in short circuit protections.

The major drawbacks of the forced switching circuits are the limited switching frequency and the complexity of the commutating sequences. In applications related to power systems, the switching behavior represents a relatively secondary problem, since switching at high frequency is not needed.

It has been demonstrated that the costs in association with the losses have a major impact on the system as a whole and on the operation costs [10, 11]. Consequently, due to the low conduction losses and the acceptable life time, the investment amortization costs of the static breakers can be significantly reduced. Moreover, instead of the cooling water, the air forced cooling can be used. From the economical point of view, static breakers using thyristors could be more competitive in comparison with other solutions.

Taking into account the cost issue in industrial applications, thyristor based systems have a great opportunity to be integrated in the near future in the existing grids.

Though a complex ancillary circuit is necessary, in order to permit the forced extinction, thyristors offer a comparative advantage, while the expensive drivers and the isolation circuitry can be avoided by the use of optically controlled thyristors.

In comparison with an IGCT's (insulated gate controlled thyristors) breaker, the blocking time is longer, leading to higher short circuit current values. However, taking into account the time constant values at 50 Hz or 60 Hz, particularly for power systems, it has been found that a low switching rate (1 ms in comparison with 400 μ s) is quite acceptable.

In general, these considerations lead to the conclusion that forced switching circuits still could offer an interesting alternative for applications using power breakers in medium voltage systems.

V. EXPERIMENTAL RESULTS

In the following, the by-pass technology using thyristors in order to limit short circuit currents is presented.

The by-pas short circuit current of the limiter circuitry, flowing through the power contact K1 is depicted in Fig. 8.

The limiter circuitry represents mainly a H thyristor bridge, consisting in the thyristors T1, T2, T3 and T4, the reverse current diodes D1, D2, D3 and D4 and the resonant load of the static breaker formed by the inductance $L_r=50$ mH and the capacitor $C_r=140$ μ F.

The above values of the inductance L_r and the capacitor C_r have been used in the experimental model. The load impedance corresponding to the normal operating regime is depicted by L_n and R_n and the load impedance corresponding to the short circuit regime is depicted by L_{sc} and R_{sc} in Fig. 8. The two load circuits are connected through the IGBT transistors Q1 and Q2. Note that the short circuit current is approximately ten times the value of the normal operating load current.

At the occurrence of a short circuit, the command of the transistor Q2 commutes the current on the load path corresponding to the short circuit regime. Further, the oscillation process of the resonant L_r - C_r circuitry starts when the thyristors T1 and T3 are triggered (Fig. 8).

It is well known that at the beginning of an oscillatory process for a resonant circuitry, the capacitor C_r might be charged from an external supply source. This is needed because when the circuit starts, thyristors T1 and T2 will be turned on, the path of the current is flowing through the load and having zero initial value will flow through T1, L_r , C_r and T3 cancelling the phase displacement from the steady state operation. Thus, at the moment of the turn on command for thyristors T2 and T4, the necessary reactive energy in the switching process no longer exists, determining a short circuit in the commutating circuit.

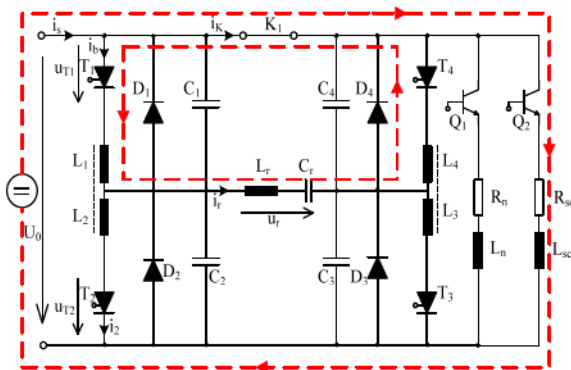


Fig. 8. The reverse current flow through the diode D_4 .

The above considerations are sustained when the extinction of the thyristors from the by-pass circuitry is assured by hard

commutation provided by ancillary extinction thyristors. For the circuit depicted in Fig.8, the extinction group is formed by the extinction capacitors C_1 - C_4 and the extinction magnetically coupled inductances L_1 - L_2 and L_3 - L_4 respectively. The advantage of this extinction group is that when the circuit is connected, the extinction capacitors C_1 - C_4 begin to charge to a voltage equal to $U_0/2$ providing the necessary reactive energy of the extinction process [12].

When thyristor T_3 is turned off, by the turn on of the thyristor T_4 , the current flowing through the group L_r - C_r will flow also through the reverse current diode D_4 , being injected in the opposite direction through the contact K_1 of the electromechanical breaker. This moment represents the moment of the injection of the reverse current and it is desirable that it occurs when the current flowing through the oscillatory circuit L_r - C_r has its maximum.

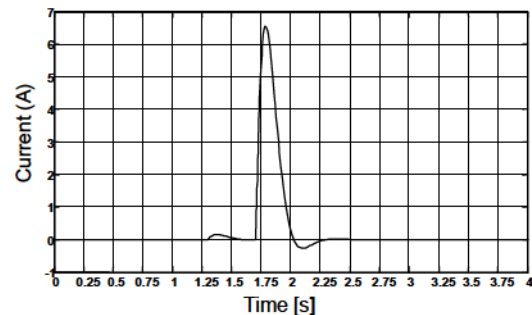


Fig. 9. Experimental determination of the reverse current

VI. CONCLUSIONS

The experimental waveform obtained for the current flowing through the resonant circuitry, injected as a reverse current through the contact K_1 is depicted in Fig. 9.

Further, due to the disconnection of the contact K_1 , the load current will flow through the short circuit impedance R_{sc} - L_{sc} , the diode D_4 , the resonant circuitry L_r - C_r and the thyristor T_1 that is turning off, desirable at the moment when the current flowing through the oscillatory circuitry L_r - C_r becomes zero.

Analyzing the oscillogram depicted in Fig. 9, one may observe a 6.5 A maximum value of the injected reverse current, that will determine a reduction of the short circuit current flowing through the contact K_1 , to approximately 35% from the rated value of the current. Besides, the short circuit duration time is 100 ms shorter.

It is also important to highlight that a reduction of the short circuit current to an amount of 35% of the rated current is generally quite difficult to be obtained in direct current grids, since direct current grids do not present the advantages of alternating current grids, i.e. the periodic zero crossings of the voltage and of the current.

REFERENCES

- [1] Hnatiuc, E. „Aparate electrice”, Editura Tehnopress, Iași, 2011.
- [2] Hnatiuc, E., ș.a. „Bazele teoretice ale funcționării aparatelor electrice”, Editura Venus, Iași 2004.

- [3] Hortopan, Gh., s.a. „Aparate electrice de comutație. Tehnica fenomenelor rapide”, Editura Tehnica, Bucuresti. 1985.
- [4] Baraboi, A., s.a. „Tehnici moderne în comutația de putere”, Editura A 92, Iași, 1996.
- [5] Ryan H., Jones G., „SF₆ Switchgear”, Peter Peregrinus Ltd, London, United Kingdom, 1989.
- [6] Genji, T., Isozaki, M., Yamada, M., Morita, T., and Kaneda, M.: “400 V class high speed current limiting current breaker for electric power system”, IEEE Trans. Power Deliv., 1994, 9, (3), pp. 1428–1435.
- [7] Roodenburg, B., Huijser, T., and Evenblij, B.H.: “Simulation of an electro-magnetic (EM) drive for a fast opening circuit breaker contact”. IEE Pulsed Power Symp., Basingstoke, UK, 8 September 2005, ISBN 0-86341-558-x, pp. 4/1–4/6
- [8] B. Roodenburg, A. Taffone, E. Gilardi, S.M. Tenconi, B.H. Evenblij, M.A.M. Kaanders, “Combined ZVS–ZCS topology for high-current direct current hybrid switches: design aspects and first measurements”, IET Electr. Power Appl., 2007, 1, (2), pp. 183–192.
- [9] R. K. Smith *et al.*, “Solid state distribution current limiter and circuit breaker: Application requirements and control strategies” IEEE Trans. Power Delivery, vol. 8, no. 3, pp. 1155–1164, Jul. 1993.
- [10] A. Ekström, P. Bennich, M. De Oliveira, and A. Wilkström, “Design and control of a current-controlled current limiting device” in Proc. EPE’01 Conf., Graz, Austria, 2001.
- [11] S. Sugimoto, S. Neo, H. Arita, J. Kida, Y. Matsui, and T. Yamagiwa, “Thyristor controlled ground fault current limiting system for ungrounded power distribution systems” IEEE Trans. Power Delivery, vol. 11, no. 2, pp. 940–945, Apr. 1996
- [12] Elena STEFAN, Horia BALAN, Mircea BUZDUGAN, Petros KARAISSAS, “Study of the DC voltage circuit breakers commutation with EMTPWORKS software simulations”, 10th International Conference on Applied and Theoretical Electricity ICATE 2010, ISSN 2069-0150.

Axial-flux vs. radial-flux permanent-magnet synchronous generators for micro-wind turbine application

Adrian Augustin POP, Florin JURCA, Claudiu OPREA, Mihai CHIRCA, Stefan BREBAN,
Mircea M. RADULESCU

TECHNICAL UNIVERSITY OF CLUJ-NAPOCA

22 Memorandumului street, 400114

Cluj-Napoca, Romania

Tel.: +40264 401 829.

E-Mails: Augustin.Pop@emd.utcluj.ro, Florin.Jurca@emd.utcluj.ro,
Claudiu.Oprea@emd.utcluj.ro, Mihai.Chirca@mae.utcluj.ro, Stefan.Breban@emd.utcluj.ro,

Mircea.Radulescu@emd.utcluj.ro

URL: <http://www.utcluj.ro/>

Keywords

«Permanent-magnet synchronous generator», «Direct drive», «Wind energy conversion systems», «Field analysis», «Design».

Abstract

This paper presents a comparative study between the axial-flux and radial-flux permanent-magnet synchronous generators for a 3 kW wind turbine application. This study emphasizes the most cost-effective solution to be implemented by the industrial partner. There are three constructive types of electric generators considered in this work. All are based on permanent-magnet synchronous generators (PMSGs), but one has an axial-flux topology, the other one is a radial-flux outer-rotor machine and the third one is a radial-flux inner-rotor machine. Finite-element field analysis was made for the three PMSGs in order to compare their efficiency and active materials estimated cost. The results show that the axial-flux PMSG is the best solution for micro-wind turbine application.

Introduction

Two major reasons are advocating for cost-effective micro-wind turbine power systems: the need to give a feasible alternative solution to classical and pollutant energy production and the need to make it affordable for the middle-class citizens, especially in Eastern-Europe where the GDP per capita is lower than in Western-Europe. This paper presents a part of the work endeavored to be made within a research project in partnership between the Technical University of Cluj-Napoca, Romania and an industrial small company. The solutions investigated are starting from a few premises: the micro-wind power system should be implemented mainly in urban areas, thus it should be very efficient in converting energy at low wind speeds; the electric generator is directly driven by the turbine and the associated electronic power converters should be controlled in a maximum-power-point-tracking strategy for connection to power grid, and should satisfy the voltage constraints for connection to isolated loads.

The three constructive types of wind-turbine generator considered in this work are permanent-magnet synchronous generators (PMSGs), but one has an axial-flux (AF-PMSG) topology, the other one is of radial-flux outer-rotor (RFOR-PMSG) type, while the third one is of radial-flux inner-rotor (RFIR-PMSG) type. In the following sections, each of the three PMSG topologies are investigated using finite-element field analysis to comparatively show their relative merits and demerits.

Axial-flux permanent-magnet synchronous generator (AF-PMSG)

Axial-flux (AF) PMSGs have a number of distinct advantages over their radial-flux counterparts, i.e. they can be designed to have (i) higher power-to-weight ratio, resulting in less core material,

(ii) planar and easily adjustable air-gaps, (iii) reduced noise and vibration levels. Moreover, the direction of the airgap flux path can be varied, so that additional topologies can be derived [1, 2]. The comparison of different AF-PMSGs is a difficult task. Many researchers try to force comparisons through subjective constraints. The outcome is often that the constraints themselves favor one configuration over the other, leading to inconclusive results and arbitrary selection.

There are possible many variations in the AF-PMSG basic design [3], including single-sided [4], double-sided [5], toroidal [6], and multi-disc designs. The AF-PMSG topology considered in this paper is a three-phase double-rotor one-stator topology with 8 pole-pairs, 3 kW rated power and 200 [rpm] rated speed. The magnets are of high-energy NdFeB-type, and are glued on both sides of the two solid-iron disc-rotors. The stator is made of non-magnetic material.

Slotted stators in the AF-PMSG machine increase notably the amplitude of the airgap flux density due to shorter airgap. This reduces the required amount of rotor-PMs, thus leading to savings in the AF-PMSG cost. Moreover, copper losses in slotted-stator AF-PMSG are lower than those of its slotless-stator counterpart. On the other hand, the use of slotted-stator armature winding results in significant cogging torque and content of harmonics in the back-emf waveform. Both problems may be tackled efficiently from the design point of view.

In [7] and [8], the authors reason the application of slotted-stator concentrated winding in AF-PMSGs. When concentrated windings are used, prefabricated coils can simply be inserted in the stator structure, and the winding process becomes cheaper. Furthermore, the space occupied by the end-windings and thus the corresponding Joule losses are minimized. However, due to the disposition of concentrated-winding coils there are space-harmonic components in the generated armature-reaction m.m.f.

Analytical preliminary design of the small-scale AF-PMSG

From the general sizing equation applied to the small AF-PMSG under study, the outer surface diameter D_o can be obtained as

$$D_o = \left[\frac{8}{\pi^2} \frac{p}{f} \frac{P_{out}}{k_i k_p \eta (1 + \lambda)(1 - \lambda^2)(B_g)} \right]^{1/3} . \quad (1)$$

The total outer diameter of the considered AF-PMSG is given by

$$D_{tot} = D_o + 2W_{Cu} . \quad (2)$$

The total axial length of the AF-PMSG can be expressed as

$$L_{tot} = L_r + 2L_S + 2g , \quad (3)$$

where the rotor axial length sums the rotor-core and rotor-PM contributions, i.e.

$$L_r = L_{r,core} + 2L_{PM} = B \frac{B_u}{B_{r,core}} \cdot \frac{\pi (1 + \lambda) D_o}{8 p} + \frac{\mu_{r,PM} B_g}{B_{rem} - \frac{k_f}{k_d} B_g} k_c g \quad (4)$$

with $B_{r,core}$ defining the flux density in the rotor-disk core; B_u , the attainable flux density on the surface of the rotor-PM; $\mu_{r,PM}$ and B_{rem} , the relative permeability and the remanent flux density of the rotor-PM material, respectively; k_d and k_f , the leakage-flux factor and the peak-value-corrected radial-airgap-flux-density factor of the AF-PMSG, respectively; k_e , the back-emf factor, i.e. the armature-winding distribution factor; N_{ph} , the number of turns in series per armature-winding phase; f , the mains electrical frequency; p , the number of machine pole-pairs; D_i , D_o , the diameters of the inner and outer surfaces of the AF-PMSG, respectively; $\lambda = D_i / D_o$, the inner-to-outer diameter ratio; \hat{B}_g , the peak value of the magnetic flux density in the airgap (magnetic loading); g , the airgap axial length; k_C , the Carter factor, which takes into account the fact that large airgap length in front of the stator-slot and a small one in front of the stator-tooth makes the airgap flux density position-dependent; k_C can be expressed as [1, 6]

$$k_c = \frac{t}{t - \gamma g}, \quad \gamma = \frac{4}{\pi} \left[\frac{W_{so}}{2g} \tan^{-1} \left(\frac{W_{so}}{2g} \right) - \ln \sqrt{1 + \left(\frac{W_{so}}{2g} \right)^2} \right] \quad (5)$$

γ and W_{so} being the average slot-pitch and the slot-opening, respectively.

The stator axial length is

$$L_S = L_{s,core}, \quad (6)$$

$$\text{where } L_{s,core} = \frac{B_g}{B_{s,core}} \cdot \frac{\pi \alpha_p (1 + \lambda) D_0}{4 p} \quad (7)$$

with $B_{s,core}$, denoting the flux density in the stator core; α_p , the ratio of the average-to-peak airgap flux density; J_{slot} , the stator-slot current density; k_{Cu} , the copper-fill factor.

The design specifications and chosen parameters have been considered in determining the main dimensions of rotor and stator components of the small-scale three-phase AF-PMSG, which are listed in Table 1.

3-D finite-element field analysis of the small-scale AF-PMSG

Finite-element (FE) simulations are performed in JMAG Designer 12.0 [9], an electromagnetic field analysis software package that supports the design and development of electric machines, actuators, circuit components etc. Two types of FE simulations are carried out: in no-load (open-circuit) and resistive-load conditions [10].

In order to analyze the performances of the considered small-scale three-phase AF-PMSG, its 3D-model is first constructed, as shown in Fig.1.

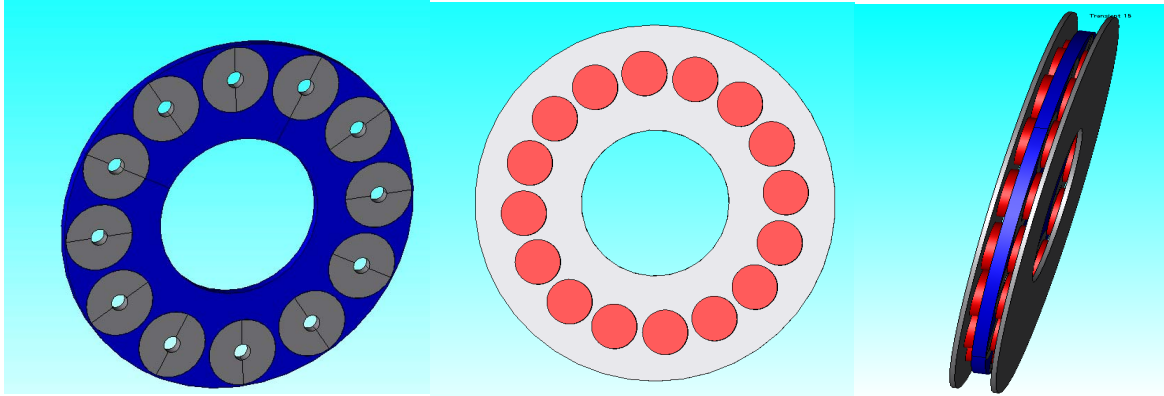


Fig. 1: 3D-model of the three-phase small-scale AF-PMSG topology [9].

The AF-PMSG has a double-rotor-one-stator topology. Rotor-PMs are of Nd-Fe-B 35SH type with axial magnetization. The PM-excitation flux of each rotor-pole travels through the sandwiched-stator and the two axial air gaps to the opposite rotor.

The three-phase stator-winding comprises 2000 [turns/ phase] of 12 [Ω] electrical resistance.

FE simulations are carried out for the three-phase small-scale AF-PMSG running at 200 [rpm] rated speed, under open-circuit and three-phase resistive load of 100 [Ω /phase] conditions, respectively. The simulation results are captured on JMAG Designer and presented in Fig.2. It can be seen that the phase back-emf waveforms have amplitudes of approximately 400 [V/phase] at open-circuit (no-load) and 300 [V/phase] at resistive-load conditions

The magnetic flux density distribution for the small-scale AF-PMSG under study is presented in Fig. 3, showing that there are not saturated zones for this design under no-load and resistive-load conditions.

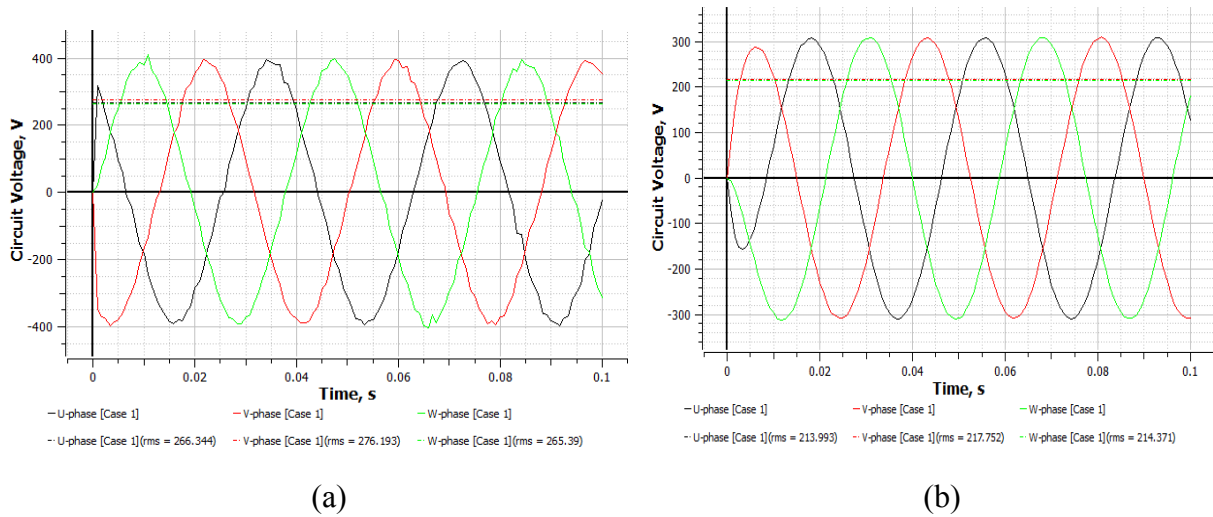


Fig. 2: Back-emf waveforms of the three-phase small-scale AF-PMSG under (a) no-load (open-circuit) and (b) balanced resistive-load conditions, at rated rotor speed.

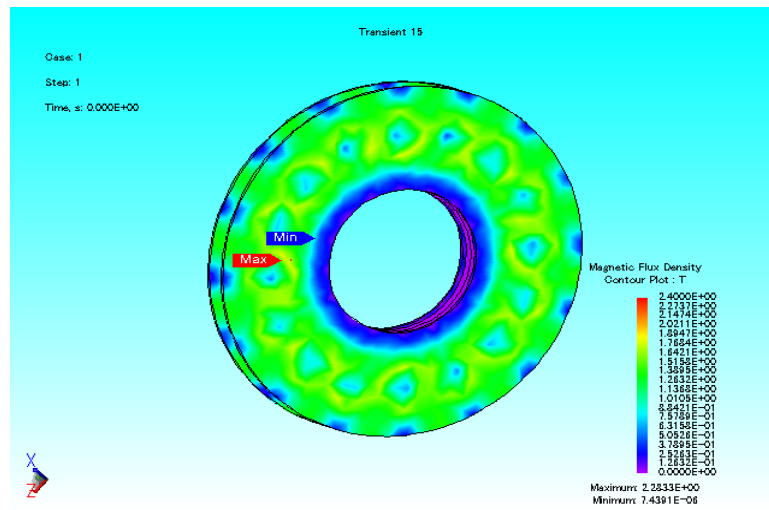


Fig. 3: Magnetic flux-density distribution for the three-phase small-scale PMSG.

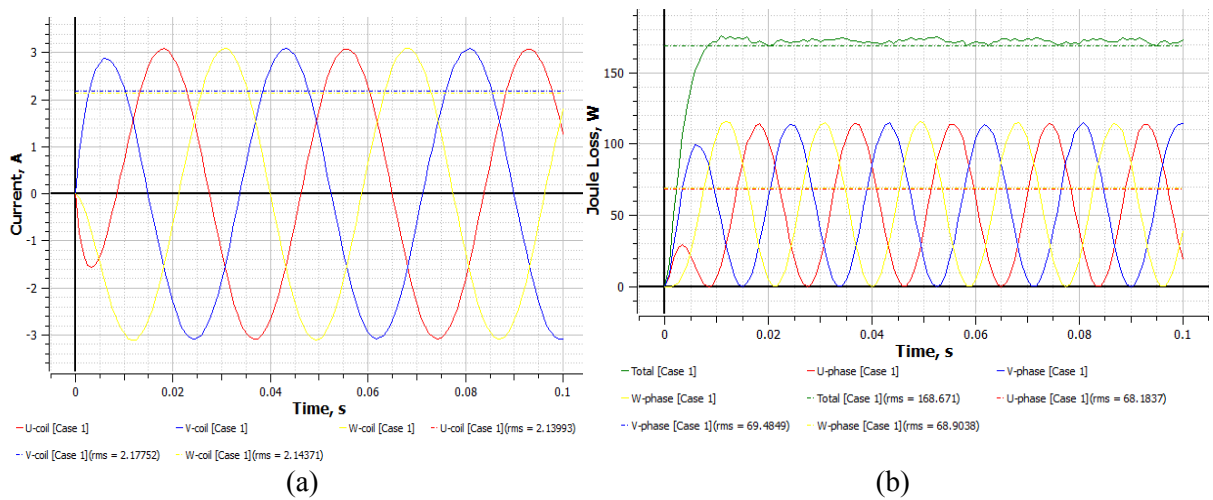


Fig. 4: Phase-current (a) and Joule-loss (b) waveforms of the three-phase small-scale AF-PMSG with balanced resistive load.

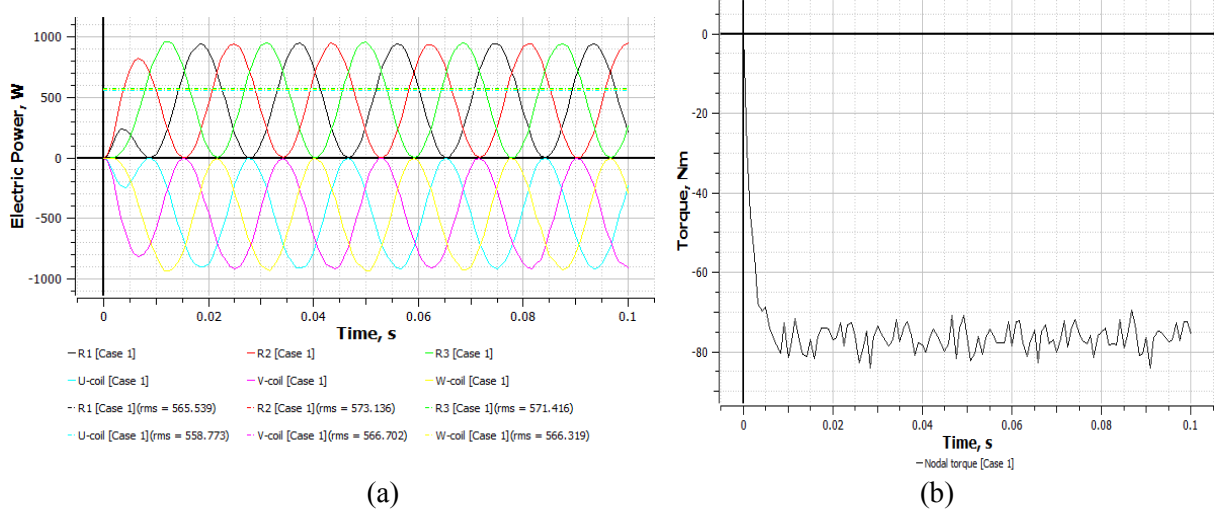


Fig. 5: Electric power / phase and electromagnetic torque of the three-phase small-scale AF-PMSG at balanced resistive-load conditions.

For the three-phase small-scale AF-PMSG under preset resistive-load conditions, the FE-simulated phase current and Joule loss waveforms are shown in Fig. 4.

The developed electric power / phase and electromagnetic torque of the three-phase small-scale AF-PMSG with balanced resistive load are presented in Fig. 5.

Radial-flux outer-rotor permanent-magnet synchronous generator (RFOR-PMSG)

The radial-flux outer-rotor permanent-magnet synchronous generator (RFOR-PMSG) considered here has 15 pole-pairs. The advantage of RFOR-PMSG compared to inner-rotor PMSG is that the magnets are more easily attached to the rotor surface (Fig. 6).

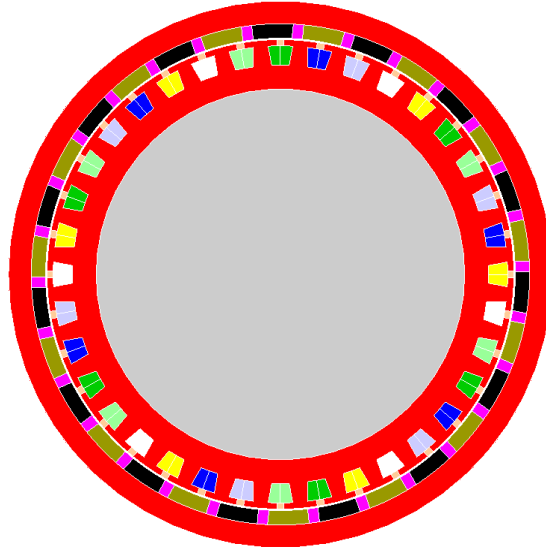


Fig. 6: Three-phase small-scale RFOR-PMSG topology.

As well known, the output power of an electric machine, when the leakage reactance is neglected, is proportional to the number of phases of the machine, n_{ph} , the phase current, $i(t)$, the induced emf, $e(t)$:

$$P_{out} = \eta \cdot \frac{n_{ph}}{T} \cdot \int_0^T e(t) \cdot i(t) dt = \eta \cdot n_{ph} \cdot k_p \cdot E_{max} \cdot I_{max} \quad (8)$$

where T is the period of an emf cycle; E_{max} and I_{max} represent the peak values of the emf and phase current, respectively; k_p is the power coefficient, and η is the estimated efficiency. The peak value of the emf is expressed by introducing the emf coefficient, k_E :

$$E_{max} = k_e \cdot N_t \cdot B_{gap} \cdot D_{gap} \cdot L_m \cdot \frac{f_s}{p}, \quad (9)$$

where N_t is the number of turns per phase, B_{gap} and D_{gap} are the air-gap flux density and diameter, L_m is the length of the machine, f_s is the supplying frequency and p is the number of pole-pairs [11]. By introducing geometric coefficient, $k_L=L_m/D_{gap}$, and current coefficient (related to its waveform) $k_i=I_{max}/I_{rms}$, and defining the phase load ampere-turns,

$$A_t = \frac{2}{\pi} \cdot N_t \cdot \frac{I_{rms}}{D_{gap}}, \quad (10)$$

it is possible to define the airgap diameter of the machine:

$$D_{gap} = \sqrt[3]{\frac{2 \cdot p \cdot P_{out}}{\pi \cdot n_{ph} \cdot A_t \cdot k_e \cdot k_i \cdot k_p \cdot k_L \cdot \eta \cdot B_{gap} \cdot f_s}}. \quad (11)$$

Based on the type of the current waveform, it is possible to define the current and power coefficients for sinusoidal waveform [10], $k_i = \sqrt{2}$, $k_p = 0.5$. All the other geometric parameters will be computed based on this airgap diameter.

The RF-PMSG designer has to choose only the PMs shape and stator slots. As materials for active parts of the machine, Nd-Fe-B PMs with 1.2 [T] remanent flux density and M530-50A steel laminations are used.

FE simulations for the considered three-phase small-scale RFOR-PMSG are carried out using Flux2D software. The magnetic flux-density distribution in the cross-section of the machine is presented in Fig. 7.

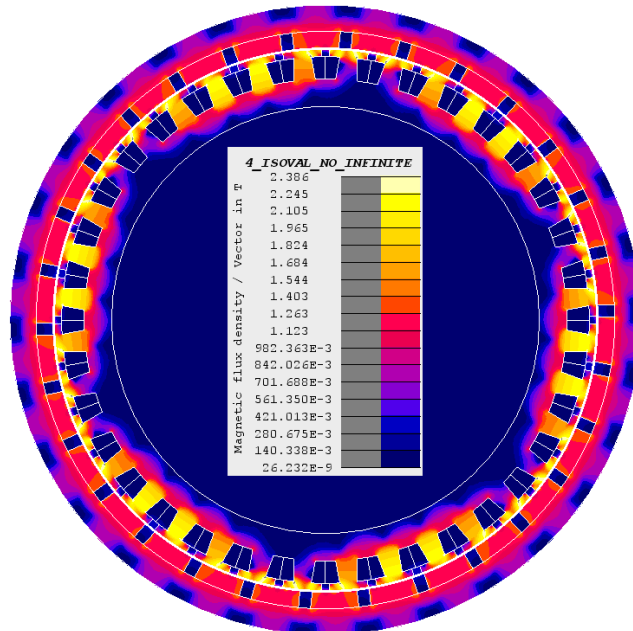


Fig.7: Magnetic flux-density distribution in the cross-section of the three-phase small-scale RFOR-PMSG.

For the three-phase small-scale RFOR-PMSG under no-load (open-circuit) and balanced resistive-load conditions, the FE-simulated back-emf waveforms are shown in Figs. 8 and 9, respectively, at rated rotor speed.

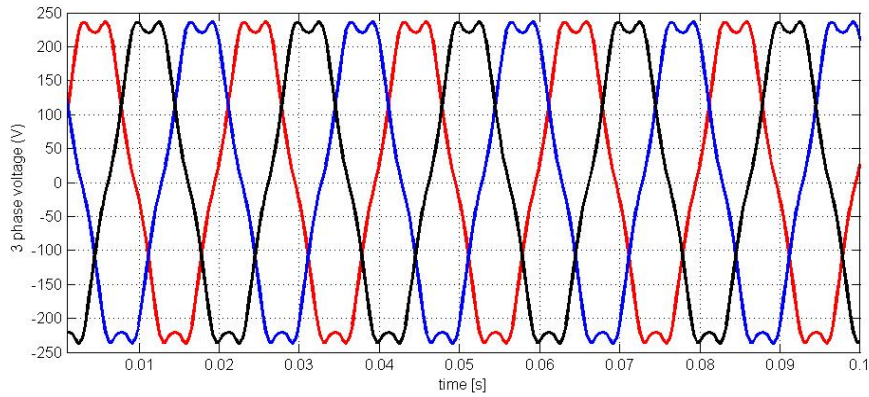


Fig. 8: Phase back-emf waveforms of the three-phase small-scale RFOR-PMSG under (no-load) open-circuit conditions, at rated rotor speed.

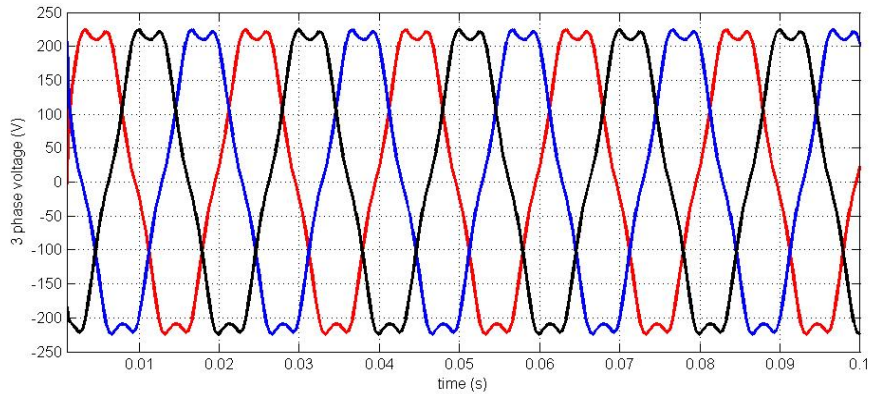


Fig. 9: Phase back-emf waveforms of the three-phase small-scale RFOR-PMSG with balanced resistive load, at rated rotor speed.

Radial-flux inner-rotor permanent-magnet synchronous generator (RFIR-PMSG)

The third three-phase small-scale PMSG topology considered here is a radial-flux inner-rotor (RFIR) one. For its preliminary design, the main geometric dimensions are obtained using the previously-sized RFOR-PMSG topology and the commercially-available electric-machine-design software SPEED, developed at the University of Glasgow, UK. The structure was dimensioned using version 9.1.2.29 of the software [12].

The chosen RFIR-PMSG structure has spoke-shaped, circumferentially-magnetized PMs, buried in the rotor (Fig.10). Due to the rotor-PM placement and magnetization, flux concentration in rotor poles toward the airgap results, and the same volume of PM material can be used for smaller airgap length. The number of stator slots / rotor poles and the three-phase winding configuration are the same as for the prior RFOR-PMSG.

By using SPEED software, extensive simulations have been performed and various geometric dimensions have been modified, in order to obtain optimal electric power, generated voltage and efficiency. The final design model has been exported in JMAG-Studio for checking its validity against FE simulations.

In Fig. 11, FE-simulations for magnetic flux-density distribution in the cross-section of the designed three-phase small-scale RFIR-PMSG, at no-load (open-circuit) and resistive load conditions are presented.

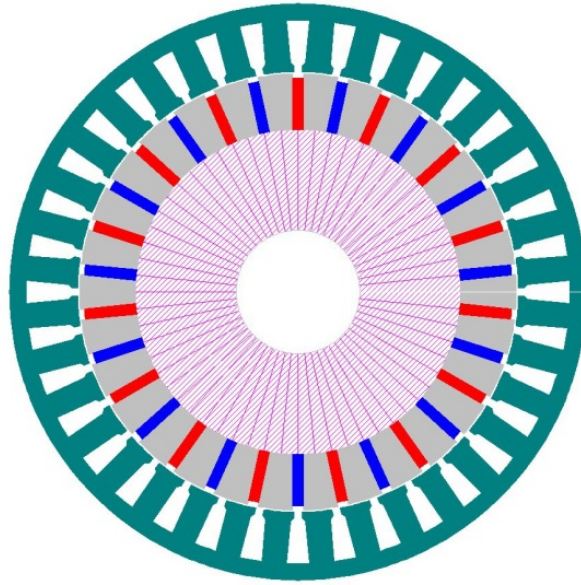


Fig. 10. Three-phase small-scale RFIR-PMSG topology with spoke-shaped, circumferentially-magnetized PMs, buried in the rotor.

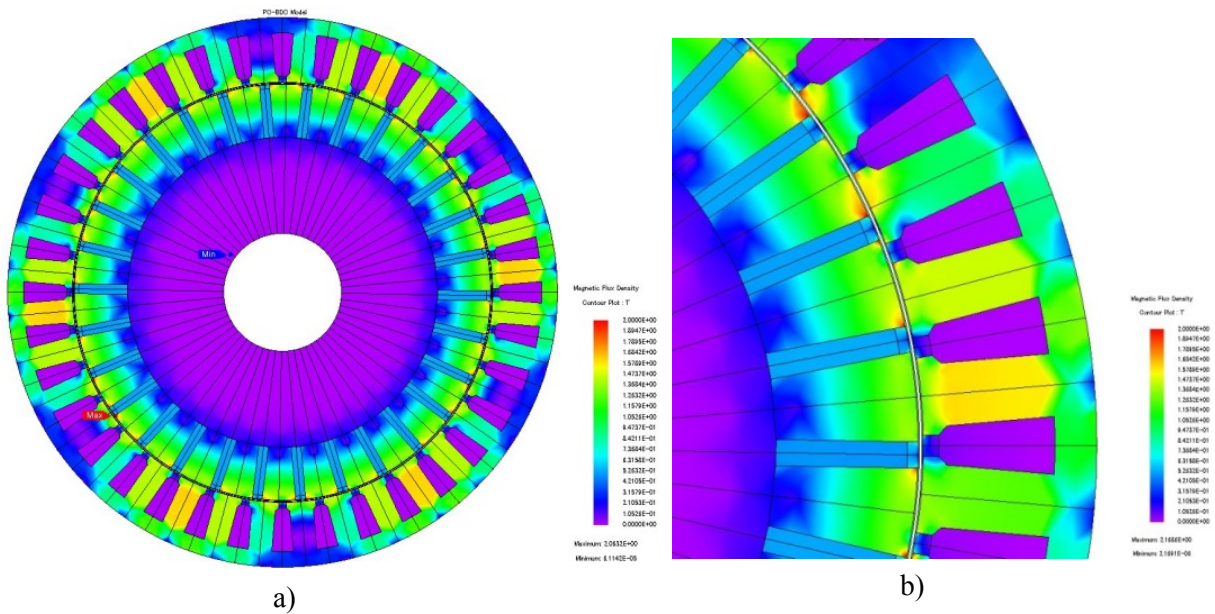


Fig. 11: Magnetic flux-density distribution in the cross-section of the three-phase small-scale RFIR-PMSG, at no-load (a) and resistive-load (b) conditions.

For 120° rotation of the three-phase small-scale RFIR-PMSG under no-load (open-circuit) and balanced resistive-load conditions, the FE-simulated back-emf waveforms are shown in Fig. 12.

The generated phase currents and developed electromagnetic torque of the RFIR-PMSG with balanced resistive load are presented in Fig. 13.

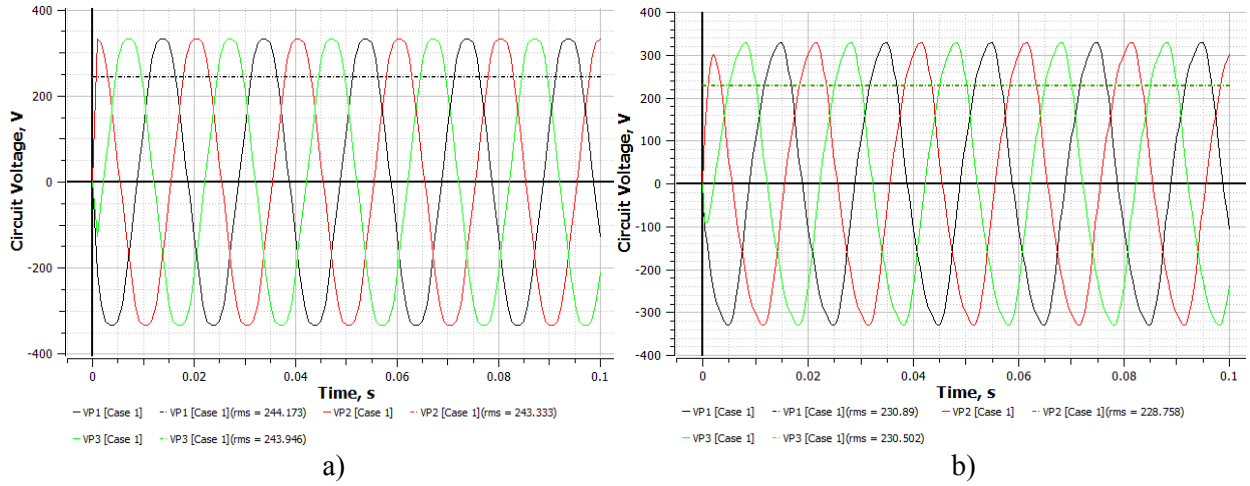


Fig. 12: Back-emf waveforms of the three-phase small-scale RFIR-PMSG under (a) no-load (open-circuit) and (b) balanced resistive-load conditions.

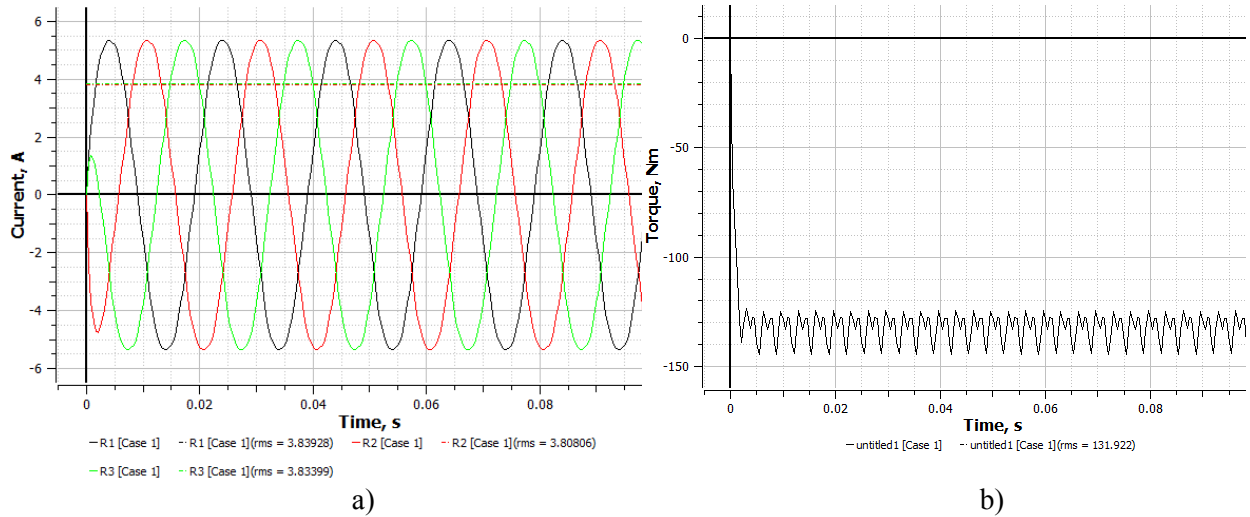


Fig. 13: Generated phase currents and developed electromagnetic torque of the three-phase small-scale RFIR-PMSG at balanced resistive-load conditions.

Comparative results and discussion

The comparative main design results for the three small-scale PMSGs under study for micro-wind turbine application are summarized in Table I. The estimated costs of active materials, i.e. copper, PMs and iron (without considering the rotor shaft) are calculated. The reference prices for them are: 50 [Euro/kg] for PMs, 7.5 [Euro/kg] for copper and 3 [Euro/kg] for stator and / or rotor iron. These prices only refer to the raw materials, disregarding the manufacturing and non-active part costs. AF-PMSG has the highest cost due to PMs needed for the double-rotor topology, but is easier to manufacture and more lightweight compared to the other two PMSGs. The RFOR- and RFIR-PMSGs have lower estimated cost of active materials compared to that for AF-PMSG. In order to estimate the total cost of the small-scale PMSG an estimated manufacturing cost factor (K) is introduced. It is thus considered that for AF-PMSG, $K = 1.5$, meaning that the manufacturing cost is 50% of the cost of active materials, while for RFOR- and RFIR-PMSGs, $K = 2$, due to more complex manufacturing processes. The lowest total estimated costs result for the three-phase small-scale AF-PMSG.

Table I: Comparative main design results of the three-phase small-scale PMSGs under study

	AF-PMSG	RFOR-PMSG	RFIR-PMSG
Copper weight	11.64 kg	8.3 kg	9.14 kg
Permanent-magnet weight	10.06 kg	7.5 kg	5.55 kg
Iron weight	18.14 kg	32.8 kg	44.69 kg
Shaft weight	-	22.3 kg	5.41 kg
Total weight	39.84 kg	70.9 kg	59.39 kg
Efficiency	92 %	89.23 %	92.32 %
Turns per phase	2000	234	282
Turns per coil	500	39	47
Wire diameter	0.56 mm ²	1.4 mm ²	1.4 mm ²
Phase resistance	12 Ohm	3.4 Ohm	2.54 Ohm
Airgap	1 mm	0.8 mm	1 mm
Number of poles (PM - rotor)	16	30	30
Outer radius	295 mm	250 mm	140 mm
Stack length	-	300 mm	200 mm
Active materials estimated cost	609.8 Euro	535.65 Euro	478.12 Euro
Manufacturing cost factor (K)	1.5	2	2
Total estimated costs	914.7 Euro	1071.3 Euro	956.24 Euro

Conclusion

Three topologies of small-scale PMSGs have been considered for micro-wind turbine application, and comparatively studied through preliminary design and FE field analysis. The main design results have shown that AF-PMSG and RFIR-PMSG topologies have similar efficiencies, slightly higher than that of RFOR-PMSG. Although AF-PMSG has the most costly active materials, its overall estimated costs are lower compared with those of RFOR- and RFIR-PMSG topologies, mainly due to its cheaper manufacturing costs.

Acknowledgement

This work was supported by Romanian Executive Unit for Financing Higher Education, Research, Development and Innovation (UEFISCDI) from the research project with the code PN-II-PT-PCCA-2011-3.2-1696.

References

- [1] B.J. Chalmers, W. Wu and E. Spooner, "An axial-flux permanent-magnet generator for a gearless wind energy system", *IEEE Trans. Energy Convers.*, Vol. 14, No. 2, pp. 251-257, 1999.
- [2] J.F. Gieras, R.-J. Wang, M.J. Kamper, *Axial flux permanent magnet brushless machines*, 2nd edition, Springer-Verlag, 2008
- [3] A. Parviainen, *Design of axial-flux permanent magnet low-speed machines and performance comparison between radial-flux and axial-flux machines*, Ph.D. Thesis, Lappeenranta Univ. of Technology, Finland, 2005.
- [4] J.R. Bumby and R. Martin, "Axial-flux permanent-magnet air-cored generator for small-scale wind turbines", *Proc. IEE – Electr. Power Applic.*, Vol. 152, No. 5, pp 1065-1075, 2005.
- [5] A.A. Pop, F. Gillon and M.M. Radulescu, "Modelling and permanent-magnet shape optimization of an axial-flux machine", *Proc. Int. Conf. Electr. Mach. – ICEM 2012*, pp. 357-363, 2012.
- [6] A. Mahmoudi, H.W. Ping and N.A. Rahim, "A comparison between the TORUS and AFIR axial-flux PM machine using finite element analysis", *Proc. IEEE Int. Electr. Mach. Drives Conf. – IEMDC 2011*, pp. 242-247.
- [7] A. Di Gerlando *et al.*, Axial-flux PM machines with concentrated armature windings: design analysis and test validation of wind energy generators, *IEEE Trans. Ind. Electron.*, Vol. 58, No. 9, pp. 3795-3805, 2011.
- [8] Y. Chen, P. Pillay and A. Khan, "PM wind generator topologies", *IEEE Trans. Ind. Applicat.*, Vol. 41, No. 6, pp. 1619–1626, 2005.
- [9] <http://www.jmag-international.com/>
- [10] F. Wang *et al.*, "Design features of low-speed permanent-magnet generator direct driven by wind turbine", *Proc. 8th Int. Conf. Electr. Mach. Syst. – ICEMS 2005*, pp. 1017-1020, 2005.
- [11] J. Chen, V.N. Chemmangot and L. Xu. "Design and finite element analysis of an outer-rotor permanent-magnet generator for directly coupled wind turbines", *IEEE Trans. Magn.*, Vol. 36, No. 5, pp. 3802–3809, 2000.
- [12] <http://www.speed-emachine-design.com/>